R. B. Holmberg
AB Svenska Fläktfabriken,
Jönköping, Sweden

Heat Transfer in Liquid-Coupled Indirect Heat Exchanger Systems

The theory of liquid-coupled indirect heat exchanger systems has been studied to ascertain optimum criteria with respect to the coupling-liquid flow rate and the distribution of total heat transfer area between the hot-side and cold-side exchanger units in the case of counterflow arrangement. The optimum coupling-liquid capacity rate is derived and given as a function of the over-all capacity rate ratio and the N_{tu} ratio between the two exchanger units. For this optimum liquid capacity rate together with the proposed over-all number of transfer units, it is shown that the over-all heat transfer effectiveness of the liquid-coupled system can be expressed in the ordinary form for individual exchanger units in true counterflow.

Introduction

This study of liquid-coupled indirect heat exchanger systems concerns heat recovery for air conditioning. The results are, however, expected to be applicable to indirect exchanger systems in other fields. The system consists of two heat exchanger units together with a circulation system for the coupling-liquid (see Fig. 1). With this arrangement the circulating liquid, selected with respect to the actual temperature level, transfers thermal energy from the hot fluid to the cold fluid.

In such a system the coupling-liquid flow rate or capacity rate (mass flow times specific heat) is an independent variable and can be chosen to maximize the over-all effectiveness for given heat transfer areas, given hot-fluid and cold-fluid capacities and given overall heat transfer coefficients. Here it is assumed that the free flow area of the liquid in practical exchanger units can be chosen so that economical optimum liquid velocity is obtained. Thus, the optimum liquid capacity rate is determined for constant liquid velocity and variable free flow area, i.e., the overall heat transfer coefficients are kept constant. Kays and London [1, 2][1] derived in connection with heat recovery in gas-turbine plants the optimum liquid capacity rate in the special case of equal hot-fluid and cold-fluid capacity rates and counterflow arrangements. They found that the optimum liquid capacity rate is equal to the capacity rates of the hot and cold fluids, which themselves are equal.

In the present paper this thermal optimum capacity rate is derived without restrictions in fluid capacity rates, while the independent problem to determine the economical optimum liquid velocity is not treated. Furthermore, thermal optimum distribution of total heat transfer area between the hot-side and cold-side exchanger units is determined for two given conditions in the case of optimum liquid capacity rate. The first condition is constant total heat transfer area, which in a qualitative way corresponds to given total exchanger volume or weight. The second condition is constant total UA value perhaps of less interest in practice [2].

The optimization rules in question can, for example, be used in sizing liquid-coupled heat recovery systems in air conditioning. In this case the capacity rate and the heat transfer coefficient of the hot fluid can be replaced by "effective" values of these parameters in order to take water vapor condensation in the hot fluid into account. The effective values includes the effect of latent heat transfer rate and are obtained by dividing the capacity rate and the heat transfer coefficient by the "sensible heat factor" [4], which means the quotient between sensible and total heat transfer rate. In this particular case the procedure of maximizing the over-all effectiveness becomes iterative, since the sensible heat factor is not known from the beginning. The performance of heat recovering systems in air conditioning is described in reference [5].

Effectiveness—N_{tu} Relations

The over-all effectiveness ϵ_o of the liquid-coupled system is derived with the assumptions that the heat exchange with the surroundings of the system and the heat generation of the pump are negligible. This is usually valid in practical cases.

The definitions of the over-all effectiveness ϵ_o, the effectivenesses ϵ_h and ϵ_c of the hot-side and cold-side units, respectively, are as follows:

$$\epsilon_o = \frac{Q}{C_{\min,o}\theta_o}, \quad \epsilon_h = \frac{Q}{C_{\min,h}\theta_h}, \quad \epsilon_c = \frac{Q}{C_{\min,c}\theta_c}, \quad (1)$$

where the heat transfer rate is

[1] Numbers in brackets designate References at end of paper.

Contributed by the Heat Transfer Division for publication in the JOURNAL OF HEAT TRANSFER. Manuscript received by the Heat Transfer Division March 20, 1975. Paper No. 76-HT-E.

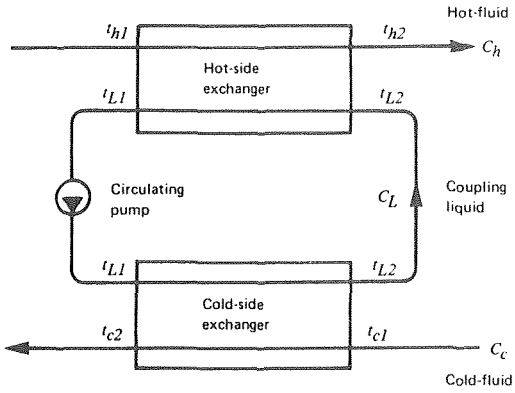

Fig. 1 Schematic view of liquid-coupled heat exchanger system in counterflow

$$Q = C_h \Delta t_h = C_c \Delta t_c = C_L \Delta t_L . \tag{2}$$

$C_{\min,o}$ is the smaller of the hot-fluid and cold-fluid capacity rates, C_h and C_c. $C_{\min,h}$ stands for the smaller of C_h and the liquid capacity rate C_L in the hot-side unit, while $C_{\min,c}$ is the smaller of the capacity rates in the cold-side unit, C_c and C_L. The temperature differences θ_o, θ_h, θ_c, Δt_h, Δt_c and Δt_L are clear from Fig. 2.

The relations (1) and (2) together with the temperature relation

$$\theta_o = \theta_h + \theta_c - \Delta t_L ,$$

obtained from Fig. 2, give the following expression for ϵ_o as a function of ϵ_h and ϵ_c:

$$\epsilon_o = \frac{1}{\dfrac{C_{\min,o}/C_{\min,h}}{\epsilon_h} + \dfrac{C_{\min,o}/C_{\min,c}}{\epsilon_c} - \dfrac{C_{\min,o}}{C_L}} . \tag{3}$$

Depending on the ratio between the three capacity rates this equation results in six different expressions, which have been derived in [2]. These equations require constant capacity rate values throughout the liquid-coupled system. In most practical cases this requirement can be fulfilled by referring the capacity rates to representative temperatures in the system, for example, mean temperatures. Furthermore, the equations can be shown to be valid without restrictions in flow arrangements. The hot-side and cold-side units can be arranged in counterflow, crossflow, etc., and need not be arranged in the same way. However, in liquid-coupled systems the exchanger units are usually arranged in counterflow, or nearly in counterflow, and therefore only the counterflow arrangement is discussed in the following.

For the case of true counterflow, the effectivenesses ϵ_h and ϵ_c of the units according to [1, 3] can be presented in the well-known form

$$\epsilon_n = \frac{1 - \exp[-N_{tu,n}(1 - R_n)]}{1 - R_n \exp[-N_{tu,n}(1 - R_n)]} \quad \text{for } R_n \neq 1,$$
$$\epsilon_n = \frac{N_{tu,n}}{1 + N_{tu,n}} \quad \text{for } R_n = 1, \tag{4}$$

with the number of transfer units

$$N_{tu,n} = U_n A_n / C_{\min,n}$$

and the capacity rate ratio

$$R_n = C_{\min,n}/C_{\max,n},$$

where n stands for c or h.

The six equations for the over-all effectiveness can be expressed in the following equations, by inserting the relations for ϵ_h and ϵ_c (4) into the equation (3):

$$\epsilon_o = \frac{1}{\dfrac{1 - R_L a}{1 - a} + \dfrac{R_L - R_o b}{1 - b} - R_L} \quad \text{for } R_L \neq 1 \text{ and } R_L \neq R_o,$$
$$\epsilon_o = \frac{1}{\dfrac{1}{N_{tu}^{\min}} + \dfrac{1 - R_o b}{1 - b}} \quad \text{for } R_L = 1 \text{ and } R_o \neq 1,$$
$$\epsilon_o = \frac{1}{\dfrac{1 - R_o a}{1 - a} + \dfrac{1}{N_{tu}^{\max}}} \quad \text{for } R_L = R_o \neq 1, \tag{5}$$
$$\epsilon_o = \frac{1}{\dfrac{1}{N_{tu}^{\min}} + \dfrac{1}{N_{tu}^{\max}} + 1} \quad \text{for } R_L = R_o = 1;$$

where

$$a = \exp[-N_{tu}^{\min}(1 - R_L)], \quad b = \exp[-N_{tu}^{\max}(R_L - R_o)],$$
$$N_{tu}^{\min} = (UA)^{\min}/C_{\min,o}, \quad N_{tu}^{\max} = (UA)^{\max}/C_{\min,o},$$
$$R_o = C_{\min,o}/C_{\max,o}, \quad R_L = C_{\min,o}/C_L .$$

The superscript min indicates that exchanger unit, which has the smaller of the hot and cold fluid capacity rates, C_h and C_c, while max indicates that unit, which has the larger of C_h and C_c. The subscripts min,o and max,o indicate the smaller and the larger of the hot-fluid and cold-fluid capacity rates, respectively, excluding the coupling-liquid capacity rate.

Optimum Coupling-Liquid Flow Rate

The coupling-liquid flow rate or capacity rate C_L is chosen to maximize the over-all effectiveness ϵ_o for given N_{tu} values. This optimum value of C_L is obtained by partial differentiation of equation (5) for $R_L \neq 1$ and $R_L \neq R_o$ according to $\partial\epsilon_o/\partial C_L = 0$ or $\partial\epsilon_o/\partial(1/R_L) = 0$.

The derivation results for constant values of $N_{tu}^{\min}$ and $N_{tu}^{\max}$

Nomenclature

A = heat transfer area
A^* = heat transfer area ratio, $A^{\min}/A^{\max}$
A_t = total heat transfer area, $A^{\min} + A^{\max}$
$\bar{A}_t$ = dimensionless A_t, $U^{\min}A_t/C_{\min,o}$
C = heat capacity rate (mass flow times specific heat)
N_{tu} = number of heat transfer units, $UA/C_{\min}$
$N_{tu}{}^o$ = over-all number of transfer units, $1/(1/N_{tu}{}^{\min} + 1/N_{tu}{}^{\max})$
$N_{tu}{}^*$ = N_{tu} ratio, $N_{tu}{}^{\min}/N_{tu}{}^{\max}$
$N_{tu,o}$ = sum of N_{tu}, $N_{tu}{}^{\min} + N_{tu}{}^{\max}$
R_L = liquid capacity rate ratio, $C_{\min,o}/C_L$
R_n = capacity rate ratio, $C_{\min,n}/C_{\max,n}$, where n stands for c or h
R_o = over-all capacity rate ratio, $C_{\min,o}/C_{\max,o}$
Δt = fluid-temperature change in passing through exchanger
U = unit over-all heat transfer coefficient
U^* = unit over-all transfer coefficient ratio, $U^{\min}/U^{\max}$
$(UA)_t$ = total UA value, $(UA)_t = (UA)^{\min} + (UA)^{\max}$
ϵ = unit heat transfer effectiveness, actual heat transfer rate divided by maximum possible heat transfer rate
ϵ_o = over-all heat transfer effectiveness
θ = temperature difference between inlet fluids to exchanger units or over-all liquid-coupled system

Subscripts

c = cold-fluid or cold-side exchanger unit
h = hot-fluid or hot-side exchanger unit
L = coupling-liquid
o = over-all liquid-coupled system
min,n max,n = the smaller and the larger of the two fluids in exchanger n, respectively, where n stands for c, h, or o

Superscripts

min, max = exchanger unit with the smaller and the larger of the hot and cold fluid capacity rates, respectively

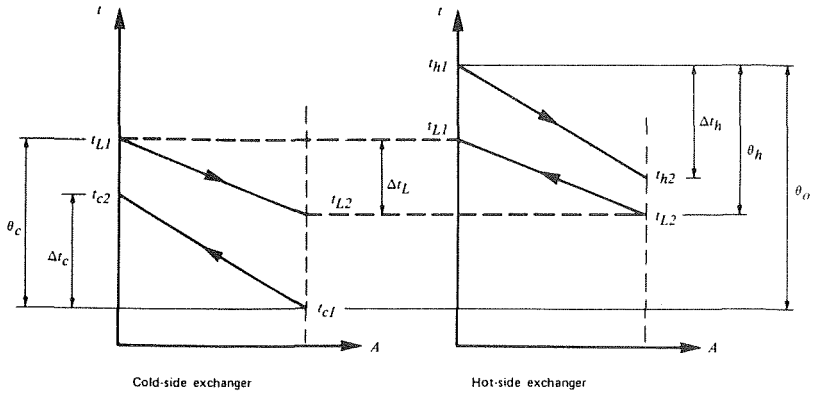

Fig. 2 Schematic temperature conditions for counterflow in heat exchanger units

in $(a-b)\,(1-a)\,(1-b) = (1-a)^2\,b \ln b - (1-b)^2\,a \ln a$.

This equation has only one solution $a = b$ within the region of definition $R_L \neq 1$ and $R_L \neq R_o$, that is $a \neq 1$ and $b \neq 1$. Thus the relation $a = b$ gives the maximum value of ϵ_o. This equality results in

$$R_{L,\,\mathrm{opt}} = \frac{N_{tu}{}^{\min} + R_o N_{tu}{}^{\max}}{N_{tu}{}^{\min} + N_{tu}{}^{\max}} = \frac{N_{tu}{}^{*} + R_o}{N_{tu}{}^{*} + 1},$$

where

$$N_{tu}{}^{*} = \frac{N_{tu}{}^{\min}}{N_{tu}{}^{\max}} = \frac{(UA)^{\min}}{(UA)^{\max}},$$

or

$$\frac{1}{C_{L,\,\mathrm{opt}}} = \frac{1}{(UA)^{\min} + (UA)^{\max}} \left(\frac{(UA)^{\min}}{C_{\min,o}} + \frac{(UA)^{\max}}{C_{\max,o}}\right).$$

Consequently, the optimum liquid capacity rate in true counterflow is obtained as the reciprocal mean value of the hot-fluid and cold-fluid capacity rates in the case of $N_{tu}{}^{*} = 1$.

This optimum value $R_{L,opt}$, that is $a = b$, gives with (5) the following simple expressions for the over-all effectiveness

$$\epsilon_o = \frac{1-a}{1-R_o a} = \frac{1-\exp[-N_{tu}{}^{o}(1-R_o)]}{1-R_o \exp[-N_{tu}{}^{o}(1-R_o)]} \quad \text{for } R_o \neq 1,$$

$$\epsilon_o = \frac{N_{tu}{}^{o}}{1+N_{tu}{}^{o}} \quad \text{for } R_o = 1,$$

where

$$\frac{1}{N_{tu}{}^{o}} = \frac{1}{N_{tu}{}^{\min}} + \frac{1}{N_{tu}{}^{\max}}$$

is the over-all number of transfer units for the liquid-coupled system. Note that $N_{tu}{}^{o}$, defined as this reciprocal sum, allows ϵ_o to be expressed in the ordinary form for individual exchanger units in true counterflow according to equation (4). The graphical representation of this equation is illustrated in Fig. 3 [1, 3]. The reciprocal definition of $N_{tu}{}^{o}$ means that the coupling-liquid can be considered as an ordinary thermal resistance in the case of optimum liquid capacity rate or flow rate.

In order to investigate how a nonoptimum liquid capacity rate affects the over-all effectiveness, ϵ_o as a function of $1/R_L$ is given in Fig. 4 and 5 for some values of the parameters R_o, $N_{tu}{}^{o}$ and $N_{tu}{}^{*}$ defined in the foregoing. It can be seen from the figures that the optimum becomes critical only for large $N_{tu}{}^{o}$ values and that it becomes less critical when R_o goes to zero.

Optimum Relation Between Hot-Side and Cold-Side Exchanger Units

In the case of optimum liquid capacity rate the area ratio $A^{*} = A^{\min}/A^{\max}$ for the two exchanger units is chosen to maximize the over-all effectiveness ϵ_o for given total heat transfer area $A_t = A^{\min} + A^{\max}$. This optimum value of A^{*} is obtained by partial differen-

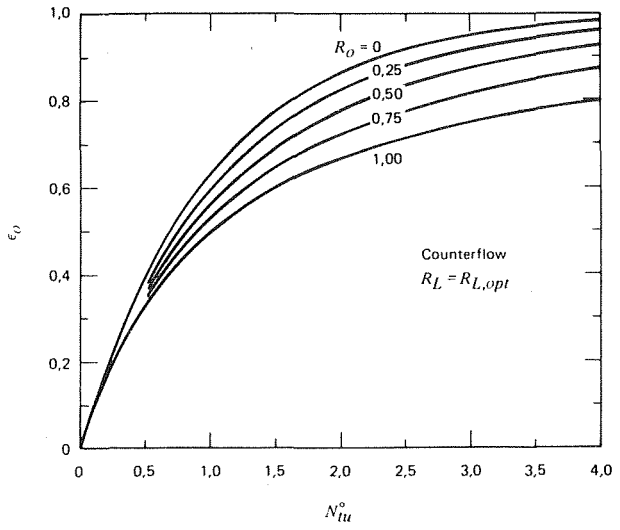

Fig. 3 Over-all effectiveness as a function of over-all number of transfer units with over-all capacity rate ratio as a parameter for optimum coupling-liquid capacity rate

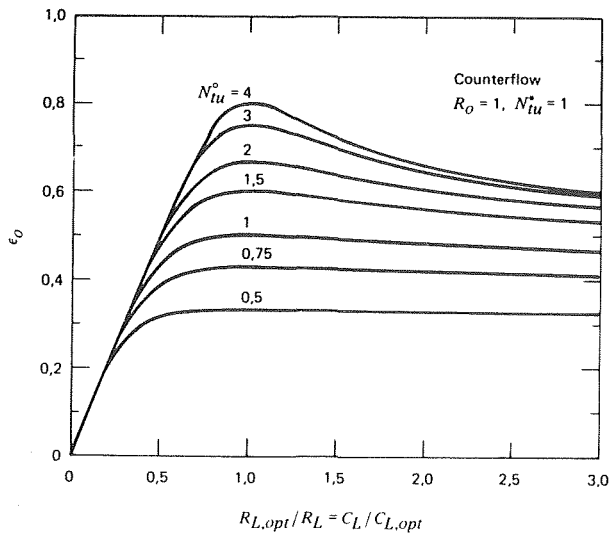

Fig. 4 Optimum conditions for coupling-liquid capacity rate with $N_{tu}{}^{o}$ as a parameter

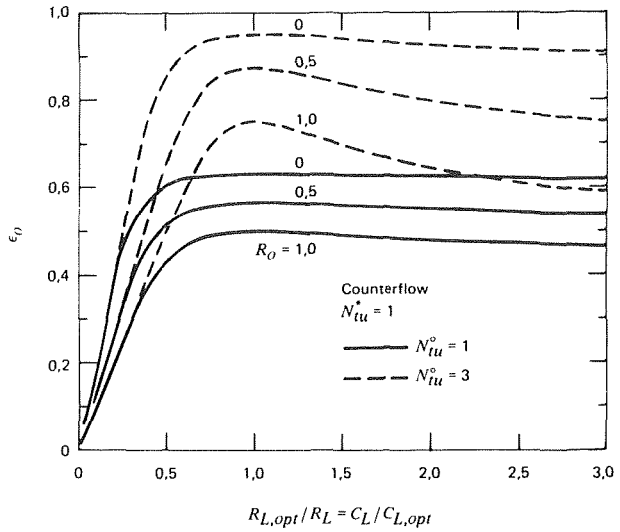

Fig. 5 Optimum conditions for coupling-liquid capacity rate with R_o as a parameter

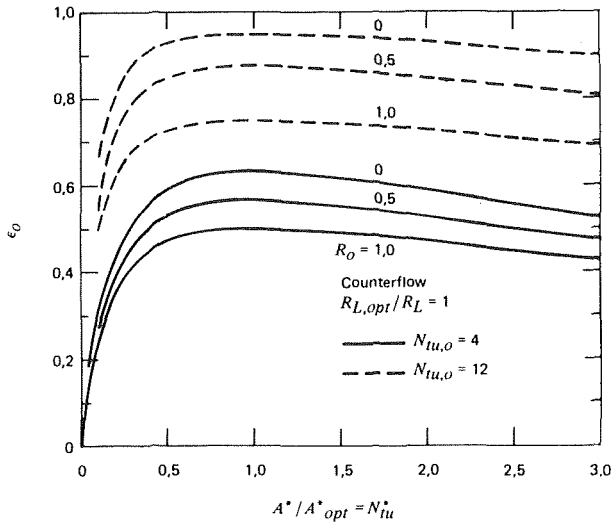

Fig. 7 Optimum conditions for heat transfer area distribution with given total *UA* value, in dimensionless form $N_{tu,o}$

tiation of ϵ_o or of $N_{tu}{}^o$.

With $N_{tu}{}^o = \dfrac{A_t U^{\min}}{C_{\min,o}} \cdot \dfrac{A^*}{(1 + U^*A^*)(1 + A^*)}$,

equation $\left(\dfrac{\partial N_{tu}{}^o}{\partial A^*}\right)_{U^*} = 0$ gives $A^*_{\text{opt}} = 1/(U^*)^{0.5}$.

This optimum relation is valid for arbitrary values of the overall capacity rate ratio R_o. It is also to be noted that the problem of minimizing the total transfer area for a given overall effectiveness is identical with the described problem.

A sometimes used alternative, perhaps of less interest in practice [2], is the optimization of A^* for given total UA value, $(UA)_t = (UA)^{\min} + (UA)^{\max}$. The partial differentiation of $N_{tu}{}^o$ gives in this case $A^*_{\text{opt}} = 1/U^*$ for arbitrary values of R_o and optimum liquid capacity rate. When $U^* = 1$ this result $A^*_{\text{opt}} = 1$ agrees with that of given A_t.

In order to investigate how a nonoptimum distribution of the total heat transfer area affects the overall effectiveness, ϵ_o as a function of A^*/A^*_{opt} is given in Fig. 6 and 7 for $R_L = R_{L,\text{opt}}$ and some values of the parameter R_o in the case of given $(UA)_t$, in dimensionless form $N_{tu,o} = (UA)_t/C_{\min,o} = N_{tu}{}^{\min} + N_{tu}{}^{\max}$. For $U^* = 1$ the curves are valid also for given A_t, in dimensionless form $\bar{A}_t = U^{\min}A_t/C_{\min,o}$. Fig. 8 shows how $U^* \neq 1$ influences the optimum character in the case of given $\bar{A}_t$. It is seen from these figures that the optimum is very flat for all values of the actual parameters. For example the overall effectiveness is decreased less than 4 percent if the area ratio is varied in the range of 0.5–2.0 times the optimum value.

Conclusions

The derived optimum coupling-liquid capacity rate $C_{L,\text{opt}}$ (or $R_{L,\text{opt}}$) and the overall number of transfer units $N_{tu}{}^o$ (the reciprocal sum of $N_{tu}{}^{\min}$ and $N_{tu}{}^{\max}$) are found to give the same ϵ-N_{tu} relation for the over-all effectiveness in counterflow as for the effectiveness of the individual exchanger units in counterflow. The reciprocal expression of $N_{tu}{}^o$ means that the coupling-liquid can be considered as an ordinary thermal resistance. The optimum value of the coupling-liquid capacity rate is critical only for large $N_{tu}{}^o$ values. The optimum area ratio A^*_{opt} for the two exchanger units is not critical for any value of the actual parameters.

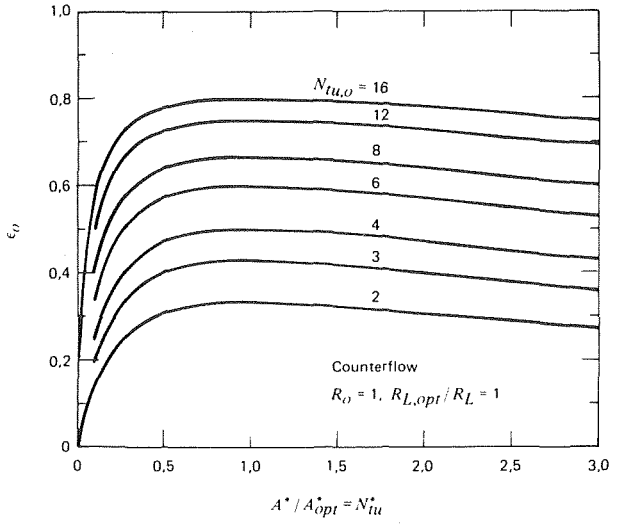

Fig. 6 Optimum conditions for heat transfer area distribution with given total *UA* value, in dimensionless form $N_{tu,o}$

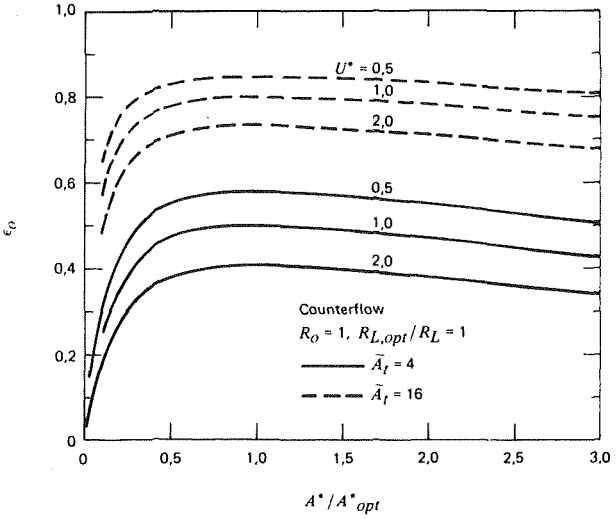

Fig. 8 Optimum conditions for heat transfer area distribution with given total transfer area $\bar{A}_t$

Acknowledgment

The author wishes to express his thanks to AB Svenska Fläktfabriken for permission to publish this paper and to Dr. O Strindehag, the head of the Research and Development Laboratory, for many valuable discussions.

References

1 Kays, W. M., and London, A. L., *Compact Heat Exchangers,* 2nd ed., McGraw-Hill, New-York, 1964.

2 London, A. L., and Kays, W. M., "The Liquid-Coupled Indirect-Transfer Regenerator for Gas-Turbine Plants," TRANS. ASME, Vol. 73, 1951, pp. 529–542.

3 Bošnjaković, F., Viličić, M., and Slipčević, B., "Einheitliche Berechnung von Rekuperatoren," *VDI-Forschungsheft,* No. 432, 1951, pp. 5–26.

4 Ashley, C. M., "Psychrometric Factors in the Air Conditioning Estimate," *Trans. ASHVE,* Vol. 55, 1949, pp. 91–110.

5 Strindehag, O., and Holmberg, R. B., "A Liquid-Coupled Heat System for Recovery From Exhaust Gases," to be published.

A. P. Watkinson
O. Martinez

Department of Chemical Engineering,
University of British Columbia,
Vancouver, B. C. Canada

Scaling of Heat Exchanger Tubes by Calcium Carbonate

Scaling of copper heat exchanger tubes has been studied under conditions that promote rapid and severe scaling. Artificially hardened water of high dissolved and suspended solids is recirculated through a heated test section operated at constant steam temperature. The effects of flow velocity, tube diameter, and bulk temperature on the asymptotic fouling resistance have been determined. Results are interpreted in terms of mathematical models of the scaling process.

Introduction

The fouling of heat transfer surfaces which has long been an operating problem in heat exchange equipment is beginning to receive the attention of research workers. Recent progress in the understanding of fouling processes has been summarized by Taborek, et al. [1, 2].[1] Laboratory studies have been carried out on fouling of gas oils [3] and iron oxide suspensions [4]. The mechanisms of calcium carbonate and calcium sulphate scale formation have been investigated [5, 6]. Heat Transfer Research Inc. has carried out a wide ranged study of cooling tower water fouling [1, 2], the quantitative aspects of which have not been published. The velocity and temperature dependence of the asymptotic fouling resistance, for example, are not given. Although some generalizations can be drawn from this work, as might be expected, the fouling process is to a large extent specific to the chemical system involved. Thus, in the foregoing studies the rate of fouling, or the fouling resistance has been found to depend somewhat differently on process parameters, and in most cases the rate controlling steps in the fouling processes are different.

Even the relatively simple problem of scaling of $CaCO_3$ is not yet completely understood. Hasson [5] has shown that under certain conditions the deposition of calcium carbonate scale can be mass transfer controlled. In a series of experiments at uniform heat flux, and at velocities below 0.9 m/s the amount of scale deposited increased uniformly with time and the rate of scaling increased with velocity. A previous study in the author's laboratory under constant wall temperature conditions where an asymptotic fouling resistance occurs indicated that at velocities above 0.8 m/s the asymptotic fouling resistance decreased with increasing velocity, in agreement with the qualitative results reported by Taborek, et al., for cooling tower water scaling.

The objects of the present work were to study the scaling of salt solutions due to $CaCO_3$ formation as a function of tube side velocity and bulk temperature in tubes of different diameters under constant wall temperature conditions. The velocity and diameter effects were of particular interest. The choice of tube diameter in severe fouling situations is not the same optimization problem between heat exchanger size and pressure drop as for the case of clean tubes, since the fouling resistance itself is a strong function of velocity [1–4]. Some compromise is reached between the rule-of-thumb that large diameter tubes should be used in fouling situations to prevent tube blockage once fouling starts, and the positive effect of high velocity and hence smaller tube diameter in reducing both the fouling resistance and the tube side convective film resistance. One aim of the work was, therefore, to determine if there was a significant tube diameter effect on the asymptotic scaling resistance.

Experimental

The apparatus and method have been described in detail elsewhere [7]. The apparatus consisted of a steam condenser containing two copper tubes in parallel through which artificially hardened water was circulated. The inlet liquid temperature was held constant in most of the work at 329 ± 1 K. Tap water at a fixed flowrate was circulated through the tubes for long enough to establish the heat transfer coefficient under clean nonfouling conditions, then salt solutions were added to give an initial composition of 1.35 g/l NaCl, 1.39 g/l $CaCl_2$ and 1.23 g/l $NaHCO_3$. This solution when heated above temperatures of 330 K gave very rapid scale formation on the tube walls. Five copper tubes from 5.3 to 20-mm ID were tested. The film heat transfer coefficient was calculated from the outside wall temperature measurements:

$$h = \frac{WC_p}{A} \ln ((\bar{T}w_0 - Tb_1)/(\bar{T}w_0 - Tb_2)) \quad (1)$$

After addition of the scaling salts, the outlet fluid temperature decreased as scale deposited in the tubes and the rate of heat transfer dropped. The recirculating liquid was analysed for dissolved and suspended solids, and pH. Suspended solids concentrations were about 400 ppm 15 min after salt addition, and increased by about 100 ppm during the experimental run of 4 hr. Dissolved solids concentrations decreased slightly from the initial value of 3000 ppm,

[1] Numbers in brackets designate References at end of paper.

Contributed by the Heat Transfer Division for publication in the JOURNAL OF HEAT TRANSFER. Manuscript received by the Heat Transfer Division June 12, 1975. Paper No. 76-HT-H.

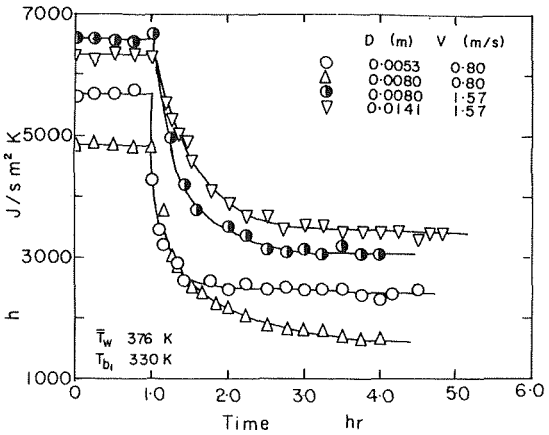

Fig. 1 Typical plot of heat transfer coefficient versus time

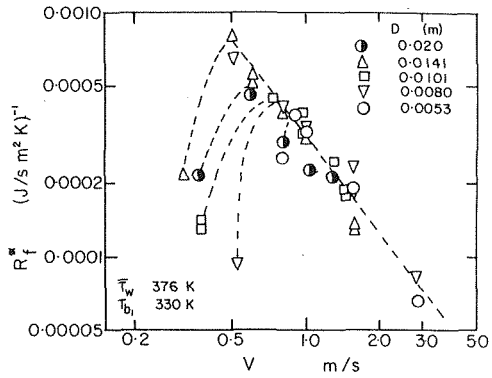

Fig. 2 Effect of velocity on fouling resistance

and the pH increased typically from 7.7 to 8.3 during each experiment. These operating conditions allowed a very rapid approach to the asymptotic fouling condition. Such accelerated tests while not necessarily being valid to establish design values of the asymptotic fouling resistance, are of considerable use in evaluating the effects of certain variables and geometries on the fouling tendency.

Heat Transfer Results

A plot of typical heat transfer results with time as shown in Fig. 1. The heat transfer coefficient h, remains constant for the first hour before the salts were added. As expected, clean coefficients increase with increasing velocity and decreasing tube diameter. Immediately after salt addition a rapid decrease in h begins and a steady-state value h^* is reached after about 2 hr. Earlier work using this technique showed that the asymptote was stable at least for 24 hr [7], and further addition of scaling salts had no effect on the value of h^*. The asymptotic fouling resistance R_f^* is calculated from the steady-state value, and the initial value of the heat transfer coefficient

$$R_f^* = (1/h^* - 1/h^0) \tag{2}$$

All experiments were run with the wall and steam chest temperatures held constant with time so that as the deposit builds up, the temperature at the deposit/liquid interface drops. This drop decreases the tendency for scale formation since the driving force for further scaling, the supersaturation, is lowered. Deposits were found [7] to consist essentially of $CaCO_3$ with loss on ignition at 1000°C of 42.7 percent and calcium content of 50.4 percent. Examination of the tubes after a run showed the deposit to be made up of an easily removable sludge on top of a compact crystalline layer.

The effect of liquid velocity on the scaling of tubes of different diameters is shown in Fig. 2. Fouling resistance for each tube at first increases with velocity, goes through a maximum and then decreases. Possible reasons for the velocity maximum were discussed elsewhere [7]. As the tube diameter is increased, the maximum R_f^* increases, and occurs at lower velocity. Fig. 3 shows that R_f^* generally decreases for all tubes at Reynolds numbers above 12,000.

In Fig. 4, R_f^* is plotted versus tube diameter at three values of the bulk velocity. Although there is some scatter, the trend of the data is clear. Increasing tube diameter from 8 to 20 mm causes a 33 percent drop in R_f^* at $V = 1$ m/s. This effect of diameter is confounded by bulk temperature effects, since at fixed velocity and inlet temperature increasing the tube diameter results in lower bulk liquid temperature and hence scale temperature along the tube.

The effect of bulk temperature was determined in a separate series of experiments in a 10-mm dia tube. The inlet temperature was varied from 320 to 360 K. Results are shown in Fig. 5. The asymptotic fouling resistance goes through a maximum with increasing $\bar{T}_b{}^0$. The reason for the maximum will be discussed later. Runs of different tube diameters and fixed T_{b_1} also fall on the same line. This suggests that the observed diameter effect (Fig. 4) is a result of the average bulk temperature decrease as D increases.

For design purposes the effect of diameter at either fixed flowrate or fixed pressure drop is more important than at fixed velocity. At equal flowrates as tube size is increased any decrease in R_f^* due to the tube diameter effect is far outweighed by the increase in R_f^* due to the drop in tubeside velocity (Fig. 2). Thus, for example, at $\dot{V} = 1.5 \times 10^{-4}$ m³/s tubes of 8–20 mm could be selected with velocities varying from 3 to 0.48 m/s, respectively. Fig. 6 shows that the fouling resistance of the 20-mm tube is about five times that of the 8-mm tube. The clean coefficient is also larger for the small diameter tube.

Mathematical Models of Scaling

The predictions of current models of the fouling process were

Nomenclature

a = constant
A = inside area of tube m²
b = slope of temperature solubility curve mol/m³K
B = constant in equation (19) 1/s
C = concentration mol/m³
C_p = heat capacity J/kg K
D = inside tube diameter m
E = activation energy KJ/kg-mol
f = friction factor
h = inside heat transfer coefficient J/s m²K
k = thermal conductivity J/sm K
k_r = crystallization rate constant kg/m²s (Mol/m³)^n
m = constant
n = constant
r = statistical correlation coefficient
R_f = fouling resistance (J/sm²K)$^{-1}$
R_g = gas constant KJ/kg-mol K
t = time hr
T = temperature K
V = velocity m/s
$\dot{V}$ = flowrate m³/s
W = mass flowrate kg/s
x = deposit thickness m
β = function
τ = shear stress at tube wall N/m²
Φ = term in equation (6) m/s
ρ = density kg/m³

Subscripts

b = bulk liquid
1 = inlet of tube
2 = outlet of tube
D = deposition
R = release
n = constant
s = scale
w = wall

Superscripts

* = asymptotic value
0 = at time zero
− = average value

examined for comparison with the experimental data. The original Kern-Seaton [8] model for dirt deposition predicts a strong diameter effect at fixed velocities:

$$R_f^* \propto W/\tau \propto D^2/Vf \tag{3}$$

whereas the models of Watkinson and Epstein developed for particulate fouling [9] predict

$$R_f^* \propto (1/V\sqrt{f})^m \tag{4}$$

where $m = 1$, 2, or 3 for deposition steps controlled by transfer of particles to the surface adhesion at the surface and both steps respectively. If the tube is hydrodynamically smooth, equation (4) predicts R_f^* increases with $D^{0.125}$ to $D^{0.375}$ depending on m through the effect of Reynolds number on the friction factor. Otherwise R_f^* is expected to be independent of tube diameter. Applying equations (3) or (4) R_f^* should correlate with V and possibly with D. Experimental data for $N_{Re} > 12000$ were correlated within ±14 percent by the equation

$$R_f^* = 0.000101/V^{1.33}D^{0.23} \tag{5}$$

It is evident that equations (3) or (4) with integer values of m do not fit the experimental velocity dependence.

Expressions (3) and (4) are based on the Kern equation [8] where the rate of scale formation is given as the difference between a deposition term Φ_D and a release or removal term ϕ_R

$$\frac{dx}{dt} = \Phi_D - \Phi_R \tag{6}$$

The release term was given by Kern as being dependent on the shear stress at the wall and the deposit thickness i.e., $\phi_R = a\tau x$. Tests showed that in the present study a fouling layer deposited at a low velocity could be substantially removed by a short surge of high velocity fluid. This implies that a removal or suppression force does exist and argues for the inclusion of a release term in the mathematical description. The increase in suspended solids content over the course of the run suggests that particulate fouling is not the major deposition process occurring, but rather the deposit is formed from solution. The deposition term thought appropriate in the present case was originally formulated by Reitzer [10] who considered the rate of scale formation for inverse solubility salts in evaporators to be dependent on the supersaturation raised to a power n.

$$\frac{dx}{dt} = k_r(C_b - C_s)^n/\rho_s \tag{7}$$

No release or suppression term was given. He assumed that the inverse temperature-solubility relationship could be approximated by a linear equation

$$C_b - C_s = b(T_s - T_b) \tag{8}$$

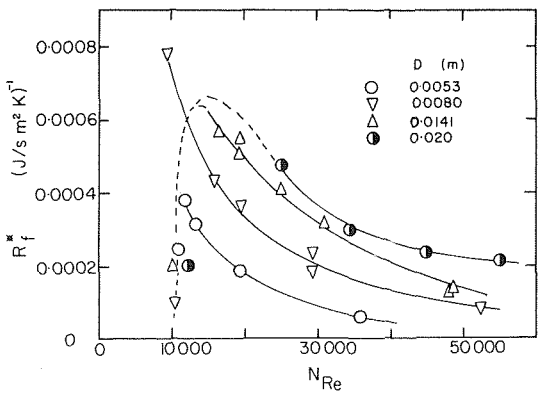

Fig. 3 Fouling resistance versus Reynolds number

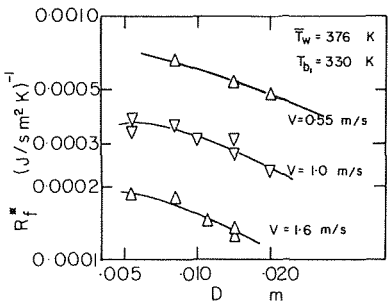

Fig. 4 Effect of tube diameter on fouling resistance

and wrote the scale surface temperature in terms of the wall temperature.

$$T_s - T_b = \frac{T_w - T_b}{(1 + hx/k_s)} \tag{9}$$

Combining (6)–(9) we obtain:

$$\frac{dx}{dt} = \frac{k_r}{\rho_s}\left(\frac{b(T_w - T_b)}{1 + hx/k_s}\right)^n - a\tau x \tag{10}$$

This equation differs from those used in other models in that the deposition term is not constant with time. The asymptotic fouling resistance is obtained by setting $dx/dt = 0$ in equation (10) and putting $R_f^* = x/k_s$ and $\tau = fV^2\rho/2$

$$R_f^*(1 + R_f^*h)^n = \frac{2b^n k_r(T_w - T_b)^n}{ak_s fV^2\rho_s\rho} \tag{11}$$

Now the crystallization rate constant k_r is a function of the scale surface temperature T_s, and would be expected to follow an Arrhenius equation:

$$k_r = k_{r_0} \exp -E/R_g T_s \tag{12}$$

Calculations using equation (9) show that over the course of the experiment T_s drops typically from 375 K to about 350 K. Using the activation energy of 25,150 kcal/g-mole given by Hasson [11] the rate constant k_r would be expected to drop by a factor of 13 over the course of the run. This strong temperature dependence of the crystallization process would tend to explain the very rapid approach to asymptotic conditions (Fig. 1) and the failure of attempts to correlate R_f^* with the wall temperature using an Arrhenius type equation [7]. The latter could be more easily done if experiments were carried out in a constant heat flux exchanger where T_s would remain constant with time.

Combining equation (9) and (12), equation (11) becomes:

$$R_f^*(1 + hR_f^*)^n = \frac{2k_{r_0}b^n}{\rho_s a k_s \rho} \exp\left[\frac{-E}{R_g\left(T_b^* + \dfrac{T_w - T_b^*}{1 + hR_f^*}\right)}\right]$$

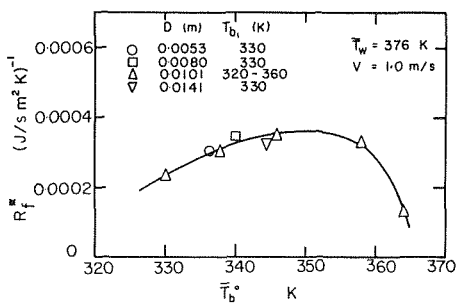

Fig. 5 Effect of average bulk liquid temperature at $t = 0$ on fouling resistance

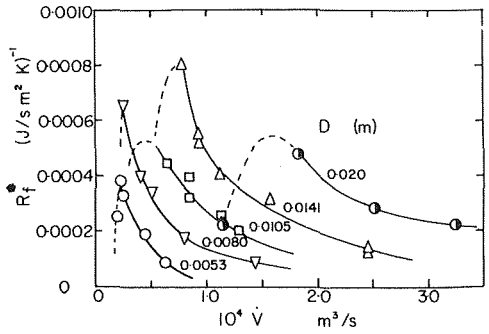

Fig. 6 Fouling resistance versus volumetric flowrate

$$\cdot \frac{(T_w - T_b)^n}{fV^2} \tag{13}$$

For the present purposes the functional dependence of the wall and bulk temperature can be simplified to

$$R_f^*(1 + hR_f^*)^n = \frac{\beta_n}{V^2} \tag{14}$$

where $\beta_n = f(T_w, T_s, T_b)$. From the literature on crystal growth [12] n is expected to lie between 1 and 2. For most sparingly soluble salts $n = 2$ at high supersaturations. For $n = 1$ equation (14) is readily solved:

$$R_f^* = \frac{1}{2h}\left[\left[1 + \frac{4\beta_1 h}{V^2}\right]^{1/2} - 1\right] \tag{15}$$

For $n = 2$ equation (14) becomes a cubic in R_f^*

$$R_f^{3*} + \frac{2}{h}R_f^{*2} + \frac{R_f^*}{h^2} - \frac{\beta_2}{(hV)^2} = 0 \tag{16}$$

which can be solved by algebraic or numerical techniques.

Agreement of data with the models was tested by calculating β_1 and β_2 directly from equations (15) and (16) knowing R_f^*, V and h from the experiments, and testing to determine if the functions β_1 and β_2 were temperature dependent only. For data at fixed inlet bulk temperature of 330 K, equations for β_1 and β_2 were found, and the correlation coefficients determined. Bulk temperatures were below 350 K in all cases.

$$\beta_1 = 0.0000656\ \bar{T}_b\text{o} - 0.02138\ (r = 0.78) \tag{17}$$

$$\beta_2 = 0.0002751\ \bar{T}_b\text{o} - 0.08489\ (r = 0.80) \tag{18}$$

Inserting these functions into equations (15) and (16), respectively, allowed calculation of fitted results. Twenty experimental data points fitted calculated predictions within 16 percent for $n = 1$ and 10.7 percent for $n = 2$. Equations (15) and (16) predict a specific effect of V on R_f^*. Using accepted dimensional equations for clean film coefficients for water, the predicted slopes of the $R_f^* - V$ plots were found to be -1.5 to -1.6 for $n = 1$, and -1.3 to -1.4 for $n = 2$ as shown in Fig. 7. Equation (16) then gives a prediction of the velocity dependence that was confirmed experimentally (Fig. 2), whereas equation (15) does not.

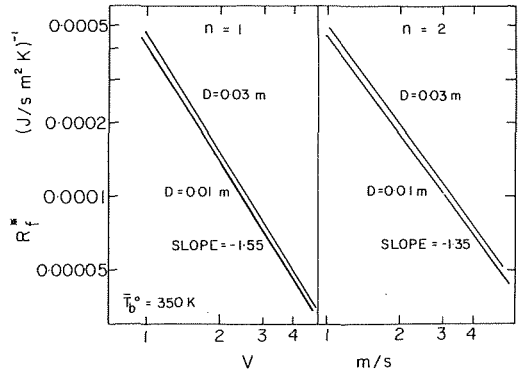

Fig. 7 Predictions of scaling models

The model also predicts the general shape of the $R_f^* - \bar{T}_b$o curve of Fig. 5. In equation (13) it is evident that as T_b increases at constant T_w the exponential term which describes the kinetics of the crystallization process will increase, whereas the term $(T_w - T_b)^n$ which is a measure of the supersaturation or driving force will decrease. This results in a maximum value of the function $R_f^*(1 + hR_f^*)^n$. For the case of $n = 2$, data of Fig. 5 and some other tests run at different wall temperatures were plotted according to equation (13). Results shown in Fig. 8 are roughly linear, and lend support to the proposed model. A least squares fit of this data yielded:

$$R_f^*(1 + hR_f^*)^2 = \frac{5.910 \times 10^{19}(\bar{T}_w - T_b^*)^2}{V^2} \exp -(17540/T_s^*) \tag{19}$$

The temperature effect is somewhat larger than that found by Hasson, who using a different analyses found $E/R_g = +12{,}657$ K. It should be noted that while the form of equation (19) lends support to the model, it is not a recommended method to evaluate the activation energy. It is based on the average scale temperature at the end of experiment during which T_s has been dropping. A constant heat flux exchanger would allow a more direct calculation of the activation energy.

Equation (10) might be expected to give a good prediction of the build-up of R_f^* with time. Unlike Reitzer's cases for evaporator scaling however, neither $(T_w - T_b)$ nor the heat flux are constant with time. The integration is further complicated by the presence of the release term which Reitzer did not consider. Because of the complicated form of the integral it was decided rather to fit the experimental data by the simple asymptotic equation of Kern [8]

$$R_f = R_f^*(1 - \exp(-Bt)) \tag{20}$$

The fit is adequate (Fig. 9) but not too accurate especially near the beginning of the scaling process. Equation (20) implies a constant deposition term in equation (6) and is therefore inconsistent with the Reitzer term. Initial rates were found to decrease with increasing V as expected from equation (10).

Conclusions

A study of the effects of velocity, bulk temperature and tube diameter on the scaling from prepared hard water containing calcium carbonate in dilute suspension was carried out in a constant wall temperature heat exchanger. At Reynolds numbers over 12000 the asymptotic fouling resistance varies with velocity to the power -1.33. At constant inlet temperature, tube diameter was found to have a weak effect on fouling resistance due to the difference in average liquid temperature as the diameter is changed. As the bulk temperature increases, the fouling resistance goes through a maximum and then decreases, because of opposing effects of scale surface temperature and supersaturation. The results of this investigation were consistent with a mathematical model of the scaling process where the deposition term was written in terms of Reitzer's model of scale formation in an inverse solubility salt, and the release term due to Kern.

Acknowledgments

This work was supported by a National Research Council of Canada Grant. The apparatus was kindly loaned by Noranda Research Centre, Pointe Claire, Quebec. This paper was presented at the 79th National Meeting at the A.I.Ch.E., Houston, Texas in March 1975.

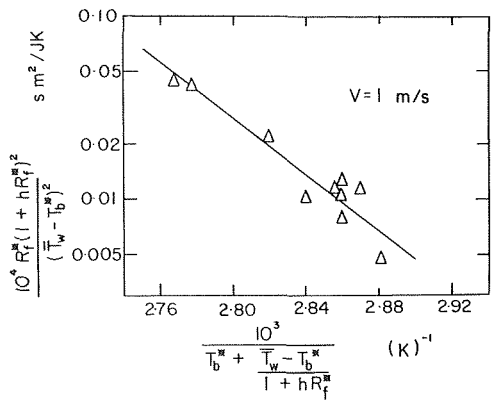

Fig. 8 Fit of data to equation (13)

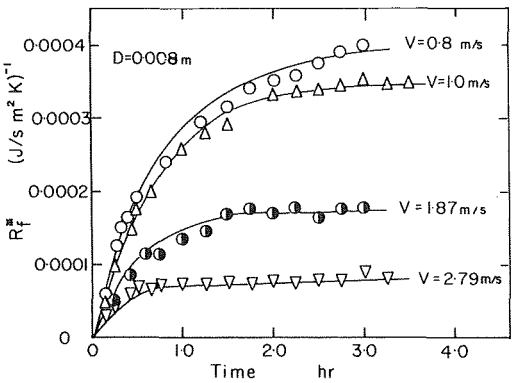

Fig. 9 Fit of typical experimental data to Kern's equation

References

1 Taborek, J., Aoki, T., Ritter, R. B., Palen, J. W., and Knudsen, J. G., "Fouling: The Major Unresolved Problem in Heat Transfer," *Chem. Eng. Progr.*, Vol. 68, No. 2, 1972, pp. 59–67.

2 Taborek, J., Aoki, T., Ritter, R. B., Palen, J. W., and Knudsen, J. G., "Predictive Methods for Fouling Behavior," *Chem. Eng. Progr.*, Vol. 68, No. 7 1972, pp. 69–78.

3 Watkinson, A. P., and Epstein, N., "Gas Oil Fouling in a Sensible Heat Exchanger," *Chem. Eng. Progr. Sym. Ser.*, Vol. 65, No. 92, 1969, pp. 84–90.

4 Hopkins, R. M., and Epstein, N., "Fouling of Heated Stainless Steel Tubes by a Flowing Suspension of Ferric Oxide in Water," 5th International Heat Transfer Conference, Tokyo, Japan, Paper HE 1-6, Sept. 1974, pp. 180–184.

5 Hasson, D., Avriel, M., Resnick, W., Rozenman, T., and Windreich, S., "Mechanism of Calcium Carbonate Scale Deposition on Heat-Transfer Surfaces," *Ind. Eng. Chem. Fund.*, Vol. 7, 1968, pp. 59–65.

6 Hasson, D., and Zahari, J., "Mechanism of Calcium Sulfate Scale Deposition on Heat-Transfer Surfaces," *Ind. Eng. Chem. Fund.*, Vol. 9, 1970, pp. 1–10.

7 Watkinson, A. P., Louis, L., and Brent, R., "Scaling of Enhanced Heat Exchanger Tubes," *Can. J. Chem. Eng.*, Vol. 52, 1974, pp. 558–562.

8 Kern, D. Q., and Seaton, R. E., "A Theoretical Analysis of Thermal Surface Fouling," *Brit. Chem. Eng.*, Vol. 4, No. 5, 1959, pp. 258–262.

9 Watkinson, A. P., and Epstein, N., "Particulate Fouling of Sensible Heat Exchangers," *Proceedings 4th Int'l Heat Transfer Conference*, Paris 1970 Vol. 1, Paper HE 1-6 12 pp.

10 Reitzer, B. J., "Rate of Scale Formation in Tubular Heat Exchangers," *Ind. Eng. Chem. Proc. Des. and Dev.*, Vol. 3, No. 4, 1964, pp. 345.

11 Hasson, D., "Rate of Decrease of Heat Transfer Due to Scale Deposition," *Sonderdruck aus Dechema—Monographien Band*, Vol. 47, 1962, pp. 233–252.

12 Konak, A. R., "A New Model for Surface Reaction-Controlled Growth of Crystals From Solution," *Chem. Eng. Sci.*, Vol. 29, 1974, pp. 1537–1543.

S. KAO

Engineering Department,
Mobil Research and Development Corp.,
Dallas, Texas

Analysis of Multipass Heat Exchangers With Variable Properties and Transfer Rate

This paper presents a matrix solution technique for multishell, multitube-pass heat exchangers with variable heat transfer film coefficients and heat capacity rates. Using this method, a series of case studies has been made, whose results are used to check the validity of certain facets of the normal design practice. Some parameters have been examined and discussed in details including the applicable range of Colburn's caloric temperature factor, effect of shell nozzle orientation, local coefficient of the multipass exchangers with tube side in laminar flow and flow instability phenomenon across the viscous flow coolers.

Introduction

Shell and tube exchangers are commonly designed using the MTD chart by Bowman, et al. [2],[1] which assumes constant heat capacity rates and heat transfer coefficients. In many applications, these assumptions are not valid. For evaporators and condensers, both capacity rate and coefficient may undergo substantial changes. In the case of viscous liquid exchangers, whose tube side flow pattern encompasses laminar, transition, and turbulent regions, a tenfold coefficient variation is possible. In fact, for some laminar flow cases, the heat transfer may reverse direction, depending on the temperature driving force profile. Therefore, the MTD concept may sometimes lead to serious errors. To compensate for the coefficients that vary linearly against temperature, Colburn [3] has formulated the caloric temperature concept for single tube-pass exchangers. In a rigorous analysis, Gardner [4] developed an MTD chart, applicable to linear variation of the controlling shell coefficient for a multipass case with infinite tube passes. Although both are satisfactory for most applications, neither can be generalized into a valid design method for both variable coefficient and capacity rate.

The purposes of the present investigation are (i) to develop a general solution for the design of multishell-pass,multitube-pass exchangers with variable heat capacity rate and coefficient, (ii) to explore, by means of case studies, the effects of various design parameters on heat exchanger performance and (iii) to re-examine the behavior of tube side laminar heat transfer inside shell and tube heat exchangers.

Mathematical Formulation and Solution

I Single Shell, TEMA E Construction [7]. Let the exchanger have one shell pass and N tube passes with type I flow arrangement as shown in Fig. 1. Across the surface element dS of each tube pass, the rate of heat transfer and temperature changes become

$$dq = (WC_t)\, dt' = (T' - t')UdS \tag{1a}$$

The heat balance requires that

$$dT' = \sum_{n=1}^{N} R_n dt_n' \tag{1b}$$

For large number of cross-baffles, it can be assumed that the surface of all tube passes is exposed to the same shell stream. Using an approach similar to reference [8], above differential equation systems can be solved by finite difference method via matrix manipulation. Let the tube surface be subdivided into K increments along the tube length as shown in Fig. 1, in vectorial form, the stream temperatures can be expressed as

$$|T'| = (T'_1, T'_2, \ldots T'_k, \ldots T'_K)^T \qquad T'_{K+1} = T'_i$$

$$|t'|_n = (t'_2, t'_3, \ldots t'_k \ldots t'_{K+1})_n^T \qquad n = 1,3,5,7\ldots$$

$$= (t'_1, t'_2, \ldots t'_k \ldots t'_K)_n^T \qquad n = 2,4,6,8\ldots$$

Across surface ΔS_{kn} of kth increment and nth pass, a difference approximation of equation (1a) becomes

$$T'_k + T'_{k+1} = (1 - \eta_{kn})t'_{kn} + (1 + \eta_{kn})t'_{k+1,n}$$

[1] Numbers in bracket designates Reference at end of paper.

Contributed by the Heat Transfer Division for publication in the JOURNAL OF HEAT TRANSFER. Manuscript received by the Heat Transfer Division March 13, 1975. Paper No. 76-HT-N.

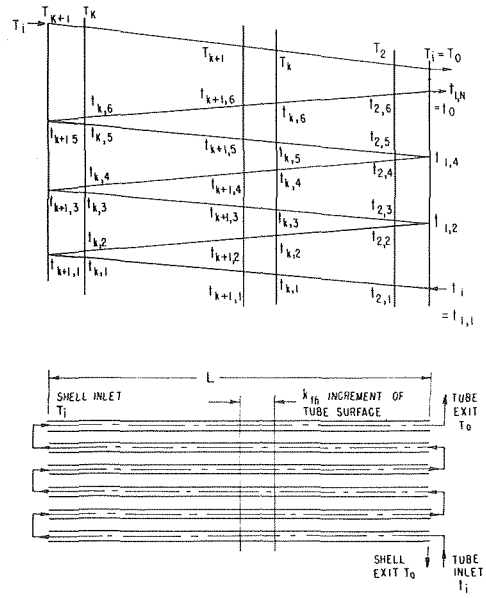

Fig. 1 Temperature and flow diagram in the shell of multipass exchanger—shell flow arrangement, type I

$$= (1 + \eta_{kn})t'_{kn} + (1 - \eta_{kn})t'_{k+1,n} \qquad n = 1,3,5,\ldots$$
$$n = 2,4,6,\ldots \quad (2)$$

in which

$$\eta_{kn} = 2(WC_t/\overline{U}\Delta S)_{kn}$$

is evaluated at the local average conditions. For all N tube passes and K increments, following relationships can be formed in terms of $K \times K$ matrices and vectors:

$$(I + a)|T'| + T'_i e_K = A_n|t'|_n + D_n|t'|_{n-1,n=1,N} \quad (3)$$

in which $|t'|_o = 0$, and A_n and D_n are defined as follows:

For odd passes, $n = 1, 3, 5\ldots$

$$A_n = I + a^T + [\eta]_n(I - a^T)$$
$$D_n = (1 - \eta_{1n})E_{11}$$

For even passes, $n = 2, 4, 6, \ldots$

$$A_n = I + a + [\eta]_n(I - a)$$
$$D_n = (1 - \eta_{Kn})E_{KK}$$

in which the unity matrix I, vector e_j and special unity matrix E_{ij} are defined in the Nomenclature [1]. The diagonal matrix operator, a, is defined as follows:

$$a = (0, e_1, e_2, \ldots, e_{J-1})^T \text{ for } J \times J \text{ matrix } (J = K)$$

Rearranging equation (3) and expressing $|t'|_n$ in terms of $|t'|_1$

$$|t'|_n = Y_n|t'|_1, \; Y_n = A_n^{-1}((A_{n-1} - D_n)Y_{n-1} + D_{n-1}Y_{n-2}), \; n = 2, \ldots N \quad (4a)$$

$$Y_1 = I, \; Y_o = 0$$

$$|t'|_1 = A_1^{-1}((I + a)|T'| + T'_i e_K) \quad (4b)$$

Difference approximation of equation (1b) across kth increment of all tube passes becomes:

$$-T'_k + T'_{k+1} = R_{k1}(t'_{k+1} - t'_k)_1 + R_{k2}(t'_k - t'_{k+1})_2 + \ldots\ldots R_{kn}(t'_k - t'_{k+1})_N, \; k = 1, \ldots K$$

$$R_{kn} \cong R_{k,n+1} \cong (R_{kn} + R_{k,n+1})/2$$
$$k = K, \text{ for } n = 1,3,5, \ldots.$$
$$= 1, \text{ for } n = 2,4,6, \ldots.$$

Following matrix relation can then be established,

$$(a - I)|T'| + T'_i e_K = \sum_{n=1}^{N} [R]_n B_n |t'|_n \quad (5)$$

Nomenclature

C_p = specific heat; C_b, at cup mixing temperature, J/kg°C, unless specified

d_o, d_i = tube OD and ID respectively, m, unless specified

e_j = unit column vector, jth element is 1, remaining elements are 0 (reference [1])

E_{ij} = special unity matrix, all elements are zero except element $ij = 1$

F_c/F_{colb} = correction for Colburn's caloric temperature factor; $t_{av} = t_c + F_{\text{colb}}(t_h - t_c)$; F_c, calculated equivalent temperature factor for multipass exchangers with variable U and WC

FMTD = normal MTD for multipass exchangers with constant U and WC°C

h = film coefficient of heat transfer based on tube outside surface; subscripts s and t refer to shell and tube sides, respectively, W/m²°C

I = unity matrix, diagonal

k = thermal conductivity, W/m°C

L = overall tube length, m

Δp = pressure drop on tube side, mPa unless specified

Q, q = total exchanger duty and rate of heat transferred, respectively, W/s

$R = WC_t/WC_s$, varies with tube pass n and tube length increment k

R_i, r = inside tube radius and radial position, respectively, m

S, ΔS = total and incremental exchanger surfaces, respectively, m²

$\Delta S/\Delta Q$ = incremental surface effectiveness, percent of additional surface required for each additional percent of duty performed

T, t = shell and tube stream temperatures, respectively; $T' = T - t_i$, $t' = t - t_i$; t_i, tube flow inlet temperature to each shell, °C

U, U_{I}, U_{II} = overall effective transfer coefficients based on FMTD; subscripts I and II refer to types I and II nozzle orientations (see Figs. 2 and 3); $\bar{U}_x$, average local coefficient over surface ΔS, W/m²°C

$\Delta t_c/\Delta t_h$ = ratio of temperature differences, cold terminal to hot terminal

v = axial velocities, m/s

W_t = tube flow rate, kg/s-tube

WC = heat capacity rate or slope of the total heat curve, W/s°C

x = axial position from the tube entrance, m; $x = m\Delta x$

μ = viscosity, mPa.s (=cp)

$\delta = (T_o - t_o)/(T_i - t_i)$, temperature approach factor

Re = Reynolds number, dimensionless

Additional matrices or vectors A, R_n, D_n, F, X, X_a, X_b ... are as defined in the text

[ ], | |, ( ) = diagonal matrix, column vector and row vector, respectively

$( )^T$ = same as column vector | | (superscript T indicate transpose operation)

Subscripts

i, o = inlet and outlet temperatures respectively for each shell

c, h = cold and hot terminal conditions respectively, (temperatures, coefficients)

k = kth surface increment, k = 1,K

m = axial position. Also it refers to the shell number starting from the shell where tube flow enter the exchanger, m = 1,M

n = tube pass number for each shell, from the pass of tube inlet, $n = 1, N$ (N; total tube passes per shell)

ex,in = exit and inlet conditions respectively for the multishell multipass heat exchangers (Figs. 1, 2, and 3)

in which

$$n = 1,3,5\ldots\ldots \qquad B_n = I - a^T - E_{KK},\ B_N = I - a^T$$

$$n = 2,4,6\ldots\ldots \qquad B_n = I - a - E_{11},\ B_N = I - a$$

Eliminating all $|t'|_n$ except $|t'|_1$ with equation (4a) and letting $F = (\sum_{n=1}^{N} [R]_n B_n Y_n)^{-1}$, equation (5) becomes

$$|t'|_1 = F((a - I)|T'| + T_i' e_K) \tag{6}$$

Solving for $|T'|$ from equations (6) and (4b), one obtains the shell temperature profile:

$$|T'| = T'_i X e_K \tag{7a}$$

in which,

$$X = ((F + A_1^{-1})I - (F - A_1^{-1})a)^{-1}(F - A_1^{-1})$$

This is really a system of K equations, relating all internal shell temperatures directly to that of the inlet. The shell outlet temperature can be readily found from the first equation, i.e., for type I arrangement,

$$T_o = (1 - x_{1K})t_i + x_{1K}T_i \tag{7b}$$

Exchanging T_o with T_i and using negative WC_s in computing R_n and X, one obtains for type II arrangement shell outlet as:

$$T_o = (1 - 1/x_{1K})t_i + 1/x_{1K}T_i \tag{7c}$$

II Multishells in Series. Let us define the intershell temperature vectors as,

$$|T_t|_m = (t_i,\ T_o)_m{}^T,\ m = 1,2,\ \ldots\ M,\ M+1$$

where for M sections in series,

$$|T_t|_1 = (t_{in},\ T_{ex})^T,\ |T_t|_{M+1} = (t_{ex},\ T_{in})^T$$

A 2×2 matrix relationship can readily be formed based on equation (7b),

$$|T_t|_{m+1} = Z_m |T_t|_m, \qquad m = 1,\ \ldots\ M \tag{8}$$

where,

$$Z_m = \left|\begin{matrix} 1 - (1 - x_{1K})/x_{1K}R, & (1 - x_{1K})/x_{1K}R \\ 1 - 1/x_{1K}, & 1/x_{1K} \end{matrix}\right|_m \text{ for type I}$$

$$= \left|\begin{matrix} 1 + (1 - x_{1K})/R, & (x_{1K} - 1)/R \\ 1 - x_{1K}, & x_{1K} \end{matrix}\right|_m \begin{matrix} \text{for type II,} \\ X \text{ based on} \\ \text{negative} \\ WC_s \end{matrix}$$

and,

$$R_m = ((T_i - T_o)/(t_o - t_i))_m$$

Eliminating $|T_t|_2, \ldots |T_t|_M$ by applying equation (8) repetitively:

$$|T_t|_{M+1} = Z_{MM}|T_t|_1,\ Z_{MM} = Z_M \cdot Z_{M-1} \ldots Z_2 \cdot Z_1$$

In terms of matrix elements z_{ij} of Z_{MM}, the exit temperatures of a multishell exchanger can now be expressed as,

$$\left|\begin{matrix} t_{ex} \\ T_{ex} \end{matrix}\right| = \left|\begin{matrix} 1 - z_{12}/z_{22}, & z_{12}/z_{22} \\ 1 - 1/z_{22}, & 1/z_{22} \end{matrix}\right| \left|\begin{matrix} t_{in} \\ T_{in} \end{matrix}\right| \tag{9}$$

The temperature profiles are well defined by equations (3)–(9), once the property matrices A_n, $[R]_n$ are calculated, based on some reasonably assumed shell temperature profile. The intershell temperatures can then be calculated from equation (8). All internal tube and shell flow temperatures can be obtained from equations (7a), (4b) and (4a)., bearing in mind that for type II, T_o' must replace T_i' in equation (4b) and negative WC_s must be used for $[R]_n$ in equation (5).

Note that the differential equation system is nonlinear, and therefore an iterative procedure between the assumed and the calculated temperature profiles is required. In reality, for normal exchanger design, A_n and $[R]_n$ are not overly sensitive to temperature, and convergence can usually be obtained with the simple trial and error procedure. In order to compare the results of this study with those of normal design practice, the usual "linear" FMTD will be used as a basis for defining the equivalent effective overall film coefficient U_I or U_{II} for respective types:

$$Q = \sum_{m=1}^{M}\sum_{k=1}^{K}((WC_s)_k(T_{k+1} - T_k))_m,\ U_I,\ U_{II} = Q/(\text{FMTD})(S)$$

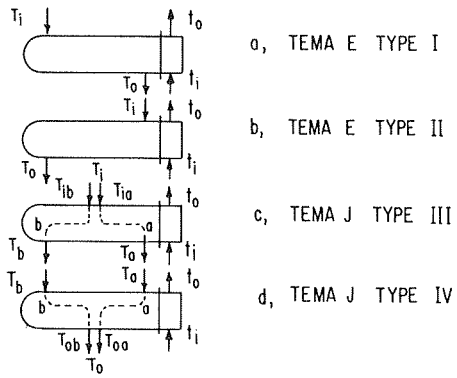

Fig. 2 Various types of shell flow arrangements

III Divided Flow Arrangement, TEMA J Shell Construction. The divided flow type shown in Figs. 2(c) and 2(d) is used to reduce shell side pressure drop. Shell flow enters at the center and splits evenly toward the sides a and b (Fig. 2). The mathematical treatment, however, is a general one, and will not be restricted to an exact nozzle location and flow quantity. For types III and IV connected in series, there are effectively two parallel streams for each side whose temperatures are T_{ib}, T_{ia} at the inlet; T_a, T_b in between the shells and T_{ob}, T_{oa} at the outlet. Naturally, for common practice, $T_{in} = T_{ib} = T_{ia}$, and $T_{ex} = \frac{1}{2}(T_{ob} + T_{oa})$. Let two $K \times K$ configuration matrices B_x and B_h be defined, which contain two nonzero elements in every column except the $(j-1)$th and jth columns:

$$B_x = \begin{vmatrix} 1 & 0 & & & & & & \\ 1 & 1 & \cdot & & & & & \\ 0 & 1 & \cdot & \cdot & 0 & & & \\ & 0 & \cdot & 1 & 0 & & & \\ & & & 1 & 1 & 0 & 0 & \\ & & & 0 & 0 & 1 & 1 & \cdot \\ & & & & & 0 & 1 & \cdot \\ & & & & & & 0 & \cdot \\ & & & & & & & 1 \\ & & & & & & & 0 \end{vmatrix} \begin{matrix} \\ \\ \\ \\ \\ \\ \cdot \\ \cdot \\ 0 \\ 1 \end{matrix},$$

$$B_h = \begin{vmatrix} 1 & 0 & & & & & & \\ -1 & 1 & \cdot & & & & & \\ 0 & -1 & \cdot & \cdot & 0 & & & \\ & 0 & \cdot & 1 & 0 & & & \\ & & & -1 & 1 & 0 & 0 & \\ & & & 0 & 0 & -1 & 1 & 0 \\ & & & & & 0 & -1 & 1 \\ & & & & & & 0 & \cdot \\ & & & & & & & \cdot \\ & & & & & & & 0 \end{vmatrix} \begin{matrix} \\ \\ \\ \\ \\ \\ \cdot \\ \cdot \\ -1 \\ 0 \end{matrix} \begin{matrix} \\ \\ \\ \\ \\ \\ 0 \\ \cdot \\ 1 \\ -1 \end{matrix}$$

And the new shell temperature vector $|T_j'|$ be defined as

$$|T'_j| = (T'_2,\ T'_3, \ldots\ T'_{j-1},\ T'_{j-},\ T'_j; \ldots\ldots\ T'_{K+1})^T$$

in which T_{j-}', T_j' are the dual shell temperatures at $k = j$ where the shell flow splits or merges, i.e., $T_{j-} = T_j = T_i$ for type III and $T_o = \frac{1}{2}(T_{j-} + t_j)$ for type IV. Previous matrix relationships,

equations (3), (4a), and (5) can still be applied, i.e., for heat balance, equation (5) for type IV becomes

$$B_h|T'_j| - T'_a e_1 + T'_b e_K = \left(\sum_{n=1}^{N}[R]_n B_n Y_n\right)|t'|_1 = F^{-1}|t'|_1 \tag{10}$$

$$F = \left(\sum_{n=1}^{N}[R]_n B_n Y_n\right)^{-1},\ Y_1 = I$$

in which, $[R]_n$ is evaluated with negative WC_s for $k = 1, \ldots j$, where shell flow direction is contrary to that of Fig. 1. Similarly, the heat transfer equation equation (3) becomes

$$B_x|T'_j| + T'_a e_1 + T'_b e_K = A_n|t'|_n + D_n|t'|_{n-1}, n = 1, \ldots N \tag{11}$$

Based on equation (4a)

$$|t'|_n = Y_n|t'|_1,\ n = 2, \ldots N$$

Hence,

$$|t'|_1 = F(B_h|T'_j| - T'_a e_1 + T'_b e_K) \tag{12}$$

In almost identical fashion, the new shell temperature $|T_j'|$ can be solved from equations (10) and (12),

$$|T'_j| = T'_a X_a e_1 + T'_b X_b e_K \tag{13}$$

in which

$$X_a = (FB_h - A_1^{-1}B_x)^{-1}(A_1^{-1} + F)$$
$$X_b = (FB_h - A_1^{-1}B_x)^{-1}(A_1^{-1} - F)$$

And A_n and Y_n are defined in equations (3) and (4a). Equation (13) is, in effect, an extension of equation (7a). Main exceptions are that WC_s must reverse its sign when $k = 1, \ldots j$ for type IV and when k = j, . . K for type III (Fig. 2). In terms of matrix elements x_{aij}, x_{bij}, of X_a and X_b, respectively, the shell inlet and outlet temperatures are related by the $(j-1)$th and jth rows of equation (13), i.e.,

$$\left.\begin{aligned} T'_{j-} &= x_{a,j-1,1}\ T'_a + x_{b,j-1,K}T'_b \\ T'_j &= x_{a,j1}\ T'_a + x_{bjK}T'_b \end{aligned}\right\} \tag{14}$$

where by common practice,

$$T_{in} = T_{j-} = T_j \quad \text{for type III}$$
$$T_{ex} = (T_{j-} + T_j)/2 \quad \text{for type IV}$$

The procedure to eliminate T_a, T_b, so as to directly relate T_{in} with T_{ex}, is a simple one, hence needs no further elaboration here.

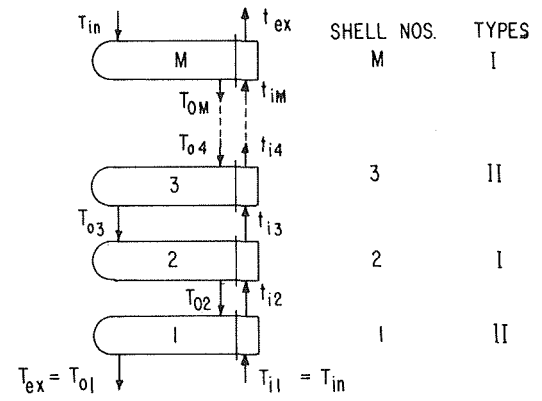

Fig. 3 Multishell in series, counter flow—TEMA E shell construction

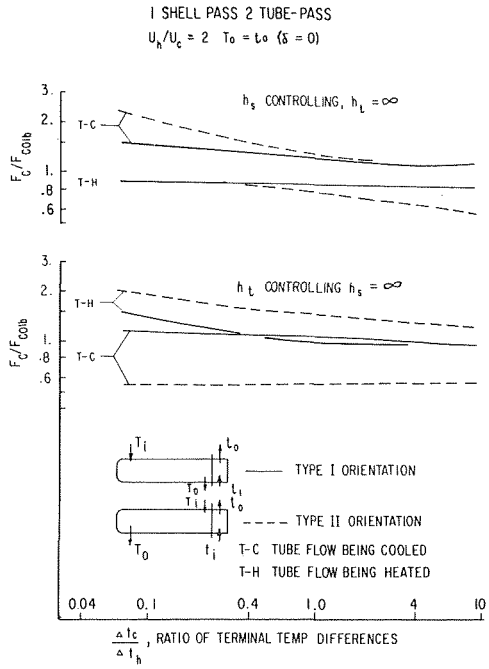

Fig. 4 Correction of Colburn's caloric temperature factor

Effects of Various Design Parameters on Exchanger Performance

Using the method developed in this paper, case studies of several heat exchangers are made and various design parameters analyzed. The applicable region of Colburn's caloric temperature factor, F_{colb}, is defined for cases with constant WC and linear variation of coefficient. The significance of the present matrix solution technique is demonstrated for exchangers with nonlinear variation of coefficient and heat capacity rate. The unique behavior of the multipass exchangers with tube side in laminar flow is explored, where the numerical integration procedures for laminar flow can be readily adapted from the available literature [11, 12] with the modification that the variable tube wall temperature be made dependent upon the shell side temperature. The problem of flow instability across the viscous flow coolers under rapid cooling is also evaluated. The results of the case studies are described as follows:

I **Linear Variation of h Versus Temperature.** In their separate analyses, the linear variation of h has been the basis by both Gardner and Colburn. Since many design methods [7, 9] require the calculation of an average coefficient based on some average temperature, caloric or otherwise, Colburn's temperature factor, F_{colb}, is used here as a basis for comparison, eventhough, for exchangers with a large tube pass and a controlling shell side coefficient, h_s, Gardner's chart can be directly applied. Several series of parametric studies are presented, including shell nozzle orientation (flow types I and II), temperature approach, and number of tube passes. All of these parameters are critically influenced by whether the shell side or tube side offers the controlling resistance.

1 *Effects of Shell Nozzle Orientation or Flow Type.* As was pointed out by Gardner [4, 5], the performance of exchangers with variable coefficient can be affected by the shell flow arrangement. To develop a meaningful correlation, hundreds of cases have been calculated. The results indicate the effects are most pronounced for exchangers with two tube-passes and a zero temperature approach. These results, expressed in terms of F_c/F_{colb} versus $\Delta t_c/\Delta t_h$, are plotted in Fig. 4 for both types I and II, with $U_h/U_c = 2$ and $\delta = 0$. The effect of the variation range of coefficient is demonstrated in Example I where a two tube-pass oil cooler is calculated

Table 1 Effect of shell flow type; U_I/U_{II}, EX I

$\Delta t_c/\Delta t_h$	U_h/U_c	U_I/U_{II}	U_h/U_c	U_I/U_{II}
0.1	2	1.14	5	1.44
1.0	2	1.16	5	1.47

Table 2 F_c/F_{colb} as affected by tube passes

	U_h/U_c = 3, $\Delta t_c/\Delta t_h$ = 0.4			
Tube passes	2	4	6	8
F_c/F_{colb}, type I	1.07	0.91	0.85	0.82
type II	0.52	0.66	0.72	0.74

with $\delta = 0$, $h_s = 5680$ while h_t decreases linearly from 1200 at the inlet. The results are as shown in Table 1:

The following observations are made:

(*a*) Colburn's F_{colb} appears to be a fair approximation for flow type I exchangers.

(*b*) When h_s controls, the use of F_{colb} does not lead to excessive errors for the majority of cases calculated.

(*c*) Avoid flow type II when the tube flow is to be cooled, and h_t is controlling. Because, a 50 percent reduction in F_{colb} may be required, indicating a 15 percent reduction in performance for the cases illustrated.

(*d*) Type II is preferrable to type I when heating the tube flow, and h_t is controlling, or when cooling the tube flow, and h_s is controlling. They are in general agreement with Gardner's observation [4].

(*e*) The effects of flow type increase with the range of coefficient variation.

2 *Temperature Approach.* In general, the performance of type II exchanger deteriorates rapidly as δ approaches zero. This is shown in Fig. 5 where the results of calculation of a few typical cases are plotted. To demonstrate the extent of heat transfer surface utilization, the incremental surface effectiveness, $\Delta S/\Delta Q$, is also shown. The following tentative conclusions are made:

(*a*) F_{colb} factor is reasonable for either type of exchanger when $\delta \geq 0.3$.

(*b*) The value of the incremental surface effectiveness, $\Delta S/\Delta Q$, should be used as a guide in determining the required number of shell passes. For cases with large coefficient variation, the use of zero temperature approach, $\delta = 0$, as a normal criterion, may no longer be reasonable.

3 *Tube Passes.* As the number of tube passes increases, there is a gradual decrease in performance for type I, and an improvement in performance for type II exchangers. A typical case is shown in Table 2, where h_t is controlling and $\delta = 0$. Apparently large difference between the two exchanger types exists only for 2 or 4 tube-passes. For tube pass greater than 10, the value of F_c/F_{colb} approaches 0.8 for either type.

II **Variable Coefficient and Capacity Rate.** For condensers, evaporators and viscous oil coolers, the film coefficient and/or capacity rate may change substantially with the flow pattern as well as the nature of the heat transfer mechanism. While these problems are too complex to be handled by any of the conventional design methods in the published literature, they can be readily solved using equations (7*a*)–(9). The significance of such solution is illustrated in Example II. It is an oil cooler whose design requirements are as follows:

Shell flow, cooling water, 39690 kg/h. C_p = 418.6. Temperatures in/out; 26.7/48.9°C. Average h_s = 5680.

Tube flow, viscous oil, 15876 kg/h. C_p = 209.3. Temperatures, in/out; 160/48.9°C. Re, in/out; 10000/1050. h_t is assumed to vary linearly from 890 @ 160°C to 125 @ 78.3°C(Re = 2100) and then becomes constant at 125 till outlet.

Exchanger configuration; 1 shell pass, 2 tube passes with 126-¾ in. 16 BWG tubes (d_o/d_i; 19 mm/15.8 mm). Tube length is to be calculated to meet the process requirements.

Both shell flow types have been calculated. The computation results are summarized in Table 3.

The performance of type I is 54 percent higher than type II, which is in line with previous observations, I1c, I1d. Needless to say, the calculated U_I,U_{II}, based on nominal FMTD, may not reflect the real coefficient, especially in the case of variable capacity rate for condensers and vaporizers.

III **Laminar Flow in Tubes of Viscous Oil Exchangers.** This is a special case where coefficient varies together with the temperature driving force profile. Using the present solution procedure, the unique behavior of viscous oil coolers can be investigated. Several series of case studies, EX III.1 to EX III.3, have been made using one viscous oil as the tube fluid. The oil properties are as follows:

$$k = 0.14 - .000075\ t,\ \text{W/m C}$$

$$C = 1.7637 + .003826\ t,\ \text{kJ/kg-°C}$$

$$\mu = \frac{0.4881}{10^5} \exp(6224.2/(t + 273)),\ \text{mPa.s or cp.}$$

$$\rho = 902.4 - 0.6334\ t,\ \text{kg/m}^3$$

A constant C_s for the shell flow is used. The coefficient is deliberately set as 5680 for 1-tubepass and 2840 for two-tubepass exchangers. All tubes, unless otherwise noted, are ¾ in. × 14 BWG (d_o/d_i; 19/15.8 mm), 20 ft long (6.1 m).

1 Coefficient versus profile of shell temperature. Contrary to the popular belief, the laminar coefficient in a multipass exchanger is somewhat dependent on the profile of the shell stream temperature. This can be seen from EX III 1*a* and 1*b*, where the 2-tubepass coolers of types I and II respectively are used to cool the oil from 143 to 140°C, while heating the shell flow from 103.6 to 137.5°C. An additional demonstration is made in EX III 1*c*, where the same duty is performed in a cooler with one counterflow tube pass. The profiles of temperatures and local coefficients are shown in Fig. 6. The following observation can be made:

(*a*) The coefficients in the counterflow pass are far greater than in the parallel pass in Example 1*a* and 1*b*.

(*b*) In the parallel tube-passes, the local coefficients decrease with the temperature driving forces. Furthermore, as the shell temperature increases steeply, (being heated by all other tube

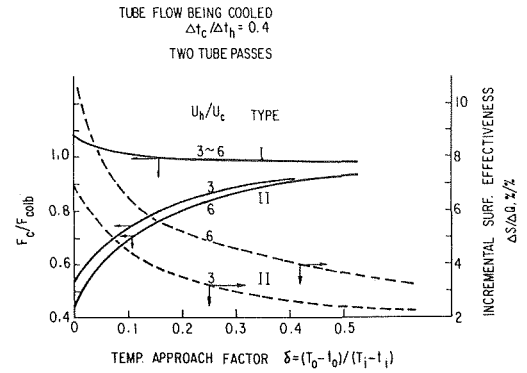

Fig. 5 Effect of temperature approach on caloric temperature factor

Table 3 Summary of calculation, viscous oil cooler, EX II

U_I	U_{II}	U_h/U_c	F_{colb}	U_{colb}
202.7	131.7	6.3	0.245	122.0

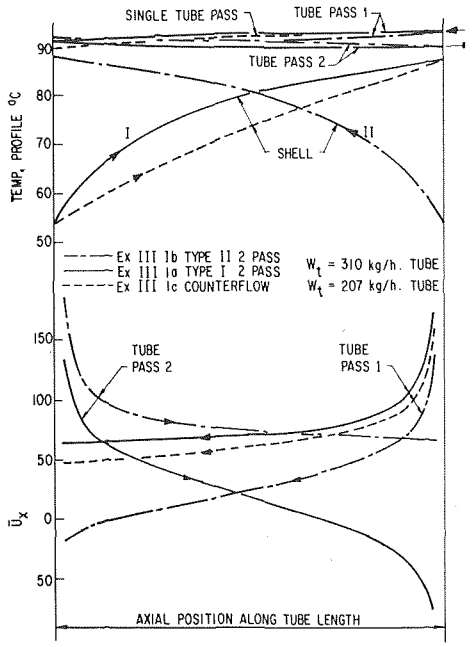

Fig. 6 Profiles of local heat transfer rate, $\bar{U}_x$, and temperatures—tube flow laminar (EX III 1)

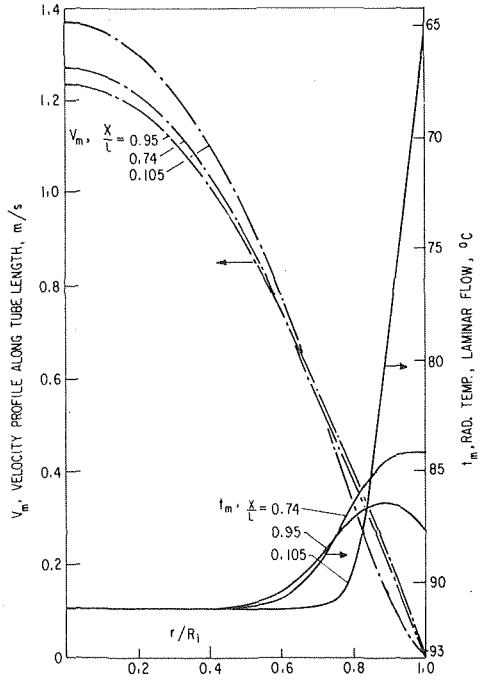

Fig. 7 Radial profiles of velocity and temperature, cold tube pass—EX III 1*a*

passes) a reversal in heat transfer is observed. Although this resembles the phenomenon in the tail end of normal exchangers with a close temperature approach, the cause is entirely different and is unique only to the laminar process. A close examination of the temperature profile, shown in Fig. 7, reveals that as t_w or T increases at a rate too fast for the heat conduction process across the liquid layers, a reversed radial temperature gradient, dt/dr, is created, resulting in a negative coefficient. Consequently, for the parallel pass of a multipass exchanger with a steep shell temperature profile, the application of correlations based on single tubepass analysis may be risky if not outright erroneous.

(*c*) With the high coefficient of a counterflow pass, the one-pass cooler of EX III 1*c* could, at least in theory, saves 25 percent in surface and 64 percent in pressure.

2 *Performance versus Shell Flow Type.* For coolers with a close temperature approach, the type II flow arrangement is slightly better than type I. This is illustrated in EX III 2*a* and 2*b*, whose calculation results are summarized in Table 4, indicating that U_{II} is 9 percent better than U_I. However, such an effect will disappear quickly for cases with a large temperature approach factor. The local coefficient and temperature profiles are not shown since they are quite similar to Fig. 6. A similar reverse heat transfer phenomenon can also be found in the parallel pass.

3 *Flow Instability and Maldistribution.* The problem of flow maldistribution across viscous flow coolers has been discussed by Mueller [10] based on a simple analogy using the available laminar solution in literature [11]. With the present computation procedure, the region of flow instability can now be more precisely determined. In Example III 3, the sample oil is to be cooled on the tube side of a single tube-pass exchanger with 26.7°C cooling medium (h_s = 5680). The flow rate, W_t, is varied over a wide range to develop the Δp-W_t profiles. To explore the effects of viscosity gradient, μ_w/μ_{in}, three different oil inlet temperatures are assumed, namely, 127, 138, and 160°C. Both ¾ and 1 in. tube sizes are used with a length of either 6.1 m or 3.2 m. As shown in Figs. 8 and 9, the results are in general agreement with Mueller's prediction. The following conclusions can be made:

(*a*) Critical Flow Rate. For any viscosity gradient, there is a critical flow rate above which the flow behavior is stable. This minimum flow rate, however, must be determined for each individual cooling requirement and cooler configuration, unless the viscosity gradient is very small.

(*b*) Viscosity Gradient, μ_w/μ_{in}. For the sample cases, the critical viscosity gradient appears to be about 180, below which multiple flow rates could coexist for different tubes across the same tube bundle. This would cause the flow maldistribution hence performance deterioration. Even at a critical gradient, the flow rate could vary substantially with Δp which could be easily influenced by the velocity of the inlet nozzle. As a good design practice, the actual gradient must be much smaller than this value. Needless to say, this critical value of 180 applies to the sample oil only, and would vary with the fluid viscosity index as Mueller indicated.

(*c*) Effect of Tube Size and Tube Length. From Figs. 8 and 9, it appears that the critical viscosity gradient will not be significantly affected by either the tube size or tube length. However, the critical (minimum) flow rate can be substantially lowered by shortening the tube length, or increasing the tube size, if the allowable pressure drop is limited.

Table 4 Performance of 2-tubepass coolers, EX III.2

Cases	Flow types	W_t	T_{in}/T_{out}	t_{in}/t_{out}	U
III.2*a*	I	31	26/59.2	93/60.8	27.7
III.2*b*	II	31	26/60.0	93/60.0	30.1

Conclusions

For multipass exchanger design with variable h and WC, the matrix solution, equations (7*a*)–(9) and equations (13) and (14) can be used for TEMA construction types E and J. Numerous case studies have been made to investigate the significance of various design parameters. One of the interesting conclusions is, for cases with linear coefficient variation and constant WC, the application of the conventional MTD in conjunction with Colburn's caloric temperature, is still reasonably accurate, if there are six or more tube passes per shell and $\delta \geq 0.3$.

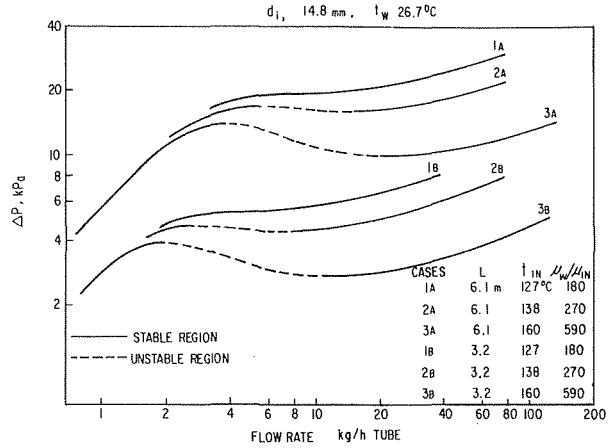

Fig. 8 Instability of laminar flow with large viscosity gradient—EX III 3, ¾-in. tube

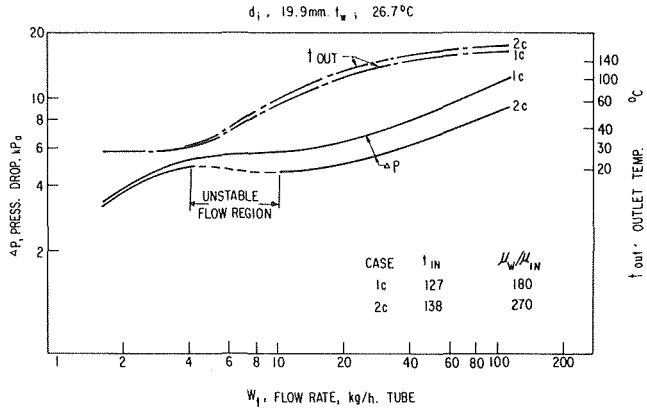

Fig. 9 Instability of laminar flow with large viscosity gradient—EX III 3, 1-in. tube

For laminar flow in tubes of multipass exchangers, the coefficient is sensitive to the profile of the temperature driving force. With a close temperature approach and a steep shell temperature gradient, the local coefficient in a parallel tube pass may become negative. This indicates that theoretical analyses or empirical correlations for a single tube may not be adequate for designing multipass exchangers. For stable operation of viscous flow coolers, some critical (minimum) tube flow rate must be maintained, unless the viscosity gradient is well below a certain critical value (180 for the oil in sample illustrations). Both can be determined using the presently developed solution procedures.

Acknowledgment

Acknowledgment is made to Mobil Research & Development Corp. for permission to publish this paper. The writer also thanks Messrs. E. S. Yu and J. M. Sirman of the same company for their assistance in preparing the manuscript.

References

1 Bodewig, E., *Matrix Calculus*, Second ed., North-Holland Publishing Co., Amsterdam, 1959, p. 5.

2 Bowman, R. A., Mueller, A. C., and Nagle, W. M., "Mean Temperature Difference in Design", TRANS. ASME, Vol. 62, 1940, p. 283.

3 Colburn, A. P., "Mean Temperature Difference and Heat Transfer Coefficient in Liquid Heat Exchangers," *Ind. Engg. Chem.*, Vol. 25, 1933, pp. 873–877.

4 Gardner, K. A., "Variable Heat Transfer Rate Correction in Multipass Exchangers, Shell Side Film Controlling," TRANS. ASME Vol. 67, 1945, p. 31.

5 Gardner, K. A., "Mean Temperature Difference in Unbalanced-Pass Exchangers," *Ind. Engg. Chem.*, Vol. 33, 1941, p. 1215.

6 Gardner, K. A. "Mean Temperature Difference in Multipass Exchangers," *Ind. Engg. Chem.*, Vol. 33, 1941, p. 1495.

7 *Standards of Tubular Exchanger Manufacturers Association*, TEMA, Fifth ed., 1968.

8 Kao, S., "Design Analysis of Multistream Hampson Exchanger With Paired Tubes," JOURNAL OF HEAT TRANSFER, TRANS. ASME, Vol. 87, 1965, p. 202.

9 Mcadams, W. H. *Heat Transmission*, Third ed., McGraw-Hill, N. Y. 1954, p. 191.

10 Mueller, A. C., "Criteria for Maldistribution in Viscous Flow Coolers," *Proceedings of International Heat Transfer Conference*, Heat Transfer, Vol. 5, 1974, p. 170.

11 Kwant, P. B., Zwaneveld, A. , and Dukstra, F. C., "Non-Isothermal Laminar Pipe," *Chem. Engg. Science*, Vol. 28, 1973, p. 1303.

12 Kays, W. M. "Numerical Solution for Laminar-Flow Heat Transfer in Circular Tubes," TRANS. ASME, Vol. 77, 1955, p. 1265; also discussion by Lipkis, p. 1273.

J. K. Hagge[1]
Research Asst.

G. H. Junkhan
Assoc. Professor.

Department of Mechanical Engineering,
Iowa State University,
Ames, Iowa

Mechanical Augmentation of Convective Heat Transfer in Air

An experimental investigation was conducted into augmentation of forced convection heat transfer in air by mechanical removal of the boundary layer. A rotating blade element passing in close proximity to a flat plate convective surface was found to increase the rate of convective heat transfer by up to eleven times in certain situations. The blade element effectively scrapes away the boundary layer, thus reducing the resistance to heat flow. Parameters investigated include scraping frequency, scraper clearance, and type of boundary layer. Increased coefficients were found for higher scraping frequencies. Significant augmentation was obtained with clearance as large as 0.15 in. (0.0038 m) between the moving blade element and the convective surface. The technique appears most useful for laminar and transitional boundary layers, although some improvement was obtained for the turbulent boundary layers investigated. The simple surface renewal theory developed for scraped surface augmentation in liquids was found to approximately predict the coefficients obtained. A new relation is proposed which gives a better prediction and includes the effect of scraper clearance.

Introduction

Applications where heat must be transferred across a solid/gas interface are quite common. Unfortunately, the film coefficients associated with gaseous convection are quite low. In particular, the most difficult part of any nonexpendable-coolant cooling system which must reject heat to the atmosphere is usually the thermal coupling between the solid convective surface and the cooling air. It is well known that boundary layers provide the primary resistance to heat flow from the solid surface to the gas. It would seem logical then that an approach which could remove these boundary layers would substantially increase the heat flow. Surface scraping is proposed as a means to remove the gaseous boundary layers. A scraping blade in close proximity to the convective surface is periodically moved across the surface to remove the insulating boundary layers.

An extensive literature search was carried out to determine if the scraped-surface[2] technique had previously been used with gaseous convection. While there is apparently no report in the literature of the scraped-surface technique being applied to gaseous convection, a considerable amount of work has been done using scraped-surface augmentation with liquids where up to an order of magnitude increase in film coefficients are obtained. The scraped-surface technique with liquids has found application with falling film evaporation apparatus for saline water conversion, chemical distillation, and fractionation, and in the food processing and chemical process industries. A discussion of the literature concerning scraped-surface heat transfer with liquids from 1928 to the present is given in reference [1].[3]

Two simple theories, or a combination thereof, have been advanced to model scraped-surface heat transfer with liquids. Kern and Karakas [2], Kirschbaum and Dieter [3], and Lustenader, et al. [4] have utilized a stagnant-film theory which assumes all resistance to heat transfer occurs in a stagnant film of thickness δ and thermal conductivity k in contact with the convective surface. The film thickness is generally taken as the scraper clearance or some fraction thereof. The effective film coefficient is therefore

[1] Presently with Collins Radio, Rockwell International, Cedar Rapids, Iowa.

Contributed by the Heat Transfer Division of THE AMERICAN SOCIETY OF MECHANICAL ENGINEERS and presented at the 1975 ASME-AIChE National Heat Transfer Conference, August 11–13, 1975. Revised manuscript received by The Heat Transfer Division September 19, 1975. Paper No. 75-HT-42.

[2] Note that the term "scraped-surface" is widely used for both situations where the scraper actually comes in physical contact with the surface, and for those situations where it is just in close proximity to the surface. This investigation is concerned only with the close proximity situation.

[3] Numbers in brackets designate References at end of paper.

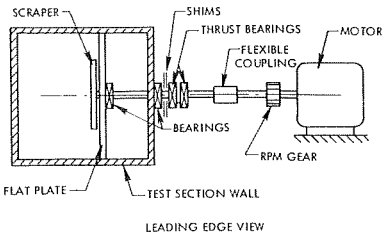

Fig. 1(*a*) Scraper drive train

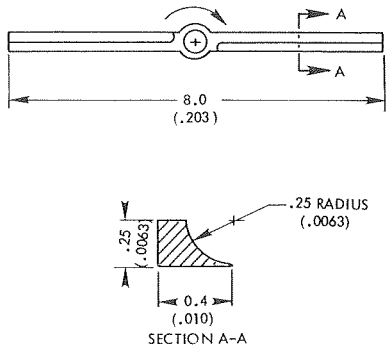

Fig. 1(*b*) Scraping blade

Fig. 1 Scraper mechanical and geometric arrangement—dimensions in inches (meters)

$$h = \frac{k}{\delta} \tag{1}$$

Harriot [5], Kool [6], and Latinen [7], have utilized a surface renewal/penetration theory which assumes the convective surface is periodically wiped clean, and fresh fluid at the bulk temperature comes instantaneously in contact with the convective surface. The effective coefficient for this theory is given by

$$h = \frac{2}{\sqrt{\pi}} \sqrt{\frac{\rho c_p k}{\tau}} \tag{2}$$

where ρ and c_p are fluid density and specific heat and τ is the time between surface renewals.

For liquids, each of the theories is found to describe particular but different limit cases. The stagnant-film theory has been applied with relatively good success to highly viscous liquids with laminar flows. The surface renewal/penetration theory, which by its nature must include some local turbulence or small scale mixing, has been relatively successful with liquids of low viscosity. Combinations of these theories have been proposed by Penney and Bell as cited by Penney [8], Thomas and Mohler [9], and Toor and Marchello [10]. A preliminary experimental investigation into several parameters involved in the use of surface scrapers to enhance convective heat transfer coefficients for gas boundary layers is described in the following and comparison of results with the models referenced is discussed.

Experimental Investigation

All experiments were performed in the subsonic wind tunnel of the Mechanical Engineering Department at Iowa State University. The wind tunnel is an open circuit suction type, with a 60 in. (1.52 m) long test section that is 14 × 14 in. (0.36 × 0.36 m) in cross section. The maximum free stream turbulence intensity for the range of tunnel velocities used was less than 0.6 percent.

An instrumented flat plate was installed with its leading edge vertical in the wind tunnel. A motor driven shaft through the back side of the wind tunnel and flat plate drove a surface scraper in close proximity to the front heated surface of the plate as shown in Fig. 1(*a*). A 0.625 in. (0.016 m) dia hollow shaft with a bearing support on the back of the flat plate and at the test section wall drove the scraping blade. The 8 in. (0.203 m) blade used in these tests is shown in Fig. 1(*b*). The shaft was driven by a ⅛ hp (93 W) universal motor operated on regulated d-c voltage. A series of shims allowed positioning of the thrust bearing housing for varying scraper clearance. Four clearances, 0.15 in. (0.00371 m), 0.10 in. (0.00254 m), 0.050 in. (0.00127 m), and 0.030 in. (0.000381 m), were used.

The front surface of the flat plate was a printed circuit board with a serpentine resistance pattern etched from 0.0013 in. (3.3×10^{-5} m) thick cupronickel foil on the surface to provide the heated surface. A similar printed circuit board was located in the interior of the flat plate as a guard heater for losses through the back of the plate. Thermocouples and pressure taps were mounted flush with the front surface of the plate from the interior in the locations shown in Fig. 2. a-c power was supplied to the various heating elements with variable transformers. Construction of the flat plate is described in more detail in reference [1].

Thermocouple EMF was measured on a multichannel recorder referenced to an ambient thermocouple within the tunnel located upstream of the plate's leading edge. The ambient temperature in the tunnel was in turn referenced to a 32°F (0°C) ice bath and monitored with a potentiometer.

The rotational speed of the shaft was monitored using a magnetic pickup in proximity to a 12 tooth steel gear on the shaft shown in Fig. 1. The output of the magnetic pickup was monitored on an oscilloscope to determine rpm.

Power to the heaters was monitored by measuring the voltage across the heater elements together with previously determined resistance values which were corrected in each test for temperature changes in resistance. Separate current and voltage leads were run

Nomenclature

C_f = skin friction coefficient
c_p = specific heat
h = convective film coefficient
k = thermal conductivity
N = revolutions per unit time
Nu_x = local Nusselt number = hx/k
Nu_δ = clearance Nusselt number = $h\delta/K$
Pr = Prandtl number = $\mu c_p/k$ ($\mathrm{Re}_{\mathrm{eff}}$ = effective Reynolds number = $(U_\infty + U_B)x/\nu$
Re_x = local Reynolds number = $U_\infty x/\nu$
Re_δ = clearance Reynolds number = $U_B\delta/\nu$
s = unheated starting length
U_B = blade velocity
U_∞ = free stream velocity
x = distance from leading edge
y = distance from wall
δ = film or boundary layer thickness, scraper clearance
ν = kinematic viscosity
ϕ = dimensionless clearance = $\delta\sqrt{\mathrm{Re}_x}/5x$
ρ = density
τ = time between surface renewals
τ_w = wall shear stress
μ = absolute viscosity

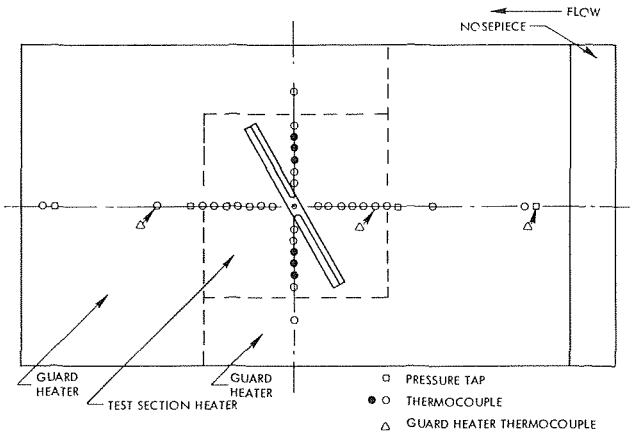

Fig. 2 Thermocouple and pressure tap locations on flat plate

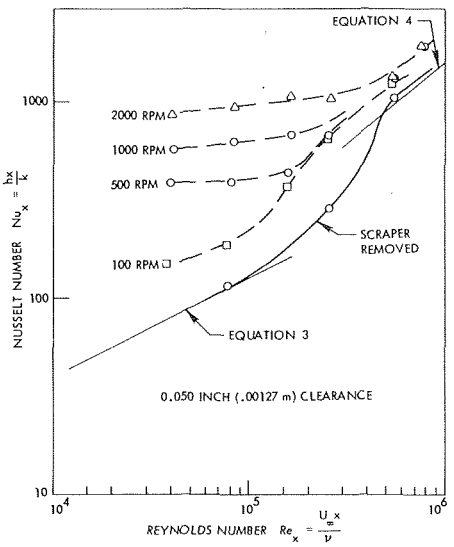

Fig. 4 Scraped performance with δ = 0.050 in. (0.00127 m)

to the heater elements to eliminate measuring any power dissipation losses in the lead wires.

The position of the flat plate was adjusted in the wind tunnel to give a zero pressure gradient along the plate surface using the pressure taps shown in Fig. 2. Prior to installing the scraper mechanism, the shaft hole was filled and smoothed, and boundary layer velocity profiles were measured with a small total pressure probe. These tests indicated excellent agreement with a Blasius velocity profile for Re_x up to 1.79×10^5. The shaft bearing supports were then adjusted to align the scraping blade parallel to the plate surface, with shims installed at the thrust bearing to give the appropriate clearance.

With the scraper speed and the free stream velocity at the desired levels, power was supplied to the test section and the adjacent heaters to provide a uniform heat flux over the surface of the plate. Corrections for losses from the front and back of the plate were made utilizing measured data and were each typically less than 10 percent of the total power.

Convective coefficients were calculated using data obtained from the spanwise thermocouples shown as filled circles in Fig. 2. An uncertainty analysis indicates the experimental determinations of Nusselt number are of the order of ±10 percent.

Results

For comparison with existing theory a series of tests were run with the scraper removed and the shaft hole filled and smoothed. Heat transfer coefficient relations for a uniform surface heat flux are given by Kays [11, pp. 222, 244]; for Pr = 0.706 these relations reduce to

$$Nu_x = 0.403\ Re_x^{0.5} \tag{3}$$

for laminar boundary layers, and to

$$Nu_x = 0.0249\ Re_x^{0.8} \tag{4}$$

for turbulent boundary layers. Equations (3) and (4) are plotted in Fig. 3 along with the data for the tests with the scraper removed showing reasonable agreement with theory from the laminar range up to the turbulent range. The effect of the 2 in. (0.051 m) unheated starting length of the nosepiece was accounted for by applying the appropriate correction factors to the Nusselt number. For laminar flow Eckert's correlation [12] was used

$$Nu_{corrected} = Nu_x \left[1 - \left(\frac{s}{x}\right)^{0.75}\right]^{-1/3} \tag{5}$$

For turbulent flow Rubesin's correlation [13] was used

$$Nu_{corrected} = Nu_x \left[\left[1 - \left(\frac{s}{x}\right)^{39/40}\right]^{-7/9}\right] \tag{6}$$

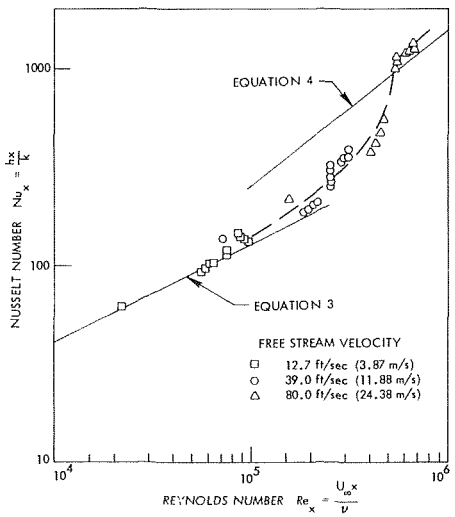

Fig. 3 Tests with scraper removed

Fig. 4 shows the experimental results for various rotational speeds with one of the four scraping clearances tested. The indicated Nusselt numbers have been corrected for the unheated starting length. This correction is somewhat arbitrary for the scraped-surface situation but has been applied to maintain what is thought to be a fair comparison between the scraped and unscraped performance. Fig. 4 indicates up to eleven times improvement in heat transfer in normally laminar flows, with the highest scraping speeds providing the most augmentation. Above 100 rpm the augmentation increases approximately linearly with scraping speed, with the rate of increase being much higher in laminar flow than in turbulent flow. Fig. 5 indicates that the effect of scraper clearance is small for the range of clearances tested, with the maximum augmentation being at most inversely proportional to the fourth root of clearance. However, much of the data indicates an even smaller influence due to clearance. Fig. 5 is plotted as a function of the dimensionless scraper clearance ϕ, where ϕ is defined by

$$\phi = \frac{\delta}{5x}\sqrt{Re_x}$$

For laminar flow ϕ is equivalent to the ratio of scraper clearance δ

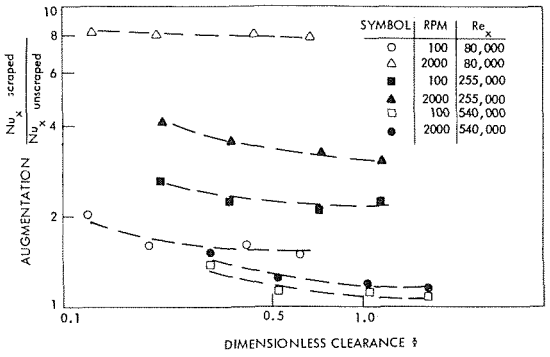

Fig. 5 Effect of clearance

to the normal unscraped boundary layer thickness.

Discussion

The stagnant-film and surface renewal/penetration models were proposed for conditions where free-stream Reynolds number effects are small relative to surface scraping effects, corresponding to conditions where the effect of free-stream Reynolds number is small. For the clearance of Fig. 4, the effect of free-stream Reynolds number is small for scraper speeds of 1000 and 2000 rpm below $Re_x = 10^5$ and for scraper speeds of 500 and 100 rpm below $Re_x = 4 \times 10^4$. The boundary layer approaching the scraped section at these Reynolds numbers is laminar according to the surveys made without the scraper. These data together with similar data for other clearances are shown in Fig. 6, where a line representing the surface renewal/penetration model is included. The time between renewals is taken as one-half the period of revolution for a two-bladed scraper. Agreement is good except at short time intervals where the model predicts lower heat transfer coefficients.

The same data are also shown on coordinates appropriate to the stagnant-film model in Fig. 7, where the model is represented by the horizontal dashed line. The implication here appears to be that the effective thickness of the stagnant film does not remain constant nor have a simple relationship to scraper rotational speed. Noting that the purpose of the scraper is to disturb the boundary layer, some improvement in correlation is obtained by use of the simple heat transfer-momentum transfer analogy and the assumption of turbulent flow between the scraper and the plate.

For the uniform incompressible flow past a flat plate at zero incidence, the analogy is [14]

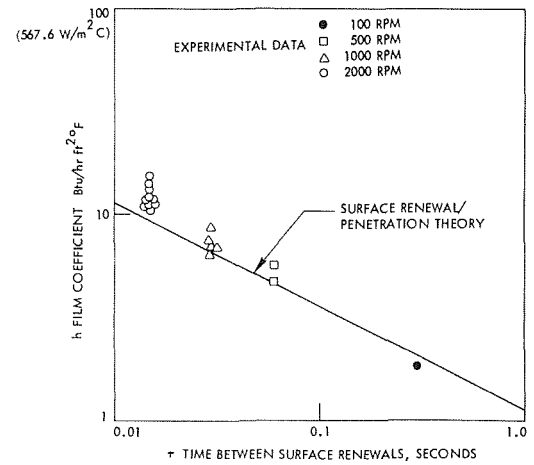

Fig. 6 Comparison with surface renewal/penetration theory

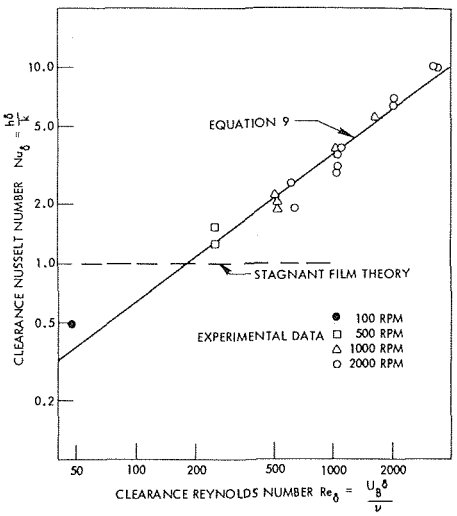

Fig. 7 Comparison with stagnant film theory and equation (9)

$$Nu_x = Re_x \left(\frac{C_f}{2}\right) Pr^{1/3} \tag{7}$$

The skin friction coefficient can be expressed for turbulent flow as [14]

$$\frac{C_f}{2} = 0.0228 \left(\frac{\nu}{U_\infty \delta}\right)^{1/4} \tag{8}$$

Inserting equation (8) into (7) and multiplying by the ratio δ/x,

$$Nu_\delta = 0.0228\, Re_\delta^{0.75}\, Pr^{1/3} \tag{9}$$

In equation (8), δ is the boundary layer thickness, taken in this case to be impressed on the test area as the scraper clearance by the blade moving with a velocity U_B. The free-stream velocity is then considered as U_B in equation (9). A line representing equation (9) with the Prandtl number taken for air is also shown in Fig. 7. The agreement is better, suggesting that a type of turbulent flow exists between the scraper blade and the plate surface. Note that this occurs even for low scraper rotational speeds, corresponding to low blade velocities.

Assuming then, that the effect of surface scraping in air is related to the turbulence generated by the blade, it is reasonable to ask whether similar augmentation could be obtained by a free-stream flow with high turbulence intensity and no scraper. For the condition of a flat plate with zero pressure gradient, it has been shown by Junkhan and Serovy [15], among others, that the effect of free-stream turbulence alone on the heat transfer coefficient is negligible; the major manifestation of the turbulence is simply an earlier transition from a laminar to a turbulent boundary layer. The Nusselt numbers would be predicted by equation (4) at lower Reynolds numbers for such conditions. The Nusselt numbers obtained with the scraper are significantly higher than those predicted by equation (4), implying that the scraper is responsible for the augmentation observed.

The experiments performed in this study also included data taken for conditions where free-stream Reynolds numbers had an effect on the Nusselt number. Nusselt numbers for the overall range of Reynolds numbers investigated have been correlated within 25 percent by using an empirical relation formed from the conventional turbulent flow equation by adjusting the Reynolds number to reflect the effect of the surface scraping. The effective Reynolds number was redefined by

$$Re_{eff} = \frac{(U_\infty + U_B)x}{\nu} \tag{10}$$

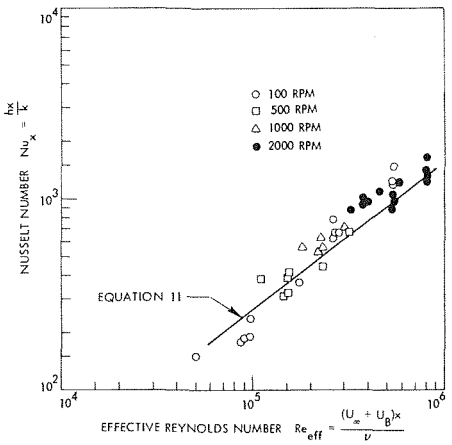

Fig. 8 Comparison of all tests with equation (11)

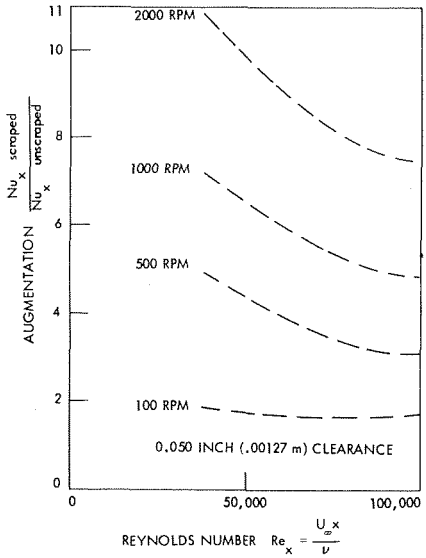

Fig. 9 Augmentation in laminar flow

and the heat transfer relation is

$$Nu_x = 0.0249\ Re_{eff}^{0.8} \tag{11}$$

A comparison of all the experimental data for surface scraping with equation (11) is shown in Fig. (8).

Conclusions

The test results for the particular geometry and flow conditions studied lead to the following conclusions:

1 Up to an order of magnitude increase in convective heat transfer coefficients can be obtained with the surface scraping technique.

2 Scraping speed is the dominant parameter, with augmentation approximately proportional to scraping speed for speeds above 100 rpm.

3 Clearance between the scraper blade and plate surface has a relatively minor effect on convective coefficient augmentation for clearances from 0.030 to 0.150 in. (0.0007–0.0038 m). These relatively large clearances still produced significant augmentation. Note that the proposed relation given by equation (9) will predict significantly greater augmentation as the clearance is reduced. Such data has not yet been obtained and extrapolation to small clearances should be done with caution.

4 Augmentation appears to be due to turbulent-type flow between the scraper and the plate surface, with the most significant increases occurring for normally laminar boundary layers. Based upon the data obtained for plate Reynolds numbers which are normally laminar, Fig. 9 shows the augmentation realized in this investigation.

5 Augmentation for laminar boundary layers is considerably greater than would be obtained from an induced transition to turbulent flow at the same Reynolds number.

6 Heat transfer performance for conditions where a laminar boundary layer would exist without the scraper is fairly well predicted by the surface renewal/penetration theory or by equation (9). In situations where a turbulent boundary layer would exist without the scraper, the performance is approximately predicted by the relation given as equation (11).

The scraped-surface method offers potential augmentation for heat exchangers with normally laminar boundary layers. Examples of such cases might be in electronics equipment or low face velocity plate type heat exchangers.

Acknowledgments

The writers are indebted to the Engineering Research Institute of Iowa State University, John Deere and Company, and Collins Radio Company for their partial support of this work. We would like to thank Mr. R. W. Wright and Mr. V. J. Grondahl of Collins Radio for the use of Collins' facilities in fabricating the printed circuit heating elements of the apparatus, and the assistance of Mr. D. D. Miller in this endeavor. Acknowledgment is made to a conversation many years ago with Mr. H. J. Bronson and Mr. V. L. Carlson from which recently germinated the idea of augmenting gaseous convection with surface scraping.

References

1 Hagge, J. K., and Junkhan, G. H., "Experimental Study of a Method of Mechanical Augmentation of Convection Heat Transfer Coefficients in Air," Technical Report HTL-3/ISU-ERI-AMES-74158, Engineering Research Institute, Iowa State University, Ames, Iowa, Nov. 1974.

2 Kern, D. Q., and Karakas, H. J., "Mechanically Aided Heat Transfer," *Chem. Eng. Prog. Symp. Ser.* Vol. 55, No. 29, 1958, pp. 141–148.

3 Kirschbaum, E., and Dieter, K., "Warmeübergang und Teildestillation in Dunnschichtverdampfern," *Chem.-Ing.-Tech.*, Vol. 30 1958, pp. 715–720.

4 Lustenader, E. L., Richter, R., and Neugebauer, F. J., "The Use of Thin Films for Increasing Evaporation and Condensation Rates in Process Equipment," JOURNAL OF HEAT TRANSFER, Series C, Vol. 81, 1959, pp. 297–307.

5 Harriot, P., "Heat Transfer in Scraped-Surface Exchangers," *Chem. Eng. Prog. Symp. Ser.*, Vol. 55, No. 29, 1958 pp. 137–139.

6 Kool, J., "Heat Transfer in Scraped Vessels and Pipes Handling Viscous Materials," *Trans. Instn. Chem. Engrs.*, Vol. 36, 1958, pp. 153–158.

7 Latinen, G. A., "Discussion of the Paper 'Correlation of Scraped Film Heat Transfer in the Votator' by A. H. Skelland," *Chem. Eng. Sci.*, Vol. 9, 1959, pp. 263–266.

8 Penney, W. R., "The Spiralator-Initial Tests and Correlations," Paper presented at the Eighth National Heat Transfer Conference of the AIChE-ASME, Los Angeles, Calif., Aug. 8–11, 1965.

9 Thomas, L. C., and Mohler, R. A., "Mathematical Model for Close Clearance Heat Exchangers," ASME Paper No. 71-HT-32, 1971.

10 Toor, H. L., and Marchello, J. M., "Film-Penetration Model for Mass and Heat Transfer," *AIChE Journal*, Vol. 4, 1958, pp. 97–101.

11 Kays, W. M., *Convective Heat and Mass Transfer*, McGraw-Hill, New York, 1966.

12 Eckert, E. R. G., *Introduction to the Transfer of Heat and Mass.*, McGraw-Hill, New York, 1950.

13 Rubesin, M. W., "The Effect of an Arbitrary Surface Temperature Variation Along a Flat Plate on the Convective Heat Transfer in an Incompressible Turbulent Boundary Layer," NACA TN 2345, 1951.

14 Schlichting, H., *Boundary Layer Theory*, Fourth ed., McGraw-Hill, New York, 1960.

15 Junkhan, G. H., and Serovy, G. K., "Effects of Free Stream Turbulence and Pressure Gradient on Flat-Plate Boundary-Layer Velocity Profiles and on Heat Transfer," JOURNAL OF HEAT TRANSFER, Series C, Vol. 89, 1967, pp. 169–176.

M. C. Jones
R. G. Peterson

Cryogenics Division,
Institute for Basic Standards,
National Bureau of Standards,
Boulder, Colo.

A Study of Flow Stability in Helium Cooling Systems[1]

Methods have been developed for the computation of the frequency response and stability of helium cooling systems in the frequency range of the density wave instability. While more generally applicable, these methods were developed for a study of superconducting power transmission. Special features are the use of helium thermodynamic properties derived at every point from the exact equation of state, and the full accounting of the effect of compressibility. Classical linear control theory is employed throughout. By using a finite difference approach to the integration of the conservation equations over the space coordinate, the accuracy obtainable is limited only by the computation time available. Examples are given for representative transmission line parameters with the helium at a variety of supercritical pressures. It is concluded that, while density wave instability is a real potential problem in superconducting power transmission lines, it is not difficult to select operating parameters in a safe stable regime.

Introduction

Although the analysis and computations described in this paper are equally applicable to any helium cooling system, the work was prompted by the peculiar demands of superconducting power transmission line development. There are now several research and development projects being carried on in laboratories in the United States and abroad and it appears certain that the next five years will see large scale experimental and prototype power transmission lines being built [1].[2] This study has to do with the well known, but not well documented, phenomenon of oscillations in helium flow systems. The purpose was to make analyses and computations to determine the effect of system parameters on stability and to define areas of stable operation.

In particular, the paper deals with the type of flow system instability, well known in both subcritical and supercritical heat exchangers at high temperatures, in which disturbances are propagated through the coolant channel at the fluid velocity. This is commonly called a density wave instability or oscillation [2], the frequency being given by $\frac{1}{2}\tau$, where τ is the residence time of the fluid in the channel. It is recognized at the outset that other modes of oscillation are possible, particularly acoustic modes. These are the subject of continuing study.

The density wave instability has been studied for supercritical cryogenic fluids by Zuber [3] and by Friedly, et al. [4] using a two-zone equation of state that was originally intended for subcritical systems. In the two-zone approximation the specific volume (or density) is assumed to be constant in the first zone representing subcooled liquid. From the saturation point onward the specific volume is assumed to be linear with the enthalpy, and the effect of pressure on specific volume is ignored. Fig. 1 plotted from [5] shows the specific volume plotted against enthalpy for helium at a variety of pressures, and if the effect of pressure is ignored, one can see that the two-zone approximation would indeed be reasonable below the critical pressure (0.2275 MPa = 2.245 atm). However, above the critical pressure such an approximation is obviously weak and the zone boundary somewhat arbitrary. The transposed critical temperature at a given pressure has been suggested as a suitable zone boundary, but Fig. 1 shows that this indicates nothing more than a weak knee in the isobars. In view of our concern for accuracy and for realistic predictions, therefore, we decided to discard the two-zone approximation and, instead, to work out methods that would enable the fluid at all points to be represented by its true equation of state. Furthermore, we have not ignored the compressibility of the fluid, the neglect of which, as we will show, is not a conservative approximation.

One of the system parameters which was found to be important in higher temperature studies is the heat capacity of the coolant channel wall and the rate of heat exchange between the wall and coolant. We have also included this interaction, which leads to a stabilizing effect, but we find that at helium temperatures this interaction may be entirely ignored.

In the following sections we derive the working equations and describe two methods of solution. The first does make the assumption of zero compressibility, but this approximation proves useful in understanding the phenomenon. It has also been useful in providing a reference calculation in the development of the second method, which is quite general. Finally, we show some results of

[1] Contribution of the National Bureau of Standards and not subject to copyright.

[2] Numbers in brackets designate References at end of paper.

Contributed by the Heat Transfer Division and presented at the Winter Annual Meeting, New York, N. Y., November 17–22, 1974, of THE AMERICAN SOCIETY OF MECHANICAL ENGINEERS. Revised Manuscript received by the Heat Transfer Division January 13, 1975. Paper No. 74-WA/HT-24.

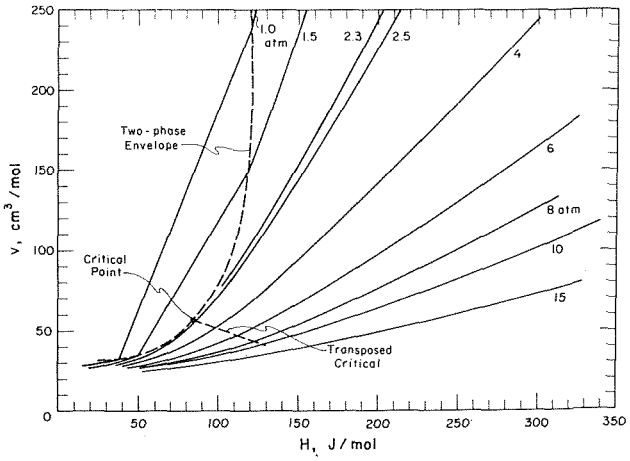

Fig. 1 The $v(H,p)$ representation of the thermodynamic states of helium I

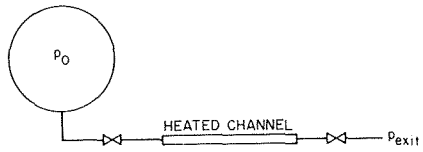

Fig. 2 Simple blow-down system

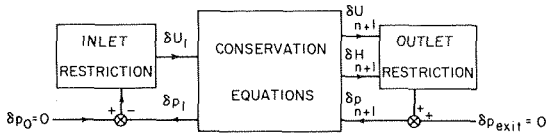

Fig. 3 Block diagram for simple blow-down system

computations illustrating the effect of some of the system parameters for possible power transmission line configurations.

Analytical Approach

In this study we have used the classical methods of linear control theory [6] to investigate the local stability of various chosen operating conditions. The analysis is most conveniently carried out by taking the Laplace transform with respect to time of the linearized time-dependent conservation equations. Setting initial conditions for the perturbed variables to zero, the ratio (output/input) for chosen variables of the total system gives its unit impulse response or transfer function $F(s)$ for the system. As is well known, instability is indicated by singularities of this function (or zeroes of the denominator) for positive values of the real part of the Laplace transform variable s. The system transfer function for any feedback system can be reduced to the form

$$F(s) = \frac{J(s)}{1 + J(s)H(s)} \tag{1}$$

where $J(s)$ is the forward transfer function and $H(s)$ is the feedback transfer function. (To avoid confusion with the enthalpy H the feedback transfer function is always written here as $H(s)$.) We thus seek roots of the characteristic equation

$$1 + J(s)H(s) = 0 \tag{2}$$

for positive values of the real part of s. This is done by making the Nyquist plot of the function $J(s)H(s)$ called the open loop transfer function. The theory of the Nyquist criterion of stability is given in standard texts on control theory [6].

Implicit in this approach is the need to integrate along the heat load channel the linearized conservation equations for the perturbations of the thermodynamic and hydrodynamic variables. As will be seen, this is the heart of the problem. In our approach we subdivide the channel into sections and use average steady-state thermodynamic and hydrodynamic parameters over each.

To be more concrete, we derive the working equations below for the simplest cooling system possible: a blow-down system, Fig. 2. In this system the refrigerant flows from a constant pressure reservoir, via a flow restriction, through the channel of the heat load, and via another flow restriction to a second constant pressure reservoir. As has been pointed out many times, this system is dynamically unchanged if the final flow restriction is choked. Anticipating the derivation of the working equations below, the block diagram for this system is given in Fig. 3. In all the work described we have selected δU_1, the perturbation in velocity at the inlet of the heated channel, as output and δp_0 as input. The feedback is thus δp_1, the perturbation in pressure at inlet.

Derivation of the Working Equations

Basic Assumptions. Referring to Fig. 2, it is assumed for this analysis that dense supercritical helium flows from a reservoir at constant pressure p_0 through a flow restriction into the channel of the heat load. The transfer of heat from high temperature surroundings and the a-c electrical dissipation in conductor and dielectric together produce a uniform mean heat flux q. However, due to perturbations in helium conditions, the nonzero heat capacity of the channel walls, and the temperature dependence of the losses, the heat flux to the helium will also, in general, experience perturbations δq. The instantaneous transfer of heat from channel wall to helium is described by a steady-state heat transfer coefficient h. This is acceptable in all cases of interest in transmission

Nomenclature

$\mathcal{A}$ = cross-sectional area, m^2
C_p = heat capacity of helium coolant, J/kg-K
$F = f\mathcal{P}/\mathcal{A}$, m^{-1}
$F(s)$ = system transfer function, m^2-s/kg
f = friction factor
G = mass flow per unit area, kg/m^2-s
H = enthalpy of helium coolant, J/kg
$H(s)$ = feedback transfer function, kg/m^2-s
h = heat transfer coefficient, W/m^2-K
$J(s)$ = forward transfer function, m^2-s/kg
k_I, k_E = orifice coefficients for inlet and exit flow restrictions, respectively
$\dot{m}$ = mass flow rate, kg/s
n = number of computational zones of heated channel
p = pressure, Pa
$\mathcal{P}$ = channel perimeter, m
q = heat flux into fluid, W/m^2
s = Laplace transform variable with respect to time
T = temperature, K
t = time, s
U = fluid velocity, m/s
v = specific volume, m^3/kg
x = axial length coordinate of heated channel, m
$\beta = q\mathcal{P}/\dot{m}$, J/kg-m
δ = prefix denoting infinitesimal perturbation
ρ = density, kg/m^3
τ = time constant or residence time, s
Ω = reaction frequency, s^{-1}, defined in text

Subscripts

i = inlet of computational zone
j = zone index
n = final zone
$n+1$ = conditions at outlet of final zone
o = supply reservoir conditions

Superscripts

$-$ = steady-state part of time dependent variable

line studies on account of the long periods of oscillations to be expected.

One-dimensional equations of conservation for mass, energy, and momentum are used throughout; thus, fluid parameters such as enthalpy, density, etc., refer to mean cross-sectional values, and we limit this study at the outset to perturbations traveling along the axis of the flow channels. In order not to limit the study to circular channels the geometry is described in terms of wetted perimeter $\mathcal{P}$ and cross-sectional area $\mathcal{A}$.

Conservation Equations and the Equation of State. The general one-dimensional equations for conservation of mass, energy, and momentum for horizontal flow are well known and are given without further comment.

$$\frac{D\rho}{Dt} = -\rho \frac{\partial U}{\partial x} \tag{3}$$

$$\rho \frac{D}{Dt}(H + U^2/2) = \frac{q\mathcal{P}}{\mathcal{A}} + \frac{\partial p}{\partial t} \tag{4}$$

$$\rho \frac{DU}{Dt} = \frac{-\partial p}{\partial x} \frac{-\rho f U^2 \mathcal{P}}{2\mathcal{A}} \tag{5}$$

These equations relate the density ρ, velocity U, enthalpy H, and the pressure p of helium within the channel. x is the length coordinate along the axis of the channel, t is the time coordinate, f is the friction factor and q is the uniform flux of heat entering the fluid stream from the wall. The operator D/Dt is $(\partial/\partial t + U\partial/\partial x)$.

In addition, we assume that an equation of state for thermodynamic equilibrium is always applicable and relates the density or specific volume v to the enthalpy and pressure:

$$v = v(H, p) \text{ or } \rho = \rho(H, p) \tag{6}$$

Now the most comprehensive description of the thermodynamic and volumetric properties of helium is given by the equation of state of McCarty [7]. This is in the more conventional form with temperature and density as independent variables; however, Arp has recently produced explicit expressions of the form (6), [8]. In the steady-state solutions given in the following, the older form was used since a computer program was already available for this.

Steady-State Solution. For the steady state, the x variation of the helium thermodynamic properties and the velocity may be obtained from equations (3), (4), (5), and (6) without regard to the conduction of heat in the channel walls. Thus, equations (3) and (4) can be integrated immediately, without knowledge of the equation of state, when we neglect the variation of U^2 compared to that of H. This will always be true at the velocities encountered in this problem. The result is:

$$\rho U = \text{const.} = \dot{m}/\mathcal{A} \tag{7}$$

$$(H - H_i) = \frac{q\mathcal{P}}{\dot{m}}(x - x_i) \tag{8}$$

where the subscript i denotes the value of a variable at some known inlet point (in this case either the entrance to the whole channel or one section of it) and $\dot{m}$ is the total mass flow rate of helium.

Also, in terms of thermodynamic derivatives obtained from the equation of state, the momentum equation (5) becomes

$$\frac{dp}{dx} = \frac{\frac{-\dot{m}}{\mathcal{A}}\left(\frac{\partial v}{\partial H}\right)_p \frac{q\mathcal{P}}{\mathcal{A}} - \frac{f\dot{m}^2\mathcal{P}v}{2\mathcal{A}^3}}{1 + \frac{\dot{m}^2}{\mathcal{A}^2}\left(\frac{\partial v}{\partial p}\right)_H} \tag{9}$$

This equation must be integrated numerically because of its nonlinear nature. We note that, when the variation of U^2 is neglected, equations (8) and (9) are completely equivalent to the equations for dp/dx and dT/dx given by Arp [9], which are written in terms of more customary thermodynamic derivatives.

Equations for the Perturbations. The variables U, H, p, q, and ρ or v are now written as the sum of a steady part and a time dependent perturbation, for example, $U = \bar{U} + \delta U(t)$. These substitutions are made in (3), (4), and (5), the steady-state equations subtracted, and only first order terms retained, leading to a set of linearized equations of conservation for the perturbed variables: equations (10), (11), and (12).

$$\frac{\partial \delta\rho}{\partial t} + \bar{\rho}\frac{\partial \delta U}{\partial x} + \delta\rho\frac{\partial \bar{U}}{\partial x} + \bar{U}\frac{\partial \delta\rho}{\partial x} + \delta U\frac{\partial \bar{\rho}}{\partial x} = 0 \tag{10}$$

$$\frac{\partial \delta H}{\partial t} + \bar{U}\frac{\partial \delta H}{\partial x} + \delta U\frac{\partial \bar{H}}{\partial x} + \frac{\bar{U}}{\bar{\rho}}\delta\rho\frac{\partial \bar{H}}{\partial x} - \frac{1}{\bar{\rho}}\frac{\partial \delta p}{\partial t} - \frac{\mathcal{P}}{\bar{\rho}\mathcal{A}}\delta q = 0 \tag{11}$$

$$\bar{\rho}\frac{\partial \delta U}{\partial t} + \bar{\rho}\delta U\frac{\partial \bar{U}}{\partial x} + \delta\rho\bar{U}\frac{\partial \bar{U}}{\partial x} + \bar{\rho}\bar{U}\frac{\partial \delta U}{\partial x} + \frac{\partial \delta p}{\partial x} + (2\bar{\rho}\bar{U}\delta U + \delta\rho\bar{U}^2)\frac{f\mathcal{P}}{\mathcal{A}} = 0 \tag{12}$$

The procedure of linearization limits the validity of these equations, and hence any deduction therefrom, to an infinitesimal region about the steady-state solution for the dependent variables. We can, therefore, also use a local equation of state; i.e.,

$$\delta v = -\frac{\delta\rho}{\bar{\rho}^2} = \left(\frac{\partial v}{\partial H}\right)_p \delta H + \left(\frac{\partial v}{\partial p}\right)_H \delta p \tag{13}$$

With this equation, $\delta\rho$ can be eliminated from (10), (11), and (12). We also take the Laplace transform with respect to time neglecting initial values and arrive at equations (14), (15), and (16).

$$(s - \bar{U}' + \bar{U}L)\delta H + \frac{\beta}{\Omega}(\bar{U}' - \bar{U}L)\delta U + r(s - \bar{U}' + \bar{U}L)\delta p = 0 \tag{14}$$

$$(s - \Omega + \bar{U}L)\delta H + \beta\delta U - (r\Omega + \frac{s}{\bar{\rho}})\delta p - \frac{\mathcal{P}}{\bar{\rho}\mathcal{A}}\delta q = 0 \tag{15}$$

$$(\bar{U}' + \frac{F\bar{U}}{2})\delta H - \frac{\beta}{\Omega}(s + \bar{U}' + F\bar{U} + \bar{U}L)\delta U + [r(\bar{U}' + \frac{F\bar{U}}{2}) - \frac{\beta}{\bar{\rho}\Omega}L]\delta p = 0 \tag{16}$$

Here we have used the notation L for the operator $\partial/\partial x$, $\bar{U}'$ is written for $\partial\bar{U}/\partial x$ and we have introduced the following constants

$$\Omega \equiv \frac{\left(\frac{\partial v}{\partial H}\right)_p q\mathcal{P}}{\mathcal{A}} \text{ (units: } \text{s}^{-1}\text{)}$$

(This is the so-called reaction frequency introduced by Zuber and used also by Friedly)

$$\beta = \frac{q\mathcal{P}}{\dot{m}} \text{ (units: J.cm}^{-1}\text{g}^{-1}\text{)}$$

$$F = \frac{f\mathcal{P}}{\mathcal{A}} \text{ (units: cm}^{-1}\text{)}$$

$$r = \left(\frac{\partial v}{\partial p}\right)_H / \left(\frac{\partial v}{\partial H}\right)_p = -\left(\frac{\partial H}{\partial p}\right)_v \text{ (units: J. Pa}^{-1}\text{g}^{-1}\text{)}$$

In general, in order to make this set soluble, a further equation is required—the energy equation for the channel wall—embodying a description of the perturbed part of the wall heat flux δq in terms of the other perturbations. However in all cases considered in this study δq was found to be quite negligible on account of the low wall heat capacity at superconductor temperatures and the small temperature dependence of superconductor losses.

Pressure-Drop Perturbations Across Flow Restrictions. If the steady-state pressure drop Δp may be related to the kinetic energy of the upstream fluid by

$$\Delta p = k\rho U^2 \tag{17}$$

where k is the empirical orifice coefficient for the restriction, and we assume that on the time scale of the anticipated flow oscillations hydrodynamic equilibrium always exists, then the perturbation in pressure drop is given in terms of δH and δU at inlet to the restriction by

$$\delta\Delta p = \frac{-kG^2\left(\frac{\partial v}{\partial H}\right)_p \delta H + 2kG\delta U}{1 + kG^2\left(\frac{\partial v}{\partial p}\right)_H} \tag{18}$$

For the inlet flow restriction in the blow-down system of Fig. 2, $\delta H = 0$ and, typically, the denominator will approximate 1.0. Equation (18) gives the pressure drop perturbation across the flow restriction in response to the velocity fluctuation δU. Thus

$$\delta \Delta p = 2k_I G \delta U_0 \tag{19}$$

with k_I referring to the orifice coefficient of the inlet restriction. Cases of most interest to us here have involved quite small inlet restrictions. In other words, we have been interested in low source impedance. In this case $\delta U \approx \delta U_1$. Referring to Fig. 3, the forward transfer function $J(s)$ is thus simply

$$J(s) = \text{constant} = \frac{1}{2k_I G}$$

For the downstream flow restriction, for either choked flow or where the downstream pressure is regulated, equation (18) gives the pressure fluctuation at the exit from the heat load channel. Since this will be the nth zone we have

$$\delta p_{n+1} = \frac{-k_E G^2 [(\frac{\partial v}{\partial H})_p \delta H]_{n+1} + 2k_E G[\delta U]_{n+1}}{1 + k_E G^2 [(\frac{\partial v}{\partial p})_H]_{n+1}} \tag{20}$$

Here we have usually been interested in rather large restrictions permitting expansion almost to atmospheric pressure and hence, no approximations have been made.

Methods of Solution

With reference to Fig. 3 we identify the feedback transfer function, $H(s)$ as $\delta p_1/\delta U_1$. Then with the system of equations described in the foregoing, the open loop transfer function $J(s)H(s)$ of equation (2) can be calculated once we have, first, the steady-state solution, i.e.; $\bar{U}$, $\bar{H}$, and $\bar{p}$, as a function of the x coordinate of the channel. Second, it is required to integrate equations (14), (15), and (16), along the x coordinate, subject to the boundary conditions $\delta H_1 = 0$ and δp_{n+1} given by (20), to get δp_1. For any given value of s we have used two methods to do this. The first to be described is an approximate method in that the helium compressibility is neglected, ie., $r \to 0$. The second method is exact in the sense that a finite difference numerical approach is used to solve the complete unabridged set of equations.

Steady-State Solution. The steady-state solution is computed by numerical integration of the T, p equivalents of (8) and (9), using the Adams-Moulton predictor-corrector method, with a variable x increment to achieve any predetermined accuracy. At each point the equation of state of McCarty is called to produce the correct values of the thermodynamic variables and appropriate derivatives. Transport properties are also supplied at each point from correlations also given by McCarty [5]. These are used to evaluate a Reynolds number and hence a friction factor by a standard formula for turbulent flow. A heat transfer coefficient is also computed at each point using the correlation of Giarratano, et al. [10].

Approximate Solution with Neglect of Compressibility in the Perturbed Equations (Method 1). This simplified solution follows the previous work of Zuber [3] and Friedly, et al. [4] for supercritical fluids. It is a very useful approximation in that analytical solutions may be obtained. These authors used a two-zone model (a constant density zone and one of constant thermal expansion, $(\partial v/\partial H)_p$) and defined the zone boundary in terms of an appropriate thermodynamic state. Thus, at the zone boundary, fluid properties were constant, but the space coordinate was perturbed. In our solution we permit any number of zones and solve the equations for a general zone of constant $(\partial v/\partial H)_p$. We define zone boundaries in terms of the space coordinate x at which, in steady-state solution, the appropriate thermodynamic state is found. Thus, in our solution the thermodynamic variables are perturbed at zone boundaries, but the space coordinate is not. The two approaches to defining a zone are equivalent, but we feel the one chosen here is more useful in a multizone computation.

Considering then, a general zone, we set $r = 0$ in equations (14) and (15). We also neglect the term $s\,\delta p/\bar{p}$ in (15), which is always negligible at frequencies of interest, and noting that for $r = 0$, $\bar{U}' = \Omega$, we arrive at (21) and (22).

$$(s - \Omega + \bar{U}L)\delta H + (\beta/\Omega)(\Omega - \bar{U}L)\delta U = 0 \tag{21}$$

$$(s - \Omega + \bar{U}L)\delta H + \beta \delta U = 0 \tag{22}$$

Simultaneous solution of (21) and (22) for constant Ω and β yields

$$\delta U = \text{constant} = \delta U_i \tag{23}$$

and

$$\delta H = \frac{\beta \delta U}{s - \Omega}(e^{(\Omega - s)\tau} - 1) + \delta H_i e^{(\Omega - s)\tau} \tag{24}$$

The subscript i always refers to conditions at the zone inlet, and we have used the usual definition of residence time, τ. Thus

$$\tau \equiv \int_{x_i}^{x} dx/\bar{U}(s) \tag{25}$$

Finally, we employ equation (16) with, again, $r = 0$, $\bar{U}' = \Omega$ and $L\delta U = 0$ to get the pressure drop perturbation for the jth zone.

$$(\delta p_i - \delta p)_j = \frac{G\Omega}{\beta} \int_{x_i}^{x} \frac{1}{\bar{U}} [(\Omega + \frac{F\bar{U}}{2})\delta H - \frac{\beta}{\Omega}(s + \Omega + F\bar{U})\delta U] dx \tag{26}$$

By substitution from (24) this integration can be carried out. When the pressure drop perturbations for the n zones are summed and added to δp_{n+1} from (20) we arrive at the required δp_1, or $\delta p_1/\delta U$, since δU is a common factor.

Equations (23) and (24) show how disturbances at the inlet to a zone are propagated: in the case of δU, with no change, but in the case of δH, in a complicated way. To understand physically the nature of this propagation it is necessary to transform (24) back to the time domain. Friedly [11] has considered this same solution as illustrating the nature of the response of hyperbolic systems. The first term is the response to the internal disturbance δU, while the second is the response to the disturbance δH_i at the boundary. The inverse transforms, when δU is a unit impulse disturbance, are, respectively,

$$\delta H_1(t) = \beta e^{\Omega t}[1 - \mathcal{H}(t - \tau)] \tag{27}$$

$$\delta H_2(t) = e^{\Omega \tau} \delta H_i(t - \tau) \tag{28}$$

The first shows an exponentially increasing contribution due to the velocity disturbance which is cut off by the Heaviside function $\mathcal{H}$ after a time τ, the time taken for the furthermost fluid (i.e., at the inlet) to reach the end of the zone. The second contribution due to the inlet enthalpy disturbance makes itself felt after a time delay τ. Thus, as is well known, the disturbances are propagated at the velocity of the fluid. In particular, we note that the specific volume disturbance is directly proportional to the enthalpy disturbance and we can visualize a density or thermal expansion wave travelling at the fluid velocity.

We note also that δH_i for the zone under consideration will be given by (27) and (28) applied to the preceding zone; so that, assuming δH_i was zero for the first zone, the net result for δH at the end of the last zone is a piecewise smooth exponentially increasing function of time cut off at $\tau = \Sigma_j \tau_j$ as sketched in Fig. 4.

In contrast to the enthalpy disturbance propagation at finite velocity, equation (26) shows that the pressure drop disturbance resulting from δH and δU appear across the zone without further delay, in this approximation. Equation (20) shows that this is true also for the pressure drop perturbation across the downstream flow restriction which will be delayed exactly by the total residence time α from the initiation of the impulse δU.

Exact Solution (Method 2). For a given value of s, equations (14), (15), and (16) are a set of first order, ordinary differential equations for the dependent variables δU, δH, and δp in the independent variable x. However, we find a complicated x dependence in the coefficients $\bar{U}'$, Ω, r, $\bar{\rho}$, and F. For an accurate solution, therefore, it appeared that only a numerical method would suffice.

The boundary conditions specify δU_1 and δH_1 at the inlet to the

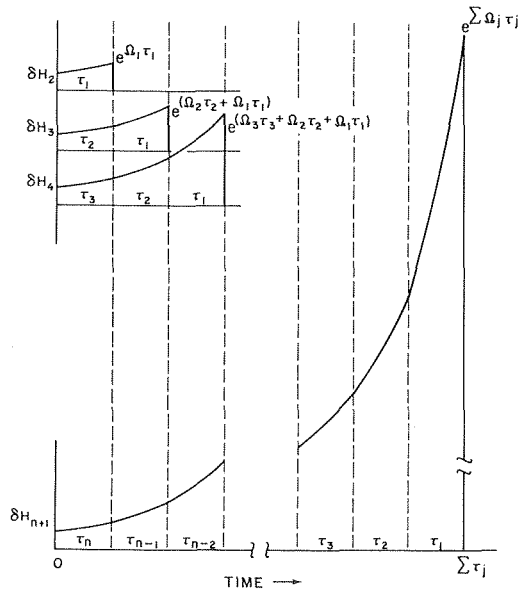

Fig. 4 Illustration of time development of enthalpy perturbation in response to a unit impulse velocity disturbance at inlet

heated channel, but δp_{n+1} at the outlet. Therefore, an implicit finite difference scheme must be used. Thus, we select n zones over each of which we assume the dependent variables and the x dependent coefficients are linear. Then for the jth zone we have, for example

$$\delta H = (\delta H_j + \delta H_{j+1})/2 \tag{29}$$

$$L\delta H = (\delta H_{j+1} - \delta H_j)/\Delta x_j \tag{30}$$

where Δx is the zone length. The subscript j refers to the inlet of the jth zone and $j + 1$ the outlet. In this way we can write down $3n$ equations and we shall have $3(n + 1) - 3 = 3n$ unknowns for the dependent variables at the zone boundaries. For the jth zone we have the equations

$$\begin{aligned} a_j\delta H_j + b_j\delta U_j + c_j\delta p_j + a_j'\delta H_{j+1} + b_j'\delta U_{j+1} + c_j'\delta p_{j+1} &= 0 \\ d_j\delta H_j + e_j\delta U_j + f_j\delta p_j + d_j'\delta H_{j+1} + e_j\delta U_{j+1} + f_j\delta p_{j+1} &= 0 \\ g_j\delta H_j + h_j\delta U_j + i_j\delta p_j + g_j\delta H_{j+1} + h_j'\delta U_{j+1} + i_j'\delta p_{j+1} &= 0 \end{aligned} \tag{31}$$

The coefficients a_j, b_j, etc., may be complex on account of the Laplace transform variable s. In matrix form we have equation (32).

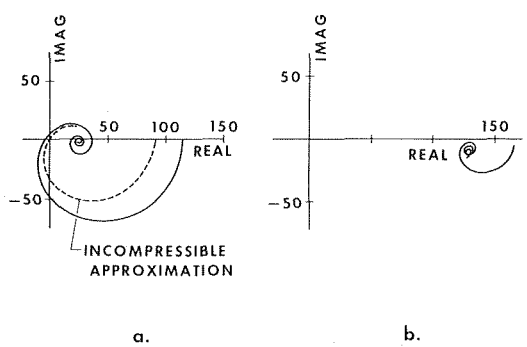

Fig. 5 (*a*) Nyquist plot of the open loop transfer function for a channel of length 240.0 m, dia 0.5 cm, heat load 0.15 W/m—$\dot{m}$ = 1.0 g/s, T = 4.5 K, p = 2.5 atm, k_I = 20.0, k_E = 20.0, n = 96. (*b*) Nyquist plot of the open loop transfer function for a superconducting power transmission line. Representative Nb_3Sn conditions: length 5.0 km, dia 5.0 cm, heat load 0.40 W/m—$\dot{m}$ = 138 g/s, T = 6.5 K, p = 10.0 atm, k_I = 20.0, k_E = 2000, n = 50.

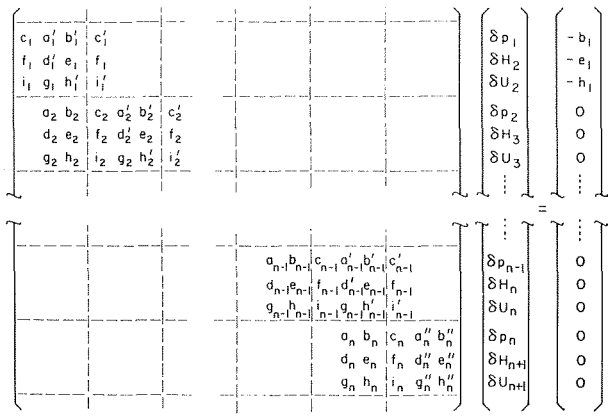

By partitioning into block-tridiagonal form followed by triangular decomposition [12], this set is solved without having to invert a more than 3×3 matrix.

Setting $\delta U_1 = 1$ the solution gives $\delta p_1/\delta U_1$ for the particular value of s chosen so that a Nyquist plot can be constructed. Typically, for 100 values of s the computation for $n = 30$ takes 2 min.

Results of Computations

Accuracy of the Computations. Confidence in the accuracy of the methods described was established by computations on the problem defined in Fig. 5(*a*). This problem was chosen for its closeness to the critical point, and the fact that the helium crosses the transposed critical line in its course along the heated channel. It was felt that this problem represented as severe a variation in helium properties as would be encountered in practice, and therefore, if it could be accurately computed, all problems of practical interest could be computed with at least the same accuracy.

We first determined that at least 8 zones were required in Method 1 for the quantity $|J(s)H(s)|$ to be within one percent of its asymptotic value. Method 1, which uses closed form integration, could then be used to check Method 2 in the incompressible approximation, i.e., using the same input data but setting $r = 0$, $U' = \Omega$ and neglecting the term $s\ \delta p/\rho$ in equation (15). This would establish the validity of the finite difference approach of Method 2. For the Method 2 calculations we set $n = 96$. We found the agreement most encouraging. The worst discrepancy, as might be expected, is at the point of resonance indicated by a peak in the system gain. Here there was a 2.6 percent discrepancy in $|J(s)H(s)|$. Over most of the range of s the discrepancy was less than 0.5 percent.

The problem was next recomputed using Method 2 in the full compressible case with $n = 96$ again. The Nyquist plot of $J(s)H(s)$ for this case is shown in Fig. 5(*a*). In Fig. 6 we show the system

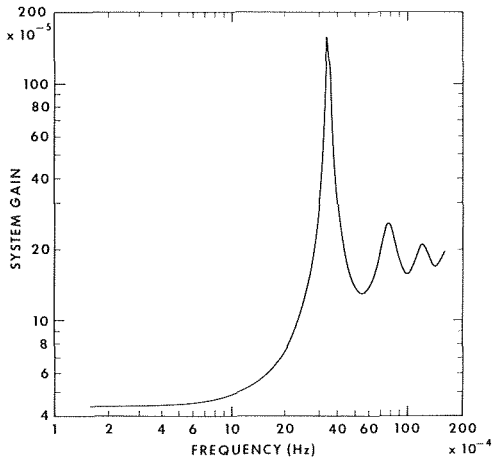

Fig. 6 System transfer function plotted versus frequency for conditions of Fig. 5(*a*)

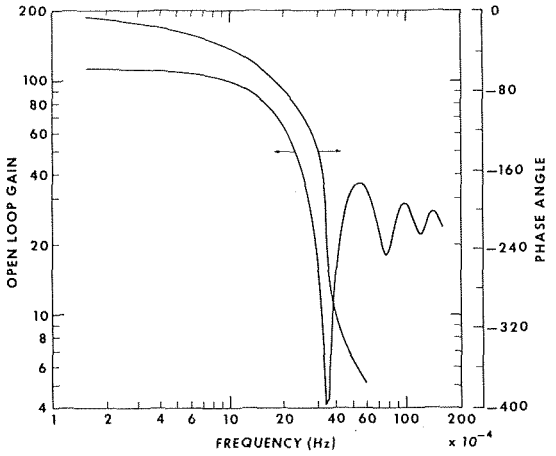

Fig. 7 Open loop transfer function and phase angle versus frequency for conditions of Fig. 5(*a*)

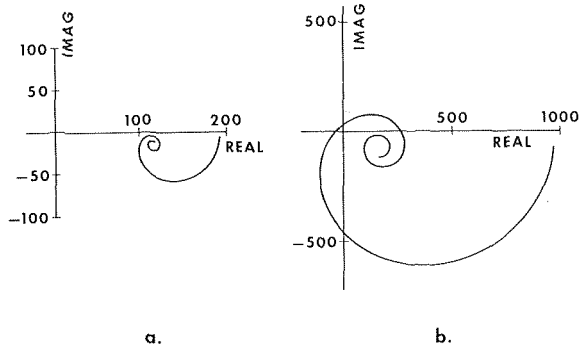

Fig. 8 (*a*) Nyquist plot of the open loop transfer function for a superconducting power transmission line. Representative Nb conditions: length 5000 m, dia 3.0 cm, heat load 0.120 W/m—$\dot{m}$ = 52.7 g/s, T = 4.5 K, p = 3.0 atm, k_I = 20.0, k_E = 900, n = 50. (*b*) Off-design conditions for line of Fig. 8(*a*): heat load 0.250 W/m, $\dot{m}$ = 43.9 g/s (other conditions unchanged).

gain, $F(s)$, plotted against frequency in Hz showing a sharp resonance at 0.0034 Hz. Fig. 7 shows the open loop gain $|J(s)H(s)|$ with the phase angle superimposed in the usual Bode plot. For comparison we have indicated in Fig. 5(*a*) the results of the aforementioned incompressible calculation.

From these plots we see that neglect of compressibility is not conservative as regards stability prediction. Whereas the incompressible computation predicted (fortuitously) marginal stability, the rigorous computation predicts a definite instability at the resonant frequency. The error in $|J(s)H(s)|$ caused by this neglect ranges from 17 percent at s = 0–82 percent in the region of resonance.

Although the accuracy obtained with n = 96 is certainly very adequate, the computation time for 100 values of s was 7 min. With n = 30 the same computation took 2 min. We therefore wished to know the error involved in relaxing the space grid this much. A comparison showed the worst error to be 6 percent in the frequency range examined. However, in the vicinity of the resonance it was only 0.4 percent. We, therefore, felt that for most purposes nothing important was lost by so relaxing the grid.

In conclusion, it appears that Method 2 is capable of very acceptable accuracy for quite reasonable computation times, and by taking full account of compressibility in the calculation some considerable errors are avoided.

Illustrative Examples. In this section we give results computed by Method 2 for some selected cooling system parameters which we believe to be representative of possible a-c superconducting power transmission lines.

Computations were performed for two different conductors: pure niobium (Nb) and niobium tin (Nb_3Sn). Each requires a different set of operating conditions. Thus, for Nb we selected temperatures of 4.5 K at inlet and 5.3 K at outlet. For Nb_3Sn we selected 6.5–8.5 K. In order to achieve sufficient density, the Nb_3Sn cable must operate at 10 atm while the Nb cable may operate at 3 atm. Specifying the length at 5000 m leaves only the channel diameter and wall heat flux to be specified; the mass flow rate of helium then follows.

We selected total wall heat fluxes—a-c losses, dielectric losses, and heat in-leak—of 2.55 W/m^2 for Nb_3Sn and half of this for Nb, these being typical projected figures.

As a representative example of the Nb_3Sn case, we give in Fig. 5(*b*) the Nyquist plot of $J(s)H(s)$ for a 5 cm dia helium channel computed by Method 2 with n = 50, k_I = 20 and k_E = 2000. The value chosen for k_I represents a small restriction—an orifice diameter 50 percent of the pipe diameter. k_E was chosen for a nozzle permitting expansion down to about 1.5 atm. Several variations of this case were also computed with different k_E and different diameters, but all show essentially the same thing: that this is a very stable operating condition.

In Fig. 8(*a*) we give the Nyquist plot for a Nb case with a 3 cm dia channel again computed with n = 50 and k_I = 20. Because of the lower pressure in this case the orifice coefficient at the exit is limited to about 1600 if the return pressure is set at no less than 1.5 atm. We arbitrarily chose 900 for this calculation. Again, many variations were computed for the Nb case, but all showed that at 3 atm, with a temperature range 4.5–5.3 K the system is stable.

The operating temperature range for the Nb case was purposely chosen to stay below the transposed critical temperature (5.58 K at 3.0 atm) and this indeed proved a wise choice. For suppose now that through a partial vacuum insulation failure, for example, the heat load were doubled in the above 3 cm dia case, and, to avoid excessive pressure drop, the flow rate were reduced slightly such that the temperature at outlet increased to 6.38 K. The Nyquist plot of Fig. 8(*b*) illustrates this case and it is apparent that this circumstance has driven the system into an unstable condition. The cause of this instability is to be found in the expansion which takes place across the 5000 m of transmission line. In the Nb_3Sn case the specific volume ratio at outlet to inlet is 1.5. In the Nb case for normal operation this ratio is 2.0 while in this off-design case it is 6. We note that the Nb_3Sn case under normal conditions operated in a temperature range encompassing the transposed critical temperature (8.15 K at 10 atm), so there is here no possibility of developing a similar instability through an accidental increase in heat load.

Acknowledgment

Vincent Arp is to be thanked for his constant interest in this work and in particular for the computer program for the computation of the steady-state conditions. The continued encouragement of Eric Forsyth and Jack Jensen of the Brookhaven National Laboratory is also highly appreciated.

References

1 Bogner, G., "Transmission of Electrical Energy by Superconducting Cables," *Superconducting Machines and Devices*, Plenum Press, New York, 1974 pp. 401–562.

2 Bouré, J. A., Bergles, A. E., and Tong, L. S., "Review of Two-Phase Flow Instability," ASME Paper No. 71-HT-42.

3 Zuber, N., "An Analysis of Thermally Induced Flow Oscillations in the Near-Critical and Supercritical Thermodynamic Region," Final Report NAS8-11422, NASA Marshall Space Flight Center, Huntsville, Ala., May 1966.

4 Friedly, J. C., Manganaro, J. L., and Kroeger, P. G., Final Report NAS8-21014, NASA Marshall Space Flight Center, Huntsville, Ala., Oct. 1967.

5 McCarty, R. D., "Thermophysical Properties of Helium-4 From 2 to 1500 K With Pressures to 1000 Atmospheres," Nat. Bur. Stand. (U.S.) Technical Note, Nov. 1972, p. 631.

6 Murphy, G. J., *Basic Automatic Control Theory*, Van Nostrand, Princeton, N. J., 1957.

7 McCarty, R. D., "Thermodynamic Properties of Helium 4 From 2 to

1500 K at Pressures to 10^8 Pa.," *J. Phys. Chem. Ref. Data,* Vol. 2, No. 4, 1973, pp. 923–1041.
8 Arp, V. D., "New Forms of State Equations for Helium," *Cryogenics,* Vol. 14, No. 11, Nov. 1974, pp. 593–598.
9 Arp, V. D., "Refrigeration of Superconducting Rotating Machinery," Nat. Bur. Stand. (U. S.) NBSIR, June 1973, pp. 73–331.
10 Giarratano, P. J., Arp, V. D., and Smith, R. V., "Forced Convection Heat Transfer to Supercritical Helium," *Cryogenics,* Vol. 11, 1971, p. 385.
11 Friedly, J. C., *Dynamic Behavior of Processes,* Prentice-Hall, N. J., 1971.
12 Westlake, J. R., *A Handbook of Numerical Matrix Inversion and Solution of Linear Equations,* Wiley, New York, 1968.

E. M. Sparrow
R. J. Goldstein
M. A. Rouf

Department of Mechanical Engineering,
University of Minnesota,
Minneapolis, Minn.

Effect of Nozzle—Surface Separation Distance on Impingement Heat Transfer for a Jet in a Crossflow

Measurements were made of the local heat transfer coefficients resulting from the impingement of a turbulent jet which interacts with a crossflow. The experiments were performed for separation distances between the exit of the jet nozzle and the impingement surface ranging from 3 to 12 times the jet exit diameter. The ratio of jet to crossflow mass velocity was varied from 4 to 12. To evaluate the heat transfer coefficients, local recovery temperatures were also measured. The results for the larger mass velocity ratios indicated that as the separation distance is varied, the impingement point heat transfer coefficient attains a maximum when the separation distance is 5–6 times the jet diameter. On the other hand, at a smaller mass velocity ratio such as 4, the maximum is attained at a substantially smaller separation distance. Experiments were also performed to examine how the transfer coefficients are affected by the presence or absence of a simulated duct wall at the exit of the jet nozzle. The differences between the results for the two configurations were confined to dimensionless separation distances greater than 4, with the largest effects at low mass velocity ratios.

Introduction

In recent years, cooling or heating of a surface by impinging jets has become an established technique. Since relatively high local coefficients are obtainable compared with those for nonimpinging flows, the jet impingement technique provides a designer with a means for more effective control of the temperature of the system being heated or cooled. In response to a need for basic heat transfer information, a number of investigations of impinging jets have been performed. In the main, these studies have been concerned with jets impinging normal to a surface situated in an otherwise quiescent environment. There are, however, practical applications where the jet interacts with a crossflow. Such a crossflow interaction is encountered, for example, in the internal cooling of turbine blades.

The present investigation is concerned with impingement heat transfer associated with a turbulent jet situated in a crossflow. The research was undertaken with two main objectives. The first was to determine how the local heat transfer coefficients on the impingement surface are affected by variations of the separation distance between the jet nozzle and the surface. In particular, it was of special interest to explore whether the heat transfer coefficient at the impingement point attained a maximum value as the separation distance was varied.

A second objective was to investigate the influence of the jet exit configuration on the local heat transfer results. To this end, two exit configurations were employed. In one, the end of the tube from which the jet issued was fitted with a plate aligned with the crossflow direction. The intended function of the plate was to inhibit flow field phenomena induced by the presence of the jet tube from influencing the interaction of the jet with the main stream. Such flow field phenomena would, of course, be absent if the jet were to issue from an aperture in a wall. In the second case, the plate was omitted, thereby permitting a freer interaction.

The experiments were performed with air as the fluid for both the jet flow and the crossflow. During the course of the work, the ratio of separation distance to jet exit diameter was varied from 3 to 12. A second parameter that was varied was the ratio of the mass velocities of the jet and the crossflow. This ratio ranged from 4 to 12.

Contributed by the Heat Transfer Division for publication in the JOURNAL OF HEAT TRANSFER. Manuscript received by the Heat Transfer Division March 6, 1975. Paper No. 76-HT-F.

There have been very few publications dealing with turbulent impinging jets in the presence of a crossflow, and those have been purely experimental. Kercher and Tabakoff [1][1] investigated the impingement cooling characteristics of a two-dimensional array of circular jets. A controlled crossflow was not employed in the experiments, but the spent air from the other jets in the array was, in effect, a crossflow. The separation distance to jet diameter ratio was confined to small values. In the range investigated, the heat transfer coefficient increased monotonically with the distance-diameter ratio and a maximum was not encountered.

Metzger and Korstad [2] measured average heat transfer coefficients on a surface on which there impinged a single line of circular jets situated in a crossflow. Measurements were made for three values of the separation distance—jet diameter ratio (2, 3.5, and 6.7), but the results did not show a clear cut trend as the ratio was varied. Recently, Bouchez and Goldstein [3] performed experiments with a turbulent jet in a crossflow and determined local heat transfer coefficients, impingement cooling effectiveness values (analogous to film cooling effectiveness), and impingement point locations. Inasmuch as the experiments were carried out for only two values of the ratio of separation distance to jet diameter (6 and 12), the detailed effect of spacing could not be definitely established. The impingement point transfer coefficients were higher at the smaller separation distance.

Experiments on impinging turbulent jets without crossflow have demonstrated that the impingement point heat transfer coefficient attains a maximum value as the ratio of separation distance to jet diameter is varied. Gardon, et al. [4, 5] found the maximum to occur when the ratio was in the range from 6 to 9, depending on the jet Reynolds number and nozzle diameter. A literature survey by Gauntner, Livingood, and Hrycak [6] concluded that the maximum heat transfer coefficient should occur when the impingement plate is separated from the nozzle exit by the length of the potential core. The survey also points out that various core lengths have been obtained by different investigators. A core length of 6.1 jet dia was recommended for applications in which the actual core length is not known.

Apparatus and Experimental Procedure

Experimental Apparatus. The description of the apparatus and procedure will be aimed at presenting a clear picture of the experimental work, but without exhaustive details. These details are contained in the thesis from which this work is drawn [7] as well as that of Bouchez [8].

The experiments were performed in a wind tunnel having a 15.2 by 20.3 cm rectangular cross section (height by width) and a length of about 115 cm. Air from the laboratory room was drawn through a contraction section into the wind tunnel by a blower situated at the downstream end. The tunnel throughflow served as the crossflow for the impinging jet. The air for the jet flow was taken from a regulated building air supply. The insulated pipeline that delivered the jet air to the upper wall of the wind tunnel contained regulating and flow control valves, an orifice metering station, and electric heaters to facilitate temperature control.

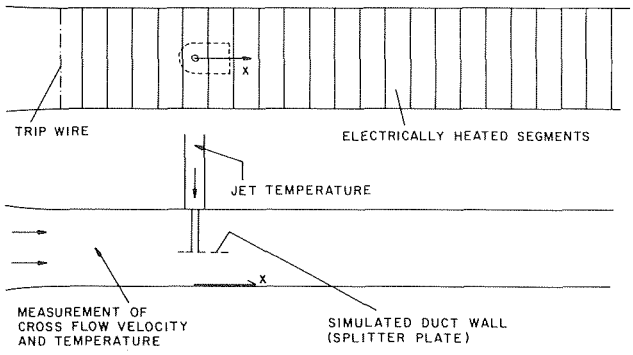

Fig. 1 Schematic top and side views (upper and lower diagrams, respectively) of the experimental apparatus

Schematic diagrams showing top and side views of the wind tunnel are presented in Fig. 1. As seen in the side view (lower diagram), the jet air passes from its delivery pipeline into a tube which protrudes downward into the wind tunnel from the upper wall. Tubes of various lengths were employed to obtain the desired range of separation distances between the jet exit plane and the lower wall of the wind tunnel, which served as the impingement surface. All tubes had a common internal diameter of 1.27 cm.

As discussed earlier, some of the data runs were made with a plate affixed to the lower end of the jet tube. The plate, which will hereafter be referred to as the splitter, was aligned parallel to the tunnel throughflow. Its purpose was to isolate the jet—crossflow interaction from the flow patterns induced by the presence of the jet tube. The plate dimensions (10.16 cm long by 6.35 cm wide) depicted in Fig. 1 are to scale with the duct dimensions. The planform of the plate is shown in the upper diagram of the figure.

As can be seen in the upper diagram, the impingement surface (lower wall of wind tunnel) was made up of 21 electrically heated segments. Each segment was a 0.00254-cm thick stainless steel foil, electrically isolated from its neighbors; the foils were connected in series and carried a common current. This heating arrangement gave rise to a nearly uniform heat flux to the flowing air. The heater segments spanned the 20.3-cm width of the wind tunnel and had a length of 5.08 cm in the flow direction. For support and insulation, the segments were bonded to a textolite plate backed with styrofoam (textolite is a phenolic and cotton fabric laminate).

Thermocouples were affixed to the rear surfaces of the heater segments by copper oxide cement. A total of 55 thermocouples were longitudinally distributed along the center span of the segments, that is, along the x axis. The thermocouples were heavily concentrated on the segments that encompassed the expected impingement region of the jet. There were eight thermocouples on each such segment. All of the thermocouples were made from a calibrated roll of wire.

In addition to the instrumentation already mentioned, sensors were installed to measure the velocity and total temperature of the

[1] Numbers in brackets designate References at end of paper.

Nomenclature

c_p = specific heat at constant pressure
D = jet exit diameter
h = local heat transfer coefficient, equation (3)
h_0 = local heat transfer coefficient due to crossflow alone
L = separation distance between nozzle and surface
M = ratio of mass velocities, equation (1)
q = local heat transfer per unit time and area
r = recovery factor, equation (4)
T_j = static temperature at jet exit
$T_j°$ = total temperature of jet
T_r = recovery temperature
T_w = wall temperature
T_∞ = static temperature of crossflow
$T_\infty°$ = total temperature of crossflow
u_j = jet exit velocity
u_∞ = crossflow velocity
x = streamwise coordinate
ρ_j = density at jet exit
ρ_∞ = density of crossflow

crossflow and the total temperature of the jet flow. For the latter, a thermocouple was placed in the jet delivery pipeline, where the velocity is relatively low. As indicated in Fig. 1, the thermocouple is about 10 jet dia upstream of the exit of the delivery pipeline. Corroborating thermocouples were also installed on the wall of the pipe. The velocity and total temperature of the crossflow were measured at half height and midspan in a cross section 19 cm upstream of the jet discharge. An impact probe and a wall static tap, in conjunction with a capacitance type pressure meter, were used for the velocity measurement, and the temperature was measured with a thermocouple.

The thermocouples that were installed to measure total temperatures actually read recovery temperatures. Computations indicated that for the conditions of the experiments, the difference between the stream total and probe recovery temperatures is about 0.02°C, which is negligible.

Experimental Procedure. A given data run was defined by setting the velocity of the crossflow, the velocity and total temperature of the jet, and the separation distance between the jet exit and the impingement surface. These enabled evaluation of the ratios

$$(a)\ M = (\rho u)_j/(\rho u)_\infty, \qquad (b)\ L/D \tag{1}$$

where M is the mass velocity ratio, L is the separation distance, and D is the jet exit diameter. The mass velocity ratio M was employed in lieu of other candidate groupings involving ρ_j, u_j, ρ_∞, and u_∞ because it had been found to be an effective correlating parameter by Bouchez and Goldstein.

There is virtually an unlimited number of choices that can be made in setting the temperature of the jet relative to that of the crossflow. The effect of temperature level was explored by Bouchez and Goldstein [3] and was not one of the research objectives of the present investigation. Consistent with the present objectives, it was deemed appropriate to select a standard temperature operating condition, namely, a matching of the total temperatures of the jet and the crossflow. If $T°$ denotes the total temperature, then the matching condition is

$$T_j° = T_\infty° \tag{2}$$

A data run consisted of two distinct parts, with the velocity and air temperature conditions maintained constant throughout. In the first part, the temperature distribution along the impingement surface (i.e., along the x axis) was measured under the condition that no electric power was supplied to the heater segments. These measurements yielded recovery temperatures $T_r(x)$ associated with the jet impingement (the crossflow velocities were too low to cause a recovery effect). The maximum value of $T_r(x)$, relative to $T_j°$ or $T_\infty°$ was about 2°C. In the second part, electric power was supplied to the heater segments, and measurements were made of the wall temperature distribution $T_w(x)$ and of the power input. The power level was selected so that variable property effects in the air would be negligible ($T_w - T_\infty < 20$°C). As will be discussed shortly, the data from both parts of a data run were needed in evaluating local heat transfer coefficients.

Results and Discussion

Presentation Variables and Parameters. Local heat transfer coefficients were evaluated from the definition

$$h = q/(T_w - T_r) \tag{3}$$

The local heat flux q for each heater segment was determined from the measured electric current flow in conjunction with the resistance of the segment. The determination of T_w and T_r has already been discussed in the prior section of the paper. The use of $(T_w - T_r)$ as the thermal driving force for convective heat transfer is well established for flows in which there is temperature recovery when the wall is adiabatic. Among all candidate thermal driving forces for such flows, only $(T_w - T_r)$ goes to zero when q goes to zero. Furthermore, it was demonstrated in [3, 8] that heat transfer coefficients defined in accordance with equation (3) are independent of the level of the heat flux q.

The effect of using $(T_w - T_\infty)$ in the definition of h instead of $(T_w - T_r)$ will be illustrated later. For the present, it is relevant to note that if the temperature difference between the wall and the fluid were large, the recovery effect would be unimportant. Under these conditions, it is not necessary to know T_r to apply the results. In the present experiments, the wall-fluid ΔT's were small at some surface locations, so that the use of $(T_w - T_r)$ was appropriate.

To present the results on a dimensionless basis and, at the same time, to provide a comparison that is of practical interest, the local heat transfer coefficients are expressed in terms of the ratio h/h_0. In this ratio, h is the local coefficient in the presence of the jet and the crossflow, whereas h_0 is the local coefficient (at the same streamwise location) due to the crossflow alone. Measurements of h_0 were made with the tunnel free of any obstructions, i.e., neither the jet tube nor the splitter were present. The departure of h/h_0 from unity identifies the surface locations at which the jet augments the transfer coefficients. The streamwise distributions of h/h_0 will be plotted against the streamwise position coordinate x/D. As illustrated in Fig. 1, the origin of the x coordinate is situated directly beneath the center of the tube from which the jet emerges.

The streamwise distribution of h/h_0 will be parameterized by the mass velocity ratio $M = (\rho u)_j/(\rho u)_\infty$ and the dimensionless separation distance L/D. The velocities u_j and u_∞, respectively, represent the mean jet velocity and the free stream crossflow velocity.

The measured recovery temperatures were also expressed in terms of a dimensionless group, the recovery factor r,

$$r = \frac{T_r - T_j}{u_j^2/2c_p} = 1 + \frac{T_r - T_j^0}{u_j^2/2c_p} \tag{4}$$

where T_j is the static temperature of the jet at exit. Inasmuch as $u_j^2/2c_p$ represents the difference between the stagnation and static temperatures of the jet, the recovery factor affords a comparison between the recovery temperature rise and the stagnation temperature rise. The streamwise distributions of r are parameterized by M and L/D.

To complete the parametric description of the experimental results, two additional specifications are relevant. The first has to do with the relative temperatures of the jet and the crossflow and, in the present investigation, total temperatures were matched as indicated in equation (2). The second relates to the velocity range of the crossflow. Owing to the trip wire situated at the upstream end of the test section (see Fig. 1, upper diagram), a fully turbulent boundary layer can readily be obtained along the lower wall of the wind tunnel [8]. In view of this, there is little motivation to parametrically vary the crossflow velocity. Therefore, for all data runs, the velocity was held fixed at 12 m/s, which corresponds to a Reynolds number of 720,000 per meter (220,000 per foot). The streamwise distribution of h_0 corresponding to this flow condition will be presented later. For the jet, the nozzle exit Reynolds numbers ranged from 38,000 to 115,000.

Local Heat Transfer Coefficients. To show how the local heat transfer coefficients respond to changes in the dimensionless nozzle-to-plate separation distance L/D, Figs. 2–4 are presented. Each figure contains two graphs, with each graph corresponding to a specific L/D. In this way, the three figures give results for six values of L/D: 12, 10, 8, 6, 5, and 3. The case $L/D = 12$ corresponds to the situation in which the nozzle exit is flush with the upper wall of the wind tunnel. To conserve space, results for other L/D values within this range are not presented here, but are available in [7]. Figs. 2–4 are for the data runs with the splitter affixed to the lower end of the jet tube. The results for the data runs without the splitter show identical trends and are discussed later.

In each graph, h/h_0 is plotted as a function of the dimensionless streamwise coordinate x/D. The curves are parameterized by the

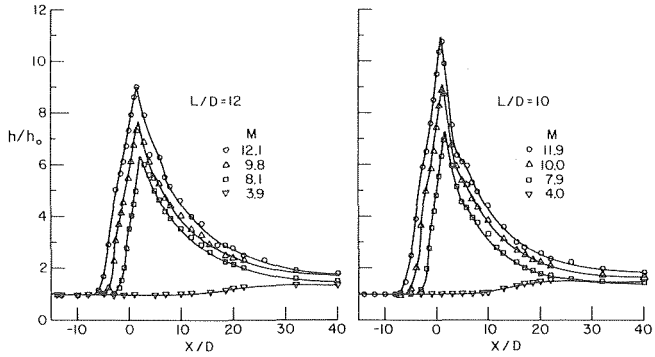

Fig. 2 Streamwise variation of the local heat transfer coefficient along the impingement surface, L/D = 12 and 10, with splitter

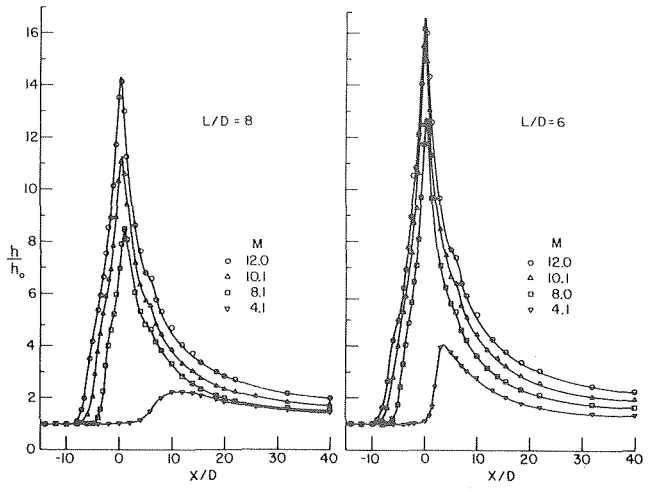

Fig. 3 Streamwise variation of the local heat transfer coefficient along the impingement surface, L/D = 8 and 6, with splitter

mass velocity ratio $M = (\rho u)_j/(\rho u)_\infty$, with nominal values of 4, 8, 10, and 12. Each curve depicts the distribution of h/h_0 along the x axis.

For the higher jet velocities, M = 8, 10, and 12, the distribution curves all have a common behavior. At locations that are substantially upstream of the impinging jet, h is within a few percent of h_0. As the impingement region is approached, h/h_0 increases. This increase in h/h_0 is manifested several jet diameters upstream of the actual zone of impingement. As identified in flow visualization studies by Bouchez and Goldstein [3, 8] and others (e.g., [9]), there is a highly turbulent recirculation zone situated upstream of the impingement area which is responsible for the upstream augmentation of h. The upstream penetration of the recirculation zone is increased with increases of the mass velocity ratio, and the heat transfer coefficients also increase. A similar outcome is brought about by decreases in the separation distance.

Within the impingement zone, the curves rise to a peak, the height of which is accentuated with increasing values of the mass velocity ratio. For a fixed value of the mass velocity ratio, the peaks grow higher as L/D diminishes from 12 to 5, but further decreases in L/D bring about a lowering of the peak. This interesting result will be further illuminated shortly.

Downstream of the impingement zone, a wall jet develops along the surface and the h values decrease, tending to approach h_0. Considerable augmentation still remains, however, even at x/D = 40 (e.g., $h/h_0 \sim 2$ for M = 12). At a fixed separation distance, the distribution curves in the downstream region are consistently ordered according to increasing values of the mass velocity ratio.

An exception to the trends cited in the last several paragraphs occurs when the jet does not impinge directly on the surface, but rather is swept downstream by the crossflow. This behavior is in evidence for the lowest mass velocity ratio M = 4 and at the largest separation distances L/D = 12 and 10. As the separation distance is diminished, the distribution curves for the M = 4 case display a steadily growing peak at the impingement point.

To provide further perspective about the effect of separation distance on the impingement point transfer coefficients, the peak values from Figs. 2–4, together with additional data from [7], have been brought together in Fig. 5. In this figure, $(h/h_0)_{peak}$ is plotted against L/D for parametric values of M. The curves in the left-hand graph correspond to data runs with the splitter plate present, whereas those in the right-hand graph are for the case of no splitter.

With the splitter present, the curves for M = 8, 10, and 12 take on their respective maximum values at L/D = 5. However, for M = 4, it appears that the largest of the peak values will be encountered when $L/D < 3$. For the case of no splitter plate, the results display their largest peak values at approximately the same L/D as the aforementioned; for M = 12 and no splitter, the maximum appears to be closer to L/D = 6. A graph similar to Fig. 5 was prepared [7] in which h (rather than h/h_0) was plotted as a function of L/D. From this graph, which is omitted to conserve space, it was observed that the L/D corresponding to the largest of the peak values of h is the same as the L/D at the largest of the peaks of h/h_0.

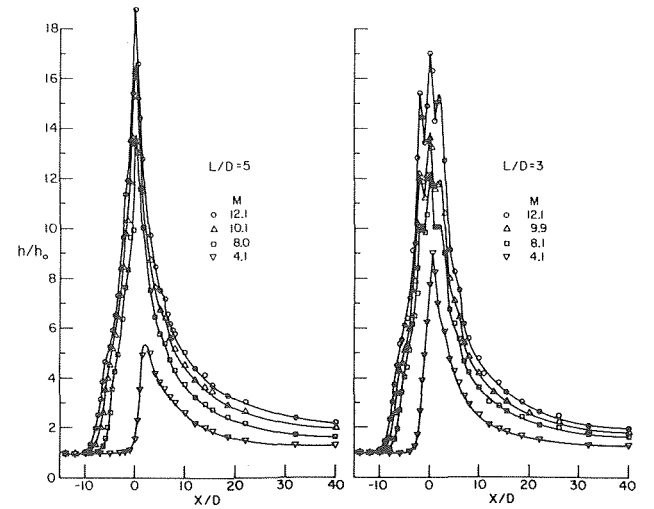

Fig. 4 Streamwise variation of the local heat transfer coefficient along the impingement surface, L/D = 5 and 3, with splitter

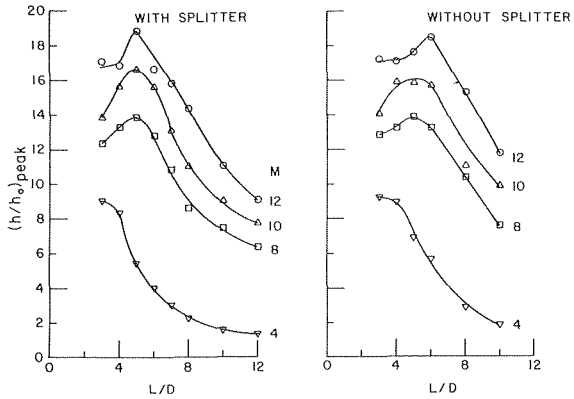

Fig. 5 Dependence of the impingement point transfer coefficient on separation distance

It is interesting to compare the just-determined L/D corresponding to the largest impingement point transfer coefficient to those obtained by prior investigators in the absence of crossflow. Gardon and Cobonpue [4] found L/D in the range from 6 to 9, with the spread primarily due to a variation in the nozzle diameter. For their largest nozzle diameter (~0.9 cm), which is somewhat smaller than the 1.27 cm dia nozzle of the present experiments, their results indicated an L/D value of about 6. The Gauntner literature survey [6] recommended a value of $L/D = 6.1$, albeit without a firm basis. The present experiments give $L/D \sim 5$–6 for $M = 8$, 10, and 12, and this is in very close agreement with the findings for no crossflow. However, for a low mass velocity ratio such as $M = 4$, the separation distance corresponding to the largest impingement point transfer coefficient is substantially less than that for no crossflow.

The existence of an optimal separation distance which affords a maximum impingement point transfer coefficient has been well explained by Gardon and Akfirat [5], so that only a brief discussion will be included here. At small separation distances, when a potential core exists within the jet, the impinging core velocity will be essentially unchanging as the separation distance increases. On the other hand, measurements have shown that the turbulence level within the core flow increases. Consequently, the impingement point heat transfer coefficients should also increase. With further increases in separation distance, the core is ultimately engulfed by the jet mixing processes and the impingement velocity decreases and, subsequently, the turbulence also decreases. This brings about a decrease in the impingement heat transfer coefficient. This pattern of an initial increase and a subsequent decrease of the transfer coefficient with increasing separation distance is consistent with the experimental results.

Attention may now be turned to a comparison of the local transfer coefficients obtained with and without a splitter plate. Local coefficients for the no-splitter case were measured for six separation distances, and these are available in [7]. For establishing the relationship between the results for the splitter and the no-splitter cases, observations obtained by overlaying corresponding figures for the two cases will be reported. In addition, for purposes of corroboration, results for the no-splitter case for two L/D values (8 and 3) are presented in Fig. 6.

From the aforementioned comparisons, it is found that at larger and intermediate separation distances (down to $L/D = 5$), the h/h_0 results in the presence of the splitter are somewhat lower than those for the no-splitter case. The differences between the two sets of results are primarily confined to the impingement and downstream regions. On a percentage basis, the largest effects are in evidence for the smallest mass velocity ratio $M = 4$ where, for instance, for $L/D = 8$, the peak values for the two cases differ by about 25 percent. In addition, in the presence of the splitter, the downstream deflection of the $M = 4$ jet is greater than in the absence of the splitter. As a tentative explanation of these findings, it can be reasoned that since the splitter inhibits fluid from above the jet exit plane from participating in the jet mixing process, the turbulence level of the jet is somewhat reduced. This should reduce the heat transfer coefficients of the impinging jet. Another effect of the blockage of fluid downflow by the splitter is to decrease the pressure downstream of the jet. This lowering of the pressure tends to pull the jet downstream, resulting in a greater deflection.

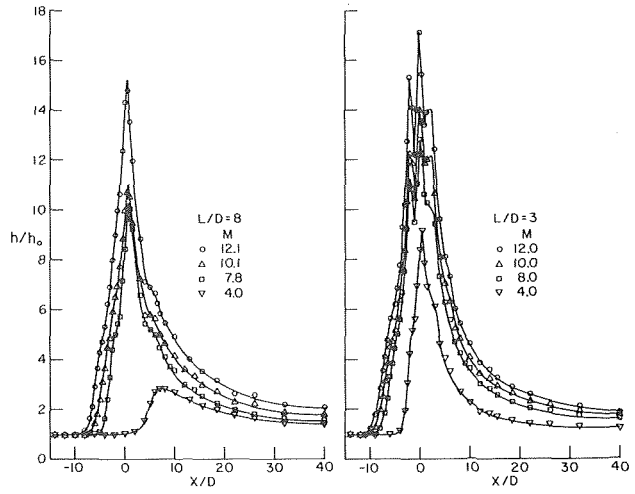

Fig. 6 Distributions of the local heat transfer coefficient for the no-splitter case

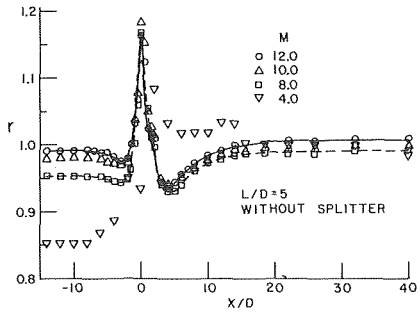

Fig. 7 Illustrative recovery factor results

At the smaller separation distances ($L/D = 4$ and 3), the h/h_0 curves for the two cases are very nearly coincident. It is, thus, seen that the influence of the splitter is confined to separation distances greater than $L/D = 4$, with the greatest effects at low mass velocity ratios.

Before concluding this section of the paper, there are a few additional observations that may be made about the distribution curves of Figs. 2, 3, 4, and 6. The first relates to the shifting of the location of the peak with variations of L/D and M. This shifting is related to the degree of deflection experienced by the jet owing to the action of the crossflow. The extent of the deflection and the corresponding downstream movement of the peak is accentuated at larger L/D and lower M. The second item of interest is the local maxima that flank the main peak in the distribution curves when the separation distance is small. These local maxima become more prominent at larger M values. They are believed to indicate a transition from laminar to turbulent boundary layer flow. Similar local maxima were encountered previously by Gardon and co-workers [4, 5] in the absence of a crossflow.

Other Results. A complete presentation of recovery factor results is available in [7], and only a single figure, Fig. 7, will be given here for illustration. In Fig. 7, r is plotted versus x/D for the case of $L/D = 5$ and no splitter. The trend in the data for $M = 8$, 10, and 12 is typical of that encountered at the other separation distances, except for differences in detail. On the other hand, the plotted points for $M = 4$ are, in a sense, random. This is because the temperature difference $(T_r - T_j°)$ which enters the definition of r (equation (4)) is typically in the range of 0.1–0.2°C for $M = 4$. Thus, a measurement uncertainty of a few hundredths of a degree (due, for example, to variations in the air temperature) can have a significant effect on r. Fortunately, temperature recovery played an inconsequential role in the evaluation of the heat transfer coefficients for $M = 4$.

Perhaps the most noteworthy feature of Fig. 7 is the fact that $r > 1$ in the impingement region. It is believed that this finding is related to the fact that the jet static temperature at the nozzle exit is less than that of the surrounding crossflow and, as a consequence, the jet gains enthalpy as it entrains surrounding fluid. In order that the higher enthalpy of the entrained fluid have a significant effect on the impingement point recovery factor, it must penetrate

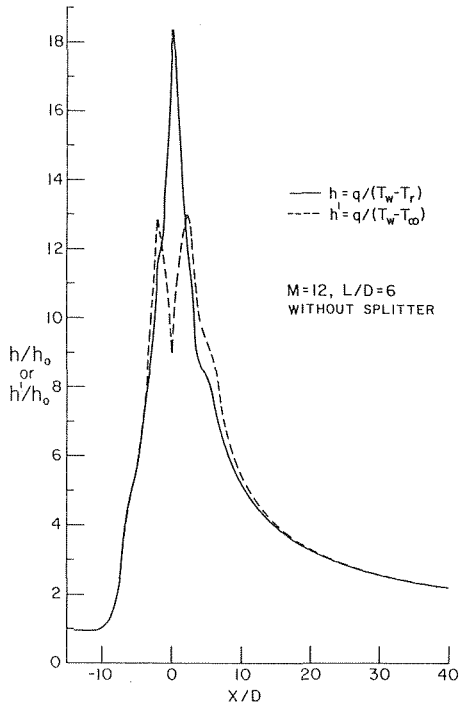

Fig. 8 Influence of the temperature difference used in the definition of the heat transfer coefficient

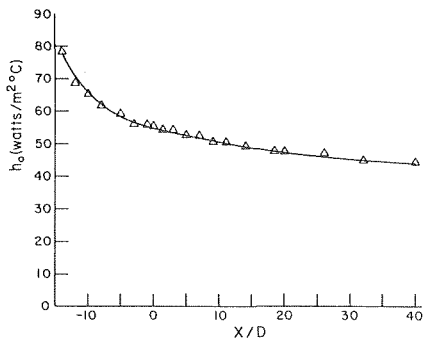

Fig. 9 Local surface heat transfer coefficients for the crossflow without jet impingement

to the center of the jet, that is, the jet mixing region must engulf the potential core. The plate-to-nozzle separation distance at which the potential core is engulfed by the mixing process is not known in the presence of a crossflow. Consequently, the L/D range in which the aforementioned entrainment process is a major contributor to $r > 1$ cannot be definitely established. In this connection, it is interesting to note that at the smallest L/D of these tests, $L/D = 3$, the value of r at the impingement point is only slightly in excess of unity (~1.04). This suggests that at this separation distance, there is a potential core that is not much affected by the entrainment.

At locations away from the impingement region, the velocities are quite low so that $T_r \simeq T_\infty \simeq T_\infty°$. Furthermore, since $T_\infty° = T_j°$ in these experiments, it follows that $T_r - T_j = T_j° - T_j = u_j^2/2c_p$, which gives $r = 1$ in accordance with equation (4).

The significance of employing $(T_w - T_r)$ as the thermal driving force in the definition of h is illustrated by the results shown in Fig. 8. In this figure, there are two curves, one based on $(T_w - T_r)$ and the other based on $(T_w - T_\infty)$. The differences between the two curves are confined primarily to the impingement region. The curve based on $(T_w - T_\infty)$ actually displays a local minimum at the impingement point. When $(T_w - T_r)$ is used as the thermal driving force, the local minimum is eradicated and, instead, the distribution curve takes on a maximum at the impingement point. As M decreases, the difference between the results based on $(T_w - T_r)$ and $(T_w - T_\infty)$ diminishes since T_r approaches T_∞. At $M = 4$, the difference is essentially undetectable.

The importance of the recovery effects in the present experiments is due to the fact that the wall-to-fluid temperature differences were small. If the temperature differences had been larger, then the h and h' curves would have been nearly coincident.

The local heat transfer results presented in this paper were made dimensionless by employing the local coefficients h_0 for the crossflow without jet impingement. For various purposes, the actual values of h may be desired rather than the h/h_0 ratio. To facilitate the determination of the h values, a graph of h_0 versus x/D is presented in Fig. 9. It has been demonstrated by Bouchez [8] that the h_0 distribution corresponds to a turbulent boundary layer with a virtual origin situated about 35 cm upstream of the trip wire and with heating being initiated at the virtual origin.

Concluding Remarks

The deflection of the jet by the crossflow was found to be small for mass velocity ratios $M \geq 8$, and for these mass velocities the impingement point heat transfer coefficient achieves a maximum value at separation distances L/D of 5–6. Prior studies without crossflow have found a maximum at comparable L/D values. For a mass velocity ratio $M = 4$, the maximum is attained at smaller separation distances owing to the substantial deflections experienced by the jet at larger L/D. The influence of the presence or the absence of the splitter plate was confined to cases where $L/D > 4$, with the largest effects at the lowest mass velocity ratio.

Acknowledgment

This research was supported, in part, by the Power Branch of the Office of Naval Research.

References

1 Kercher, D. M., and Tabakoff, W., "Heat Transfer by a Square Array of Round Air Jets Impinging Perpendicular to a Flat Surface Including the Effect of Spent Air," *Journal of Engineering for Power,* Series A, Vol. 92, 1970, pp. 73–82.

2 Metzger, D. E., and Korstad, R. J., "Effects of Cross Flow on Impingement Heat Transfer," *Journal of Engineering for Power,* Series A, Vol. 94, 1972, pp. 35–41.

3 Bouchez, J. P., and Goldstein, R. J., "Impingement Cooling From a Circular Jet in a Cross Flow," *International Journal of Heat and Mass Transfer,* Vol. 18, 1975, pp. 719–730.

4 Gardon, R., and Cobonpue, J., "Heat Transfer Between a Flat Plate and Jets of Air Impinging on It," *Proceedings, 2nd International Heat Transfer Conference,* 1962, pp. 454–460.

5 Gardon, R., and Akfirat, J. C., "The Role of Turbulence in Determining the Heat Transfer Characteristics of Impinging Jets," *International Journal of Heat and Mass Transfer,* Vol. 8, 1965, pp. 1261–1272.

6 Gauntner, J. W., Livingood, J. N. B., and Hrycak, P., "Survey of Literature on Flow Characteristics of a Single Turbulent Jet Impinging on a Flat Plate," NASA TN D-5652, 1970.

7 Rouf, M. A., "Effect of Separation Distance on the Local Impingement Heat Transfer Coefficient in the Presence of Cross Flow," MS thesis, Department of Mechanical Engineering, University of Minnesota, Minneapolis, Minn., 1975.

8 Bouchez, J. P., "Heat Transfer to an Impinging Circular Jet in a Cross Flow," PhD thesis, Department of Mechanical Engineering, University of Minnesota, Minneapolis, Minn., 1973.

9 Colin, P. E., and Olivari, D., "The Impingement of a Circular Jet Normal to a Flat Surface With and Without Cross Flow," Von Karman Institute for Fluid Dynamics, Report No. 1, 1969.

R. E. Mayle
Pratt and Whitney Aircraft, East Hartford, Conn.

F. J. Camarata
United Technologies Research Center, East Hartford, Conn.

Multihole Cooling Film Effectiveness and Heat Transfer

Adiabatic film effectiveness and heat transfer measurements with injection of secondary air through arrays of holes in a flat plate into a turbulent boundary layer are presented. Measurements were taken both within and downstream of the multihole pattern for different hole pitch-to-diameter ratios and blowing rates. The hole configurations considered were regular patterns of staggered holes. The holes were angled 30 deg to the plate's surface and 45 deg to the mainstream. A comparison between the measured adiabatic film effectiveness and a model based on the superposition of point heat sinks is made.

Introduction

The continuing trend toward higher turbine inlet temperatures in modern gas turbine engine development has resulted in ever increasing heat loads to turbine components. Consequently, in order to maintain acceptable life requirements, greater demands are continually being made on component cooling schemes. One type of cooling scheme which has been introduced in response to these demands develops a cooling film on the surface by discharging coolant into the mainstream through an array of numerous small diameter holes in the surface. This scheme, called multihole cooling, relies on the convective cooling within the holes as well as the protective film where, in general, each contribute an equal share to the overall cooling effectiveness of the scheme. This, which is the attractive feature of multihole cooling, also presents difficulties in experimentally determining the surface heat load.

In contrast to most film cooling schemes where the heat load is found some distance downstream from the point of injection, the heat load for a multihole cooling scheme must be determined within the injection region. Most film cooling work to date has been done for injection through slots or rows of closely spaced holes, as recently summarized by Goldstein [1],[1] with much of the effort concentrating on determining the adiabatic wall temperature, commonly expressed as a film cooling effectiveness,

$$\eta = \frac{T_e - T_{aw}}{T_e - T_c}$$

at different coolant-to-mainstream mass flux ratios, $M = \rho_c U_c / \rho_\infty U_\infty$. The most relevant information for multihole cooling is that concerned with discrete hole injection [2–5], which also include a model for the film effectiveness in the neighborhood of three-dimensional injection.

The only investigations of multihole-cooling surface heat loads are those of LeBrocq, et al. [6] and Metzger, et al. [7]. LeBrocq presents a study on the influence of hole stagger, coolant-to-mainstream density ratio and blowing rate on the film effectiveness, but fails to give sufficient information to form an empirical or semiempirical correlation. On the other hand, Metzger's work, the first to include measurements of both film effectiveness and heat transfer, treats injection in a direction normal to the surface at relatively low coolant-to-mainstream mass flux ratios and provides, in this blowing regime, sufficient information to determine the surface heat loads for one in-line and one staggered multihole configuration. Consequently, at this time, only a meager amount of information is available and many areas remain to be investigated before surface heat loads for different injection geometries and blowing rates can be reasonably determined. Accordingly, the present work was undertaken to furnish information in one of these areas, namely, the influence of hole and row spacing.

In the following, film effectiveness and heat transfer measurements are presented for air discharged into a turbulent boundary layer through regular arrays of staggered holes. The holes, each 2.5 mm in diameter, are inclined 30 deg to the surface with an angle of 45 deg between the projection of the hole center line on the surface and the mainstream as measured from the downstream direction. The hole pattern, shown in Fig. 1 and described by the hole pitch-to-diameter ratio, P/D, covers approximately the same streamwise distance on the surface for each of the three P/D ratios, 8, 10, and 14.

Description of Experiment

The experiments were performed in a closed-circuit wind tunnel with the airflow supplied by a centrifugal blower. Downstream of the blower, after a honeycomb section and screens, the flow is accelerated through a nozzle into a rectangular test section where, as shown in Fig. 2, the multihole test plate forms the lower wall. A 6-mm divergence in height is provided over the length of the test

[1] Numbers in brackets designate References at end of paper.

Contributed by the Heat Transfer Division and presented at THE AMERICAN SOCIETY OF MECHANICAL ENGINEERS. Revised manuscript received by the Heat Transfer Division June 5, 1975. Paper No. 74-HT-9.

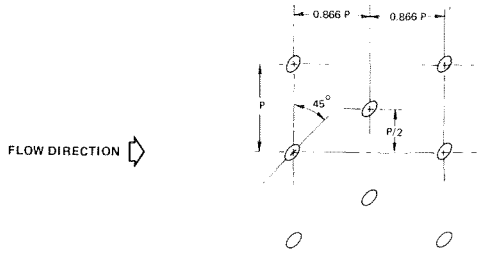

Fig. 1 Hole pattern

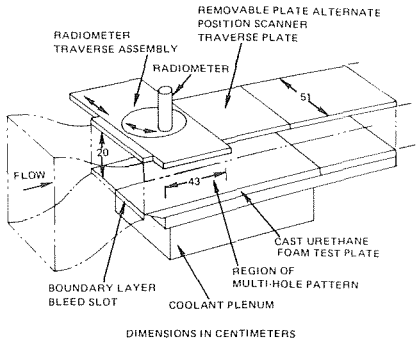

Fig. 2 Test section

section to partially compensate for boundary layer growth and the displacement effect associated with coolant injection. As a result, only a 3 percent variation in the mainstream velocity is found for the highest coolant flowrate. At the test plate leading edge, the mainstream velocity and temperature are uniform and nominally maintained at 23 m/s and 35°C, respectively. On the test plate, 5.1 cm downstream from the leading edge, a 0.75-mm trip wire is placed. This wire induces a turbulent boundary layer which at the first row of holes may be represented by a one-fifth velocity profile having a momentum thickness of 0.58 mm. Beneath the plate, a plenum fitted with inlet baffles and a porous foam pad is provided for the coolant. The coolant flow distribution within the hole pattern was checked by measuring the plenum pressure at a number of holes and found uniform. The air temperature in the plenum is maintained about 27°C below the mainstream temperature for the film effectiveness tests, while that for the heat transfer tests is maintained equal to the mainstream temperature.

For the film effectiveness tests, the upper wall of the test section is fitted with a radiometer (Barnes Engineering RM-2A) and traverse assembly as shown in Fig. 2. The radiometer is aligned to look vertically downward and measure the average plate surface temperature within a circular area 0.5 mm in diameter. The traverse assembly may be located in either of two positions which permits scanning both within and downstream of the hole pattern. In general, traverses of at least two hole pitches were made midway between each row of holes, except between the first two rows where additional traverses were made, and at intervals of between 2.5 and 5.0 cm downstream of the last row. Approximately eight readings were recorded per centimeter of spanwise travel.

Three film effectiveness test plates, one for each P/D hole geometry, were cast using urethane foam. Each plate is 2.5 cm thick and contains the hole pattern as cast. The upper surface is coated with black paint having a known emissivity except for a white line which is used to orient the radiometer traverses. A thermocouple buried in the plate surface permits checking the radiometer, while others located at coolant hole exits and on the lower surface allow an evaluation of the heat losses.

Three heat transfer test plates were also made. The bulk of the plate consists of 2.5 cm thick urethane foam identical to the film effectiveness test plates. The upper surface, however, is covered by a mosaic of film heaters, each in turn covered by a 0.75 mm thick copper plate. All bonds are formed by a high temperature rubber cement. The heaters are about 0.25 mm thick and consist of a Nichrome filament embedded between two Kapton strips. Each copper plate is drilled to conform to the hole geometry and contains a chromel-alumel thermocouple. Gaps of about 0.5 mm are left between adjacent heaters and copper plates and are filled with a low conductivity foam adhesive. Finally, the entire surface is coated with a black paint.

The streamwise length of a copper plate in the hole region is equal to the distance between rows. Each such streamwise strip is divided roughly into thirds in the spanwise direction with the heater and copper plate in the center used for obtaining data, while the flanking heaters and copper plates act as guards. The spanwise length of the center heaters is equal to an integer number of hole spacings within a row. Also, the portion of the plate upstream and downstream of the hole region is heated and, as that within the hole pattern, divided into thirds spanwise. During the test, the plate upper surface is maintained at a uniform temperature of 55°C and the power to each heater recorded. Again, as with the effectiveness plates, thermocouples are located on the lower surface to allow an evaluation of the heat losses and a trip wire is used to induce a turbulent boundary layer at the first row of holes.

Heat loss corrections were mainly calculated by considering a one-dimensional heat balance for the test plates. The result for the film effectiveness plates, which accounts for the heat loss through the plate and increase in coolant exit temperature, indicates the difference between the film effectiveness, η, and that obtained using the actual surface and plenum temperatures, η_m, is about $0.07(1 - \eta_m)$. Corrections for the heat transfer measurements include those for power dissipated by the heater leads and radiation as well as for back losses attributed to conduction through the foam and heater and thermocouple leads. Representative values of these corrections are 8, 9, and 7 percent of the measured power, respectively. In order to estimate the error involved by using the one-dimensional approach, a conduction analysis for a vertical

Nomenclature

D = hole diameter
M = coolant-to-mainstream mass flux ratio
P = hole pitch or spacing in a single row
Pe = Peclet number, $U_\infty D/\alpha_t$
Re_x = Reynolds number based on distance from effective origin of the thermal boundary layer
S = row spacing
St = Stanton number
T = absolute temperature
U = velocity
X = streamwise coordinate distance measured in number of hole diameters
Z = spanwise coordinate distance measured in number of hole diameters
α_t = turbulent thermal diffusivity
η = adiabatic film effectiveness
η_m = film effectiveness using measured surface temperature and plenum air temperature
$\bar{\eta}$ = spanwise averaged adiabatic film effectiveness
$\bar{\eta}_r$ = spanwise averaged adiabatic film effectiveness downstream of a single row of holes
ρ = density

Subscripts

∞ = mainstream state
aw = evaluated at surface of an adiabatic wall
c = coolant or injected fluid state

hole in a plate having a constant surface temperature was examined. The result indicates that the maximum heat loss with blowing is about 2.5 times the correction used for back loss through the foam alone and probably represents a maximum inaccuracy in the reported heat transfer coefficients of about 8 percent. Although this uncertainty appears somewhat high, it is, at least for the scale and hole geometry of the present experiments, one which is both difficult to reduce and accurately calculate.

Results

Two typical spanwise distributions of film effectiveness are shown in Fig. 3. The streamwise locations selected are between the first and second row of holes and about halfway through the hole pattern. Here the main feature to notice is that the spanwise variation of η remains highly nonuniform within the pattern. This situation is found even downstream of more than twenty rows of holes and points out the integrity of the individual jets.

Measurements of η, such as shown in Fig. 3, were area averaged over a multiple of the hole pitch to obtain a spanwise-averaged film effectiveness, $\bar{\eta}$. The streamwise variation of $\bar{\eta}$ for each P/D geometry at different mass flux ratios are presented in Fig. 4. In all cases, the film effectiveness rises quite rapidly near the beginning of the hole pattern and the rate of increase gradually diminishes with distance downstream. in the case of M = 0.5, the rate becomes essentially zero for all hole pitch-to-diameter ratios at a distance of about 100 dia downstream. This result indicates a balance is nearly reached between the jet-mainstream mixing, which reduces the cooling effect, and the periodic coolant injection which, of course, is intended to increase cooling. At higher mass flux ratios, the film effectiveness is seen to be still increasing at the last row of holes, however, the rate of increase is reduced from that in the first half of the pattern. Besides being a consequence of the film approaching the coolant temperature, with the result that each successive injection is less effective when based on the original coolant-mainstream temperature difference, the reduced rate of increase is also a consequence of jet coalescence. Evidence of this could be seen from the spanwise η distributions and was particularly noticeable for the P/D = 8 geometry over the last half of the pattern. This situation was also detected by flow visualization tests using powder dusted on the surface and appears to arise from a net spanwise drift of fluid near the surface caused by the spanwise component of injection. The interesting point is that the film effectiveness for the P/D = 8 and 10 geometries are nearly equal. This result is probably caused by the spanwise drift, which is particularly large for the P/D = 8 case, and subsequent coalescence of jets which, as with the in-line schemes of LeBrocq and Metzger, proves to be detrimental. Downstream of the hole pattern, the film effectiveness gradually decreases as a result of the continual mixing between the film and mainstream. In Fig. 4, this decay is only shown for the P/D = 10 and 14 geometries, since that for P/D = 8 was affected by mainstream fluid swept into the region from the tunnel sidewalls as a result of the spanwise motion near the surface.

The heat transfer results are presented in Fig. 5 in which the Stanton numbers are plotted against a length Reynolds number. The length Reynolds number is based on the distance from an effective origin of the thermal boundary layer which in turn was established by matching the Stanton numbers measured on the plates between the trip and the first row of holes with the flat plate correlation of Reynolds, et al. [8]. Measurements of Stanton number with no injection were compared to the correlation using this method and found to be in agreement within a scatter of about 12 percent except for a slight deviation in the hole region of the P/D = 8 and 10 plates. This deviation is attributed to roughness introduced by the heater plate junctions and tape patches which were used to seal the holes during the test. The effective origins used in Fig. 5 are 6.3 cm upstream of the first row of holes for the plates having P/D = 8 and 10 and 5.5 cm for the P/D = 14 plate which gives estimated enthalpy-thickness Reynolds numbers at the first row of holes of 360 and 327, respectively.

The heat transfer results indicate significant increases of the heat transfer coefficient are associated with injection. Within the hole pattern, the Stanton number increases as P/D decreases and as the mass flux ratio increases. For the larger hole density geometries and mass flux ratios the Stanton number remains essentially constant within the hole pattern and is approximately given by St = $0.038(D/P)M^{0.28}$. This indicates that the flow near the surface is streamwise periodic and dominated by the coolant jets. Thus, it appears that as the hole spacing is decreased or the coolant flow increased, a transition is gradually made in which the usual

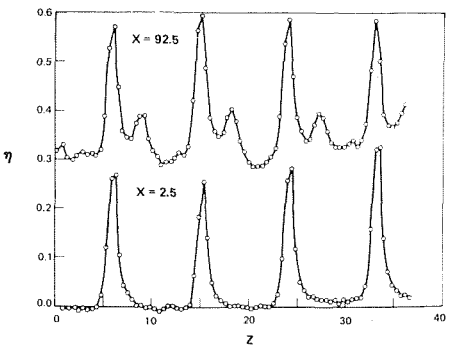

Fig. 3 Spanwise variation of film effectiveness, P/D = 10, M = 1.0

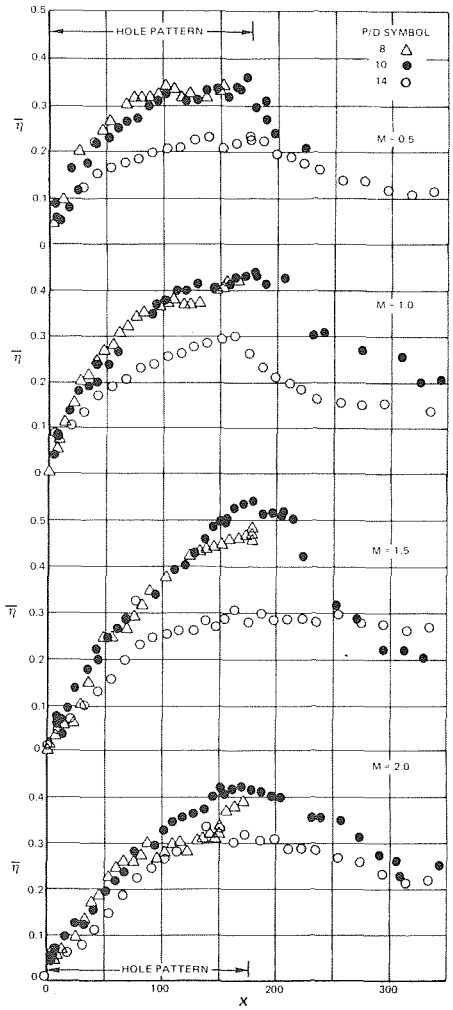

Fig. 4 Streamwise variation of average film effectiveness

streamwise growth of the thermal boundary layer yields to a periodic growth governed by the jets.

Downstream of the hole pattern, the Stanton number decreases rapidly to the flat plate correlation. Similar behavior for uniform suction and blowing heat transfer experiments have also been observed by Kays [9]. Again, as in the presentation of the film effectiveness data, and for the same reason, results for the $P/D = 8$ geometry in this region have been omitted.

Comparison with Point Sink Model

An adiabatic film effectiveness model for discrete hole injection has been presented by Ramsey, et al. [4] and a method for superposing the film effectiveness for individual jets proposed by Goldstein, et al. [2]. In the following, the suggested model will be compared to the present film effectiveness measurements.

The model is based on the solution of the energy equation for a point sink (or source) of heat moving at a constant velocity in an infinite conducting medium. As a result, the adiabatic film effectiveness is given by

$$\eta = \frac{1}{8}\frac{M\mathrm{Pe}}{\sqrt{X^2+Z^2}} \exp\left\{-\frac{1}{2}\mathrm{Pe}\left[\sqrt{X^2+Z^2}-X\right]\right\} \tag{1}$$

where the Peclet number, Pe, is defined as $U_\infty D/\alpha_t$ and must be determined experimentally.

The variation of average film effectiveness may be found by first determining the spanwise averaged film effectiveness for all jets in a single spanwise row and then superposing the result for each row. Assuming linear superposition, the averaged η downstream of an infinite row of holes, spaced a distance P apart is found to be

$$\bar{\eta}_r(X) = \frac{1}{4}\left(\frac{D}{P}\right) M\mathrm{Pe}\, e^{1/2\,\mathrm{Pe}X} K_0\left(\frac{1}{2}\mathrm{Pe}X\right) \tag{2}$$

where K_0 is the modified Bessel function of the second kind of order zero. This result is, of course, identical to that obtained for an infinite line sink moving in an infinite medium and having the same strength per unit length as that for the row of point sinks in equation (1). For typical values of Pe, PeX is generally greater than 10, so equation (2) is well represented by

$$\bar{\eta}_r = \frac{\sqrt{\pi}}{4}\left(\frac{D}{P}\right) M\sqrt{\frac{\mathrm{Pe}}{X}} \tag{3}$$

The streamwise variation of the film effectiveness, $\bar{\eta}$, now may be found by superposing the effectiveness of the individual rows in the multihole pattern. Linear superposing of the average effectiveness was tried at first without success. The streamwise variation was then found using the "additive film" method of superposition first proposed by Sellers [10]. Using Sellers' argument, namely that the gas temperature used to determine the film effectiveness downstream of an injection location should be the adiabatic film temperature due to all injections upstream of that location, it is not difficult to show that the effectiveness at the streamwise location X is given by

$$\bar{\eta} = 1 - \exp\left\{\sum_{k=1}^{n} \ln\left(1 - \bar{\eta}_r\left[X - (k-1)\frac{S}{D}\right]\right)\right\}$$

where n is the number of rows upstream of the position X and S, the row spacing. However, for hole pitch-to-diameter ratios of the order of ten, $\bar{\eta}_r$ is usually less than 0.1, so to a good approximation

$$\bar{\eta} = 1 - \exp\left\{-\sum_{k=1}^{n} \bar{\eta}_r\left[X - (k-1)\frac{S}{D}\right]\right\}$$

Substituting equation (3) into the foregoing, one obtains for uniform blowing

$$\bar{\eta} = 1 - \exp\left\{-\frac{\sqrt{\pi}}{4}\left(\frac{D}{P}\right) M\sqrt{\mathrm{Pe}}\sum_{k=0}^{n-1}\left(X - k\frac{S}{D}\right)^{-1/2}\right\} \tag{4}$$

This expression was evaluated midway between each row of holes and compared to measurements for each mass flux and P/D ratio.

Typical results of the comparison within the hole pattern are shown in Fig. 6 for the geometry of $P/D = 10$. The values of the Peclet numbers used in the comparison are 55, 22, 12 for mass flux ratios of 0.5, 1.0, and 1.5, respectively. Note that equation (4) displays a proper streamwise behavior only for the case having a mass flux ratio of 1.0 and is less satisfactory for the other blowing rates. Since similar discrepancies are also found for the other cases and the Peclet numbers which give best agreement are different than those quoted above, it is apparent that further analytical work in this area is necessary.

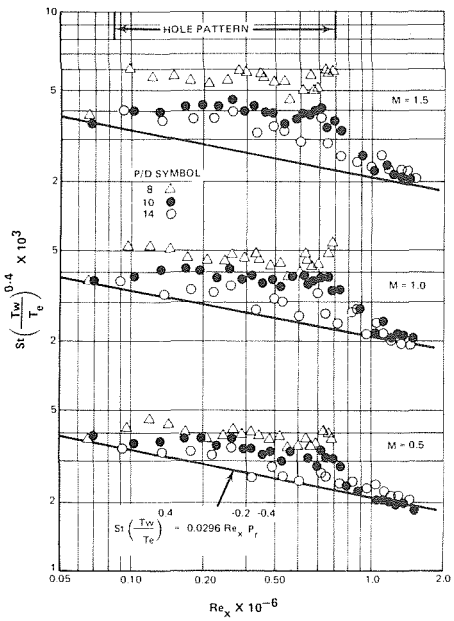

Fig. 5 Streamwise variation of Stanton number

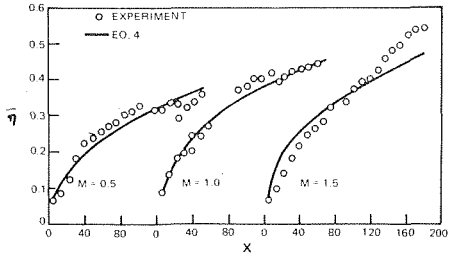

Fig. 6 Comparison of measured and calculated film effectiveness

Conclusions

Within a pattern of holes discharging coolant into a turbulent boundary layer, the film effectiveness was found to be highly nonuniform and reflected the integrity of individual jets. This integrity and the possibility of jet coalescence or interaction, which may adversely affect the development of an effective cooling film, will have to be considered in any film effectiveness analysis of a multihole cooling scheme. In this respect, the model using a superposition of point sinks does not appear too promising.

The heat transfer coefficient within the hole pattern was found to increase significantly as either the mass flux ratio or hole density was increased. Since increases as high as 2.5 were found in the average heat transfer coefficient, it is apparent that greater increases in local values are to be found. Consequently, the variation of the local heat transfer coefficient within the hole pattern must be considered together with the film effectiveness distribution before the multihole-cooling surface heat load may be determined.

Acknowledgment

This work was conducted under Contract F33615-72-C-1902 granted by the Air Force Aero Propulsion Laboratory and is reported in AFAPL-TR-73-30.

References

1 Goldstein, R. J., "Film Cooling," *Advances in Heat Transfer,* Academic Press, Vol. 7, 1971, pp. 321–379.

2 Goldstein, R. J., Eckert, E. R. G., Eriksen, V. L., and Ramsey, J. W., "Film Cooling Following Injection Through Inclined Circular Tubes," NASA CR-72612, Nov. 1969.

3 Ramsey, J. W., and Goldstein, R. J., "Interaction of a Heated Jet With a Deflecting Stream," NASA CR-72613, Apr. 1970.

4 Ramsey, J. W., Goldstein, R. J., and Eckert, E. R. G., "A Model for Analysis of the Temperature Distribution With Injection of a Heated Jet Into an Isothermal Flow," *Heat Transfer 1970,* Elseuiar, Amsterdam, 1970.

5 Eriksen, V. L., "Film Cooling Effectiveness and Heat Transfer With Injection Through Holes," NASA CR-72991, Aug. 1971.

6 LeBrocq, P. V., Launder, B. E., and Priddin, C. H., "Discrete Hole Injection as a Means of Transpiration Cooling—An Experimental Study," Imperial College of Science and Technology, Report EHT/TN/A/26, June 1971.

7 Metzger, D. E., Takeuch, D. I., and Kuenstler, P. A., "Effectiveness and Heat Transfer With Full-Coverage Film Cooling," *Journal of Engineering for Power,* TRANS. ASME, Series A, Vol. 95, Apr. 1973.

8 Reynolds, W. C., Kays, W. M., and Kline, S. J., "Heat Transfer in a Turbulent Incompressible Boundary Layer, I-Constant Wall Temperature," NASA Memo 12-1-58W, 1975.

9 Kays, W. M., "Heat Transfer to the Transpired Turbulent Boundary Layer," NASA Report NGL05-020-134, 1971, (Thermal Division Department of Mechanical Engineering Stanford University Report HMT-14, June 1971).

10 Sellers, J. P., "Gaseous Film Cooling With Multiple Injection Stations," *AIAA Journal,* Vol. 1, Sept. 1963, pp. 2154–2156.

M. F. Blair

Research Engineer,
United Technologies Research Center,
East Hartford, Conn.
Mem. ASME

R. D. Lander

Assistant Project Engineer,
Pratt & Whitney Aircraft Division,
East Hartford, Conn.

New Techniques for Measuring Film Cooling Effectiveness

Techniques to measure local film effectiveness distributions on large-scale models of turbine blade and vane sections were developed for use in subsonic, room-temperature wind-tunnel environments. Highly detailed film cooling effectiveness distributions were obtained on near-adiabatic, cast rigid foam test models using infrared radiometer scanning techniques. Sample results from both flat-plate film cooling studies and airfoil leading-edge film cooling studies are presented.

Introduction

Turbine airfoil metal temperatures in many current high temperature gas turbines are maintained at acceptable levels by means of film cooling. In order to predict the exterior wall temperature and convective heat flux distribution on turbine components cooled in this manner, both surface adiabatic wall effectiveness distributions and surface heat transfer coefficient distributions are required. The present paper deals with low temperature IR techniques developed to obtain detailed effectiveness distributions near coolant injection sites where nonuniform cooling is commonly observed. The techniques described in this paper can be employed for model surface temperatures as low as 0°C while IR sensitive film, which has been used by other workers for measuring temperature distributions in hot rig tests, requires a source temperature of approximately 480°C for practical exposure times. Thus, the techniques presented herein are practical for basic engineering research studies carried out in test facilities which operate at near room temperature.

Test Models

Near-adiabatic models, for the measurement of film effectiveness distributions, were fabricated by casting the desired configurations from rigid urethane foam (Witco Chemical—ISOFOAM®) in accordance with the manufacturer's instructions. Urethane foam was employed because the thermal conductivity of the resulting bodies is very low ($8–12 \times 10^{-5}$ gm-cal/cm-s K) and because it can be cast in the shapes required for injection configurations. Excellent aerodynamic bodies can be fabricated with this rigid foam because the castings are dimensionally stable and a thin skin results naturally on the surface of the foam. The casting skin is as smooth as the mold surface in which the model was made. The foam models can be subjected to steady temperatures of 60°C without distortion. The low thermal conductivity of the foam models resulted in reduced conduction errors from the test surface to the coolant plenum on the model's back surface. The backloss errors for the present tests were significantly reduced compared to those which occurred for previous tests using Micarta or fiberglass models. An analysis presented in the Appendix delineates the in-place backloss calibration procedure.

Traversing-Spot-Radiometer Technique

A spot radiometer was used to measure surface temperatures for a film cooling investigation on a flat plate model with an array of coolant injection holes. The tests were conducted in a low-speed, continuous recirculating flow wind tunnel in which the flow passes through a rectangular test section, 20.3 cm high by 50.8 cm wide. A detailed description of the tunnel in the region of the test plate is shown in Fig. 1. The test plate was 122 cm long and formed the lower wall of the test section with the leading edge of the plate at the duct entrance. A coolant plenum designed to produce uniform flow from the coolant holes was mounted beneath the test plate. Spanwise variations of the coolant flow from hole to hole were imperceptible within the central region of the plate where effectiveness measurements were obtained. The upstream boundary layer was removed through a 0.6 cm wide slot, inclined at 30 deg to the test surface, between the test plate sharp leading edge and the lower wall of the nozzle. Velocity surveys at various distances above the test plate indicated only slight nonuniformities in the duct flow outside the wall boundary layers. A temperature difference between main and coolant flows of approximately 28°C was obtained by refrigerating the coolant approximately 22°C below room temperature and by operating the tunnel at approximately 6°C above room temperature. Film effectiveness data were obtained

Contributed by the Heat Transfer Divsion and presented at the — THE AMERICAN SOCIETY OF MECHANICAL ENGINEERS. Revised manuscript received by the Heat Transfer Division April 7, 1975. Paper No. 74-HT-8.

for a freestream velocity of 22.8 m/s and over a coolant Reynolds number range (based on the coolant hole diameter of 1.27 cm) from 2×10^3 through 25×10^3, a span which encompasses typical current engine conditions. The upper surface of the test section was formed in part by a traversing mechanism which supports the radiometer (Barnes Engineering Model RM-2A). This radiometer measured the test plate surface temperature within a 0.05 cm dia spot. The combination of translational and rotational motions of the traverse and the removable alternate plate shown in Fig. 1, permitted the radiometer to scan a region approximately 102 cm long in the streamwise direction. The upper surface of the plate was coated with a high emissivity flat-black paint (3M C-101 Black Velvet®) except for a white reference line which was used to orient the radiometer traverses. The paint emissivity was checked against a laboratory black body standard and was found to be independent of the number of coats applied. The measured emissivity of the paint ranged from $\epsilon = 0.956$–0.979. The radiometer was calibrated in place periodically during each test to obtain approximately ±1.0°C accuracy. The data from the radiometer and a location indicating potentiometer were fed to an analog-to-digital converter and punched on paper tape for processing on a digital computer. The surface temperature, coolant temperature, and external flow temperature data were processed to obtain the film effectiveness at each surface temperature measurement location. The results from each spanwise traverse were linearly interpolated to construct a rectilinear array with 1600 points of effectiveness. This array in turn was used to construct an isoeffectiveness contour map on a memory oscilloscope.

For the Flat Plate Models, the uncertainties in the measured free stream temperatures were approximately ±0.25°C while the uncertainties in the measured coolant plenum temperatures were approximately ±1.0°C. As previously discussed, the uncertainties in the temperatures indicated by the spot radiometer were approximately ±1.0°C. Using the procedure described in reference [4],[1] with the foregoing uncertainties in the measured temperatures, the effectiveness data obtained for the Flat Plate Models were estimated to be accurate within ±0.05.

A sample "map" of effectiveness contours is presented in Fig. 2. For the model sketched in Fig. 2, the coolant hole diameter was 1.27 cm, the lateral hole spacing/hole diameter was 2.0, and the holes were inclined at 30 deg to the surface. These results are presented in terms of the standard film cooling parameter, $\eta_{\text{film}} = (T_e - T_{aw})/(T_e - T_c)$. Although coolant injection was present across the entire 50.8 cm width of the test surface, the isoeffectiveness contours were only constructed for a representative 10 cm wide streamwise strip near the tunnel center line within which effects of the tunnel sidewalls were considered negligible.

The principal feature of Fig. 2 is the extreme spanwise variation of the measured effectiveness indicating that very little lateral spreading of the coolant fluid occurred. This result, little lateral spreading of the cooling effect, is in qualitative agreement with the data of references [1, 2] which were obtained downstream of a single slanted hole on a flat plate. A quantitative comparison of the present results with those from the single hole of references [1, 2] is difficult because the lateral separation of the holes for the present study was so small the hole cooling patterns overlap and influence each other. The coolant hole pattern of the model of Fig. 2, with staggered rows of two-dimensionally spaced holes, is near the minimum practical spacing for a drilled hole film cooling scheme. The lateral variations of effectiveness for Fig. 2 indicate that even for this spacing the cooling pattern was not a uniform two-dimensional film. Additional effectiveness results obtained for these flat plate models at various coolant injection rates and with various coolant hole patterns can be found in reference [3].

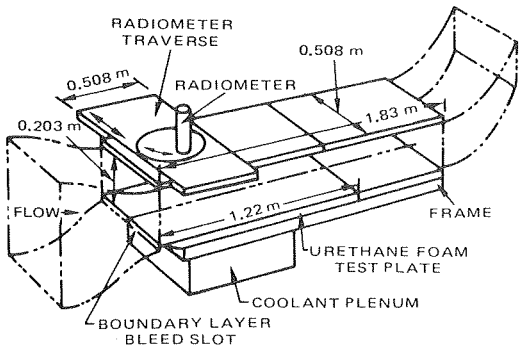

Fig. 1 Sketch of test plate installation for effectiveness measurements

Scanning Radiometer Technique

A second measurement technique was developed to obtain detailed film effectiveness data on large-scale models of turbine airfoil leading-edge regions using a scanning infrared camera. Data for this investigation were obtained in an open circuit, low-speed wind tunnel which draws from the room air into a low turbulence convergence section, through a 30 × 50 cm test section and returns the air to the room. The test section velocity can be varied from 0 to 36 m/s and the test section turbulence intensity increased from a minimum value of 0.5–11.0 percent by installing various turbulence generating grids. A sketch of the tunnel in the region of the test model is presented in Fig. 3. Effectiveness distributions were again obtained on a nearly-adiabatic model fabricated of cast rigid urethane foam. The rear portion of the test model was designed to eliminate unsteady flow in the leading edge region resulting from a rear body wake and to prevent separation within the test region which extends from the stagnation line to the point of maximum thickness on the body. For these tests, the film cooling was simulated by air which was heated to a temperature approximately 28°C hotter than the mainstream air.

[1] Numbers in brackets designate References at end of paper.

Nomenclature

C_p = specific heat at constant pressure, gm-cal/gm K
h = convective heat transfer coefficient, W/cm²-K
h_i, h_e = interior and exterior wall convective heat transfer coefficent, respectively, W/cm²-K
k = thermal conductivity, gm-cal/cm-s K
q_i, q_e = interior and exterior heat flux, W/cm²
Re = Reynolds number, $U_e x/\nu$, dimensionless
St = Stanton number, $h/(\rho_e U_e C_p)$, dimensionless
t = wall thickness, cm
T = temperature, K
T_{c_p}, T_{c_e} = temperature of coolant at plenum and hole exit, respectively, K
T_{w_i} T_{w_e} = temperature of wall on inside and outside surface, respectively, K
x = distance from leading edge, cm
η_{film} = effectiveness parameter, $(T_e - T_{aw})/(T_e - T_c)$, dimensionless
η_0 = experimentally measured effectiveness (equation (A-6)), dimensionless
η_{NF} = no-flow effectiveness parameter, (equation (A-4)), dimensionless
ν = kinematic viscosity, cm²/s
ρ = density, gm/cm³

Subscripts

aw = adiabatic wall
c = coolant
e = free-stream value

The surface temperature of the curved surface models was determined using a Bofors IR scanning camera. This camera had a depth of field of approximately 5 cm when focused on the test section 35 cm from the camera. The IR camera viewed the test surface through a sheet of Vinylidene Chloride-Vinyl Chloride co-polymer (Saran Wrap food wrap) which served as an infrared window in the tunnel sidewall. The camera was calibrated with the Saran Wrap in place to account for any "tailoring" of the detector sensitivity resulting from slight infrared absorption. The test surface of the model was coated with the same high emissivity flat-black paint as previously described except for a 0.6 cm wide strip of aluminized mylar tape which was used to orient the infrared camera displays. The thermocouple measurements provided accurate temperature measurements at sixteen locations and the IR scanning camera provided isotherm contours at selected temperature levels which would have been possible only with a multitude of thermocouples.

For each coolant flow rate approximately eight separate isothermal levels were "mapped." Three sample isotherm displays are presented in Fig. 4. For these test conditions, the uncertainties in the surface temperature measurements were approximately ±1.0°C. The individual isothermal contours were assembled into a composite temperature distribution from which isoeffectiveness contour plots were constructed. A sample plot of local effectiveness contours is presented in Fig. 5. For this leading edge model the rows of hole were located at 17 and 47 deg from the nose stagnation line and the holes were inclined at 30 deg to the surface. The model leading edge radius was 3.2 cm and the diameter of the coolant holes was 0.674 cm. The data are presented in a plane view of the curved leading edge model with the coolant holes shown cross hatched. For the Leading Edge Film Cooling Models, the uncertainties in the measured free stream temperatures were approximately ±0.25°C while the uncertainties in the measured coolant plenum temperatures were approximately ±1.0°C. As previously discussed, the uncertainties in the temperatures indicated by the Bofors Scanning camera were approximately ±1.0°C. Using the procedure described in reference [4], with the foregoing uncertainties in the measured temperatures, the effectiveness data obtained

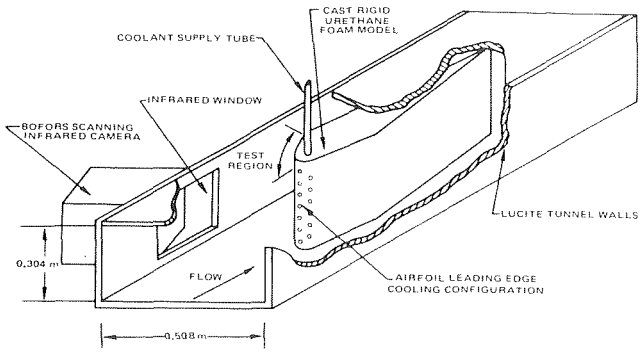

Fig. 3 Sketch of leading edge model installation

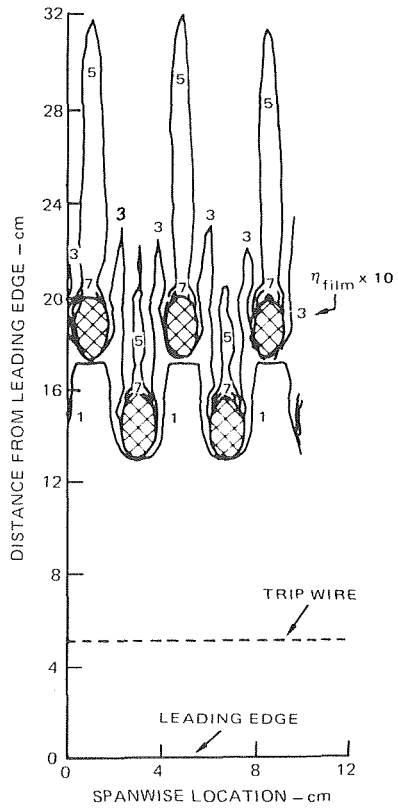

Fig. 2 Isoeffectiveness distribution for flat plate film cooling

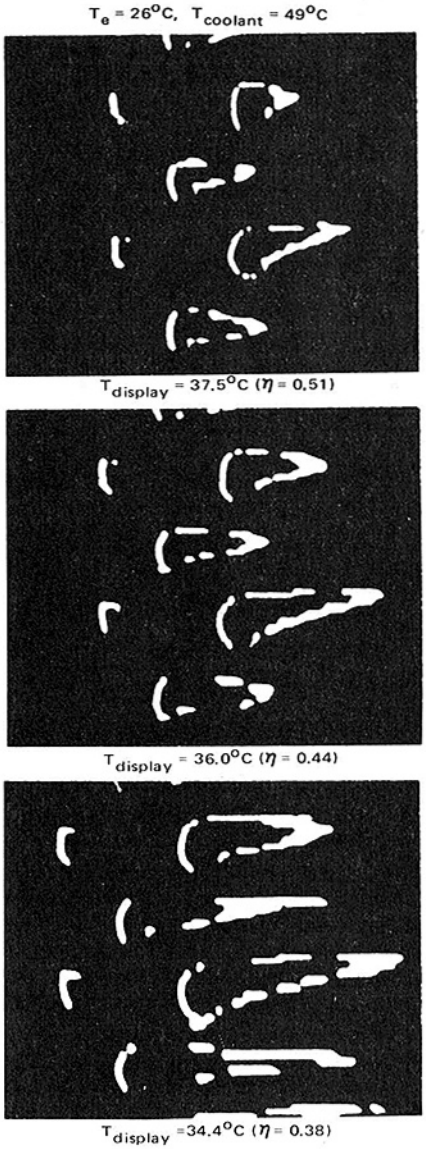

Fig. 4 Typical Bofors infrared camera displays for airfoil leading edge cooling configuration tests

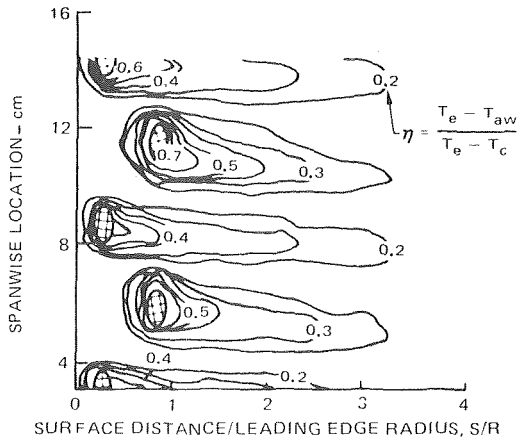

Fig. 5 Isoeffectiveness distribution for airfoil leading edge cooling configuration

for the Leading Edge Models were estimated to be accurate within ±0.05.

The principal features of these results are the large streamwise and spanwise variation in film cooling effectiveness. Despite the dissimilarities between the two flow situations the present results, for a leading edge injection scheme, are qualitatively similar to the results presented in reference [2] for a laterally slanted single hole in a flat plate. The contours of constant effectiveness presented for the single hole inclined at 35 deg to the flat plate surface and 90 deg to the flow direction are similar in shape to the present results.

Concluding Remarks

The successful employment of cast urethane foam fabrication techniques and infrared scanning has demonstrated the potential of these techniques for the acquisition of highly detailed film effectiveness data in low temperature facilities.

Acknowledgment

The authors are grateful to Messrs. F. J. Camarata and B. V. Johnson of the United Technologies Research Center and Dr. R. E. Mayle of Pratt & Whitney for their suggestions during the development of these techniques.

References

1 Goldstein, R. J., Eckert, E. R. G., and Ramsey, J. W., "Film Cooling With Injection Through a Circular Hole," NASA CR-54604, May 1968.

2 Goldstein, R. J., Eckert, E. R. G., Eriksen, V. L., and Ramsey, J. W., "Film Cooling Following Injection Through Circular Tubes," NASA CR-72612, Nov. 1969.

3 Muska, J. F., Fish, R. W., and Suo, M., "The Additive Nature of Film Cooling From Rows of Holes," ASME Paper No. 75-WA/GT-17.

4 Kline, S. J., and McClintock, F. A., "Describing Uncertainties in Single Sample Experiments," *Mechanical Engineering*, Vol. 75, No. 1, 1953, pp. 3–8.

APPENDIX

Film Cooling Effectiveness Conduction Corrections

The following analysis leads to an equation for determining the adiabatic wall film effectiveness from data obtained with the low-thermal-conductivity test plates. A direct measurement of the adiabatic wall recovery temperature cannot be achieved with finite conductivity material. However, the use of low-thermal-conductivity material, such as the urethane foam, minimizes the heat conduction and small heat flux corrections for backlosses can be incorporated into the data reduction procedure.

For an adiabatic wall the standard film cooling effectiveness parameter is defined

$$\eta_{\text{film}} = \eta_f = \frac{T_e - T_{aw}}{T_e - T_{c_e}} \tag{A-1}$$

where T_e = free-stream adiabatic wall recovery temperature, T_{aw} = adiabatic wall temperature in the presence of film cooling, and T_{c_e} = coolant temperature at the exit from the coolant hole. A simple one-dimensional backloss correction will be formulated in the following paragraphs. Calculations indicate that the local conduction effects resulting from the flow through the coolant holes are concentrated within approximately one coolant hole diameter of an injection site and the results developed here should be applicable to all other regions of the test surface. This correction was applied to the data presented for the flat plate model only.

For the film cooled plate with finite conductivity, shown in the following,

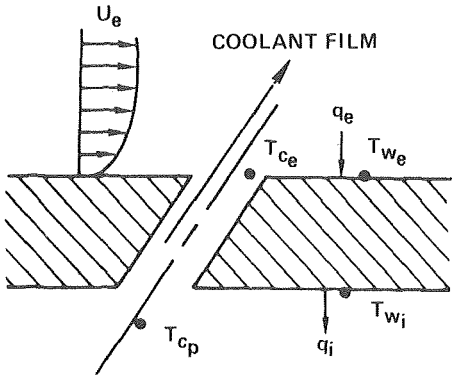

a one-dimensional heat flux analysis of the plate yields

$$q_e = h_e\,(T_{aw} - T_{w_e}) = q_{\text{cond}} = \frac{k}{t}\,(T_{w_e} - T_{w_i}) = q_i = h_i\,(T_{w_i} - T_{c_p}) \tag{A-2}$$

where q is the local heat flux, h is the local external or internal heat transfer coefficient, k is the material thermal conductivity, and T is the local temperature. The equations of (A-2) can be combined to obtain

$$\eta_f = \frac{T_e - T_{aw}}{T_e - T_{c_e}} = \frac{T_e - T_{w_e}}{T_e - T_{c_e}} - \frac{T_{w_e} - T_{c_p}}{T_e - T_{c_e}}\left(\frac{1/h_e}{1/h_i + t/k}\right) \tag{A-3}$$

Although the temperatures are measured, the overall heat transfer parameter, $(1/h_e)/(1/h_i + t/k)$, is unknown and must be determined before the adiabatic film effectiveness, η_f, can be evaluated.

Although the thermal conductivity of the material can be measured, measurement of the internal heat transfer coefficient would be difficult. Consequently, the heat transfer parameter was obtained with an in-place calibration by passing flow through the coolant plenum behind the flat plate configuration with the coolant holes plugged and measuring the test plate, coolant, and external flow temperatures. These were combined to obtain a no-flow effectiveness parameter

$$\eta_{\text{no flow}} = \eta_{NF} \equiv \frac{T_e - T_{w_{eNF}}}{T_e - T_{c_p}} \tag{A-4}$$

where $T_{w_{eNF}}$ = exterior wall temperature with no flow passing through the coolant holes. The value of η_{NF} was experimentally determined to vary from 0.04 to 0.06 depending on the plenum flow rate—a constant value of 0.05 was used as a reasonable approximation for all coolant flow rates.

Using the one-dimensional heat flux balance shown previously, the following equation was obtained to relate the measured temperature to the no-flow effectiveness parameter and heat transfer coefficient parameter of equation (A-3)

$$\frac{T_e - T_{w_{eNF}}}{T_{w_{eNF}} - T_{c_p}} = \frac{1/h_e}{1/h_i + t/k} = \frac{\eta_{NF}}{1 - \eta_{NF}} \tag{A-5}$$

If we assume that $h_{eNF} = h_e$ and $h_{iNF} = h_i$, the adiabatic film effectiveness is obtained in the following form:

$$\eta_f = \frac{T_e - T_{c_p}}{T_e - T_{c_e}}\left[(\eta_0) - \left(\frac{\eta_{NF}}{1-\eta_{NF}}\right)(1-\eta_0)\right] \quad \text{(A-6)}$$

where $\eta_0 = (T_e - T_{w_e})/(T_e - T_{c_p})$ is the experimentally measured effectiveness and the temperature ratio, $(T_e - T_{c_p})/(T_e - T_{c_e})$, is a measure of the heat absorbed by the coolant air in the injection hole. A measurement of the coolant temperature at the exit of the coolant holes indicated that the temperature rise along the hole was negligible and $(T_e - T_{c_p})/(T_e - T_{c_e}) = 1$. Thus, the adiabatic wall film effectiveness is related to the experimentally measured effectiveness with the following relationship:

$$\eta_f = \eta_0 - \left(\frac{\eta_{NF}}{1-\eta_{NF}}\right)(1-\eta_0) \quad \text{(A-7)}$$

A. J. Suo-Anttila
Graduate Research Asst.

I. Catton
Assoc. Professor.
Assoc. Mem. ASME

School of Engineering and Applied Science,
University of California, Los Angeles, Calif.

The Effect of a Stabilizing Temperature Gradient on Heat Transfer From a Molten Fuel Layer With Volumetric Heating

The Landau method is used to determine the heat transfer to the upper and lower surfaces of a volumetrically heated layer of molten fuel for various fixed values of the upper and lower surface temperatures. To use the Landau method, the Stuart shape assumption is imposed and solutions to the linearized stability problem are used. The results are generalized in terms of two Nusselt numbers (upper and lower surface heat transfer) which are presented as a function of the Rayleigh number based on the internal heat generation rate for various values of an external Rayleigh number based on the surface to surface temperature difference. Results are also presented for a molten UO_2 layer for various typical values of decay heat. Comparison is made with experiment, where possible, and found to be good.

Introduction

In nuclear reactor design and safety, postulated reactor core meltdowns have led to the consideration of heat transfer from molten fuel layers with internal heat generation. In one failure mode, the containment of the molten layer will depend upon the downward heat flux. Earlier work [1][1] in this area has been restricted to a molten layer which is confined above and below by a crust of solid fuel. However, the crust of solid fuel may not form if a large upward thermal resistance exists above the molten layer. In this situation, the molten fuel layer is confined below by solid fuel and above by some other material whose temperature is greater than the melting point of the fuel. The situation described is stabilizing and decreases the amount of convection in the layer. An example of this could be a molten layer of UO_2 covered by a molten layer of iron. The downward heat flux can be considerably enhanced when the fluid layer is stabilized. In this report an estimate is made of the heat flux when a molten layer of fluid with internal heat generation is bounded by rigid surfaces with the upper surface temperature such that a stabilizing temperature gradient is imposed.

Earlier work in this area has been restricted to equal upper and lower surface temperatures. Kulacki and Goldstein [2] made experimental measurements of the downward heat flux and maximum temperature in the layer. Jahn and Reineke [4] made similar measurements and numerical calculations as well. They report slightly different results from those of Kulacki and Goldstein. Catton and Suo-Anttila [3] made numerical computations of the heat transfer under these same circumstances using the Landau method and reported good agreement with the experimental results of Kulacki and Goldstein.

Many investigators have calculated the heat transfer-Rayleigh number relationship for the Bénard problem. Malkus and Veronis [5] used the Landau power-integral method (see Landau and Lifschitz [6]) to study the case without internal heat generation. The Landau method has also been used by Edwards and Catton [7] to predict heat transfer in confined regions, by Catton [8] to predict heat transfer across an infinite horizontal layer under the influence of rotation, by Catton and Ayyaswamy [9] for momentum transfer between concentric cylinders with the inner cylinder rotating, and by Sharman, Catton, and Ayyaswamy [10] for heat transfer across the gap between concentric cylinders with the inner cylinder rotating. In all cases, excellent agreement between theory and experiment was obtained up to 10,000 times the critical value of the parameter governing the onset of motion. For example, good results were obtained for the Bénard problem up to Rayleigh numbers of 10^7. In this work the Landau Power Integral method is used to study the case of internal heat generation with an imposed external stabilizing temperature gradient. The heat transfer-Rayleigh

[1] Numbers in brackets designate References at end of paper.

Contributed by Heat Transfer Division and presented at the Winter Annual Meeting, New York, N.Y., November 17–22, 1974, of THE AMERICAN SOCIETY OF MECHANICAL ENGINEERS. Revised manuscript received by the Heat Transfer Division January 27, 1975. Paper No. 74-WA/HT-45.

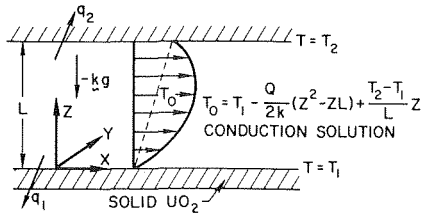

Fig. 1 Configuration and coordinate system used in application of the power integral method

number relationship obtained is compared with Kulacki and Goldstein's [2] experiments.

Governing Equations

Initially a quasi-incompressible (Boussinesq) fluid element with internal heat generation (see Fig. 1) is heated from above to establish a temperature gradient parallel to the gravitational body force (along the z axis). The initial velocity and temperature distributions are given by

$$\mathrm{u}_0 = 0$$

$$\frac{dT_0}{dz} = -\frac{Q}{k_f}\left(z - \frac{L}{2}\right) + \frac{T_2 - T_1}{L} \tag{1}$$

where Q is the internal heat generation rate per unit volume and k_f is the fluid thermal conductivity. The fluid is confined between rigid, fixed-temperature walls. The corresponding boundary conditions are

$$\mathrm{u} = 0, \; T = \text{constant} \tag{2}$$

on both surfaces.

The instability is assumed to appear via a marginal stationary state; hence the governing dimensionless disturbance equations are

$$\nabla \cdot \mathrm{u} = 0 \tag{3}$$

$$\mathrm{Pr}^{-1}(\nabla \times \mathrm{u}) \times \mathrm{u} = -\nabla\left(p \times \frac{\mathrm{u}^2}{2}\right) + \theta \mathrm{k} - \nabla \times (\nabla \times \mathrm{u}) \tag{4}$$

$$\mathrm{u} \cdot \nabla\theta + \mathrm{u} \cdot \mathrm{k}(-\mathrm{R}_I(z - \tfrac{1}{2}) + \mathrm{R}_E) = \nabla^2\theta \tag{5}$$

where $\mathbf{u}$, θ, and p are the velocity, temperature, and pressure measured in units of κ/L, $\nu\kappa/\alpha g L^3$, and $\rho\nu\kappa/L^2$, respectively. All dimensions are scaled by the layer thickness L. The Prandtl number, $\mathrm{Pr} = \nu/\kappa$ appears as a multiplicative factor in the inertial terms and the parameters R_I and R_E are given by

$$\mathrm{R}_I = \frac{\alpha g Q L^5}{\nu\kappa k_f} \quad \text{internal modified Rayleigh number} \tag{6}$$

$$\mathrm{R}_E = \frac{\alpha g L^3 (T_2 - T_1)}{\nu\kappa} \quad \text{external Rayleigh number} \tag{7}$$

where g is the gravitational body force, α is the fluid coefficient of thermal expansion, and ν is the fluid thermal diffusivity.

Equations (3), (4), and (5) together with the boundary conditions given by equation (2) are sufficient to solve the stability problem. The onset of motion, the lowest mode, has been obtained by Kulacki and Goldstein [2]. In this work the higher modes are needed, thus requiring resolving the problem. The equations are linearized by neglecting the inertial terms in the momentum equation and the second order convective terms in the energy equation. An approximate solution (variational approach) to a similar problem has been obtained by Chandrasekhar [11]. His approach yields a relationship between the characteristic Rayleigh number and the wavelength of the disturbance. These results will be combined with the Landau method to yield the heat transfer.

The Onset of Motion

The stability problem reduces to solving the following set of equations (see Chandrasekhar [11, p. 90]),

$$(D^2 - a^2)\theta = -\mathrm{R}_I W(z - \tfrac{1}{2}) + \mathrm{R}_E W \tag{8}$$

$$(D^2 - a^2)^2 W = a^2\theta \tag{9}$$

where θ and W, the temperature and vertical velocity component, have been analyzed into normal modes to remove the x and y dependence, a is the wave number and

$$D = \frac{d}{dz} \tag{10}$$

The associated boundary conditions are

$$W = DW = \theta = 0 \tag{11}$$

on the bounding horizontal surfaces.

Briefly, the stability problem is solved by letting

$$F = (D^2 - a^2)^2 W = a^2\theta \tag{12}$$

and rewriting the differential equations in the forms

$$(D^2 - a^2)^2 W = F \tag{13}$$

$$(D^2 - a^2)F = -\mathrm{R}_I a^2 W(z - \tfrac{1}{2}) + \mathrm{R}_E W a^2 \tag{14}$$

with boundary conditions on F being the same as θ at the rigid horizontal surfaces.

Since F will be even or odd, it is expanded in a sine series of the form

$$F = \sum_m F_m = \sum_m A_m \sin(m\pi z) \tag{15}$$

The corresponding W_m are solutions to equation (13) with the boundary conditions given by equation (11). Solutions to equation (13) are

Nomenclature

a = wave number
D = derivative with respect to z
g = gravitational acceleration
k = thermal conductivity
k = vertical unit vector
L = depth of fluid layer
Nu = Nusselt number = heat flux at boundary/conductive heat flux at boundary
Pr = Prandtl number = ν/κ
q = surface heat flux
Q = volumetric heat generation rate
R_E = external Rayleigh number, $\alpha g L^3(T_2 - T_1)/(\nu\kappa)$
R_I = modified internal Rayleigh number, $\alpha g Q L^5/(\nu\kappa k)$
T = temperature
u = velocity
v = velocity
w = vertical component of velocity
W = dimensionless vertical component of velocity which has been analyzed into normal modes
z = vertical coordinate
α = isobaric coefficient of thermal expansion
θ = dimensionless temperature
κ = thermal diffusivity $k/(\rho c)$
ν = kinematic viscosity
ρ = density

Subscripts

1 = downward or bottom of layer
2 = upward or top of layer
0 = initial
f = fluid
m = mode or term in series expansion
n = term in series expansion
z = vertical component

$$W = \sum \frac{A_m}{(m^2\pi^2 + a^2)^2}\{B_1^{(m)} \sinh az + A_2^{(m)} z \cosh az + B_2^{(m)} z \sinh az + \sin m\pi z\} \quad (16)$$

where

$$B_1^{(m)} = m\pi(a + (-1)^m)/\Delta$$

$$A_2^{(m)} = -m\pi(\sinh^2 a + (-1)^m a \sinh a)/\Delta$$

$$B_2^{(m)} = m\pi\{(\sinh a \cosh a - a) + (-1)^m(a \cosh a - \sinh a)\}/\Delta$$

$$\Delta = \sinh^2 a - a^2 \quad (17)$$

Substituting for F and W in equation (14), multiplying by $\sin(n\pi z)$ and integrating from $z = 0$ to one yields

$$\sum A_m\{\frac{(m^2\pi^2 + a^2)}{2a^2}\delta_{nm} - R_i\int_0^1 W_m(z - \frac{1}{2})\sin(n\pi z)dz + R_e\int_0^1 W_m \sin(n\pi z)dz\} = 0 \quad (18)$$

which is a set of linear homogeneous equations for the coefficients A_m. The determinant of equation (18) must vanish if the A_m are to be nontrivial. Thus

$$\left|\left|\frac{(m^2\pi^2 + a^2)^3}{2a^2}\delta_{nm} - R_I\int_0^1 W_m(z - \frac{1}{2})\sin(n\pi z)dz + R_E\int_0^1 W_m \sin(n\pi z)dz\right|\right| = 0 \quad (19)$$

is a characteristic equation for the R_I.

Equation (19) was solved for a series of values of R_E and the results are presented in Table 1. Equation (19) yields both positive and negative values of R_I. The negative values are solutions to the problem when a heat sink is present and are not reported here. The smallest R_I, resulting from a solution to equation (19), is identical to that reported by Kulacki and Goldstein [2]. The larger R_I, higher modes, have not heretofore been calculated.

Table 1 Critical Rayleigh numbers, wave numbers, and transport coefficients

R_E	m	R_I	a	N	R_E	m	R_I	a	N
0	1	3.73×10^4	4.00	.1061	10^4	1	1.07×10^5	5.03	.0986
	2	7.35×10^5	8.36	.1018		2	8.87×10^5	8.24	.0723
	3	4.45×10^6	11.8	.0491		3	4.72×10^6	11.9	.0495
	4	1.59×10^7	15.4	.0314		4	1.68×10^7	15.7	.0330
	5	4.37×10^7	18.9	.0209		5	4.67×10^7	19.4	.0229
	6	1.04×10^8	25.5	.0127		6	1.12×10^8	25.6	.0149
10^6	1	3.37×10^6	9.94	.0636	10^8	1	2.76×10^8	23.7	.0741
	2	1.06×10^7	9.26	.0461		2	9.67×10^8	24.1	.0429
	3	1.83×10^7	12.2	.0272		3	1.37×10^9	20.9	.0208
	4	3.36×10^7	15.5	.0199		4	1.78×10^9	18.5	.0124
	5	6.53×10^7	18.9	.0156		5	2.20×10^9	19.7	.00828
	6	1.26×10^8	22.2	.0122		6	2.60×10^9	23.4	.00595

Heat Transfer

The method by which power integrals could be used for the horizontal layer problem was first deduced by Malkus and Veronis [5] and their approach will be closely followed. The method involves averaging of various equations with the assumption that the amplitude but not the shape of the disturbances changes with increasing Rayleigh number. This is sometimes known as the Stuart shape assumption [12]. In the following development, either the energy or momentum equation could be used. The energy equation is chosen for convenience.

The temperature is defined as a perturbation temperature T' plus a horizontally averaged temperature $\bar{T}$,

$$T = T' + \bar{T} \quad (20)$$

with $\bar{T}' = 0$. Using this expression for temperature, the energy equation (5), in dimensional form, becomes

$$\kappa\nabla^2 T' = -\kappa\frac{\partial}{\partial z}(\frac{\partial \bar{T}}{\partial z}) + v\cdot\nabla T' + v\cdot\nabla\bar{T} \quad (21)$$

Subtracting the horizontally averaged energy equation from equation (21), multiplying by T' and volume averaging gives

$$\overline{\langle\kappa T'\nabla^2 T'\rangle} + \langle -\frac{\partial \bar{T}}{\partial z}\overline{v_z T'}\rangle = 0 \quad (22)$$

where the bar denotes a horizontal or area average and the $\langle\ \rangle$ denotes an average along a vertical line between the bounding surfaces. The horizontal averaged energy equation is integrated and the constant of integration eliminated by volume averaging and subtracting. The result is

$$\frac{\partial \bar{T}}{\partial z} = \langle\frac{\partial \bar{T}}{\partial z}\rangle - \frac{1}{\kappa}\{\langle\overline{v_z T'}\rangle - \overline{v_z T'}\} - \frac{Q}{k}(z - \frac{L}{2}) \quad (23)$$

Substituting for the horizontally averaged temperature gradient in equation (22) yields the convective contribution to the heat transfer

$$\langle\overline{v_z T'}\rangle = \frac{Q\kappa L}{k}N\{1 + \frac{\langle\kappa T'\nabla^2 T'\rangle}{Q/k\langle\overline{v_z T'}(z - \frac{L}{2})\rangle} + \frac{\langle\overline{v_z T'}\rangle\langle -d\bar{T}/dz\rangle}{Q/k\langle\overline{v_z T'}(z - \frac{L}{2})\rangle}\} \quad (24)$$

where

$$N = \frac{\overline{\langle\overline{v_z T'}\rangle\langle v_z T'(\frac{z}{L} - \frac{1}{2})\rangle}}{\langle\overline{v_z T'^2}\rangle - \langle\overline{v_z T'}\rangle^2} \quad (25)$$

By defining the Nusselt number as the ratio of the heat flux at the boundary to the heat flux at the boundary due to conduction alone

$$Nu_2 = \frac{q_2}{q_{cond}} = \frac{-k\frac{d\bar{T}}{dz}\Big|_{z=L}}{\frac{QL}{2} + k\langle -d\bar{T}/dz\rangle} \quad (26)$$

a relationship for the convective contribution given by equation (24) is found to be

$$Nu_2 - 1 = \frac{\langle\overline{v_z T'}\rangle}{(\kappa QL/2k) + \kappa\langle -d\bar{T}/dz\rangle} \quad (27)$$

Scaling velocity and temperature with the same factors used in the stability problem allows equation (24) to be written as

$$\langle\overline{v_z T'}\rangle = N\{1 + \frac{\langle\overline{\theta\nabla^2\theta}\rangle + \langle\overline{w\theta}\rangle R_E}{R_I\langle\overline{w\theta}(z - \frac{1}{2})\rangle}\}\frac{\kappa QL}{k} \quad (28)$$

If it is assumed that the shape of the disturbance is adequately described in terms of normal modes and that only the amplitude changes with increasing Rayleigh number [12], then multiplying equation (8) by θ and integrating over the entire layer yields

$$R_{I_{cr}} = -\frac{\langle\overline{\theta(D^2 - a^2)\theta}\rangle + \langle\overline{w\theta}\rangle R_E}{\langle\overline{w\theta}(z - \frac{1}{2})\rangle} \quad (29)$$

This allows $\langle\overline{v_z T'}\rangle$ to be related to $R_{I_{cr}}$ and R_I. Using the relationship given by equation (29) and the definitions of R_I and R_E in equation (27) yields

$$Nu_2 - 1 = \frac{N}{\frac{1}{2} - R_E/R_I}(1 - R_{I_{cr}}/R_I) \quad (30)$$

for each individual mode. $R_{I_{cr}}$ is the eigenvalue, N is a result of prescribed integrations of the products of the eigenfunctions, R_E is the imposed external Rayleigh number, and R_I is the internal modified Rayleigh number at which one desires the Nusselt number.

If it is assumed that the interactions between the individual modes can be neglected and that the eigenvalues and eigenfunctions of the linearized equations can be used, then

$$Nu_2 - 1 = \left(\frac{1}{2} - \frac{R_E}{R_I}\right)^{-1} \sum_m N_m \left(1 - \frac{R_{I_m}}{R_I}\right) U(R_I - R_{I_m}) \quad (31)$$

$$Nu_1 - 1 = -\left(\frac{1}{2} + \frac{R_E}{R_I}\right)^{-1} \sum_m N_m \left(1 - \frac{R_{I_m}}{R_I}\right) U(R_I - R_{I_m}) \quad (32)$$

where R_{I_m} is the mth characteristic Rayleigh number, $U(R_I - R_{I_m})$ is the unit step function, and N_m is the result of substituting the mth eigenfunctions into equation (25).

Results were obtained for R_I up to 10^9 and for $0 \leq R_E \leq 10^9$. Some results are shown in Fig. 2 for comparison with the experimental results of Kulacki and Goldstein [2]. In Fig. 3, a series of constant Nusselt number results, Nu_1, are presented on an $R_I - R_E$ coordinate graph. The effect of thermal stabilization on downward heat transfer is made apparent in this type of presentation.

Discussion of Results

A comparison of the Nusselt number predicted by this method with experiment can only be done for the case of $R_E = 0$ since no other measurements are known to the authors. Fig. 2 shows the experimental data of Kulacki and Goldstein. The solid line is the Nusselt number predicted in this work. As can be seen, there is good agreement. The dashed line is the experimental correlation of Jahn and Reineke. There is a small difference in slope and in the value of the Nusselt number. The reason for this discrepancy is not known at the present time. Since the predictions obtained for $R_E = 0$ appear to be good, one could assume that Nusselt number predictions for $R_E \neq 0$ will give reasonable approximations because nonzero R_E is stabilizing and amplitudes of ω and θ will be smaller. It was found that the temperature profile deviated strongly from experiment away from bounding walls. Finite amplitude effects on the temperature profile for $R_E = 0$ were addressed by Catton and Suo-Anttila [3].

Fig. 3 shows a plot of constant Nusselt numbers for downward heat transfer with R_I and R_E as the axes. There are three regions of interest. In the first region the Nusselt number is constant and independent of the external Rayleigh number. Here, the applied external temperature difference is not large enough to cause a change in the convective flow pattern. In the second region the external temperature difference is large enough to cause a change in the convective flow pattern. This results in the upward curvature of the lines of constant Nusselt number. The final region appears at very large Rayleigh numbers. The Nusselt numbers approach asymptotes with a slope of unity.

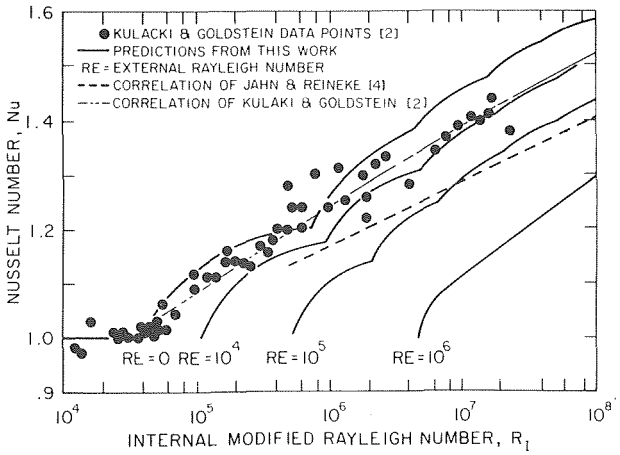

Fig. 2 Comparison of predictions with experiment

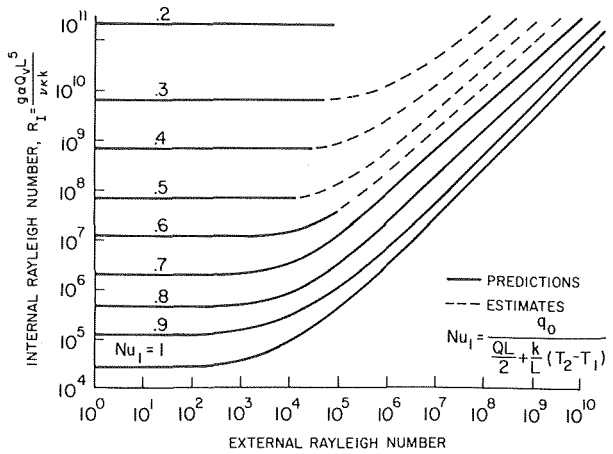

Fig. 3 The effect of stabilization on heat transfer

In applying these results to post-accident heat removal (PAHR) situations, only very large Rayleigh numbers ($R_I > 10^9$) are of interest. If one assumes that a 10 cm deep molten layer of UO_2 is covered by molten iron such that the upper surface is 200°C hotter than the lower surface, then $R_E = 4 \times 10^8$. The corresponding Ri for 3 cal/cm^3 s internal heating is 10^{11}. By extrapolating the results given in Fig. 3 it is found that 25 percent of the heat is transferred to the lower surface rather than the 12–13 percent which would occur with equal upper and lower surface temperatures.

The temperature rise of the upper surface required for complete stabilization of the molten layer can be found from the asymptotic part of the Nu = 1 curve. The approximate relationship is

$$R_E = 0.3\, R_I, \; R_I > 10^6 \quad (33)$$

which reduces to

$$\Delta T = 0.3\, QL^2/k \quad (34)$$

Substituting values for molten UO_2 results in

L	ΔT
1 cm	127°C
10 cm	17,200°C
20 cm	68,800°C

for a decay heat of 3 cal/cm^3 s. As can be seen, the predicted temperatures are far too high, hence complete stabilization would not occur except for very thin layers.

Summary and Conclusions

A solution has been obtained by the power integral method for the heat transfer from a horizontal layer of fluid with internal heat generation and a stabilizing temperature gradient confined by rigid boundaries. It was found that a stabilizing temperature gradient, which can result from a high thermal resistance above the molten layer, causes significant increases in the downward heat transfer. Complete stabilization of a molten layer is not expected to occur.

Future work in this area should include experimental verification of the predictions presented here. Additional numerical and experimental work could include the effect of a free boundary at the upper surface since low viscosity fluids could be superposed above molten fuel layers.

Acknowledgment

This research was supported by the Reactor Research Division and the Directorate of Licensing of the Atomic Energy Commission and by the National Science Foundation. The conclusions reached in this study should not be interpreted as representing official opinion or policy of the Atomic Energy Commission. Further acknowledgment is given the UCLA Computer Center for computational support.

References

1 Catton, I., and Erdmann, R. C., *Post-Accident Core Retention for LMFBR's*, UCLA-ENG-7343, July 1973.

2 Kulacki, F. A., and Goldstein, R. J., *Journal of Fluid Mechanics*, Vol. 55, 1972, pp. 271–280.

3 Catton, I., and Suo-Anttila, A. J., *Proceedings of the Fifth International Heat Transfer Conference*, Vol. III, Sept. 1974, pp. 69–73.

4 Jahn, M., and Reineke, H. H., *Proceedings of the Fifth International Heat Transfer Conference*, Vol. III, Sept. 1974, pp. 74–78.

5 Malkus, W. V. R., and Veronis, G., *Journal of Fluid Mechanics*, Vol. 4, 1958, pp. 225–260.

6 Landau, L. D., and Lifshiftz, E. M., *Fluid Mechanics*, Pergamon Press, London, 1959.

7 Edwards, D. K., and Catton, I., *The International Journal of Heat Mass Transfer*, Vol. 12, 1969, pp. 23–30.

8 Catton, I., *Proceedings of the Fourth International Heat Transfer Conference*, Paris, France, Vol. IV, 1970.

9 Catton, I., and Ayyaswamy, P. S., *Journal of Applied Mechanics*, Vol. 39, 1972, pp. 33–36.

10 Sharman, R. D., Catton, I., and Ayyaswamy, P. S., *Chemical Engineering Progress Symposium Series*, 1972.

11 Chandrasekhar, S., *Hydrodynamic and Hydromagnetic Stability*, Oxford Press, England, 1961.

12 Stuart, J. T., *Journal of Fluid Mechanics*, Vol. 4, 1958, pp. 1–13.

G. C. Vliet
Assoc. Professor.

D. C. Ross
Graduate Student.

Department of Mechanical Engineering,
University of Texas at Austin,
Austin, Texas

Turbulent Natural Convection on Upward and Downward Facing Inclined Constant Heat Flux Surfaces

Local heat transfer data were obtained for turbulent natural convection on vertical and inclined upward and downward facing surfaces. The test surface consisted of a 1.83 m (6 ft) wide × 7.32 m (24 ft) high plate with a constant heat flux obtained by electrical resistive heating of a metal foil on the surface. The tests were conducted in air for modified Grashof numbers up to 10^{15}. Measurements were made of the local surface temperature for this constant heat flux condition, for the plate inclined at angles from 30 deg to the vertical (upward facing, unstable) through the vertical to 80 deg to the vertical (downward facing, stable).

The results show the location of the transition to be a function of the plate angle. For the unstable case, the transition length decreases as the plate angle increases from the vertical while for the stable case the position of transition increases with the angle from the vertical. The laminar data for both orientations are correlated as:

$$Nu_x = 0.55\,(Gr_x{}^*Pr)^{0.20}$$

in which the gravity is the component along the surface, g cos θ. The turbulent natural convection data are correlated quite well by the relation:

$$Nu_x = 0.17\,(Gr_x{}^*Pr)^{0.25}$$

In the turbulent case the correlation is independent of angle for the unstable case, whereas for the stable case the data correlate best when the gravity is modified by $\cos^2\theta$, where θ is measured from the vertical. Thus, there is a significant influence of angle on the convective heat transfer for the stable turbulent region.

Introduction

Several physical phenomena involve turbulent natural convection on inclined surfaces: thermal convection during the thermal stratification of liquids in vessels (of primary interest in the cryogenic industry), natural convection mass transfer during cavity development in solution mining, and thermal convection along sloping terrain—a meteorological phenomenon. The problem of thermal natural convection along inclined surfaces for the thermally unstable orientation (upward facing heated surfaces) has been examined to some extent. The constant heat flux inclined plate data of Vliet [1][1] for water exhibit a strong effect of angle on transition; show the laminar data are correlatable at various angles using the gravity component along the surface; and show the turbulent data to be independent of angle (except for location of transition). Lloyd and Sparrow [2] have experimentally examined the nature of transition on inclined surfaces. Recently, instability analyses for natural convection flow on inclined surfaces have been performed by Pera and Gebhart [3], Haaland and Sparrow [15, 16], Iyer and Kelly [4], and Kahawita and Meroney [17]. Other inclined plate investigations [5, 6] have also been made. A number of experimental investigations of turbulent natural convection on vertical surfaces have also been conducted [7–13]. In general these turbulent data exhibit a very weak variation of the local heat transfer coefficient with length, and it correlates with the inclined unstable turbulent data using the vertical gravity vector.

Contributed by the Heat Transfer Division and presented at the Winter Annual Meeting, New York, N. Y., November 17–22, 1974, of THE AMERICAN SOCIETY OF MECHANICAL ENGINEERS. Revised manuscript received by the Heat Transfer Division, August 14, 1975. Paper No. 74-WA/HT-32.

[1] Numbers in brackets designate References at end of paper.

Some of the foregoing naural convection phenomena involve convection along inclined surfaces such that the density gradient normal to the surface is negative (stable): natural convection heat transfer from a surface facing downward, natural convection mass transfer near the bottom of a cavity in solution mining, and the case of flow down sloping terrain when the ground is cooler than the air (i.e., cold surface facing upward). It is expected that the laminar flow for these cases can be correlated using the gravity component along the surface as for the laminar flow region for the unstable case. However, the effect of the surface angle on the turbulent convective flow is not immediately evident. This paper presents the results of an experimental investigation [19] and an extension of this work dealing with the effect on the transition and turbulent convection heat transfer for heated inclined surfaces with primary emphasis on the thermally stable condition—heated surface facing downward.

Experimental Apparatus

The experimental apparatus was designed with the goal of providing at least a 2 orders of magnitude range of fully turbulent Grashof number, since one of the shortcomings of many previous turbulent natural convection studies has been an inadequate range of turbulent flow beyond transition. The measurements were conducted in air rather than water as had been done previously by one of the authors. To achieve the desired range of turbulent flow in air, a rather large test surface is required; thus a constant heat flux surface was selected, as it is considerably less expensive to build, easier to control and instrument and more closely approximates some physical processes of interest. To achieve the two-dimensional turbulent natural convection boundary layer flow desired, it is essential that the experimental test surface be:

(*a*) long enough in the flow direction to achieve Grashof numbers at least two orders of magnitude greater than transition;

(*b*) wide enough to minimize edge effects;

(*c*) located in a fluid of uniform temperature; and

(*d*) isolated from disturbances present in the room.

The experimental test surface used in this investigation consisted of a 1.83 m (6 ft) wide × 7.32 m (24 ft) high (long) constant heat flux plate as shown in Fig. 1. The constant heat flux condition was achieved by the electrical resistance heating of a thin (0.05 mm, 0.002 in.) stainless steel foil mounted on an insulated and thermally guarded structural surface as shown in Fig. 1. The structural surface consisted of a steel frame with a plywood substrate. Laid upon the plywood was a layer of urethane foam insulation, a screen guard heater, a second layer of urethane foam insulation, then a fiberglass-phenolic sheet to which the stainless steel foil was bonded with pressure sensitive adhesive. The stainless steel foil surface consisted of three 0.61 m (2 ft) wide × 7.32 m (24 ft) long pieces laid side by side, with a small gap (approximately 1 mm) between, and connected in series to match the d-c power supply. The wire screen guard heater, sandwiched between the two foam layers, was electrically heated and operated near the average surface foil temperature to minimize conduction losses through the back of the plate. 25 thermocouples for surface measurements were located near the plate center line at approximately 0.305 m (1 ft) intervals along the surface. Two similar spanwise thermocouples were located across the plate at 6.1 m (20 ft) from the leading edge to detect spanwise variations in surface temperature. These thermocouples for measurement of surface temperature were 0.25 mm dia and introduced through the insulated back of the plate, with the junction against the back of the phenolic substrate (Fig. 1). Five guard heater thermocouples were located near the guard heater in the urethane foam between the surface and guard heaters to monitor guard heater temperature and permit it to be operated near the surface temperature. 12 thermocouples were used to monitor the *ambient* air temperature along the plate.

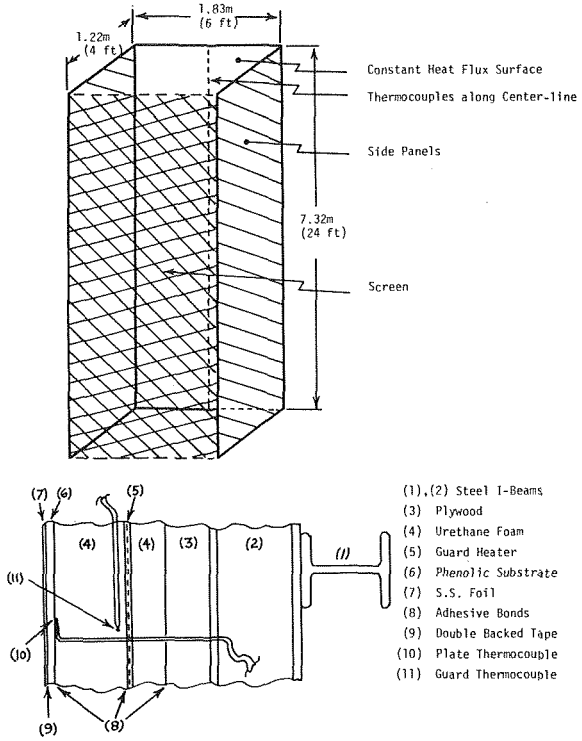

Fig. 1 Natural convection heat transfer apparatus

The test plate was installed with perpendicular side panels, which extended the full length of the plate, to reduce edge effects. At the outer edge of these side panels, a layer of standard window screen was installed to minimize the effects of ambient room disturbances on the natural convection flow. Rather than locating the test apparatus (heated surface, panels and screen) in a separate room, it was located in a large bay and tests were conducted after or prior to normal working hours while the air in the room was thermally unstratified and when convective disturbances in the room were minimal. For these tests the bottom of the test surface was located no closer than approximately 20 cm (8 in.) above the floor.

With this apparatus and heat fluxes of approximately 57 W/m^2 (18 Btu/hrft^2) (i.e., approximately 20°C (35°F) temperature difference in the turbulent region) Gr*Pr $\simeq 4 \times 10^{14}$ at the top of the plate. This provides approximately 3 orders of magnitude in Gr*Pr of turbulent flow for the vertical or unstable orientations. For the stable orientations the extent of turbulent flow is less and decreases with shallower angles. Boundary layer profile measurements have not been made at this date. However, using the velocity profile data of Cheesewright [8] for a constant temperature plate in air, the 0.95 boundary layer thickness for the present 7.32 m long vertical surface and the above conditions is approximately 45 cm, or approximately ¼ the plate width.

Smoke tests were conducted with the test apparatus in the vertical orientation which indicated that the width of the surface, the presence of the side panels and the screening produced an essen-

Nomenclature

g = standard gravity

Gr_x = local Grashof number

Gr_x^* = modified local Grashof number, Nu_xGr_x

Nu_x = local Nusselt number

Pr = Prandtl number

q_u'' = surface heat flux

ΔT_p = plate to bulk temperature difference

θ = angle relative to the vertical

Table 1 Natural convection data summary

		Angle to Vertical (degrees)	Heat Dissipation[1] w/m²	(B/hf²)	Average[2] Percent Corrections Cond.	Rad.	Actual[3] Heat Flux W/m²	(B/hf²)	Bulk[4] Temp °C	(°F)	Temp. Diff[4] °C	(°F)	Gr^*Pr[5] x 10^{14} (-)
Unstable	a	30	28.0	(8.9)	1.2	23	21.1	(6.7)	33.4	(92.1)	9.6	(17.2)	1.7
	b		72.0	(22.8)	1.0	19	58.0	(18.4)	33.4	(92.2)	19.6	(35.3)	4.3
Vertical	c	0	27.0	(8.6)	0.0	22	21.4	(6.8)	25.2	(77.3)	9.5	(17.1)	1.7
	d		69.6	(22.1)	−0.9	18	58.0	(18.4)	22.8	(72.9)	19.1	(34.4)	4.8
Stable	e	10	71.2	(22.6)	−1.8	19	59.0	(18.7)	21.6	(70.9)	20.7	(37.3)	5.1
	f	20	27.1	(8.6)	−1.2	22	21.4	(6.8)	25.4	(77.7)	9.4	(16.9)	1.9
	g		70.3	(22.3)	−2.7	19	58.3	(18.5)	27.2	(80.0)	20.0	(36.0)	4.5
	h	30	26.4	(8.4)	2.4	21	20.2	(6.4)	24.2	(75.6)	9.2	(16.5)	1.8
	i		71.5	(22.7)	−2.2	21	58.3	(18.5)	28.1	(82.6)	21.6	(38.9)	4.2
	j	45	26.8	(8.5)	−5.9	25	21.4	(6.8)	22.6	(72.7)	10.7	(19.2)	2.1
	k		68.5	(21.7)	−1.8	23	53.9	(17.1)	23.6	(74.5)	23.5	(42.3)	4.1
	l	60	26.5	(8.4)	2.4	30	17.6	(5.6)	22.7	(72.8)	12.8	(23.0)	1.7
	m		70.6	(22.4)	0.0	27	51.7	(16.4)	23.2	(73.8)	27.6	(49.8)	4.0
	n		96.8	(30.7)	−3.6	28	72.5	(23.0)	24.2	(75.5)	37.4	(67.4)	5.2
	o	70	26.8	(8.5)	4.7	40	14.8	(4.7)	32.6	(90.7)	15.3	(27.6)	1.1
	p		54.8	(17.4)	−2.3	34	36.5	(11.6)	35.1	(95.2)	25.1	(45.2)	2.3
	q	80	28.0	(8.9)	6.7	40	14.8	(4.7)	31.8	(89.1)	16.5	(29.6)	1.1
	r		52.0	(16.5)	5.5	41	29.0	(9.2)	34.9	(94.7)	28.4	(51.0)	1.7

(1) Electrical heat dissipation per unit area
(2) Average percent corrections for conduction and radiation losses, positive refers to loss
(3) Average of actual convective heat flux over upper 40 percent of plate
(4) Average over upper 40% of plate
(5) Value at top of plate (using standard gravity)

tially two-dimensional boundary layer flow in the central one-third to one-half of the plate over its length, with no noticeable effect of ambient disturbances on the flow, under the conditions of test.

The test surface could be orientated at any angle for either the thermally stable or unstable conditions, using hoists and cables; however the primary interest herein is in the thermally stable orientation and only limited unstable data are presented.

The time constant to reach a steady-state condition for the plate was approximately 3 hr, due to the low heat transfer coefficients and the thermal capacitance of the surface. The tests were conducted in the late evening or early morning when disturbances in the laboratory were minimal, there was little thermal stratification, and the air exhibited little temperature variation over a 3–4 hr period. Preliminary tests were performed to determine the relative plate and guard power levels to permit operation of the guard heater near the plate surface temperature at various operating conditions. For each test, plate and guard powers were set at appropriate levels after which plate, guard and bulk thermocouple temperature data were recorded for the duration of the run. From this record the requirements of reaching steady state, maintaining low bulk thermal stratification and maintaining guard and plate temperatures nearly equal could be insured. For the lower heat flux tests the average nonuniformity of the bulk temperature was ±5 percent of the plate to bulk temperature difference while for the higher heat flux tests the average bulk temperature nonuniformity was ±3 percent.

Experimental Results

A summary of the natural convection tests discussed herein is presented in Table 1. The thermal energy generated in the foil is dissipated by natural convection, conduction through the insulated backing, and by radiation to the surroundings; thus the convective heat flux was obtained by correcting for the conductive and radiative losses. The conductive loss was computed from the temperature difference between the foil and guard, and the thickness and thermal conductivity of the polyurethane foam insulation. The presence of the guard heater limited the conductive losses to an average of 2.6 percent of the dissipated electrical energy or a maximum of 6.7 percent in all cases (see Table 1). The net radiation loss from the stainless surface was computed using a radiation network which included: the stainless steel foil surface (of 0.11 emissivity[2]); the galvanized wire screen (of 0.25 emissivity and 65 percent porosity); the particle board side panels (of 0.95 emissivity) and the open upper end of the enclosure. The side panels and screen were both assumed to be at the ambient temperature. As can be seen from Table 1 the necessary radiation corrections varied from 18 to 41 percent of the dissipated electrical energy with an average of 26 percent. Corrected convective heat fluxes were computed at each of the plate thermocouple locations along the plate. Local heat transfer coefficients were computed from the local corrected fluxes and the local plate to bulk temperature differences. Fluid properties were evaluated at the average film temperature.

Fig. 2 presents the variation of surface to bulk temperature difference ΔT_p along the plate for seven orientations (30 deg unstable, vertical and 30, 45, 60, 70, and 80 deg stable) all for the low heat flux condition. It is seen from this figure that: (*a*) there is no pronounced maximum in plate temperature prior to transition as is the case for similar constant heat flux natural convection tests in water [1, 9]; (*b*) the plate-bulk temperature difference (and, therefore, the heat transfer coefficient) exhibited little variation in the turbulent region as has been evidenced in previous investigations [1, 7, 8, 9, 10]; and (*c*) as the surface is inclined at larger angles to the vertical, there is an increase in ΔT_p (decrease in the heat transfer coefficient) in the turbulent region and an extension of the apparent laminar region.

No specific method[3] for determining the initiation of transition (end of laminar flow) and approach to fully turbulent flow was used, other than inferring it from the characteristics of the plate temperature variation. Laminar flow was assumed to terminate where the plate temperature leveled out or reached a weak maximum as it did in some cases. Fully turbulent flow was assumed to begin where the plate temperature became reasonably constant. The transition range was designated as between these two locations. These locations were not consistently distinct but did generally exhibit: earlier transition with increasing angle from the vertical for the unstable case, delayed transition with increasing angle from the vertical for the stable orientation, and earlier transition with increasing heat flux. Fig. 3 shows these approximate transition regions in terms of $Gr_x{}^*Pr$ as a function of angle. The general trend with angle is apparent; however, the erratic behavior is also obvious. The instability analysis of Iyer and Kelly [4] indicates a delay in transition with increasing angle from the vertical for the stable case, which is to be expected.

[2] This was the same stainless steel used in [1] for which this emissivity was measured by a Gier-Dunkle radiometer.

[3] Neither detailed flow visualization nor hot wire measurements were made to specifically detect the transition region.

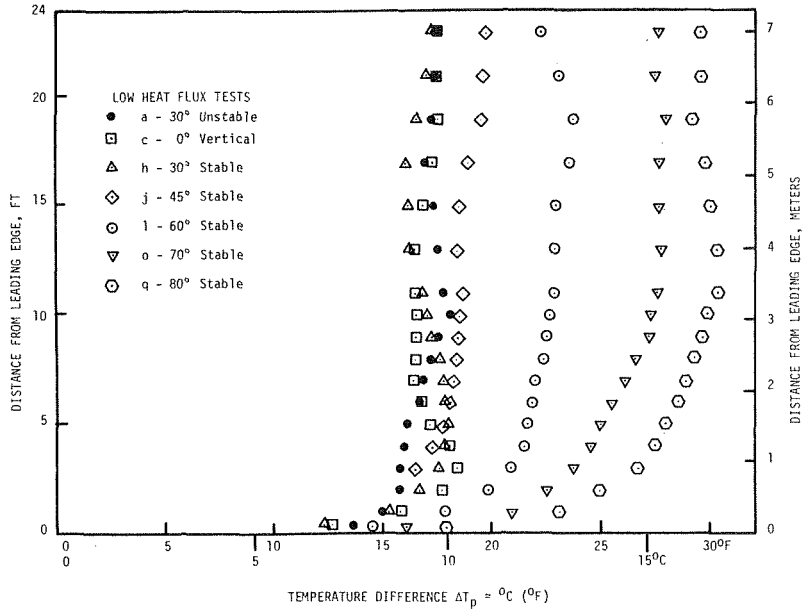

Fig. 2 Temperature difference variation, various angles

Also presented for comparison are the transition ranges for the inclined plate water and air data of [1]. The one data point for air is consistent with the present data; however, the $Gr_x{}^*Pr$ range for water in general falls above the air data. This is qualitatively consistent with the work of Godaux and Gebhart [18].

A correlation of the laminar portion of the data is presented in Fig. 4, in which the gravity in the modified Grashof number is replaced by the component along the plate, $g \cos \theta$, where θ is the angle measured from the vertical for both the stable and unstable orientations. The criterion for the end of laminar flow is as stated in the foregoing. The work of Dotson [14] for air on a vertical plate: $Nu_x = 0.55\ (Gr_x{}^*Pr)^{0.2}$; and that of Vliet [1] for water on inclined (unstable) surfaces: $Nu_x = 0.6\ (Gr_x{}^*Pr)^{0.2}$ are shown with the present data for comparison. The spread in the present data is at least partially attributable to nonconstant heat flux in the laminar region where the heat flux corrections varied with length, and to the bulk temperature variation which was generally greatest near the leading edge of the plate.

All of the turbulent high heat flux data (stable and unstable) are plotted in Fig. 5 in terms of Nu_x versus $Gr_x{}^*Pr$ where the acceleration in $Gr_x{}^*$ is the vertical gravity vector g. The unstable data are seen to correlate very well with the vertical data as has been previously reported [1]; however, there is seen to be a monotonic deviation of the stable turbulent data. A cross plot of these data indicated that the stable data could be correlated by replacing the acceleration in $Gr_x{}^*$ by $g \cos^2 \theta$. All of the turbulent inclined surface data are presented in Fig. 6 in the form of Nu_x versus $Gr_x{}^*Pr$, where for the unstable orientation the vertical gravity vector is used, but for the stable orientation g is replaced by $g \cos^2 \theta$. Although this correlation of data also exhibits substantial scatter (±15 percent), the correlation is greatly improved. The relation ascribed to this data $Nu_x = 0.17\ (Gr^*Pr)^{0.25}$ may be compared to the turbulent inclined plate constant heat flux water data of Vliet [1] which was best described by $Nu_x = 0.302\ (Gr_x{}^*Pr)^{0.24}$. The present data fall approximately 30 percent below this earlier data for water. It is to be noted that the vertical constant temperature turbulent data for air of Warner [7] and Cheesewright [8] correlate approximately as:

$$Nu_x = C(Gr^*Pr)^{1/3}$$

where the coefficients C are approximately 0.088 and 0.122 for the two sets of data, respectively. If this relation is recast as

$$Nu_x = C'(Gr_x{}^*Pr)^{1/4}$$

then the coefficients C' are approximately 0.16 and 0.21 for the two sets of data, respectively, and thus the agreement of the present data with [7, 8] is quite good.

The reduction in the turbulent heat transfer coefficient with increasing angle from the vertical for the stable case may be attributed principally to the damping of the turbulence due to the thermally stable condition of the boundary layer flow for this orientation, and the decrease in the gravity component along the surface.

The implications of this effect are significant in some physical phenomena such as prediction of cavity shape development in solution mining (natural convection mass transfer), and warm air above colder sloping terrain (meteorological phenomenon), since the reduction in the convective transfer coefficient with angle is substantial.

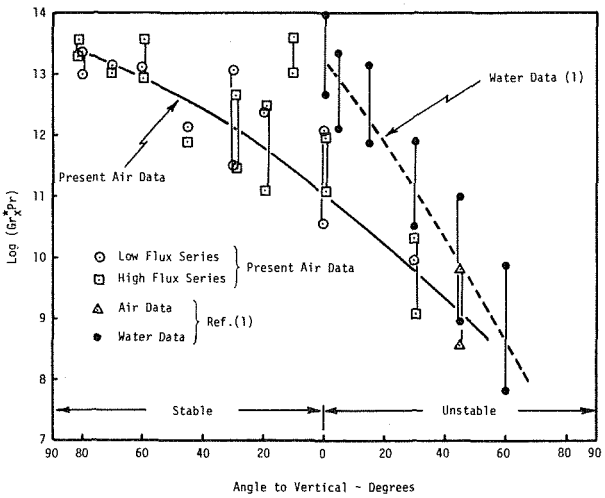

Fig. 3 Transition range as interpreted from local temperature behavior

Conclusions

There is a very pronounced effect of surface orientation on the

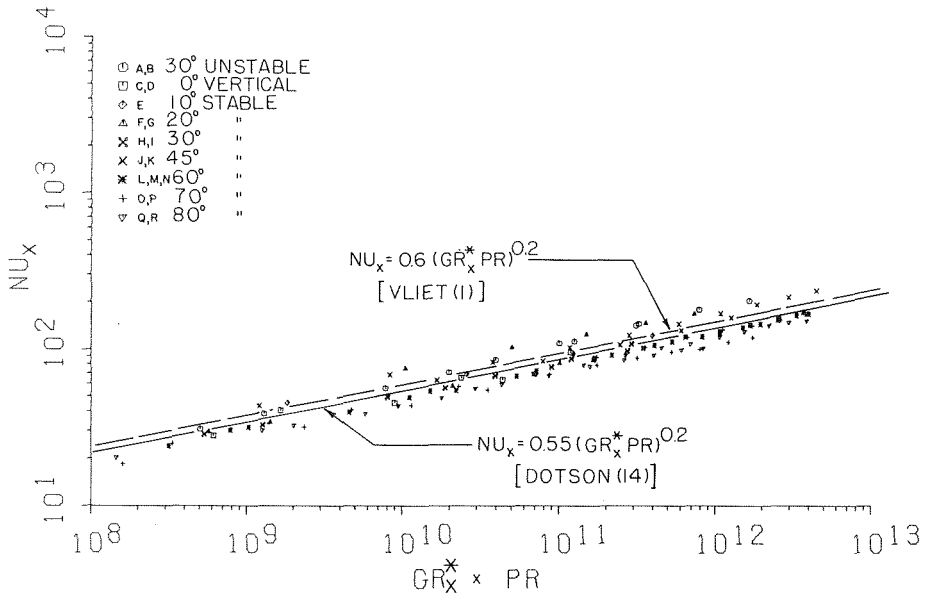

Fig. 4 Laminar flow region

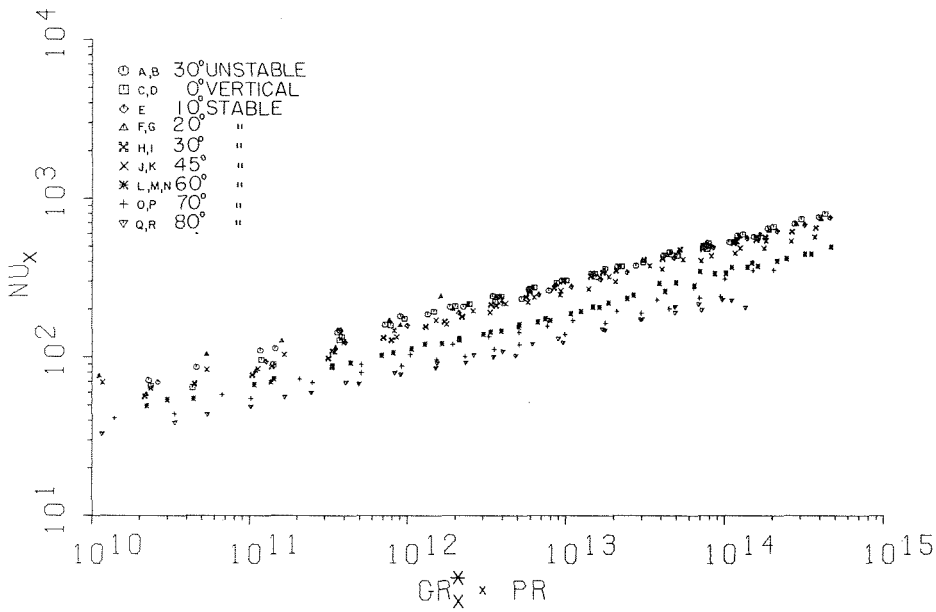

Fig. 5 Turbulent flow region

turbulent natural convection transfer coefficient for the stable orientation. Whereas the turbulent data for the unstable orientation is a function of the vertical gravity vector, turbulent natural convection transfer coefficients decrease significantly with angle from the vertical for the stable orientation and the data are best correlated with the acceleration replaced by $g \cos^2 \theta$.

Acknowledgments

This research was sponsored by the Bureau of Engineering Research, The University of Texas at Austin.

References

1 Vliet, G. C., "Natural Convection Local Heat Transfer on Constant Heat Flux Inclined Surfaces," JOURNAL OF HEAT TRANSFER, TRANS. ASME, Series C, Vol. 91, No. 4, Nov. 1969, pp. 511–517.

2 Lloyd, J. R., and Sparrow, E. M., "On the Stability of Natural Convection Flow on Inclined Plates," *Journal of Fluid Mechanics,* Vol. 42, 1970, pp. 465–470.

3 Pera, L., and Gebhart, B., "On the Stability of Natural Convection Boundary Layer Flow Over Horizontal and Slightly Inclined Surfaces," *International Journal of Heat and Mass Transfer,* Vol. 16, No. 6, 1973, pp. 1147–1164.

4 Iyer, P. A., and Kelly, R. E., "The Stability of the Laminar Free Convection Flow Induced by a Heated Inclined Plate," *International Journal of Heat and Mass Transfer,* Vol. 17, No. 4, Apr. 1974, pp. 517–526.

5 Tritton, D. J., "Transition to Turbulence in Free-Convection Boundary Layer on an Inclined Heated Plate," *Journal of Fluid Mechanics,* Vol. 16, 1963, p. 417.

6 Rich, B. R., "An Investigation of Heat Transfer From an Inclined Flat Plate in Free Convection," TRANS. ASME, May 1953, p. 489.

7 Warner, C. Y., and Arpaci, V. S., "An Experimental Investigation of Turbulent Natural Convection in Air Along a Vertical Heated Flat Plate," *International Journal of Heat and Mass Transfer,* Vol. 11, 1968, p. 397.

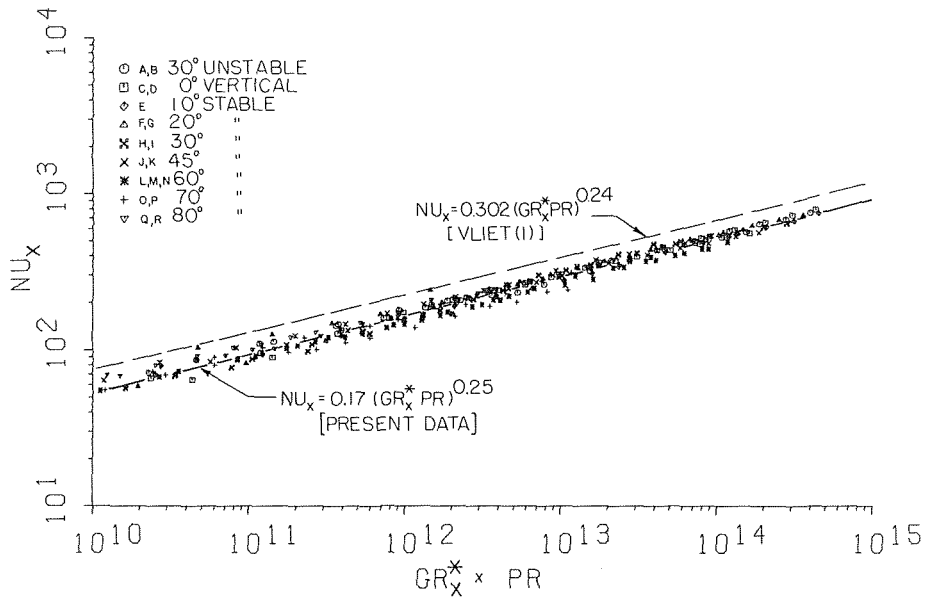

Fig. 6 Turbulent flow region correlated

8 Cheesewright, R., "Turbulent Natural Convection from a Vertical Plane Surface," JOURNAL OF HEAT TRANSFER, TRANS. ASME, Series C, Vol. 90, No. 1, Feb. 1968, pp. 1–8.

9 Vliet, G. C., and Liu, C. K., "An Experimental Study of Turbulent Natural Convection Boundary Layers," JOURNAL OF HEAT TRANSFER, TRANS. ASME, Series C, Vol. 91, No. 4, Nov. 1969, pp. 517–531.

10 Fugii, T., Takeuchi, M., Fujii, M., Suzaki, K., and Uehara, H., "Experiments on Natural Convection Heat Transfer From the Outer Surface of a Vertical Cylinder to Liquids," *International Journal of Heat and Mass Transfer*, Vol. 13, No. 5, May 1970, pp. 753–787.

11 Pirovano, A., Viannay, S., and Jannot, M., "Natural Convection in the Turbulent Regime Along a Vertical Plate," Fourth International Heat Transfer Conference (Paris-Versailles, France), Vol. 4, Paper No. NC1.8, 1970.

12 Lock, G. S. H., and Trotter, F. J. deB., "Observation of the Structure of a Turbulent Free Convection Boundary Layer," *International Journal of Heat and Mass Transfer*, Vol. 11, No. 8, 1968, pp. 1225–1232.

13 Kutateladze, S. S., et al., "Turbulent Natural Convection on a Vertical Plate and in a Vertical Layer," *International Journal of Heat and Mass Transfer*, Vol. 15, No. 2, 1972, pp. 193–202.

14 Dotson, J. P., "Heat Transfer From a Vertical Plate by Free Convection," MS thesis, Purdue University, 1954.

15 Haaland, S. E., and Sparrow, E. M., "Wave Instability of Natural Convection on Inclined Surfaces Accounting for Non-Parallelism of the Basic Flow," JOURNAL OF HEAT TRANSFER, TRANS. ASME, Series C, Vol. 95, Aug. 1973, pp. 405–407.

16 Haaland, S. E., and Sparrow, E. M., "Vortex Instability of Natural Convection Flow on Inclined Surfaces," *International Journal of Heat and Mass Transfer*, Vol. 16, Dec. 1973, pp. 2355–2367.

17 Kahawita, R., and Meroney, R. N., "Vortex Mode of Instability in Natural Convection Flow Along Inclined Plates," *International Journal of Heat and Mass Transfer*, Vol. 17, No. 5, 1974, pp. 541–548.

18 Gebhart, B., and Godaux, F., "An Experimental Study of the Transition of Natural Convection Flow Adjacent to a Vertical Surface," *International Journal of Heat and Mass Transfer*, Vol. 17, No. 1, 1974, pp. 93–107.

19 Ross, D. C., "Experimental Investigation of Natural Convection Heat Transfer on Inclined Surfaces," MS thesis, The University of Texas at Austin, May 1974.

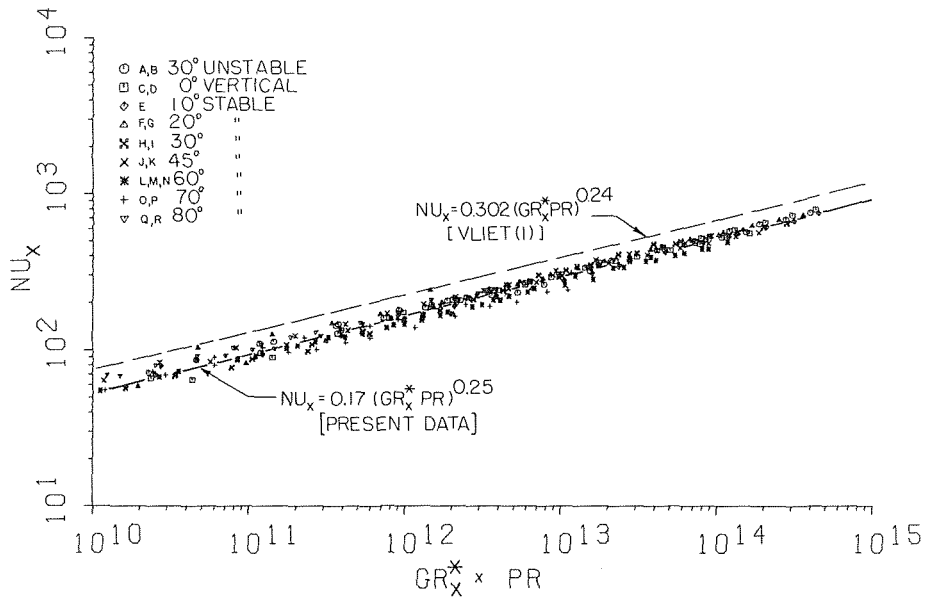

Fig. 6 Turbulent flow region correlated

8 Cheesewright, R., "Turbulent Natural Convection from a Vertical Plane Surface," JOURNAL OF HEAT TRANSFER, TRANS. ASME, Series C, Vol. 90, No. 1, Feb. 1968, pp. 1–8.

9 Vliet, G. C., and Liu, C. K., "An Experimental Study of Turbulent Natural Convection Boundary Layers," JOURNAL OF HEAT TRANSFER, TRANS. ASME, Series C, Vol. 91, No. 4, Nov. 1969, pp. 517–531.

10 Fugii, T., Takeuchi, M., Fujii, M., Suzaki, K., and Uehara, H., "Experiments on Natural Convection Heat Transfer From the Outer Surface of a Vertical Cylinder to Liquids," *International Journal of Heat and Mass Transfer*, Vol. 13, No. 5, May 1970, pp. 753–787.

11 Pirovano, A., Viannay, S., and Jannot, M., "Natural Convection in the Turbulent Regime Along a Vertical Plate," Fourth International Heat Transfer Conference (Paris-Versailles, France), Vol. 4, Paper No. NC1.8, 1970.

12 Lock, G. S. H., and Trotter, F. J. deB., "Observation of the Structure of a Turbulent Free Convection Boundary Layer," *International Journal of Heat and Mass Transfer*, Vol. 11, No. 8, 1968, pp. 1225–1232.

13 Kutateladze, S. S., et al., "Turbulent Natural Convection on a Vertical Plate and in a Vertical Layer," *International Journal of Heat and Mass Transfer*, Vol. 15, No. 2, 1972, pp. 193–202.

14 Dotson, J. P., "Heat Transfer From a Vertical Plate by Free Convection," MS thesis, Purdue University, 1954.

15 Haaland, S. E., and Sparrow, E. M., "Wave Instability of Natural Convection on Inclined Surfaces Accounting for Non-Parallelism of the Basic Flow," JOURNAL OF HEAT TRANSFER, TRANS. ASME, Series C, Vol. 95, Aug. 1973, pp. 405–407.

16 Haaland, S. E., and Sparrow, E. M., "Vortex Instability of Natural Convection Flow on Inclined Surfaces," *International Journal of Heat and Mass Transfer*, Vol. 16, Dec. 1973, pp. 2355–2367.

17 Kahawita, R., and Meroney, R. N., "Vortex Mode of Instability in Natural Convection Flow Along Inclined Plates," *International Journal of Heat and Mass Transfer*, Vol. 17, No. 5, 1974, pp. 541–548.

18 Gebhart, B., and Godaux, F., "An Experimental Study of the Transition of Natural Convection Flow Adjacent to a Vertical Surface," *International Journal of Heat and Mass Transfer*, Vol. 17, No. 1, 1974, pp. 93–107.

19 Ross, D. C., "Experimental Investigation of Natural Convection Heat Transfer on Inclined Surfaces," MS thesis, The University of Texas at Austin, May 1974.

Discussion

Y. Jaluria[4]

The authors have made an extensive experimental study of turbulent natural convection heat transfer from inclined heated surfaces and have presented a very impressive collection of important heat transfer data. Since much of the interest in such natural convection flows is in the heat transfer, these results are very valuable. However, there are a few considerations which, if taken into account, would make such a study of greater fundamental and practical significance.

From the standpoint of heat transfer, the isothermal surface condition is of greater interest due to its more frequent occurrence in practical problems. Moreover, it would allow a study of the direct variation, along the surface, of the heat transfer rate rather than of the indirect effect on the temperature difference across the boundary layer, which would be the case for a uniform flux surface. However, it is true that in order to achieve an isothermal surface, a much greater elaboration is needed in the experimental arrangement. A uniform flux surface condition would, nevertheless, be quite satisfactory in a study of the fundamental mechanisms involved, see Gebhart.[5] This is a very important consideration and a study of the velocity and temperature fields in the boundary region would add considerably to an understanding of the transport phenomenon. This would not only be of great importance in the study of turbulence in natural convection flows but in the understanding of the heat transfer data obtained as well. Given the elaborate experimental arrangement the authors have, it would be very

[4] Member of Research Staff, Western Electric Co., Engineering Research Center, Princeton, N. J.

[5] Gebhart, B., "Instability, Transition and Turbulence in Buoyancy-Induced Flows," *Ann. Rev. Fluid Mech.*, Vol. 5, 1973, p. 213.

worthwhile to pursue the problem and contribute significantly in this area. Not much work exists at the present time on this aspect of the problem, for these flows, and it will be a very valuable contribution to the field of natural convection turbulence if such a study is done. It will provide the basis for further work on similar turbulent natural convection flows.

Another important consideration concerns the question of the criterion for the determination of the onset of transition. This has been a vague and controversial point in natural convection studies. Recently, for vertical natural convection flows, Jaluria and Gebhart[6] have made a detailed study of the transition phenomenon and have considered this question at length. They found that following the growth of disturbances, turbulent bursts arose which led rapidly to a thickening of the boundary region and a distortion of the base velocity and temperature profiles. This further led to an effect on the rate of heat transfer and consequently on the measured wall temperature. Therefore, it was found that the wall temperature distribution shows a drop much farther downstream of the appearance of several events that characterize transition, like turbulent bursts and thickening of the boundary region. Taking the wall temperature distribution for determining the boundaries of the transition regime, therefore, excludes much of the actual transitional phenomenon in the boundary region. A similar study of transition over inclined surfaces would be valuable in clarifying this point for this flow configuration, and would probably indicate the proper criterion for determining the boundaries of the transition regime.

[6] Jaluria, Y., and Gebhart, B., "On Transition Mechanisms in Vertical Natural Convection Flow," *J. Fluid Mech.*, Vol. 66, 1974, p. 309.

Authors' Closure

The authors agree that the constant wall temperature boundary condition is probably more common practically than constant heat flux; however, in the turbulent range to which the present work is directed, the constant temperature and constant heat flux conditions are basically the same, since the heat transfer coefficient is essentially independent of length. In mass transfer applications the boundary condition is, of course, constant concentration, which has an analogy to the constant temperature heat transfer problem.

As to the use of the word transition, no boundary layer measurements were made to observe the onset of instability. The range of "transition" data in Fig. 3 refers to that as inferred from local surface temperature behavior and, therefore, is probably above the onset of instability; however, from a practical viewpoint the effect on heat transfer is important and it is felt that the information in Fig. 3 is of value.

The authors have attempted to obtain support to extend this work to detailed measurements of the turbulent natural convection boundary layer but to no avail.

N. Seki
Professor.

S. Fukusako
Asst. Professor.

M. Nakaoka
Graduate Student.

Department of Mechanical Engineering,
Hokkaido University,
Sapporo, Japan

Experimental Study on Natural Convection Heat Transfer With Density Inversion of Water Between Two Horizontal Concentric Cylinders

An experimental investigation concerning the effect of density inversion on steady natural convection heat transfer of water between two horizontal concentric cylinders with diameter ratio ranging from 1.18 to 6.39 is carried out. Water, as a testing fluid, has the maximum density at 4°C. Temperature of the inner cylinder is maintained at 0°C, while temperatures of the outer cylinder are varied from 1 to 15°C, with Grashof number ranging from 3.2×10^1 to 2.7×10^5. Photographs and qualitative description of the flow patterns, temperature profiles, local and average Nusselt number are presented. From the present experimental investigation, it is demonstrated that the effect of density inversion is unexpectedly large and the average Nusselt number is a peculiar function of temperature difference between outer and inner cylinder, unlike the previous results on common fluids without density inversion.

Introduction

Many studies on natural convection heat transfer related to the melting of ice have been performed. Yen [1][1] investigated the problem of the onset of natural convection in a melted layer of ice heated from below. The experimental results on the same subject but heated from above were reported by Yen and Galea [2]. Sun, et al. [3] studied both analytically and experimentally the effect of density inversion on the onset of natural convection and on the melting rate of ice. Recently, Sugawara, et al. [4] presented an experimental investigation concerning the heat transfer phenomena in a melted layer of ice heated from above under various radiant heat fluxes. They reported temperature distributions and melting rates for the cases in which the mode of heat transfer in the layer is either conductive or convective depending on a hydrodynamic instability caused by the density inversion. Watson [5] and Seki, et al. [6] investigated analytically the natural convection heat transfer of water under the influence of density inversion in a confined rectangular vessel. They showed that the average Nusselt number is a function of temperature difference between hot and cold surface temperature of opposing walls and furthermore it has a minimum value at 8°C where two counter standing eddies of approximately the same size coexist in the vessel.

Many experimental and analytical studies on the natural convection heat transfer of common fluids with a monotonic relation between density and temperature have been reported. For example, Liu, et al. [7], using five sets of cylinders, determined flow patterns, temperature profiles, and overall heat transfer relation on air, water, and silicon fluid. Grigull and Hauf [8], using air as a testing fluid, categorized the flow patterns into three regimes and evaluated experimentally the local and the mean Nusselt number on the surface of inner cylinder. And Bishop, et al. [9, 10] also investigated the same problem both experimentally and analytically and reported that one steady and three unsteady flow patterns were observed in their experiments.

The purpose of this study is to evaluate the effect of density inversion on natural convection heat transfer of a melted water contained in two horizontal concentric cylinders whose surface temperatures are kept isothermal. Five inner and two outer cylinders are used to change the diametric ratio and the curvature. Temperature of the inner cylinder T_i is uniformly maintained at 0°C, while that of the outer cylinder T_o can be varied from about 1 to 15°C. Visualized flow patterns, temperature profiles, local Nusselt number Nu_{loc}, and average Nusselt number Nu are also discussed.

[1] Numbers in brackets designate References at end of paper.

Contributed by the Heat Transfer Division for publication in the JOURNAL OF HEAT TRANSFER. Manuscript received by the Heat Transfer Division January 27, 1975. Paper No. 76-HT-G.

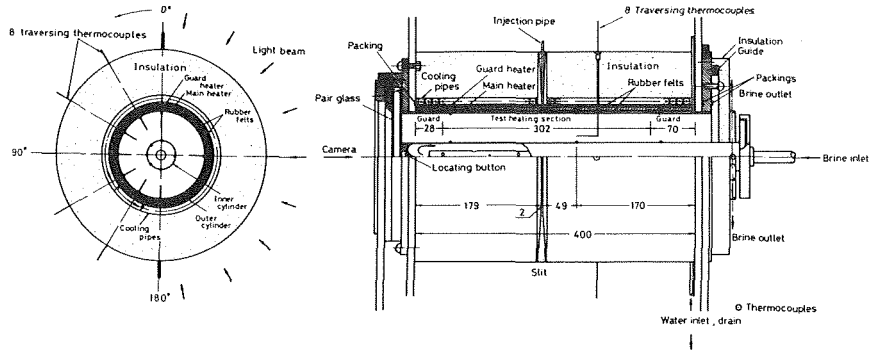

Fig. 1 A schematic diagram of experimental apparatus

Experimental Apparatus and Procedure

A schematic diagram of the experimental apparatus is shown in Fig. 1. Lucite outer cylinders of both 121.5 and 65.5 mm in diameter and 2 mm of thickness are used and values of diametric ratio d_o/d_i ranging from 1.18 to 6.39 are obtained by using the inner cylinders with diameters of 19.0 and 38.0 mm (copper), 55.4, 69.6, and 99.7 mm (lucite). Surface of the test cylinder, except a part of observing slit of the outer cylinder, is finished with a black paint to minimize the reflection of light beam. For observation of the flow patterns, an end wall of the cylinder is installed with a pairglass.

Surface temperature of the inner cylinder is uniformly kept at 0°C by a temperature-controlled coolant delivered into the cylinder. Surface temperature of the outer cylinder is uniformly maintained at a constant temperature by using twelve independent and controllable main heaters respectively prepared by guard heaters outside. Rubber felt of 1.5 mm in thickness is embedded between the main and the guard heaters. As will be shown in Fig. 1, outside of these heaters two vinyl pipes of 10 mm in diameter are equipped to provide a coolant and to avoid the heat flow from the surroundings. Three brass tubes of 2.5 mm in diameter to let tracing particles into the testing fluid are attached on the top of the outer cylinder. Eight thin probes (stainless steel pipe of 0.8 mm in diameter) with Cu-Co thermocouple of 0.1 mm in diameter are arranged at every 30 deg angular intervals from the top of the outer cylinder to measure the temperature distributions in the fluid. Uniformness of the surface temperature of outer cylinder is accomplished by adjusting the input of electric power to each of the heaters.

For visualizing the flow patterns, nine 100 W-projection lamps are arranged concentrically around the outer cylinder. The radiant heat energy of light beam is eliminated by passing through a semicircular water jacket of 20 mm in thickness. The tracing particle is a mix of aluminum powder and distilled water boiled for at least 3 hours. Photographs of flow pattern are taken by 36 mm camera with ASA 100 (DIN 21) film. The time exposure is 60 s. The slit of light beam is packed with an insulating material except the operating period of visualization. A distilled water is used as a testing fluid to minimize undesirable air bubble on the surface boundaries of the inner and the outer cylinders.

Table 1 Range of test variables, using water as testing fluid and $T_i = 0$°C

d_o mm	d_i mm	T_o °C		d_o/d_i	L mm	Gr	
121.5	19.0	1.5	9.5	6.39	51.2	4.1×10^4	2.7×10^5
	38.0	3.0	11.0	3.20	41.7	4.4×10^4	1.7×10^5
	55.4	3.0	8.0	2.19	33.0	2.2×10^4	6.3×10^4
	69.6	3.0	7.4	1.75	25.9	1.1×10^4	2.7×10^4
	99.7	3.0	7.0	1.22	10.9	8.7×10^2	1.9×10^3
65.5	19.0	3.0	15.4	3.44	23.2	8.0×10^3	4.0×10^4
	38.0	3.0	9.5	1.72	17.7	1.7×10^3	5.1×10^3
	55.4	1.0	4.0	1.18	5.0	3.2×10^1	9.0×10^1

In each run, it takes about 8–15 hr to attain a steady state. Under this condition, visualization of flow patterns and measurement of the temperature distributions are performed, while power input is recorded. T_o is varied every 1°C ranging from about 1 to 15°C. Table 1 summarizes the tests performed and the range of experimental parameters covered.

Discussion of the Results

Flow Patterns. Typical flow patterns under several T_o are shown in Figs. 2, 3, 4, 5, and 6 along with schematic drawings. In these experiments, the flow patterns are stable and symmetrical in respect to the vertical axis, and two-dimensional flow is attained.

Fig. 2 shows the flow patterns observed for 4°C and $d_o/d_i = 3.2$. The flow seems to be very stable. The movement of eddy is upward along the inner cylinder but downward along the outer cylinder. In this flow patterns, the fluid near the upper part of the vertical axis flows at a higher speed than that on the other part in the gap. The center of the eddy is clearly observed in the upper part of the annuli, while in the lower part a counter secondary eddy can be seen. However, the intensity of the eddy is so weak that tracing particles do not follow it exactly. But this secondary eddy flow disappears as the gap width L between the inner and the outer cylinder decreases. When L is very small, namely the diameter ratio in the order of 1.18 or 1.22, the flow behaviors are different from the aforementioned ones.

Nomenclature

d_i = inner cylinder diameter
d_o = outer cylinder diameter
d_o/d_i = diametric ratio
g = gravitational acceleration
Gr = Grashof number, $g\,\beta L^3\,(\Delta T)/\nu^2$
h = heat transfer coefficient
k = thermal conductivity
k_e = effective thermal conductivity, defined in equation (3)
L = gap width, $(d_o - d_i)/2$
Nu = average Nusselt number for inner cylinder, defined in equation (2)
$\mathrm{Nu}_{\mathrm{loc}}$ = local Nusselt number, defined in equation (1)
Pr = Prandtl number
Q_t = total heat transfer rate, per unit length
q = local heat flux
R = dimensionless radius, $(r - r_i)/(r_o - r_i)$
r = radius
T = temperature
ΔT = temperature difference, $T_o - T_i$ (= T_o)
β = coefficient of thermal expansion (absolute value)
θ = dimensionless temperature, $(T - T_i)/(T_o - T_i)$
ν = kinematic viscosity

Subscript

i = refers to inner cylinder
o = refers to outer cylinder

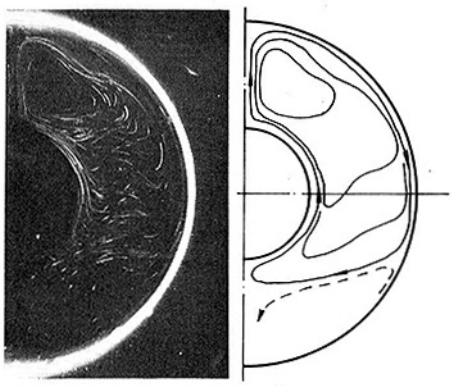

Fig. 2 A photograph and a schematic view of flow pattern, d_o = 121.5 mm, d_i = 38.0 mm, and T_o = 4°C

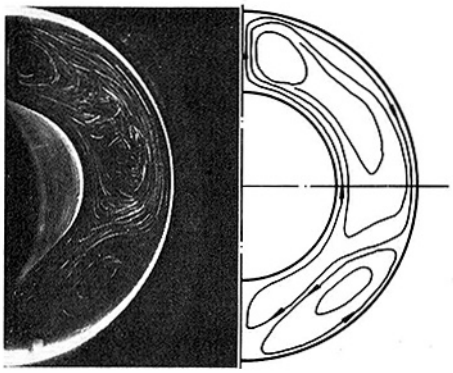

Fig. 3 A photograph and a schematic view of flow pattern, d_o = 121.5 mm, d_i = 55.4, mm and T_o = 5°C

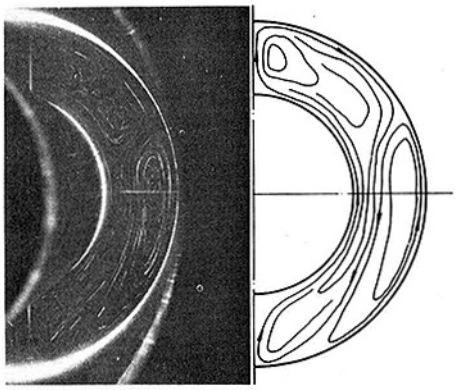

Fig. 4 A photograph and a schematic view of flow pattern, d_o = 121.5 mm, d_i = 69.6 mm, and T_o = 6°C

The flow patterns obtained for T_o = 5°C and d_o/d_i = 2.19 are almost similar to those for 4°C; however, the counter secondary eddy in the lower part can be seen more clearly, as shown in Fig. 3. The appearance of counter secondary eddy may be due to the effect of density inversion at 4°C. When T_o ranges from 6 to 7°C, the influence of density inversion becomes more evident. That is, the eddy in the lower part of the annuli becomes large and finally two counter eddies of almost equal strength exist in the gap (see Fig. 4). For L = 25.9 mm (d_o/d_i = 1.75), T_o = 6°C, aforementioned secondary eddy occurs in the upper part of the gap, as can be seen in Fig. 4. For the combinations of d_o/d_i with L ranging from 17.7 to 51.2 mm, such flow patterns as shown in Fig. 4 are always observed.

As can be seen from Fig. 5, in the case of higher T_o (= 8°C), the eddy flowing upward along the outer cylinder gradually extends its size, while another one flowing upward along the inner cylinder is getting smaller and finally disappears as T_o increases. Flow patterns for L = 10.9 mm (d_o/d_i = 1.22), T_o = 4°C are considerably different from the aforementioned ones, as shown in Fig. 6. A very small eddy which flows downward along the vertical axis is observed in the vicinity of the top of annuli for all T_o. This is believed due to the effects of L and cylinder curvature.

Temperature Distributions and Local Nusselt Numbers. Distributions of temperature T versus radial position r are obtained for all values of ΔT (= T_o) and also at selected angular positions for every aspect ratio d_o/d_i covered in this study.

It is well known that the temperature profiles of the fluid without density inversion in either annuli or concentric sphere have consistently a general trend except the case of extremely small L. In case of the concentric sphere, Bishop, et al. [11] reported that the temperature profiles had a similar feature and they might be conveniently defined by five distinct regions. It should therefore be noted that the dimensionless temperature profile at each selected angular position is similar and independent of both ΔT and a common test fluid.

The typical dimensionless temperature θ as a function of dimensionless radius R is shown in Figs. 7(a)–9(a). The corresponding local Nusselt numbers based on inner and outer cylinder are shown in Figs. 7(b)–9(b). The local Nusselt number in this study is defined as

$$\mathrm{Nu_{loc}} = \frac{q\,L}{\Delta T k} \tag{1}$$

where q is a local heat flux. The local heat flux for the outer cylinder is evaluated by electric input to each main heater. On the other hand, the local heat flux for the inner cylinder is obtained by mea-

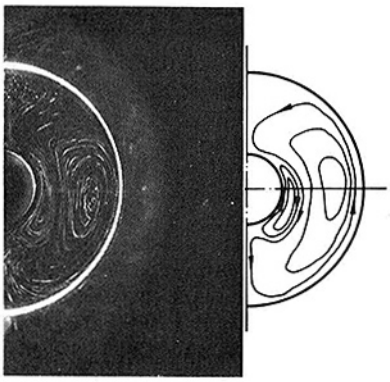

Fig. 5 A photograph and a schematic view of flow pattern, d_o = 65.5 mm, d_i = 19.0 mm, and T_o = 8°C

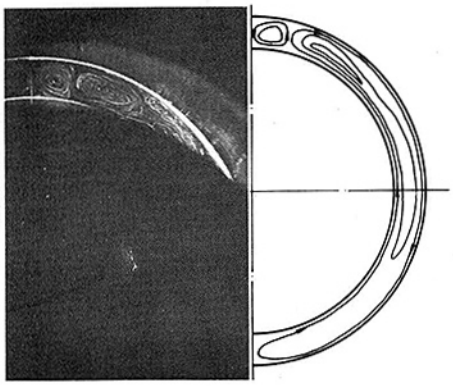

Fig. 6 A photograph and a schematic view of flow pattern, d_o = 121.5 mm, d_i = 99.7 mm, and T_o = 4°C

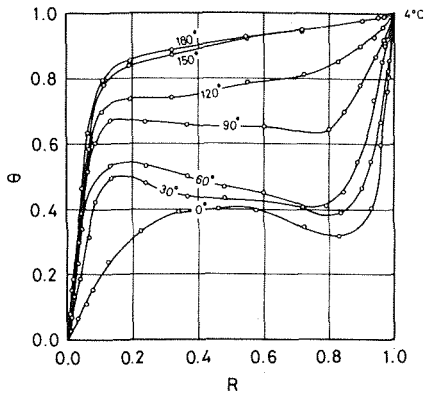

Fig. 7(*a*) Temperature profiles, $d_o/d_i = 3.20$ and $T_o = 4°C$

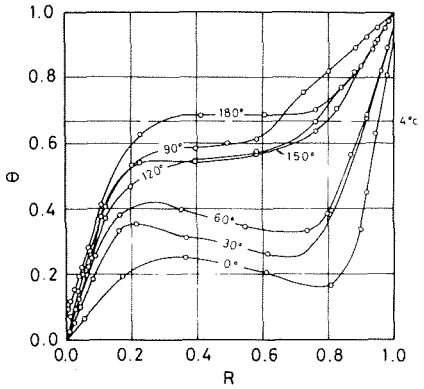

Fig. 8(*a*) Temperature profiles, $d_o/d_i = 1.75$ and $T_o = 6°C$

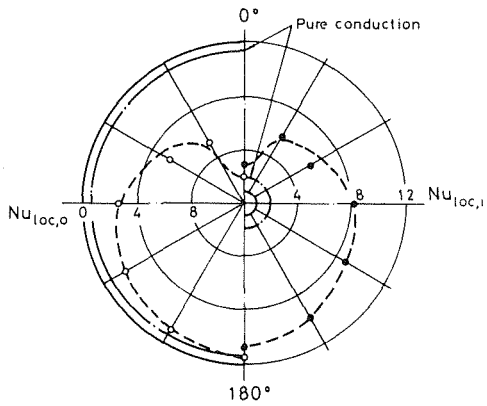

Fig. 7(*b*) Local Nusselt numbers of the inner and the outer cylinders, $d_o/d_i = 3.20$ and $T_o = 4°C$

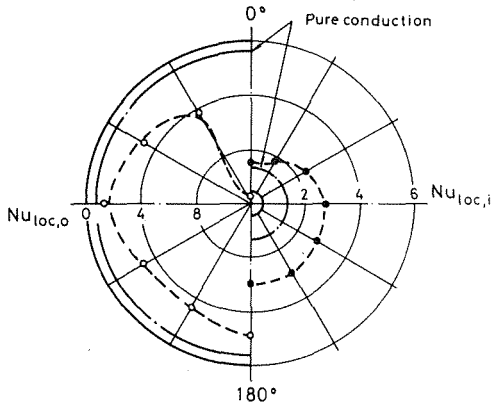

Fig. 8(*b*) Local Nusselt numbers of the inner and the outer cylinders, $d_o/d_i = 1.75$ and $T_o = 6°C$

suring a temperature gradient adjacent to the surface. In these figures, angular position is measured from the upper vertical axis and the broken lines in each temperature profile indicate the 4°C isotherm. It should be pointed out that these temperature profiles, in general, are distinctly different from the ones for common fluid, which are independent of ΔT.

Fig. 7(a) shows θ versus R in the annuli with $T_o = 4°C$. In this figure, it is understood that the region with a precipitous temperature drop is related to the high heat convection rates through the thin boundary layer near the cylinder. Magnitude of the precipitous drop near the outer cylinder decreases as the angular position increases from 0°C, but the trend is reversed near the inner cylinder. Temperature inversion is observed at every angular position ranging from 0 to 90 deg. Such a temperature inversion may imply a possibility of high heat transport by angular convection flow rather than radial one. It is also evident that magnitude of the temperature inversion increases with decreasing angular position. As will be seen in Fig. 2, little convective flow occurs in the region ranging from 160 to 180 deg.

Fig. 7(b) shows that the local Nusselt number for $T_o = 4°C$ reaches the minimum value at 0 deg of angular position on the inner cylinder and 180 deg on the outer cylinder. This characteristic feature may correspond to the aforementioned behavior of the temperature profiles as illustrated in Fig. 7(a).

Fig. 8(a) shows the result for $T_o = 6°C$ where two standing eddies of almost same size coexist. As will be estimated from the flow pattern in Fig. 4, it should be noted that the temperature near the boundary between two standing eddies sharply drops at angular positions between 90 and 150 deg as shown in Fig. 8(a) and the temperature near the outer cylinder at 180 deg where the cooled water comes down is lower than that at 90 deg. Furthermore, the temperature gradient in the vicinity of the separation region becomes relatively small. Thus, the local Nusselt number for the outer cylinder near the separation region becomes minimum value, while for the inner cylinder the local Nusselt number increases with increasing angular position as shown in Fig. 8(b).

Fig. 9(a) shows θ versus R for $T_o = 8°C$ corresponding to the flow pattern as shown in Fig. 5. The temperature at 0 deg angular position is the highest one in the gap and it decreases as the angular position increases. But it can be seen that the behavior of the temperature profiles at 90, 120, and 150 deg is a little different from those at other positions. This could be understood from the fact that these results are obtained when the measurement is made across the boundary between two eddies shown in Fig. 5. And in the vicinity of the angular positions between 0 and 30 deg, temperature is higher than the others. This implies that there is such a stagnant region where the conduction heat transfer is dominant rather than the convection one especially in the vicinity of the outer cylinder surface. Thus, as might be expected, local Nusselt number for the outer cylinder decreases as the angular position decreases and reaches a minimum value at 0 deg as shown in Fig. 9(b). But the local Nusselt number for the inner cylinder gradually decreases as the angular position increases from 90 to 180 deg, while between 90 and 0 deg it increases significantly and reaches a maximum at 0 deg. This seems to be resulted from the fact that near the top of the inner cylinder the fluid heated by the outer cylinder comes down directly near the top of the inner cylinder (see Fig. 5).

For $T_o = 12°C$ temperature profiles are inversion of those shown in Fig. 7(a) and local Nusselt number has an opposite tendency to that shown in Fig. 7(b).

Average Nusselt Number. The average Nusselt number Nu

for the inner cylinder is defined as,

$$\mathrm{Nu} = \frac{Q_t}{\pi d_i \Delta T k} \frac{L}{k} \tag{2}$$

where Q_t is the total heat transfer rate which is evaluated by summing up the heat flows of all the separated main heaters. Moreover, a convenient representation in terms of an effective thermal conductivity k_e is defined as,

$$k_e/k = \frac{Q_t \ln (d_o/d_i)}{2\pi k \Delta T} \tag{3}$$

where k_e/k represents the ratio of actual convection heat transfer rate to pure conductive heat transfer rate.

Liu, et al. [7] summarized their experimental results on common fluids as air, water, and silicon fluid and presented a correlation in terms of k_e/k and $\mathrm{Pr}^2\,\mathrm{Gr}/(1.36 + \mathrm{Pr})$. In their experimental study T_i is higher than T_o and the effect of density inversion on the heat transfer is not discussed. The present experimental results are shown in Fig. 10 along with the correlations by Liu, et al. [7] and Kraussold [12]. The present data agree fairly well with those of previous investigators in temperature ranges without the effect of density inversion, that is, $T_o \lesssim 4°\mathrm{C}$ and $T_o \gtrsim 9°\mathrm{C}$. However, the present results ranging approximately from $T_o = 4$ to 9°C shows a different tendency from the others. This appears to be caused by the existence of two eddies which are resulted from the density inversion of water in the gap. Especially in such a case that the size of these eddies is nearly the same ($6°\mathrm{C} \lesssim T_o \lesssim 7°\mathrm{C}$), it may be expected that Nu takes a minimum value.

The analytical studies reported by Watson [5] and Seki, et al. [6]

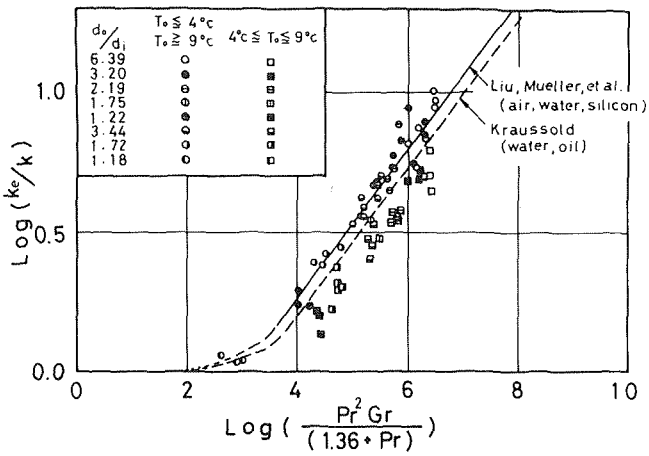

Fig. 10 Comparison of test data by previous investigators

on the natural convection heat transfer under the influence of density inversion in a rectangular confined vessel suggested that a minimum of the average Nusselt number was obtained at 8°C of the temperature difference. This discrepancy must be due to the fact that the heating area of the outer cylinder is larger than the cooling area of the inner cylinder in the present study. Furthermore, this is clearly indicated in Fig. 11 which shows the relation between Nu and ΔT ($= T_o$). In this figure, it is evident that Nu does not increase monotonously with increasing ΔT as on common fluid. That is, when a single large eddy occupies the major portion of the gap as in the case of $T_o \lesssim 4°\mathrm{C}$ or $T_o \gtrsim 9°\mathrm{C}$, Nu increases monotonously as T_o becomes higher. But, a peak of the average Nusselt number can be recognized at about $t_o = 4°\mathrm{C}$ and the minimum value appears between about 6 and 7°C. It should also be understood in Fig. 11 that the magnitude of average Nusselt numbers increases in general as the gap width L increases.

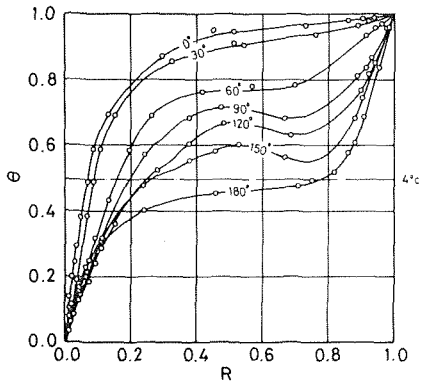

Fig. 9(a) Temperature profiles, $d_o/d_i = 3.44$ and $T_o = 8°\mathrm{C}$

Conclusion

From the aforementioned results, it can be concluded that the flow patterns of the water in the gap are variously changed on account of the density inversion, that is, the density inversion has an important effect on natural convection heat transfer in the annular gap. Especially in the case when two counter eddies of approximately same size coexist in the gap, the average Nusselt number

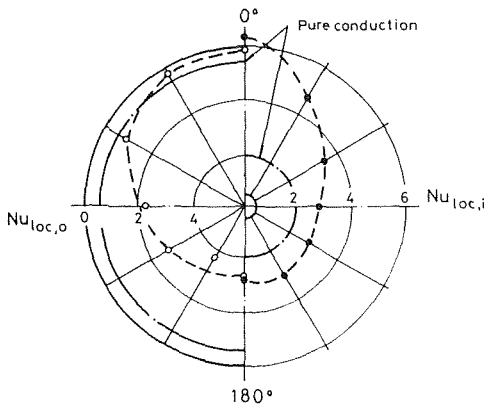

Fig. 9(b) Local Nusselt numbers of the inner and the outer cylinders, $d_o/d_i = 3.44$ and $T_o = 8°\mathrm{C}$

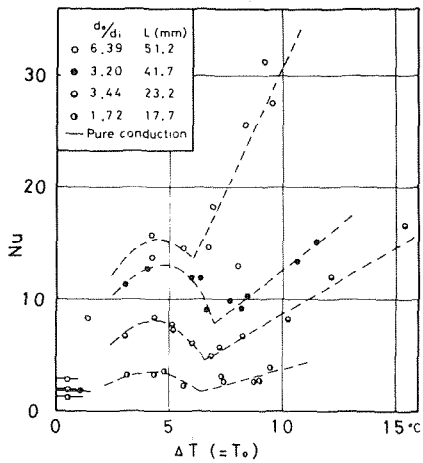

Fig. 11 Correlation of average Nusselt numbers and temperature differences

indicates a minimum value and the minimum Nu increases as the gap width increases.

The effect of the curvature of the outer cylinder on the flow patterns is observed only in small gap widths ($L \leq 10.9$ mm) in this study.

Acknowledgments

The authors are grateful to Prof. M. Arie, Hokkaido University, for a discussion of this subject and his encouragement, and to Mr. K. Sawada for his assistance in the process of producing the experimental apparatus.

References

1 Yen, Y. C., "Onset of Convection in a Layer of Water Formed by Melting Ice from Below," *The Physics of Fluids,* Vol. 11, 1968, pp. 1263–1270.

2 Yen, Y. C., and Galea, F., "Onset of Convection in a Water Layer Formed Continuously by Melting Ice," *The Physics of Fluids,* Vol. 12, 1969, pp. 509–516.

3 Sun, Z. S., Tien, C., and Yen, Y. C., "Thermal Instability of a Horizontal Layer of Liquid With Maximum Density," *AIChE Journal,* Vol. 15, 1969, pp. 910–915.

4 Sugawara, M., Fukusako, S., and Seki, N., "Experimental Studies on the Melting of a Horizontal Ice Layer," *Trans. JSME,* Vol. 40, 1974, pp. 3155–3165.

5 Watson, A., "The Effect of the Inversion Temperature on the Convection of Water in an Enclosed Rectangular Cavity," *Quarterly Journal of Mechanics and Applied Mathematics,* Vol. 15, 1972, pp. 423–446.

6 Seki, N., Fukusako, S., and Sugawara, M., "Natural Convection Heat Transfer With Density Inversion of Water by Vertical Opposite Walls in a Closed Rectangular Vessel," Preprint of JSME—Meeting of Heat Engineering, Paper No. 740-17, 1974, pp. 87–90.

7 Liu, C., Mueller, W. K., and Landis, F., "Natural Convection Heat Transfer in Long Horizontal Cylindrical Annuli," *International Developments in Heat Transfer,* Paper No. 117, Part 5, 1961, pp. 976–984.

8 Grigull, C., and Hauf, W., "Natural Convection in Horizontal Cylindrical Annuli," *Proceedings of the Third International Heat Transfer Conference,* Paper No. 60, Vol. 2, 1966, pp. 182–195.

9 Powe, R. E., Carley, C. T., and Bishop, E. H., "Free Convective Flow Patterns in Cylindrical Annuli," JOURNAL OF HEAT TRANSFER, TRANS. ASME, Series C, Vol. 91, 1969, pp. 310–314.

10 Mack, L. R., and Bishop, E. H., "Natural Convection Between Horizontal Concentric Cylinder for Low Rayleigh Numbers," *Quarterly Journal of Mechanics and Applied Mathematics,* Vol. 21, Part 2, 1968, pp. 223–241.

11 Scanlan, J. A., Bishop, E. H., and Powe, R. E., "Natural Convection Heat Transfer Between Concentric Spheres," *International Journal of Heat and Mass Transfer,* Vol. 13, 1970, pp. 1857–1872.

12 Kraussold, H., "Wärmeabgabe von Zylindrishen Flüssigkeitsshichten bei Natürlicher Konvektion," *Forsch. a. d. Geb d. Ingenieurswesen,* Vol. 5, Series 4, 1934, pp. 186–188.

T. C. Chawla
G. Leaf
W. L. Chen
M. A. Grolmes

Argonne National Laboratory,
Argonne, Ill.

The Application of the Collocation Method Using Hermite Cubic Splines to Nonlinear Transient One-Dimensional Heat Conduction Problems

A collocation method for the solution of one-dimensional parabolic partial differential equations using Hermite splines as approximating functions and Gaussian quadrature points as collocation points is described. The method consists of expanding dependent variables in terms of piece-wise cubic Hermite splines in the space variable at each time step. The unknown coefficients in the expansion are obtained at every time step by requiring that the resultant differential equation be satisfied at a number of points (in particular at the Gaussian quadrature points) in the field equal to the number of unknown coefficients. This collocation procedure reduces the partial differential equation to a system of ordinary differential equations which is solved as an initial value problem using the steady-state solution as the initial condition. The method thus developed is applied to a two-region nonlinear transient heat conduction problem and compared with a finite-difference method. It is demonstrated that because of high-order accuracy only a small number of equations are needed to produce desirable accuracy. The method has the desirable characteristic of an analytical method in that it produces point values as against nodal values in the finite-difference scheme.

Introduction

Various numerical methods have been devised for solutions to the problems of transient nonlinear heat conduction. The most common of these are finite-difference methods and finite-element methods using Galerkin or weighted residual procedures. Finite difference methods are usually of low order and therefore require the solution of large systems of equations in order to achieve a satisfactory truncation error. A large system of equations implies large storage requirements and consequently time differencing must be done with single time step methods whether explicit or implicit. In an explicit method, due to stability conditions, the largest time step that can be taken is limited. On the other hand, an implicit method will allow larger time steps, but only at a higher cost per time step. In either case, substantial machine times are encountered in solving such large systems of equations.

In contrast to low-order finite difference methods, finite-element methods based on the use of a Galerkin or a weighted residual procedure can achieve high-order accuracy thereby substantially reducing the size of the numerical system. Hence, the data handling requirements are less severe and multistep time-differencing methods can be used in order to increase the size of the time steps. On the other hand, for nonlinear problems, these methods require the computation of integrals at each time step. This in turn implies considerably more arithmetic at each time step when compared to low-order finite-difference methods. Thus, in spite of their greater accuracy, these higher-order Galerkin procedures when applied to nonlinear conduction problems may not be substantially faster than finite-difference methods.

A third method is based on collocation combined with the use of suitable approximating subspaces. For nonlinear problems, this approach has an advantage over Galerkin type procedure in that there is much less arithmetic at each time step. On the other hand, it has the disadvantage, that unless the collocation points are suitably chosen, this method produces low-order accuracy regardless of the nature of the approximating subspaces. This implies large systems of equations in order to obtain suitable accuracy, just as in the case of low-order finite-difference methods. However, as shown

Contributed by the Heat Transfer Division for publication in the JOURNAL OF HEAT TRANSFER. Manuscript received by the Heat Transfer Division April 30, 1975. Paper No. 76-HT-B.

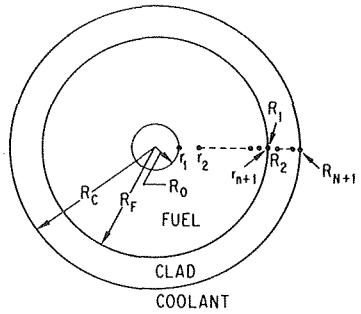

Fig. 1 Cross-sectional view of a fuel pin showing the knot sequences

in references [1–4],[1] the use of orthogonal collocation points such as the Gaussian quadrature points can provide as much accuracy as a Galerkin procedure. Hence, in this case, the advantages of a high-order Galerkin-type procedure are achieved, namely a small system of equations and the use of multistep time differencing. In addition, like finite-difference methods, it requires only a small amount of arithmetic at each time step. In this paper, we demonstrate an application of this method to the nonlinear heat conduction equation where nonlinearity is introduced by requiring the transport properties to be a function of temperature.

Description of the Problem

For this application, consider a single fuel pin for a nuclear reactor. This pin consists of a hollow cylindrical solid of mixed oxide fuel encased in a cylindrical sheath of stainless steel cladding. There is a finite contact resistance between the fuel and the clad, and the outer surface of the clad is cooled by convection. The fuel is headed by a uniform volume heat source which can vary with time. A schematic cross-sectional view of such a system is shown in Fig. 1. The figure contains dimensional nomenclature. If the volume heat source in the fuel is denoted by $\dot{q}(t)$ and if axial and circumferential conduction terms are neglected, then the heat conduction equation can be written in cylindrical coordinates as

$$\rho(T)\,C_P(T)\,\frac{\partial T}{\partial t} = \frac{1}{r}\,\frac{\partial}{\partial r}\left(rK(T)\,\frac{\partial T}{\partial r}\right) + \dot{q}(t) \tag{1}$$

When the foregoing equation is applied to the clad, the heat source term is set equal to zero. The boundary conditions which must be satisfied are:

$$\frac{\partial T_F}{\partial r} = 0 \text{ at } r = R_0 \tag{2a}$$

$$-K_F\,\frac{\partial T_F}{\partial r} = h_g[T_F(R_F^-,t) - T_C(R_F^+,t)], \text{ at } r = R_F \tag{2b}$$

$$K_F\,\frac{\partial T_F}{\partial r} = K_C\,\frac{\partial T_C}{\partial r} \text{ at } r = R_F \tag{2c}$$

$$-K_C\,\frac{\partial T_C}{\partial r} = h(t)\,[T_C(R_C,t) - T_{Na}(t)] \tag{2d}$$

Here, $T_F = T_F(r, t)$ refers to the temperature distribution in the fuel while $T_C = T_C(r, t)$ refers to the temperature distribution in the clad. The temperature of the external medium (sodium) surrounding the clad is denoted by $T_{Na}(t)$. The definition of the other symbols used is given in the Nomenclature.

The foregoing equations can be simplified somewhat by application of Kirchoff's transformation

$$\theta = \frac{1}{K_0}\int_{T_0}^{T} K(T)dT \tag{3}$$

Upon the introduction of the variable θ into equations (1) and (2), we obtain:

$$\frac{\partial\theta}{\partial t} = \alpha\left(\frac{\partial^2\theta}{\partial r^2} + \frac{1}{r}\,\frac{\partial\theta}{\partial r}\right) + \frac{\alpha\dot{q}}{K_0} \tag{4}$$

$$\frac{\partial\theta_F}{\partial r} = 0 \text{ at } r = R_o \tag{5a}$$

$$-K_{0F}\,\frac{\partial\theta_F}{\partial r} = h_g[T_F(\theta_F(R_F^-,t) - T_C(\theta_C(R_F^+,t)], \text{ at } r = R_F \tag{5b}$$

$$K_{0F}\,\frac{\partial\theta_F}{\partial r} = K_{0C}\,\frac{\partial\theta_C}{\partial r} \text{ at } r = R_F \tag{5c}$$

$$-K_{0C}\,\frac{\partial\theta_C}{\partial r} = h(t)\,[T_C(\theta_C(R_C,t)) - T_{Na}(t)] \tag{5d}$$

Here the diffusivity $\alpha = K(T)/\rho(T)C_P(T)$ must be evaluated by means of the transformation $T = T(\theta)$ which is the inverse of the transformation given in equation (3).

A Method of Collocation

We shall seek an approximate solution of equations (4) and (5) using the method of lines in conjunction with collocation. To this end, we assume that at each fixed time, the transformed temperature $\theta(r, t)$ can be approximated by a function which is a piecewise cubic polynominal in r and the function together with its first derivative is continuous. More specifically, let $[a, b]$ denote either the fuel region $[R_0, R_F]$ or the clad region $[R_F, R_C]$. Let this interval be subdivided by the set of points

$$\pi\colon a = x_1 < x_2 < \ldots < x_{n+1} = b,\ h_j = x_j - x_{j-1}$$

Relative to this partition π, the approximating subspace $H_3(\pi)$ will consist of all functions $f(x)$ such that:

[1] Numbers in brackets designate References at end of paper.

Nomenclature

A = coefficient matrix
a = inner boundary
b = outer boundary
$C_{i,k}$ = defined by equations (20)
C_P = specific heat
$F_{i,k}$ = defined by equations (18)
h = coolant heat transfer coefficient
h_g = gap heat transfer coefficient
h_j = step length in general and in fuel region
H_j = step length in clad region
$K(T)$ = thermal conductivity
K_0 = thermal conductivity at reference temperature T_0
N = number of intervals in clad region
n = number of intervals in fuel region
$\dot{q}$ = rate of power generation per unit-volume in fuel pin
r = radial coordinate
r_j = knot points in fuel
R_C = external radius of clad
R_F = external radius of fuel
R_j = knot points in clad
R_o = internal radius of fuel
T = temperature
T_{Na} = coolant temperature
t = time
x_j = knot points in general
$S_j(x)$ = basis function defined by equation (6b)
$V_j(x)$ = basis function defined by equation (6a)
α = thermal diffusivity
β, γ = constants defined by equations (15a)
δ_{ij} = Kronecker delta function
$\eta_{i,k}$ = collocation points in general and also in fuel region
θ = Kirchoff's transformed temperature defined by equation (3)
$\xi_{i,k}$ = collocation points in clad region
π_C = mesh for the clad region
π_F = mesh for the fuel region
ρ = density
$\Phi_j(r) = V_j''(r) + 1/rV_j'(r)$
$\psi_j(r) = S_j''(r) + 1/rS_j'(r)$

Subscripts

C = clad region
F = fuel region
i, j, k = indices

1 $f(x)$ is equal to a cubic polynomial in each subinterval $[x_i, x_{i+1}]$ for $1 \le i \le n$;
2 $f(x)$ and $f'(x)$ are continuous at the points x_i for $2 \le i \le n$; and
3 $f(x)$ satisfies the appropriate boundary conditions in equations (5) depending on whether the interval $[a, b]$ is the fuel or the clad.

Since this problem has two regions, we will generate two approximating sets of functions $H_3^{(F)}(\pi_F)$ and $H_3^{(C)}(\pi_C)$, one relative to a partition π_F of the fuel, the other relative to a partition π_C of the clad. These two sets of functions are required to satisfy the common interface conditions (5b) and (5c).

A convenient basis for generating either set of approximating functions is the set $\{V_j(x), S_j(x)\}_{j=1}^{n+1}$, where

$$V_j(x) = \begin{cases} (1 + \frac{x - x_j}{h_j})^2 [1 - 2(\frac{x - x_j}{h_j})] \text{ for } x_{j-1} \le x \le x_j \\ (1 - \frac{x - x_j}{h_{j+1}})^2 [1 + 2(\frac{x - x_j}{h_{j+1}})] \text{ for } x_j \le x \le x_{j+1} \\ 0 \text{ elsewhere} \end{cases} \quad (6a)$$

$$S_j(x) = \begin{cases} h_j(\frac{x - x_j}{h_j})[1 + \frac{x - x_j}{h_j}]^2 \text{ for } x_{j-1} \le x \le x_j \\ h_{j+1}(\frac{x - x_j}{h_{j+1}})(1 - \frac{x - x_j}{h_{j+1}})^2 \text{ for } x_j \le x \le x_{j+1} \\ 0 \text{ elsewhere} \end{cases} \quad (6b)$$

It is assumed that $V_1(x)$, $S_1(x)$ vanish to the left of x_1 and $V_{n+1}(x)$, $S_{n+1}(x)$ vanish to the right of x_{n+1}. From the defining equations, we observe that each of the functions has the following properties:

1 Each $V_j(x)$ and $S_j(x)$ is continuous together with its first derivative on the interval $[a, b]$.
2 Each $V_j(x)$ and $S_j(x)$ is a cubic polynomial in each subinterval and they vanish outside the subinterval $[x_{j-1}, x_{j+1}]$.

[3] $$\left.\begin{aligned} V_i(x_j) = \delta_{ij},\ V_i'(x_j) \equiv 0 \\ S_i(x_j) \equiv 0,\ S_i'(x_j) = \delta_{ij} \end{aligned}\right\} 1 \le i,j \le n+1$$

The set $\{V_i(x), S_i(x)\}_{i=1}^{n+1}$ will form a basis for the set of functions $H_3(\pi)$. Thus we assume that the transformed temperature field has the following form

$$\theta(x,t) = \sum_{j=1}^{n+1} [\theta(x_j,t) V_j(x) + \theta'(x_j,t) S_j(x)] \quad (7)$$

where $\{\theta(x_j,t), \theta'(x_j,t)\}_{j=1}^{n+1}$ are the unknown coefficients and in view of property (3), these coefficients represent, respectively, the unknown temperature and spatial derivative of temperature at each of the knot points $(x_j,\ 1 \le j \le n+1)$.

Let

$$\pi_F\colon R_o = r_1 < r_2 < \ldots < r_{n+1} = R_F$$

be a partition of the fuel, and

$$\pi_C\colon R_F = R_1 < R_2 < \ldots < R_{N+1} = R_C$$

be a partition of the clad. We seek an approximation to the temperature field $\theta(r, t)$ of the form shown in equation (7) in the fuel and the clad. Substituting equation (7) into equations (4) and (5), we obtain the following relation in the fuel

$$\frac{\partial \theta_F}{\partial t} = \sum_{j=1}^{n+1} [V_j(r) \dot{\theta}_F(r_j,t) + S_j(r) \dot{\theta}_F'(r_j,t)]$$
$$= \alpha_f(\theta_F(r,t)) \{\sum_{j=1}^{n+1} [\theta_F(r_j,t) \phi_j(r) + \theta_F'(r_j,t) \psi_j(r)]\}$$
$$+ \alpha_F(\theta_F(r,t)) \dot{q}(t)/K_{0F} \text{ for } r_1 \le r \le r_{n+1} \quad (8)$$

where

$$\phi_j(r) = V_j''(r) + \frac{1}{r} V_j'(r),\ \psi_j(r) = S_j''(r) + \frac{1}{r} S_j'(r)$$

Now

$$\frac{\partial \theta}{\partial r} = \sum_{j=1}^{n+1} [V_j'(r) \theta_F(r_j,t) + S'_j(r) \theta_F'(r_j,t)]$$

Since $V_j(r_1) \equiv 0$, $S_1'(r_1) = 1$, and $S_j'(r_1) \equiv 0$ for $j > 1$, we find that the boundary condition (5a) implies

$$\theta_F'(r_1,t) \equiv 0 \quad (9a)$$

Differentiating this expression with respect to time, we find also

$$\dot{\theta}_F'(r_1,t) \equiv 0 \quad (9b)$$

Similarly, we find the following relations at $r = r_{n+1}$ from the boundary condition (5b).

$$\theta_F'(r_{n+1},t) = -\frac{h_g}{K_{0F}} [T_F(\theta_F(r_{n+1},t) - T_C(\theta_C(R_1,t))] = F_f \quad (9c)$$

$$\dot{\theta}_F'(r_{n+1},t) = -\frac{\dot{h}_g}{K_{0F}} [T_F(\theta_F(r_{n+1},t)) - T_C(\theta_C(R_1,t))]$$
$$- \frac{h_g}{K_{0F}} [\frac{dT_F}{d\theta_F}\Big|_{\theta_F(r_{n+1},t)} \dot{\theta}_F(r_{n+1},t) - \frac{dT_C}{d\theta_C}\Big|_{\theta_C(R_1,t)}$$
$$\times \dot{\theta}_C(R_1,t)] = f_F + A_F \dot{\theta}_F(r_{n+1},t) + A_C \dot{\theta}_C(R_1,t) \quad (9d)$$

For the clad region (see Fig. 1), we find

$$\frac{\partial \theta_C(r,t)}{\partial t} = \sum_{j=1}^{N+1} [V_j(r) \dot{\theta}_C(R_j,t) + S_j(r) \dot{\theta}_C'(R_j,t)]$$
$$= \alpha_C(\theta_C(r,t)) \sum_{j=1}^{N+1} [\theta_C(R_j,t) \phi_j(r)$$
$$+ \theta_C'(R_j,t) \psi_j(r)] \text{ for } R_1 \le r \le R_{N+1} \quad (10)$$

$$\theta_C'(R_1,t) = \frac{K_{0F}}{K_{0C}} \theta_F'(r_{n+1},t) = \frac{K_{0F}}{K_{0C}} F_f \quad (11a)$$

$$\dot{\theta}_C'(R_1,t) = \frac{K_{0F}}{K_{0C}} \dot{\theta}_F'(r_{n+1},t)$$
$$= \frac{K_{0F}}{K_{0C}} [f_F + A_F \dot{\theta}_F(r_{n+1},t) + A_C \dot{\theta}_C(R_1,t)] \quad (11b)$$

$$\theta_C'(R_{N+1},t) = -\frac{h}{K_{0C}} [T_C(\theta_C(R_{N+1},t)) - T_{Na}(t)] = F_C \quad (11c)$$

$$\dot{\theta}_C'(R_{N+1},t) = -\frac{\dot{h}}{K_{0C}} [T_C(\theta_C(R_{N+1},t)) - T_{Na}(t)]$$
$$- \frac{h}{K_{0C}} [\frac{dT_C}{d\theta_C}\Big|_{\theta_C(R_{N+1},t)} \dot{\theta}_C(R_{N+1},t) - \dot{T}_{Na}(t)]$$

or

$$\dot{\theta}_C'(R_{N+1},t) = f_C + B_C \dot{\theta}_C(R_{N+1},t) \quad (11d)$$

Here, in equations (9d) and (11d), we have made the following substitutions

$$f_F = -\frac{\dot{h}_g}{K_{0F}} [T_F(\theta_F(r_{n+1},t)) - T_C(\theta_C(R_1,t))],\ A_F = -\frac{h_g}{K_{0F}} \frac{dT_F}{d\theta_F}\Big|_{\theta_F(r_{n+1},t)}$$

$$A_C = \frac{h_g}{K_{0F}} \frac{dT_C}{d\theta_C}\Big|_{\theta_C(R_1,t)},\ f_C$$
$$= -\frac{\dot{h}}{K_{0C}} [T_C(\theta_C(R_{N+1},t)) - T_{Na}(t)] + \frac{h}{K_{0C}} \dot{T}_{Na}(t)$$

$$B_C = -\frac{h}{K_{0C}} \frac{dT_C}{d\theta_C}\Big|_{\theta_C(R_{N+1},t)}$$

Substituting equations (9) into equation (8), we obtain

$$\sum_{j=2}^{n} (V_j(r)\dot{\theta}_F(r_j,t) + S_j(r)\dot{\theta}_F'(r_j,t)) + V_1(r)\dot{\theta}_F(r_1,t)$$
$$+ [V_{n+1}(r) + S_{n+1}(r)A_F]\dot{\theta}_F(r_{n+1},t) + S_{n+1}(r)A_C\dot{\theta}_C(R_1,t)$$
$$= -S_{n+1}(r)f_F + \frac{\alpha_F(\theta_F(r,t))q(t)}{K_{0F}} + \alpha_F(\theta_F(r,t))$$
$$\times \left(\sum_{j=1}^{n+1} \theta_F(r_j,t)\,\Phi_j(r) + \sum_{j=2}^{n} \theta_F'(r_j,t)\psi_j(r) + F_f\psi_{n+1}(r)\right) \text{ for } r_1 \le r \le r_{n+1} \quad (12)$$

Substituting equations (11*b*), (11*c*), and (11*d*), into equation (10), we obtain

$$\sum_{j=2}^{N} [V_j(r)\dot{\theta}_C(R_j,t) + S_j(r)\dot{\theta}_C'(R_j,t)]$$
$$+ (S_1(r)A_C\frac{K_{0F}}{K_{0C}} + V_1(r))\dot{\theta}_C(R_1,t)$$
$$+ (B_CS_{N+1}(r) + V_{N+1}(r))\dot{\theta}_C(R_{N+1},t) + S_1(r)A_F\frac{K_{0F}}{K_{0C}}\dot{\theta}_F(r_{n+1},t)$$
$$= -f_FS_1(r)\frac{K_{0F}}{K_{0C}} - f_CS_{N+1}(r) + \alpha_C(\theta_C(r,t))$$
$$\times \left(\sum_{j=1}^{N+1} \theta_C(R_j,t)\,\Phi_j(r) + \sum_{j=2}^{N} \theta_C'(R_j,t)\,\psi_j(r)\right.$$
$$\left. + \sum_{j=2}^{N} \theta_C'(R_j,t)\,\psi_j(r) + \psi_1(r)F_f\frac{K_{0F}}{K_{0C}} + \psi_{N+1}(r)F_C\right)$$
$$\text{for } R_1 \le r \le R_{N+1} \quad (13)$$

The unknown coefficients contained in equations (12) and (13) are:

$$\{\theta_F(r_j,t)\}_{j=1}^{n+1},\ \{\theta_F'(r_j,t)\}_{j=2}^{n},\ \{\theta_C(R_j,t)\}_{j=1}^{N+1} \text{ and } \{\theta_C'(R_j,t)\}_{j=2}^{N}$$

which add up to $2n + 2N$ unknowns. In order to obtain $2n + 2N$ equations, we can require that equation (12) be satisfied at $2n$ points in the fuel region and equation (13) be satisfied at $2N$ points in the clad region. Since there are n intervals in the fuel region and N intervals in the clad region, it therefore seems natural to locate two points in each interval. As recommended in references [1–4], the Gauss-Legendre quadrature points of order 2 are chosen as the collocation points in each subinterval $[x_i, x_{i+1}]$. Thus, the collocation points are given by

$$\eta_{i,k} = \frac{1}{2}(x_{i-1} + x_i) + (-1)^k\frac{h_i}{2\sqrt{3}} \quad 2 \le i \le n+1, \quad 1 \le k \le 2 \quad (14)$$

It is demonstrated by Shalev, Baruch, and Nissim [1, 2] that the use of above collocation points yields a residual error for the differential equation which satisfies the "least squares" principle. Consequently, the accuracy from a collocation method can be comparable with that from a least square method.

If we let

$$\beta = \frac{1}{2}(1 - \frac{1}{\sqrt{3}}) \text{ and } \gamma = \frac{1}{2}(1 + \frac{1}{\sqrt{3}}) \quad (15a)$$

in equation (14), we obtain

$$\left.\begin{aligned} \frac{\eta_{j,1} - x_j}{h_j} &= -\beta,\ \frac{\eta_{j,2} - x_i}{h_j} = -\gamma \\ \frac{\eta_{j,1} - x_{j-1}}{h_j} &= \beta,\ \frac{\eta_{j,2} - x_{j-1}}{h_j} = \gamma \end{aligned}\right\} \quad (15b)$$

Using these relations in equations (6) give the following expressions for the values of $V_j(x)$, $S_j(x)$, and their derivatives at the collocation points $\eta_{i,k}$.

$$\left.\begin{aligned} V_{j-1}(\eta_{j,1}) &= V_j(\eta_{j,2}) = (1-\beta)^2(1+2\beta) = V_\beta \\ V_{j-1}(\eta_{j,2}) &= V_j(\eta_{j,1}) = (1-\gamma)^2(1+2\gamma) = V_\gamma \\ S_{j-1}(\eta_{j,1}) &= -S_j(\eta_{j,2}) = h_j\beta(1-\beta)^2 = h_jS_\beta \\ S_{j-1}(\eta_{j,2}) &= -S_j(\eta_{j,1}) = h_j\gamma(1-\gamma)^2 = h_jS_\gamma \end{aligned}\right\} \quad (16a)$$

$$\left.\begin{aligned} V_{j-1}'(\eta_{j,1}) &= -V_j'(\eta_{j,2}) = -6\beta(1-\beta)/h_j = -V_\beta'/h_j \\ V_{j-1}'(\eta_{j,2}) &= -V_j'(\eta_{j,1}) = -6\gamma(1-\gamma)/h_j = -V_\gamma'/h_j \\ S_{j-1}'(\eta_{j,1}) &= S_j'(\eta_{j,2}) = 1 - 4\beta + 3\beta^2 = S_\beta' \\ S_{j-1}'(\eta_{j,2}) &= S_j'(\eta_{j,1}) = 1 - 4\gamma + 3\gamma^2 = S_\gamma' \end{aligned}\right\} \quad (16b)$$

$$\left.\begin{aligned} V_{j-1}''(\eta_{j,1}) &= V_j''(\eta_{j,2}) = -6(1-2\beta)/h_j^2 = -V_\gamma''/h_j^2 \\ V_{j-1}''(\eta_{j,2}) &= V_j''(\eta_{j,1}) = -6(1-2\gamma)/h_j^2 = -V_\gamma''/h_j^2 \\ S_{j-1}''(\eta_{j,1}) &= -S_j''(\eta_{j,2}) = -(4-6\beta)/h_j = -S_\beta''/h_j \\ S_{j-1}''(\eta_{j,2}) &= -S_j''(\eta_{j,1}) = -(4-6\gamma)/h_j = -S_\gamma''/h_j \end{aligned}\right\} \quad (16c)$$

Evaluating equation (12) at the collocation points $\eta_{i,k}$ in the fuel and noting that each $V_j(x)$, $S_j(x)$ has its support in $[x_{j-1}, x_{j+1}]$ and in particular

$$V_1(r) = 0 \text{ for } r \notin [r_1, r_2),\ V_{n+1}(r) = S_{n+1}(r) = 0 \text{ for } r \notin (r_n, r_{n+1}]$$

we obtain the following system of equations:

For $i = 2, k = 1$ (i.e., $\eta_{2,1}$)

$$V_1(\eta_{2,1})\dot{\theta}_F(r_1,t) + V_2(\eta_{2,1})\dot{\theta}_F(r_2,t) + S_2(\eta_{2,1})\dot{\theta}_F'(r_2,t) = F_{2,1} \quad (17a)$$

For $i = 2, k = 2$ (i.e., $\eta_{2,2}$)

$$V_1(\eta_{2,2})\dot{\theta}_F(r_1,t) + V_2(\eta_{2,2})\dot{\theta}_F(r_2,t) + S_2(\eta_{2,2})\dot{\theta}_F'(r_2,t) = F_{2,2} \quad (17b)$$

In general for $3 \le i \le n$, $1 \le k \le 2$,

$$V_{i-1}(\eta_{i,k})\dot{\theta}_F(r_{i-1},t) + V_i(\eta_{i,k})\dot{\theta}_F(r_i,t) + S_{i-1}(\eta_{i,k})\dot{\theta}_F'(r_{i-1},t) + S_i(\eta_{i,k})\dot{\theta}_F'(r_i,t) = F_{i,k} \quad (17c)$$

For $i = n + 1$, $1 \le k \le 2$ (i.e., $\eta_{n+1,k}$)

$$V_n(\eta_{n+1,k})\dot{\theta}_F(r_n,t) + [V_{n+1}(\eta_{n+1,k}) + S_{n+1}(\eta_{n+1,k})A_F]\dot{\theta}_F(r_{n+1},t) + S_n(\eta_{n+1,k})\dot{\theta}_F'(r_n,t) + S_{n+1}(\eta_{n+1,k})A_C\dot{\theta}_C(R_1,t) = F_{n+1,k} \quad (17d)$$

where

$$F_{2,k} = \alpha_F(\theta_F(\eta_{2,k},t))(\theta_F(r_1,t)\,\Phi_1(\eta_{2,k}) + \theta_F(r_2,t)\,\Phi_2(\eta_{2,k}) + \theta_F'(r_2,t)\,\psi_2(\eta_{2,k}) + \dot{q}(t)/K_{0F}) \text{ for } 1 \le k \le 2 \quad (18a)$$

$$F_{i,k} = \alpha_F(\theta_F(\eta_{i,k},t))(\theta_F(r_{i-1},t)\,\Phi_{i-1}(\eta_{i,k}) + \theta_F(r_i,t)\,\Phi_i(\eta_{i,k}) + \theta_F'(r_{i-1},t)\,\psi_{i-1}(\eta_{i,k}) + \theta_F'(r_i,t)\,\psi_i(\eta_{i,k}) + \dot{q}(t)/K_{0F}) \text{ for } 2 \le i \le n,\ 1 \le k \le 2 \quad (18b)$$

$$F_{n+1,k} = -S_{n+1}(\eta_{n+1,k})f_F + \alpha_F(\theta_F(\eta_{n+1,k},t))(F_f\psi_{n+1}(\eta_{n+1,k}) + \theta_F(r_n,t)\,\Phi_n(\eta_{n+1,k}) + \theta_F(r_{n+1},t)\,\Phi_{n+1}(\eta_{n+1,k}) + \theta_F'(r_n,t)\,\psi_n(\eta_{n+1,k}) + \dot{q}(t)/K_{0F}) \quad (18c)$$

It may be noted that since the collocation points do not include the end points, the value of $r_1 = R_0$ can be zero without incurring any singularity in the system.

Similarly, evaluating equation (13) at the collocations points which are denoted by $\xi_{i,k}$ and given by equation (14) for the clad region, we obtain the following system.

$$[S_1(\xi_{2,k})A_C\frac{K_{0F}}{K_{0C}} + V_1(\xi_{2,k})]\dot{\theta}_C(R_1,t) + V_2(\xi_{2,k})\dot{\theta}_C(R_2,t) + S_2(\xi_{2,k})\dot{\theta}_C'(R_2,t) + S_1(\xi_{2,k})A_F\frac{K_{0F}}{K_{0C}}\dot{\theta}_F(r_{n+1},t) = C_{2,k} \quad 1 \le k \le 2 \quad (19a)$$

$$V_{i-1}(\xi_{i,k})\dot{\theta}_C(R_{i-1},t) + V_i(\xi_{i,k})\dot{\theta}_C(R_i\,t) + S_{i-1}(\xi_{i,k})\dot{\theta}_C'(R_{i-1},t) + S_i(\xi_{i,k})\dot{\theta}_C'(R_i,t) = C_{i,k} \text{ for } 2 \le i \le N,\ 1 \le k \le 2 \quad (19b)$$

$$V_N(\xi_{N+1,k})\dot{\theta}_C(R_N,t) + (B_C S_{N+1}(\xi_{N+1,k}) + V_{N+1}(\xi_{N+1,k}))\dot{\theta}_C(R_{N+1},t) + S_N(\xi_{N+1,k})\dot{\theta}_C'(R_N,t) = C_{N+1,k} \text{ for } 1 \le k \le 2 \quad (19c)$$

where

$$C_{2,k} = -S_1(\xi_{2,k}) f_F \frac{K_{0F}}{K_{0C}} + \alpha_C(\theta_C(\xi_{2,k},t))[\theta_C(R_1,t)\,\Phi_1(\xi_{2,k}) + \theta_C(R_2,t)\,\Phi_2(\xi_{2,k}) + \theta_C'(R_2,t)\,\psi_2(\xi_{2,k}) + \psi_1(\xi_{2,k})\,F_f \frac{K_{0F}}{K_{0C}}] \quad 1 \le k \le 2 \quad (20a)$$

$$C_{i,k} = \alpha_C(\theta_C(\xi_{i,k},t))(\theta_C(R_{i-1},t)\,\Phi_{i-1}(\xi_{i,k}) + \theta_C(R_i,t)\,\Phi_i(\xi_{i,k}) + \theta_C'(R_{i-1},t)\,\Psi_{i-1}(\xi_{i,k}) + \theta_C'(R_i,t)\,\Psi_i(\xi_{i,k})) \text{ for } 2 \le i \le N,\ 1 \le k \le 2 \quad (20b)$$

$$C_{N+1,k} = -f_C S_{N+1}(\xi_{N+1,k}) + \alpha_C(\theta_C(\xi_{N+1,k}))(\theta_C(R_N,t)\,\Phi_N(\xi_{N+1,k}) + \theta_C(R_{N+1},t)\,\Phi_{N+1}(\xi_{N+1,k}) + \theta_C'(R_N,t)\,\psi_N(\xi_{N+1,k}) + \psi_{N+1}(\xi_{N+1,k})\,F_C) \text{ for } 1 \le k \le 2 \quad (20c)$$

We note that the transformed temperature $\theta(r, t)$ must be evaluated at the collocation points in order to evaluate the property functions such as the diffusivity α. For this purpose, we use equation (7). For example, in the fuel at the collocation point $\eta_{i,k} \epsilon (x_{i-1}, x_i)$ we have

$$\theta_F(\eta_{i,k},t) = \theta_F(r_{i-1},t)\,V_{i-1}(\eta_{i,k}) + \theta_F(r_i,t)\,V_i(\eta_{i,k}) + \theta_F'(r_{i-1},t)\,S_{i-1}(\eta_{i,k}) + \theta_F'(r_i,t)\,S_i(\eta_{i,k}) \quad (21)$$

Substituting for the values of the basis functions and their derivatives from equations (16) into equations (17) through (21) and rewriting the resulting equations in matrix form, we obtain:

$$[A]\{\dot{U}\} = G(U,t) \quad (22)$$

where $U(t)$ is the $2n + 2N$ dimensional vector

$$\{\theta_F(r_j,t)\}_{j=1}^{n+1} \cup \{\theta_F'(r_j,t)\}_{j=2}^{n} \cup \{\theta_C(R_j,t)\}_{j=1}^{N+1} \cup \{\theta_C'(R_j,t)\}_{j=2}^{N}$$

and $G(U, t)$ is the vector of the entire right-hand side. The details of above matrix equation are shown in Fig. 2. From an examination of Fig. 2, it is clear that the coefficient matrix $[A]$ is a band matrix. This property is a consequence of the basis functions $V_j(x)$ and $S_j(x)$ having local support. It should be noted that in general, the coefficient matrix $[A]$ will depend on the temperature because of the convective interface and boundary conditions. This dependence is explicitly shown in equations (9*d*) and (11*d*). Thus, the matrix $[A]$ has to be inverted at each iteration of every time step. The band structure is utilized in this inversion process.

With given initial values $\{U(0)\}$, the system (22) represents a system of nonlinear ordinary differential equations. This system is solved with the ordinary differential equation subroutine GEAR [5]. This ordinary differential equation routine was selected because of the modest size and the nonlinearity of the system. Thus, when this routine is used the time steps are automatically selected in accordance with the error criterion and the algebraic nonlinear system which arises at each time step is solved efficiently by this routine.

Numerical Results

The method of collocation as described previously was used for the solution of the transient conduction problem for the cylindrical fuel-clad pin configuration shown in Fig. 1. The transport properties of the materials and the dimensions of the pin are given in the Appendix. The transient was initiated by permitting the volumetric heat source in the fuel to increase exponentially with time as specified in the Appendix. The initial temperature distribution was obtained by a steady-state solution of equation (4) with boundary conditions (5) and an initial uniform heat source $\dot{q}(t = 0)$. The effect of step size or the number of knots placed in fuel and clad regions on the accuracy of the solution was investigated. A set of five calculations were made. In the first calculation, 2 knots were used in the fuel and 2 knots in the clad. Since 2 knots correspond to one subinterval, the temperature distribution in this calculation was approximated with one cubic polynomial in the fuel and another cubic polynomial in the clad. The second calculation used 3 knots in the fuel, while the fourth calculation used 4 knots in the fuel with both calculations using 2 knots in the clad. The fourth calculation used 5 knots in the fuel and 3 knots in the clad. The last calculation was made with 20 knots in the fuel and 5 knots in the clad. The positions of knots chosen both in fuel and cladding for the foregoing five examples are nonuniformly distributed. In the choice of these positions, no attempt was made to adjust these positions in order to improve the accuracy. It should be noted that it is not the selection of the knot positions which provides high order accuracy for this collocation procedure, but rather the choice of Gaussian collocation points relative to each subinterval determined by these knots.

For purposes of comparison, the solution to this problem was also approximated by a finite difference type procedure as used in the THTB program [6] which is a general purpose transient heat conduction program. In this method, the spatial interval is subdivided into subintervals (called nodes). For one-dimensional problems, the spatial approximation to the conduction equation is essentially the same as the usual three point approximation to the second derivative and is derived by means of an integral heat balance over each node. The time derivative is approximated by implicit single time step difference procedure. The implicit time differencing leads to a linear system which must be solved at every time step. This system is solved iteratively by means of the point Gauss-Seidel iterative method. With this program, 4 calculations were made. The first calculation used $N_F = 4$ and $N_C = 2$, where N_F denotes the number of nodes in fuel and N_C denotes the number of nodes in clad; the second calculation used $N_F = 6$ and $N_C = 2$; the third calculation was made with $N_F = 35$ and $N_C = 6$; the fourth calculation was made with $N_F = 80$ and $N_C = 15$. The choice of nodal boundaries as used in the foregoing four calculations were nonuniformly distributed. In addition to the effect of spatial mesh size, the effect of the size of the time steps was also investigated. For this purpose three time steps, namely, 0.01, 0.005, and 0.001 s were used with this finite difference program.

In Table 1 we have compared temperature distributions as calculated by the two methods. In this table, the time is 4 s after the initiation of the power transient. The six positions at which the temperature is shown in this table are the node positions corresponding to the case of $N_F = 4$ and $N_C = 2$ for the THTB calculation. In the case of the other three calculations, the subintervals were selected such that the original nodal positions corresponding to the case of $N_F = 4$ and $N_C = 2$ were included among these nodes. Thus, the temperatures for the THTB calculations shown in this table did not have to be interpolated. For the method of collocation, the temperature at these six positions is calculated by means of equation (7) which provides an interpolation procedure entirely consistent with the approximation procedure. We have taken the THTB calculation with $N_F = 80$ and $N_C = 15$ corresponding to time step 0.001 s as the benchmark calculation for this table. The relative percent deviation from this benchmark is shown under the corresponding temperatures in the table. The number of equations solved for each case both with the collocation method and the finite difference method (note that in case of THTB, the number of equations is equal to the total number of nodes) are also shown in this table. From this table, we note that for the same number of equations solved, the method of collocation is substantially more accurate than the finite difference method. In fact, we see that the accuracy obtained with only 12 equations in the collocation method is comparable with the accuracy obtained with 41 equations in the finite difference method corresponding to time step of 0.01 s. This table also shows the corre-

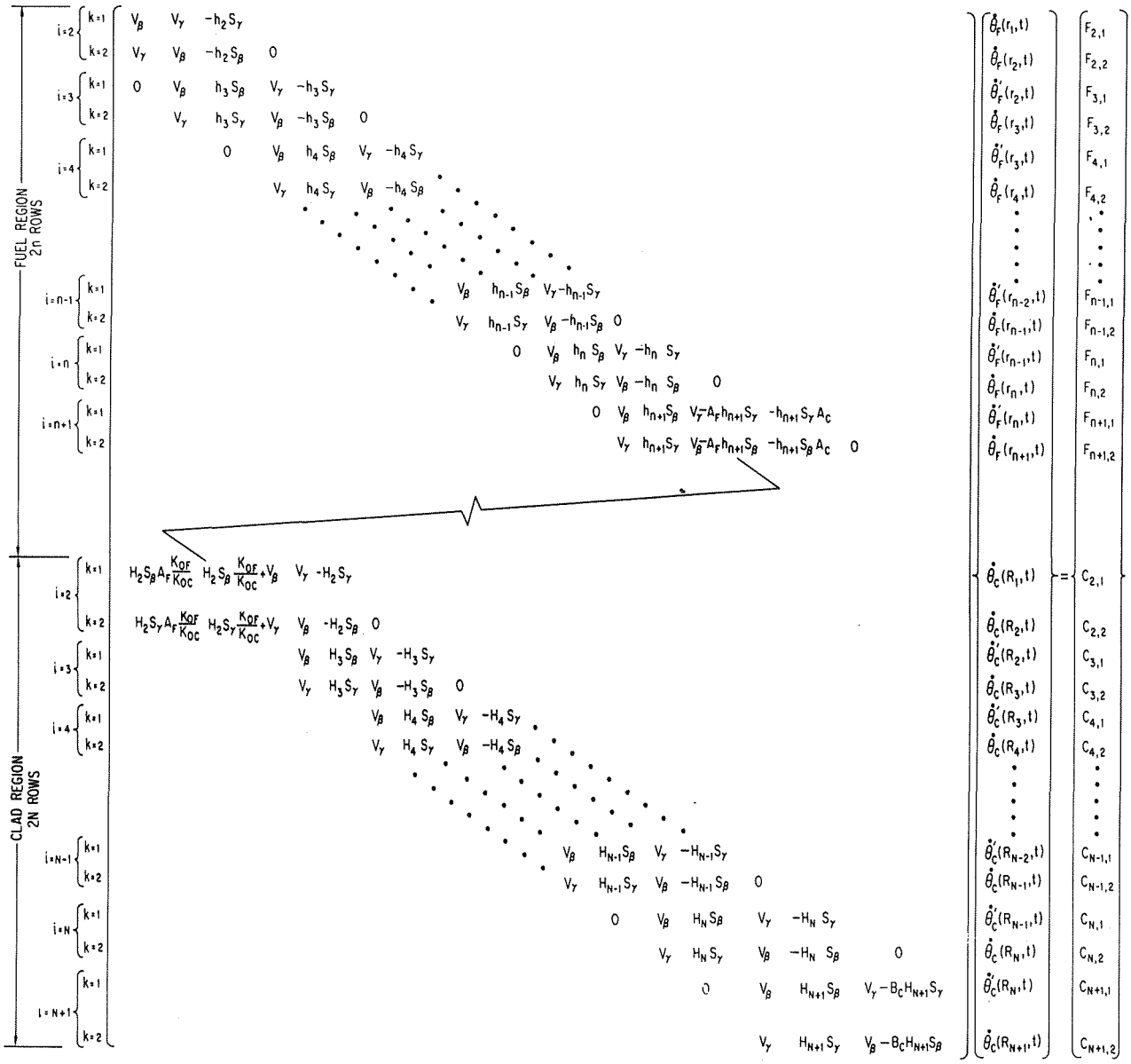

Fig. 2 Display of matrix equation (22)

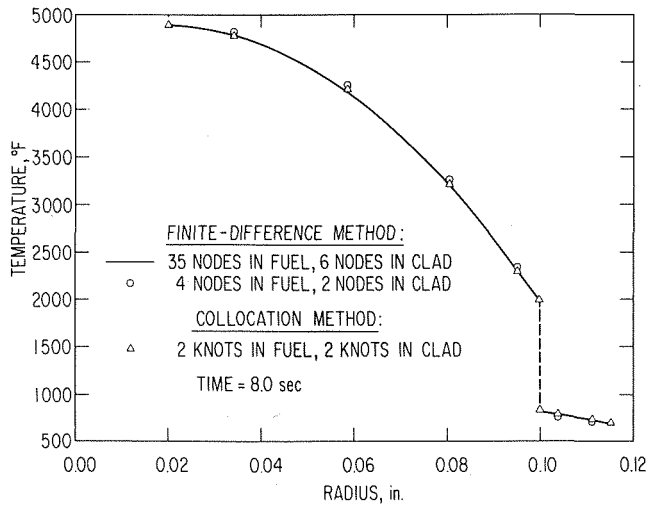

Fig. 3 Illustrative comparison of a finite difference solution with the collocation method at time = 8.0 s

Table 1 Comparison of a finite difference method with the collocation method at time = 4.0 s

	TEMPERATURE °F																					
	FINITE DIFFERENCE METHOD (THTB CODE)										COLLOCATION METHOD											
Position	80 Nodes in Fuel 15 Nodes in Clad No. of Eqs. = 95		35 Nodes in Fuel 6 Nodes in Clad No. of Eqs. = 41		6 Nodes in Fuel 2 Nodes in Clad No. of Eqs. = 8		4 Nodes in Fuel 2 Nodes in Clad No. of Eqs. = 6		2 Knots in Fuel 2 Knots in Clad No. of Eqs. = 4		3 Knots in Fuel 2 Knots in Clad No. of Eqs. = 6		4 Knots in Fuel 2 Knots in Clad No. of Eqs. = 8		5 Knots in Fuel 3 Knots in Clad No. of Eqs. = 12		20 Knots in Fuel 5 Knots in Clad No. of Eqs. = 46	
(Inches)	Time Step (sec) .001 .005 .01 Tolerance (°F) 0.1×10^{-2} CPU Time (sec)		Time Step (sec) .001 .005 .01 Tolerance (°F) 0.1×10^{-2} CPU Time (sec)		Time Step (sec) .001 .005 .01 Tolerance (°F) 0.1×10^{-2} CPU Time (sec)		Time Step (sec) .001 .005 .01 Tolerance (°F) 0.1×10^{-2} CPU Time (sec)		Time Step Variable Relative Error 0.1×10^{-2} CPU Time (sec)		Time Step Variable Relative Error 0.1×10^{-2} CPU Time (sec)		Time Step Variable Relative Error 0.1×10^{-2} CPU Time (sec)		Time Step Variable Relative Error 0.1×10^{-2} CPU Time (sec)		Time Step Variable Relative Error 0.1×10^{-2} CPU Time (sec)	
	1318	158	501	67	95	16	65	18	12		2		2		3		95	
0.03410	3490.1 —	3491.8 +.0487%	3491.2 +.0315%	3491.4 +.0372%	3488.3 -.0516%	3490.9 +.0229%	3488.0 -.0602%	3487.6 -.0716%	3517.1 +.7736%	3516.8 +.7650%	3516.5 +.7564%	3497.9 +.2235%	3493.8 +.1060%	3494.3 +.1203%	3492.9 +.0802%	3042.1 +.0724%	3492.1 +.0573%	3041.6 +.0559%	2331.9 +.0386%	1772.6 +.0226%	740.8 —	698.5 —
0.05841	3039.9 —	3041.2 +.0428%	3041.9 +.0658%	3040.8 +.0296%	3041.8 +.0625%	3041.5 +.0526%	3086.4 +1.5297%	3086.1 +1.8487%	3085.7 +1.5066%	3084.9 +1.4803%	3084.6 +1.4704%	3084.2 +1.4513%	3043.2 +.1086%	3042.0 +.0691%	3042.1 +.0724%								
0.08042	2331.0 —	2331.7 +.0300%	2331.8 +.0343%	2331.4 +.0172%	2381.2 +2.1536%	2331.4 +.0172%	2381.2 +2.1450%	2381.0 +2.1321%	2380.7 +2.1321%	2380.5 +2.1236%	2380.3 +2.1150%	2380.0 +2.1021%	2331.0 —	2331.8 +.0343%	2332.2 +.0515%							
0.09509	1772.2 —	1772.6 +.0226%	1773.3 +.0621%	1772.4 +.0113%	1782.8 +.5981%	1773.1 +.0508%	1782.7 +.5925%	1782.6 +.5868%	1782.4 +.5756%	1782.3 +.5643%	1782.2 +.5643%	1774.6 +.1354%	1772.2 —	1772.7 +.0282%	1772.8 +.0339%							
0.10380	740.8 —	740.8 —	740.8 —	740.8 —	740.1 -.0944%	740.8 —	740.1 -.0944%	740.1 -.0944%	740.1 -.0944%	740.1 -.0944%	740.1 -.0944%	740.9 +.0135%	740.8 —	740.8 —	740.8 —							
0.11129	698.5 —	698.5 —	698.5 —	698.5 —	698.0 -.0716%	698.5 —	698.0 -.0716%	698.0 -.0716%	698.0 -.0716%	698.0 -.0716%	698.0 -.0716%	697.9 -.0859%	698.6 +.0143%	698.5 —	698.5 —							

sponding Central Processing Unit (CPU) times on IBM 195/360 computer for the various time steps displayed in the table. It may be seen that CPU time for the collocation method with 12 equations is an order of magnitude less than for the case of the THTB calculation employing 41 equations yielding the same order of accuracy as the collocation method.

We may also note from this table that the collocation method with 4 equations provides a relative error in the temperature less than 1 percent which is more than adequate for many engineering calculations. It may be noted that there exists a great deal of uncertainty in some of the parameters such as gap conductance and thermal conductivity of the fuel; thus these uncertainties can produce errors in the temperature which far exceed the errors due to the collocation method. Therefore, the use of large number of collocation points may be of doubtful value for this problem.

Fig. 3 shows the temperature distribution at time = 8 s illustrating the comparative accuracies for the two methods. In addition, the figure shows the jump in the temperature at the fuel-clad interface.

Conclusions

The application of this collocation method for this type of nonlinear parabolic equations shows that this method can provide a very accurate numerical solution with a very small number of equations. The method is far more accurate and faster than the usual finite difference methods.

Acknowledgments

The authors wish to express their sincere thanks to George Hauser for his invalualbe help in programming and the data preparation. We also deeply appreciate the skill and patience shown by Debbie Lambert in typing this manuscript.

The work was performed under the auspices of the U.S. Atomic Energy Commission.

References

1 Shalev, A., Baruch, M., and Nissim, E., "Buckling Analysis of Hydrostatically Loaded Conical Shells by the Collocation Method," *AIAA Journal*, Vol. 11, No. 12, Dec. 1973, pp. 1603–1607.

2 Shalev, A., Baruch, M., and Nissim, E., "Buckling Analysis of Elastically Constrained Conical Shells Under Hydrostatic Pressure by the Collocation Method," T.A.E. Report No. 137, TECHNION-Israel Institute of Technology, Nov. 1972.

3 Villadsen, J. V., and Stewart, W. E., "Solution of Boundary-Value Problems by Orthogonal Collocation," *Chem. Eng. Sci.*, Vol. 22, 1967.

4 Finlayson, B. A., *The Method of Weighted Residuals and Variational Principles With Application in Fluid Mechanics, Heat and Mass Transfer*, Academic Press, New York, 1972, pp. 96–144.

5 Hindmarsh, A. C., "GEAR: Ordinary Differential Equation System Solver," UCID-30001, Rev. 3, Lawrence Livermore Laboratory, Dec. 1974.

6 Stephens, G. L., and Campbell, D. J., "Program THTB, for Analysis of General Transient Heat Transfer Systems," R60FPD647, General Electric Co., Apr. 1961.

APPENDIX

Properties of Fuel.

$$K_F = \begin{cases} 0.0160528/(14.17943 + 0.01183T_F)\ \text{Btu/(ft s°F)} \\ \qquad 932 < T_F(°\text{F}) < 2552 \\ 0.0003612\ \text{Btu/(ft s°F)} \end{cases}$$

$$\rho_F = 651.2\ \text{lbm/ft}^3$$

$$C_{PF} = [12.54 + 0.0170T_F(°\text{K}) - 0.117 \times 10^{-4}\ T_F{}^2(°\text{K}) + 0.307 \times 10^{-8}\ T_F{}^3(°\text{K})]/269.7664\ \text{Btu/lbm°F}$$

Properties of Cladding.

$$K_C = 2.22 \times 10^{-3} + 1.25 \times 10^{-6}\ T_C(°\text{F})\ \text{Btu/(ft s°F)}$$

$$\rho_C = 485.26\ \text{lbm/ft}^3$$

$$C_{PC} = 0.1105 + 2.632 \times 10^{-5}\ T_C(°\text{F})\ \text{Btu/lbm°F}$$

Heat Transfer Coefficients.

$$h_g = 0.2778 \text{ Btu}/(\text{ft}^2 \text{ s°F})$$
$$h = 6.944 \text{ Btu}/(\text{ft}^2 \text{ s°F})$$

Power Transient.

$$\dot{q}(t) = \dot{q}_0 \exp(0.1\ t)$$

where q_0 is the initial steady-state power set at 45266.32 $\text{Btu}/(\text{ft}^3\text{s})$ and t is the time in seconds.

W. Contreras
Caloritech, Inc.,
Manhasset, N. Y.

R. S. Thorsen
Assoc. Professor and Head,
Department of Mechanical Engineering,
Polytechnic Institute of New York,
Brooklyn, N. Y.
Mem. ASME

Transient Melting of a Solid Heated by a Condensing Saturated Vapor—Case I: Negligible Interface Curvature

A transient analysis has been performed to analytically determine the instantaneous dimensionless thickness of a vertically suspended solid at its melting temperature upon which a saturated vapor is condensing. The spatial variation and transient behavior of the melt-condensate liquid film, which is continuously drained, has also been obtained from the closed form analytical solution of the uncoupled equations for the solid-liquid and liquid-vapor interface motions under the condition of assumed negligible interface curvature. Classical boundary layer assumptions were applied to the convection process in the subcooled liquid film which was analyzed using integral techniques. From the analytic solution to the resultant interface motion equations in terms of characteristic curves, the functional dependence of the melting solid and the liquid layer thicknesses on the time and space variables was established. The liquid mass flux and heat transfer coefficient were then obtained analytically.

Introduction

The analysis of phase-change processes resulting from the interaction between an arbitrarily shaped solid at its melting temperature and a condensing gas of the same molecular species has received little attention in the past with the notable exception of Tien and Yen [1][1] who recently, using a steady-state similarity solution and restricting the interface to remain vertical at all times, found the condensate-melt liquid film to obey the same relationships as those developed by Nusselt [2] for the steady film condensation of a saturated vapor on a vertical wall, except for the appearance of the additional heat of fusion. The effect of the vapor layer and shear stress at the interface upon the liquid film was assumed unimportant and the solution limited to Prandtl numbers equal or larger than one.

This paper deals with the *transient* and steady-state vertically symmetric melting of an initially rectangular, two-dimensional solid at its melting temperature with its interface, mathematically considered to remain vertical, in contact with a vapor condensing continuously upon it. The liquid layer, assumed to drain continuously, is analyzed using integral techniques.

Analysis

Consider Fig. 1 in which an initially vertical symmetric slab of infinite depth and finite width and length, at its melting temperature T_{SL}, is suspended and in contact with a stagnant pure vapor of the same chemical composition as the solid. Upon contact between gas and solid the vapor condenses onto the surface of the solid joining the melt from the simultaneous melting of the solid to form a combined liquid film. This insulating layer of liquid, growing increasingly in thickness until a steady-state configuration is achieved, is continuously drained at the bottom. The regression of the solid continues until it is completely melted at time t_m.

In general the same classical assumptions used by Nusselt [2] and Rohsenow [3] in film condensation analyses are postulated for the condensation-melting problem. Equivalent assumptions have been recently used in reference [1] for a simplified steady-state solution. The assumptions used here are:

1 Stagnant, saturated vapor region.
2 Subcooled, nonlinear liquid film temperature profile.
3 Inertia terms throughout the liquid region are neglected.
4 Shear stresses at the liquid-vapor (L-V) interface are neglected.
5 The liquid film is of the boundary-layer type.
6 Solid at its melting temperature.
7 Condensate flow is laminar.
8 Constant physical properties.

In addition to the foregoing assumptions the solid curvature is assumed to remain negligible throughout the entire melting period,

[1] Numbers in brackets designate References at end of paper.

Contributed by the Heat Transfer Division for publication in the JOURNAL OF HEAT TRANSFER. Manuscript received by the Heat Transfer Division April 7, 1975. Paper No. 76-HT-L.

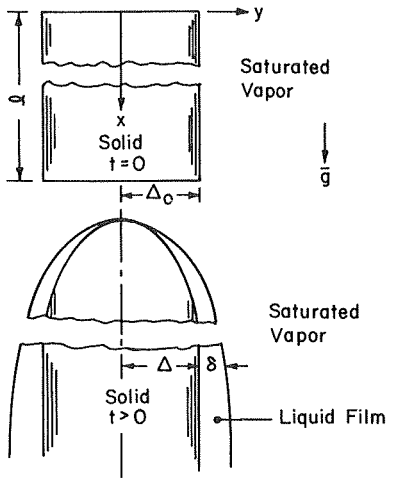

Fig. 1 Schematic representation of two-dimensional condensation-melting problem

i.e., $\Delta_x \to 0$.

Governing Equations, Boundary and Interface Conditions. The following dimensionless space, temperature and property variables are introduced, preparatory to presentation of the governing field equations and interface conditions:

$$\eta(x,t) = \frac{y}{\Delta(x,t)};\ 0 \le \eta \le 1 \tag{1}$$

$$\xi(x,t) = \frac{y - \Delta(x,t)}{\delta(x,t)};\ 0 \le \xi \le 1 \tag{2}$$

$$\theta(x,\xi,t) = \frac{T(x,\xi,t) - T_{SL}}{T_{LV} - T_{SL}} \tag{3}$$

$$S_{SL} = \frac{C_{PL}(T_{LV} - T_{SL})}{\lambda_{SL}} \tag{4}$$

$$S_{LV} = \frac{C_{PL}(T_{LV} - T_{SL})}{\lambda_{LV}} \tag{5}$$

(a) Liquid Film Conservation Equations. For the boundary layer liquid film the continuity, momentum, and energy equations then take the form

$$\frac{\partial u_L}{\partial x} + \frac{1}{\delta}\frac{\partial v_L}{\partial \xi} = 0 \tag{6}$$

$$\frac{\partial^2 u_L}{\partial \xi^2} = \left(\frac{\rho_v}{\rho_L} - 1\right)\frac{g}{\nu_L}\delta^2 \tag{7}$$

$$\left(\frac{\partial \theta_L}{\partial t}\right)_{x,y} + u_L\left(\frac{\partial \theta_L}{\partial x}\right)_{y,t} + \frac{v_L}{\delta}\left(\frac{\partial \theta_L}{\partial \xi}\right)_{x,t} = \frac{\alpha_L}{\delta^2}\left(\frac{\partial^2 \theta_L}{\partial \xi^2}\right)_{x,t} \tag{8}$$

In equation (8) care has been taken to explicitly identify the independent variables to be employed in the subsequent analysis. The variable ξ, defined by equation (2), is introduced in anticipation of equation (22) for the liquid temperature profile.

In addition, the present analysis requires that $\theta_S(x, \eta, t) = 0$ throughout the solid (assumption 6) and consideration of the energy equation for the solid is therefore unnecessary.

(b) Boundary and Interface Conditions. In addition, the following initial, boundary and interface conditions are to be satisfied.

At the solid-liquid interface ($y = \Delta$ or $\xi = 0$):

$$u_L\big|_{\xi=0} = 0 \tag{9}$$

$$v_L\big|_{\xi=0} = -\left(\frac{\rho_S}{\rho_L} - 1\right)\Delta_t \tag{10}$$

$$\theta_S\big|_{\eta=1} = \theta_L\big|_{\xi=0} = 0 \tag{11}$$

$$\left.\frac{\partial \theta_L}{\partial \xi}\right|_{\xi=0} = -\left(\frac{\rho_S}{\rho_L}\right)\frac{\delta}{\alpha_L S_{SL}}\Delta_t \tag{12}$$

$$\left.\frac{\partial \theta_L}{\partial t}\right|_{\xi=0} = -\frac{\Delta_t}{\delta}\left.\frac{\partial \theta_L}{\partial \xi}\right|_{\xi=0} \tag{13}$$

Equation (9) follows from the no-slip condition at the solid-liquid boundary under the condition of negligible curvature, while equation (10) expresses conservation of mass during phase change. The solid-liquid interface temperature is at all times equal to the melting temperature T_{SL} as expressed by equation (11) and conservation of energy with the solid at its melt temperature requires that equation (12) be satisfied.

Equation (13) arises by considering the expression for the total differential of θ_L at $y = \Delta$ or $\xi = 0$, i.e.,

$$d\theta_L = \frac{\partial \theta_L}{\partial y}\,dy + \frac{\partial \theta_L}{\partial t}\,dt \tag{14}$$

In the absence of curvature and noting that at $y = \Delta$, $d\theta_L = 0$ and $dy/dt = \Delta_t$ yields

$$\left.\frac{\partial \theta_L}{\partial t}\right|_{y=\Delta} = -\Delta_t\left.\frac{\partial \theta_L}{\partial y}\right|_{y=\Delta} \tag{15}$$

from which equation (13) follows.

At the liquid-vapor interface ($y = \Delta + \delta$ or $\xi = 1$):

$$\left.\frac{\partial u_L}{\partial \xi}\right|_{\xi=1} = 0, \tag{16}$$

$$\theta_L\big|_{\xi=1} = 1 \tag{17}$$

$$\left.\frac{\partial \theta_L}{\partial \xi}\right|_{\xi=1} = \frac{\delta}{\alpha_L S_{LV}}\left[(\Delta_t + \delta_t)\delta_x - v_L\right]_{\xi=1} \tag{18}$$

Equation (16) results from assumption 4 stated earlier and equation (17) states that at the liquid-vapor interface the tempera-

Nomenclature

g = gravitational acceleration
h = heat transfer coefficient
k = thermal conductivity
ℓ = initial height of solid
$\dot{M}_c$ = condensate mass flux
$\dot{M}_m$ = melt mass flux
Pr = Prandtl number, $(\mu C_p/k)$
S_{LV} = defined by equation (5)
S_{SL} = defined by equation (4)
t = time
t_m = time required to entirely melt solid
T = temperature
T_{LV} = temperature of saturated vapor
T_{SL} = melting temperature of solid
u = x component of velocity
v = y component of velocity
x, y = coordinates defined in Fig. 1
α = thermal diffusivity
δ = liquid film thickness measured in y-direction
Δ = solid half-thickness
Δ_0 = initial solid half-thickness
η = dimensionless coordinate defined by equation (1)
θ = dimensionless temperature defined by equation (3)
λ_{LV} = latent heat of vaporization
λ_{SL} = latent heat of fusion
μ = dynamic viscosity
ν = kinematic viscosity
ξ = dimensionless coordinate defined by equation (2)
ρ = density

Subscripts

L = pertains to liquid
LV = at liquid-vapor interface
S = pertains to solid
SL = at solid-liquid interface
SS = denotes steady state
$t = \partial/\partial t$
$x = \partial/\partial x$

Superscripts

$(\,)'$ = denotes dimensionless quantity

ture is at all times equal to the temperature of condensation, T_{LV}. Conservation of energy at the liquid-vapor interface results in equation (18) for the case of a saturated vapor.

Integration of equation (7) with respect to ξ and use of equations (9) and (16) results in

$$u_L(x, \xi, t) = (\frac{\rho_v}{\rho_L} - 1) \frac{g}{\nu_L} \delta^2 [\frac{\xi^2}{2} - \xi] \tag{19}$$

from which

$$u_L\big|_{\xi=1} = \frac{1}{2} (1 - \frac{\rho_v}{\rho_L}) \delta^2 \frac{g}{\nu_L} \tag{20}$$

Proceeding to integrate equation (8) between the limits $\xi = 0$ and $\xi = 1$, using equations (6), (11), (17), and (18), and applying Leibniz' rule it follows that

$$\frac{\partial}{\partial t}[\delta \int_0^1 \theta_L d\xi] + \frac{\partial}{\partial x}[\delta \int_0^1 u_L \theta_L d\xi] = \frac{\alpha_L}{\delta}[(1 + S_{LV}) \frac{\partial \theta_L}{\partial \xi}\Big|_{\xi=1} - \frac{\partial \theta_L}{\partial \xi}\Big|_{\xi=0}] \tag{21}$$

The functional form used in the integral procedure for establishing $\theta_L(x, \xi, t)$ is

$$\theta_L(x, \xi, t) = A(x, t) + B(x, t)\xi + C(x, t)\xi^2 \tag{22}$$

Then from equations (8), (9), (10), and (22), for $\xi = 0$, it follows that

$$\frac{\partial \theta_L}{\partial t}\Big|_{\xi=0} = [\frac{2\alpha_L}{\delta^2} C + (\frac{\rho_S}{\rho_L} - 1) \frac{\Delta_t}{\delta} \frac{\partial \theta_L}{\partial \xi}\Big|_{\xi=0}]^2 \tag{23}$$

From (11), (13), (17), (22), and (23) then

$$2\alpha_L(1 - B) + (\frac{\rho_S}{\rho_L}) \delta \Delta_t B = 0 \tag{24}$$

However, from equations (12) and (22)

$$\Delta_t(x, t) = -(\frac{\rho_L}{\rho_S}) \frac{\alpha_L S_{SL}}{\delta(x, t)} B \tag{25}$$

Then from equations (24) and (25) it follows that

$$B^2 + RB - \frac{2}{S_{SL}} = 0 \tag{26}$$

where

$$R(x,t) = \frac{2}{S_{SL}} \tag{27}$$

in the present analysis with no solid subcooling.

The solution to (26) is given by

$$B = -\frac{R}{2} \pm (\frac{R^2}{4} + \frac{2}{S_{SL}})^{1/2} \tag{28}$$

The physical requirement that $T_L \geq T_{SL}$ everywhere in the liquid film dictates that the + sign in equation (28) is to be used. Thus, from (11), (22), and (28) we have that

$$\theta_L(x,\xi,t) = [(\frac{R^2}{4} + \frac{2}{S_{SL}})^{1/2} - \frac{R}{2}] \xi - [(\frac{R^2}{4} + \frac{2}{S_{SL}})^{1/2} - \frac{R}{2} - 1] \xi^2 \tag{29}$$

From (21), (27), (28), and (29), recalling (19) and (20),

$$a\delta_t + b\delta^2\delta_x = \frac{c}{\delta} \tag{30}$$

where

$$a = \{8 + \frac{4}{S_{SL}} [(1 + 2S_{SL})^{1/2} - 1]\} \tag{31a}$$

$$b = \frac{3}{5} (1 - \frac{\rho_v}{\rho_L}) \frac{g}{\nu_L} \{18 + \frac{7}{S_{SL}} [(1 + 2S_{SL})^{1/2} - 1]\} \tag{31b}$$

$$c = 48\alpha_L \{(1 + S_{LV}) - (1 + \frac{1}{2} S_{SL}) \frac{1}{S_{SL}} [(1 + 2S_{SL})^{1/2} - 1]\} \tag{31c}$$

Similarly from (24), (27), and (28)

$$\Delta_t = \frac{2\alpha_L}{\delta} (\frac{\rho_L}{\rho_S}) \{1 - \frac{S_{SL}}{[(1 + 2S_{SL})^{1/2} - 1]}\} \tag{32}$$

Dimensionless Equations for the Solid-Liquid and Liquid-Vapor Interface Motions. The following dimensionless variables are defined:

$$t' = \frac{\alpha_S}{\Delta_0^2} t; \quad \delta' = \frac{\delta}{\Delta_0}; \quad \Delta' = \frac{\Delta}{\Delta_0}; \text{ and } x' = \frac{x}{\Delta_0} \tag{33}$$

In terms of these variables equations (30) and (32) become, after rearranging,

$$\Gamma_1' \delta' \delta'_{t'} + \Gamma_2' \delta'^3 \delta'_{x'} = 1 \tag{34}$$

$$\Delta'_{t'} = \Gamma_3' \frac{1}{\delta'} \tag{35}$$

The dimensionless *constant* coefficients are

$$\Gamma_1' = \frac{1}{12} (\frac{\alpha_S}{\alpha_L}) [\frac{2 + d'}{(1 + S_{LV}) - (1 + \frac{1}{2} S_{LV}) d'}] \tag{36a}$$

$$\Gamma_2' = \frac{1}{80} (1 - \frac{\rho_v}{\rho_L}) (\frac{\alpha_S}{\alpha_L}) \psi' [\frac{18 + 7d'}{(1 + S_{LV}) - (1 + \frac{1}{2} S_{LV}) d'}] \tag{36b}$$

$$\Gamma_3' = 2 (\frac{\rho_L \alpha_L}{\rho_S \alpha_S}) (\frac{d' - 1}{d'}) \tag{36c}$$

$$d' = \frac{1}{S_{SL}} [(1 + 2S_{SL})^{1/2} - 1] \tag{36d}$$

$$\psi' = \frac{g\Delta_0^3}{\alpha_S \nu_L} \tag{36e}$$

Equation (34) is recognized as an uncoupled, quasi-linear, parabolic partial differential equation of first order, solvable by the standard Method of Characteristics as described in Hildebrand [4], for example.

When restricted to the first quadrant of the $t' - x'$ plane, the single, real family of characteristic curves is described by:

$$\frac{dt'}{dx'} = \frac{\Gamma_1'}{\Gamma_2'} \frac{1}{\delta'^2} \tag{37}$$

$$\frac{d\delta'}{dx'} = \frac{1}{\Gamma_2'} \frac{1}{\delta'^3} \tag{38}$$

$$\frac{d\delta'}{dt'} = \frac{1}{\Gamma_1'} \frac{1}{\delta'} \tag{39}$$

subject to the conditions

$$\begin{aligned} &\delta' = 0; \quad t' = 0 \quad x' = x' \\ &\delta' = 0; \quad x' = 0 \quad t' = t' \end{aligned} \tag{40}$$

From equations (37), (38), and (39) it follows that

$$\delta'(x') = (\frac{4}{\Gamma_2'} x')^{1/4} \tag{41}$$

$$\delta'(t') = (\frac{2}{\Gamma_1'} t')^{1/2} \tag{42}$$

The limiting characteristic curve, i.e., the curve passing through

[2] It is to be stressed that $\frac{\partial \theta_L}{\partial t}\Big|_{\xi=0}$ is *not* evaluated from equation (22). Recall that y and t are the independent variables of the problem and ξ is introduced for compactness in equation (22).

the origin of the t', x' coordinates, gives rise to the steady-state solution. Thus

$$t_{ss,L}' = \Gamma_1' \left(\frac{x'}{\Gamma_2'}\right)^{1/2} \tag{43}$$

Then, from equations (41), (42), and (43) it follows that

$$\delta_{ss}' = \left(\frac{4}{\Gamma_2'}\right)^{1/4} x'^{1/4} \tag{44}$$

Furthermore, from (42)

$$\delta'(x',t' < t_{ss,L}') = \delta_{ss}'(x') \left[\frac{t'}{t_{ss,L}'(x')}\right]^{1/2} \tag{45}$$

From (43), (44), and (45), returning to dimensional variables,

$$t_{ss,L} = a_1 x^{1/2} \tag{46}$$

where

$$a_1 = \frac{\sqrt{\frac{10}{9}\frac{\rho_L}{(\rho_L - \rho_V)g}}\{2S_{SL} + [(1+2S_{SL})^{1/2} - 1]\}\,\mathrm{Pr}_L^{1/2}}{\{18S_{SL} + 7[(1+2S_{SL})^{1/2} - 1]\}^{1/2}\{2[1 + S_{SL}) + S_{LV}(\frac{1}{2} + S_{SL}) - (1 + \frac{1}{2}S_{LV})(1+2S_{SL})^{1/2}]\}^{1/2}} \tag{47}$$

Similarly

$$\delta(x, t \geq t_{ss,L}) = \delta_{ss} = a_2 x^{1/4} \tag{48}$$

where

$$a_2 = 2\left[\frac{10\rho_L \alpha_L \nu_L}{(\rho_L - \rho_V)g}\right]^{1/4} \times \left\{\frac{2[(1 + S_{SL}) + S_{LV}(\frac{1}{2} + S_{SL}) - (1 + \frac{1}{2}S_{LV})(1+2S_{SL})^{1/2}]}{18\,S_{SL} + 7[1 + 2S_{SL})^{1/2} - 1]}\right\}^{1/4} \tag{49}$$

and

$$\delta(x, t < t_{ss,L}) = a_3 t^{1/2} \tag{50}$$

where

$$a_3 = \sqrt{24\alpha_L}\left\{\frac{[(1 + S_{SL}) + S_{LV}(\frac{1}{2} + S_{SL}) - (1 + \frac{1}{2}S_{LV})(1+2S_{SL})^{1/2}]}{2S_{SL} + [1 + 2S_{SL})^{1/2} - 1]}\right\}^{1/2} \tag{51}$$

With a closed-form solution to equation (34), the solution to equation (35) can now be determined.

From equations (35) and (44) or (45) it follows that

$$\Delta_{t'}'(x', t' < t_{ss,L}') = \frac{\Gamma_3'}{\delta_{ss}'}\left(\frac{t_{ss,L}'}{t'}\right)^{1/2} \tag{52}$$

$$\Delta_{t'}'(x', t' \geq t_{ss,L}') = \frac{\Gamma_3'}{\delta_{ss}'} \tag{53}$$

where Γ'_3 is given by equations (36c) and (36d).

Proceeding to integrate equations (52) and (53) and returning to dimensional variables, results in

$$\Delta(x, t < t_{ss,L}) = \Delta_0 - a_4 t^{1/2} \tag{54}$$

where

$$a_4 = \sqrt{\frac{4}{3}\alpha_L}\left(\frac{\rho_L}{\rho_S}\right) \times \left\{\frac{\left[\frac{S_{SL}}{(1+2S_{SL})^{1/2} - 1} - 1\right](2S_{SL} + [(1+2S_{SL})^{1/2} - 1])}{2[(1 + S_{SL} + S_{LV}(\frac{1}{2} + S_{SL}) - (1 + \frac{1}{2}S_{LV})(1+2S_{SL})]^{1/2}}\right\} \tag{55}$$

Similarly

$$\Delta(x, t \geq t_{ss,L}) = \Delta_0 - a_5 x^{1/4} t \tag{56}$$

where

$$a_5 = \left[\frac{\alpha_L^2}{10}\left(1 - \frac{\rho_V}{\rho_L}\right)g\right]^{1/4}\left(\frac{\rho_L}{\rho_S}\right) \times \left\{\frac{\left[\frac{S_{SL}}{(1+2S_{SL})^{1/2} - 1} - 1\right]^4 [18S_{SL} + 7\{(1+2S_{SL})^{1/2} - 1\}]}{2[(1 + S_{SL}) + S_{LV}(\frac{1}{2} + S_{SL}) - (1 + \frac{1}{2}S_{LV})(1+2S_{SL})^{1/2}]}\right\} \times \mathrm{Pr}_L^{-1/4} \tag{57}$$

Heat Transfer Coefficient. From the usual definition of the liquid film heat transfer coefficient we have

$$h_L = \frac{k_L}{\delta}\left.\frac{\partial \theta_L}{\partial \xi}\right|_{\xi=0} \tag{58}$$

Equations (29), (48), and (58) then give rise to

$$h_L(x, t \geq t_{ss,L}) = h_{ss,L} = a_6 x^{-1/4} \tag{59}$$

where

$$a_6 = \left[\frac{k_L^3(\rho_L - \rho_V)g C_{pL}}{160\,\nu_L}\right]^{1/4} \times \left\{\frac{\{18S_{SL} + 7[(1+2S_{SL})^{1/2} - 1]\}[(1+2S_{SL})^{1/2} - 1]^4}{2S_{SL}{}^4[(1 + S_{SL}) + S_{LV}(\frac{1}{2} + S_{SL}) - (1 + \frac{1}{2}S_{LV})(1+2S_{SL})^{1/2}]}\right\}^{1/4} \tag{60}$$

Similarly from (33), (45), and (58) we obtain

$$h_L(x, t < t_{ss,L}) = h_{ss,L}\left(\frac{t_{ss,L}}{t}\right)^{1/2} \tag{61}$$

Mass Flow Rate/Unit Width. The mass flow rate per unit width is given by

$$\Gamma = \rho_L \delta \int_0^1 u_L(x, \xi, t)\, d\xi \tag{62}$$

From (19), (48), and (62)

$$\Gamma(x, t \geq t_{ss,L}) = \Gamma_{ss} = a_7 x^{3/4} \tag{63}$$

where

$$a_7 = \left[\frac{1}{3}\left(\frac{160}{3}\right)^3 \frac{k_L^3(\rho_L - \rho_V)g}{C_{pL}{}^3 \nu_L}\right]^{1/4} \times \left\{\frac{2[1 + S_{SL}) + S_{LV}(\frac{1}{2} + S_{SL}) - (1 + \frac{1}{2}S_{LV})(1+2S_{SL})^{1/2}]^{3/4}}{18S_{SL} + 7[(1+2S_{SL})^{1/2} - 1]}\right\} \tag{64}$$

Similarly from (19), (50), and (62)

$$\Gamma(x, t < t_{ss,L}) = \Gamma_{ss}\left(\frac{t}{t_{ss,L}}\right)^3 \tag{65}$$

Melt Mass-Flux. From equation (13) it follows that the melt-mass flux is given by

$$\dot{M}_m = \frac{k_L S_{SL}}{\delta\, C_{pL}}\left.\frac{\partial \theta_L}{\partial \xi}\right|_{\xi=0} \tag{66}$$

Then from (29), (27), (48) or (49) and (66)

$$\left.\dot{M}_m\right|_{t \geq t_{ss,L}} = \frac{\rho_L \alpha_L}{a_2}[(1 + 2S_{SL})^{1/2} - 1]x^{-1/4} \tag{67}$$

$$\left.\dot{M}_m\right|_{t < t_{ss,L}} = \frac{\rho_L \alpha_L}{a_3}[(1 + 2S_{SL})^{1/2} - 1]t^{-1/2} \tag{68}$$

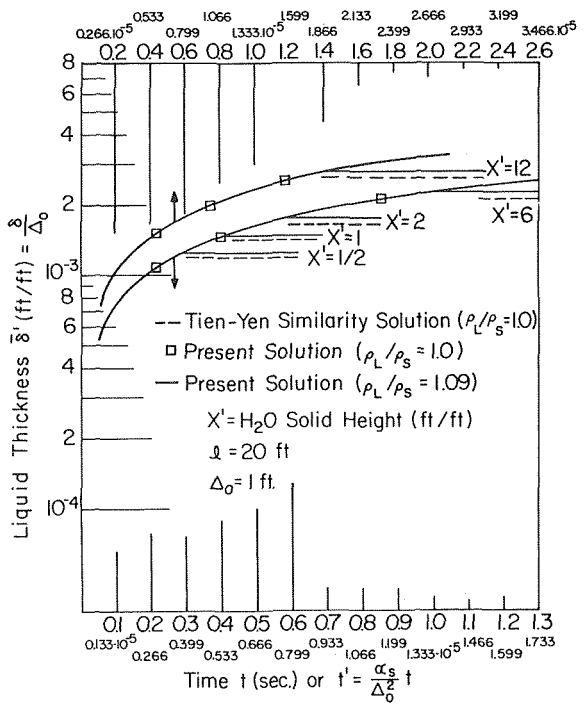

Fig. 2 Liquid film thickness variation with time for various solid height locations

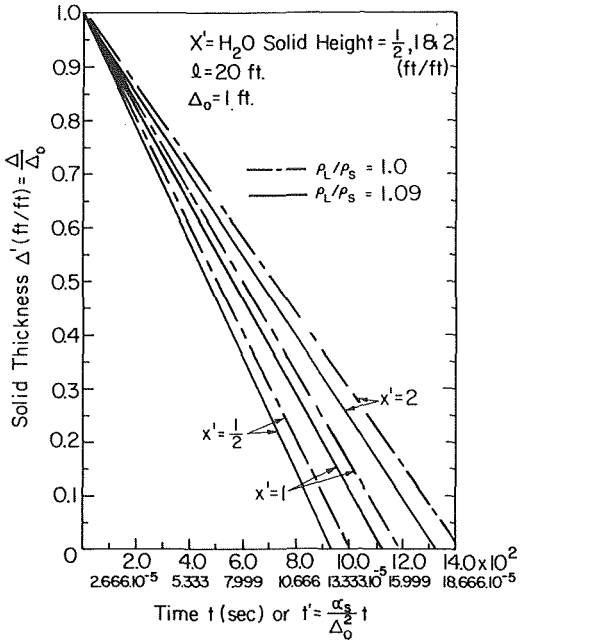

Fig. 3 Solid region thickness variation with time for solid height $x' = \frac{1}{2}$, 1, 2

Consensate Mass-Flux. From equation (18)

$$\dot{M}_c = \frac{\rho_L \alpha_L S_{LV}}{\delta} \left.\frac{\partial \theta_L}{\partial \xi}\right|_{\xi=1} \tag{69}$$

It follows from (29), (27), (48) or (49) and (69) that

$$\left.\dot{M}_c\right|_{t \geq t_{SS,L}} = \frac{\rho_L \alpha_L}{a_2} \frac{S_{LV}}{S_{SL}} \{2S_{SL} - [(1 + 2S_{SL})^{1/2} - 1]\} x^{-1/4} \tag{70}$$

$$\left.\dot{M}_c\right|_{t < t_{SS,L}} = \frac{\rho_L \alpha_L}{a_3} \frac{S_{LV}}{S_{SL}} \{2S_{SL} - [(1 + 2S_{SL})^{1/2} - 1]\} t^{-1/2} \tag{71}$$

Condensate-Melt Mass-Flux Ratios. From equations (67), (68), (70), and (71) we have

$$\frac{\dot{M}_c}{\dot{M}_m} = \left\{\frac{2S_{SL}}{[(1 + 2S_{SL})^{1/2} - 1]} - 1\right\} \frac{\lambda_{SL}}{\lambda_{LV}} \tag{72}$$

Results

An uncoupled solution has been obtained by reducing an extremely complex problem to a configuration which permitted arriving at a closed form analytical solution in terms of characteristic curves. This solution assumes $\Delta_x \to 0$ (negligible solid curvature) and $\theta_0 = 0$ (solid initially at its melting temperature) and is shown graphically in Figs. 2–4 for the case of water at one atmosphere.

Results reported by Tien and Yen [1] for their steady-state similarity solution of the condensate-melt liquid film thickness of a similar problem in which the solid and liquid densities are assumed to be the same are also shown in Fig. 2 for comparison purposes. Their values agree closely with the results obtained in this investigation.

From the results obtained for both the liquid and solid regions, the following general observations can be made:

- The liquid film does indeed reach a steady-state configuration.
- The liquid film transient is small compared to the solid melting rate.
- The solid interface velocity becomes independent of time after steady state has been achieved by the liquid film.
- The equations developed for the liquid film during the melting-condensation process parallel the relationships obtained by others (e.g., references [3, 5, 6]) for transient and steady film condensation only, except for the appearance of the heat of fusion in addition to the usual heat of vaporization.
- Close agreement with the steady-state similarity solution of Tien and Yen [1] is indicated. The small differences represent a measure of error due to the integral solution for the liquid temperature distribution used in the present work.

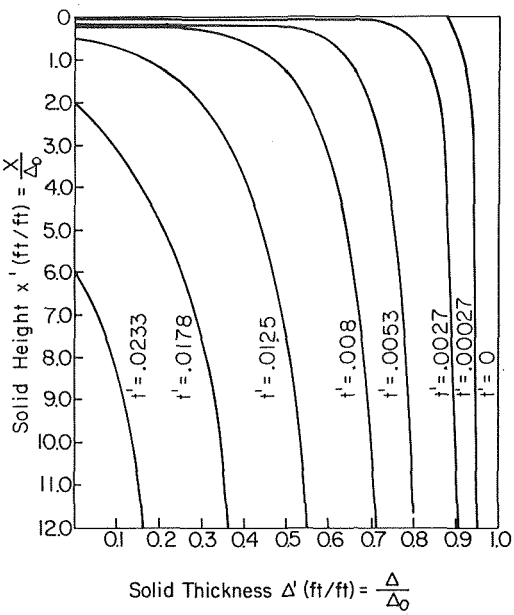

Fig. 4 Solid profile variation with time

This small difference justifies the use of the integral solution technique in a more general problem involving interface curvature and solid subcooling effects.

- The effect of the density ratio, ρ_L/ρ_S (1.00 or 1.09 in the present study), is confined primarily to the solid regression rate and is not a significant factor in the liquid film growth or steady-state configuration.

Conclusions

Analytic results for a special case of the extremely complex problem of combined melting and condensation of a solid in the presence of its vapor have been obtained. The assumptions of zero solid subcooling and negligible interface curvature together permit uncoupling of the equations governing the motion of the two interfaces. The results indicate that the solid-liquid interface, as expected, cannot remain vertical and curvature must eventually become important. As this happens and the top of the solid recedes, the validity of the present analysis must be checked against a more complete, though mathematically more complex, analysis.

The authors have undertaken and completed a study of these two effects (curvature and solid subcooling). However, because the problem does not admit an analytic solution under these more general conditions the results are not reported here. They will be published in a subsequent paper.

References

1 Tien, C., and Yen, Y. C., "Condensation-Melting Heat Transfer," Chem. Eng. Prog. Symposium Series, Vol. 67, No. 113, 1971, pp. 1–9.

2 Nusselt, W., "Die Oberflachen Kondensation des Wasserdampfles," *zeitschrift des Vereines Deutscher Ingenieure*, Vol. 60, 1916, pp. 541–569.

3 Rohsenow, W. M., "Heat Transfer and Temperature Distribution in Laminar-Film Condensation," TRANS. ASME, Vol. 78, 1956, p. 1645.

4 Hildebrand, F. B., *Advanced Calculus for Engineers*, Prentice Hall, New York, Vol. 11, 1955, pp. 368–378.

5 Sparrow, E. M., and Gregg, J. L., "A Boundary-Layer Treatment of Laminar-Film Condensation," JOURNAL OF HEAT TRANSFER, TRANS. ASME, Series C, Vol. 81, 1959, p. 13.

6 Sparrow, E. M., and Siegel, R., "Transient Film Condensation," *Journal of Applied Mechanics*, TRANS. ASME, Series E, Vol. 26, 1959, p. 120.

M. Toren
Y. Zvirin
Y. Winograd[1]

Faculty of Mechanical Engineering,
Technion—Israel Institute of Technology,
Haifa, Israel

Melting and Evaporation Phenomena During Electrical Erosion

A modeling method is presented for the evaluation of the eroded crater during electrical discharge machining. The method is based on the propagation of the melting crater when other effects such as evaporation can take place. Calculations are performed for a point heat source on the surface of copper and steel electrodes. An experimental technique for the measurement of the amount of eroded material is described: the method consists of extraction of the metal from the dielectric fluid by chemical reactions and measurement of the resulting color intensity.

1 Introduction

Electrical discharge machining (EDM) of metals has become an established method for machining, especially for complicated geometries and high accuracy. The practical techniques of EDM have developed considerably in recent years. However, in spite of the progress made in the theory of EDM, many aspects of the process are still unexplained. The process of the discharge between two electrodes (tool and workpiece) immersed in a dielectric fluid is very complicated and involves numerous phenomena, e.g., heat conduction and phase changes (melting, evaporation, ionization, excitation) of the electrodes and the dielectric fluid, electrical forces, formation and collapse of gas bubbles and energy distribution in the discharge channel. Several very simplified mathematical models for the erosion mechanisms have been suggested, but a generally accepted theory does not yet exist.

Electrical forces exerted by the electric field between the electrodes can account for the erosion only for very short pulses—up to 10^{-6} s, [1–4].[2] For longer pulses, the basic mechanism for metal removal is that of melting and evaporation [5–14]. The discharge channel is the energy source and the amount of eroded material is determined by the isotherm of the melting temperature. The mathematical models suggested [5–14] for this mechanism treat the melting process by modification of the specific heat of the material and not by sinks of latent heat. Evaporation is either neglected or it is assumed that the surface temperature does not exceed the evaporation temperature. While these assumptions can be justified for approximate calculations, a more accurate approach must take into account the latent heat of evaporation, which is much larger than that of melting. Moreover, other phenomena such as ionization and excitation of the evaporated material can occur, and the existing mathematical models cannot describe them.

Problems of heat transfer with a change of phase are also encountered in other fields, such as solidification of castings, design of shields for re-entry vehicles on the basis of aerodynamic ablation, freezing of foodstuffs and sinks for energy storage. Boley [15] and Muehlbauer and Sunderland [16] presented a thorough review of the literature published until 1963, which was limited to a single change of phase depending on a single space variable. Since 1963 several authors treated two- and three-dimensional problems, but only a single change of phase. Several of these works are mentioned by Budhia and Kreith [17], who solved the problem of melting in a wedge.

Sikarskie and Boley [18] solved the problem of heat transfer with melting caused by a heat source which varies spatially along the boundary surface. They have also suggested a method for treating the initial propagation of the melting front, based on the assumption that the problem can be regarded as one-dimensional during the initial stages. Pedroso and Domoto [19] suggested a perturbation method for solidification problems. They simplified the problem by transforming the variables such that the position of the solidification front replaces time. Lazaridis [20] presented an implicit numerical solution for the temperature field and the position of the interface for a multidimensional solidification. He treated, again, only a single phase-change.

[1] This paper is dedicated to the memory of Prof. Y. Winograd who was killed in action during the Yom-Kippur War, October 1973, while defending his country.

[2] Numbers in brackets designate References at end of paper.

Contributed by the Heat Transfer Division for publication in the JOURNAL OF HEAT TRANSFER. Manuscript received by the Heat Transfer Division September 17, 1974. Paper No. 76-HT-J.

This present work is apparently the first attempt to develop a method for treating a heat transfer problem with multiple phase changes. The method can serve as a first approximation for evaluating the propagation of the melting crater during electrical discharge machining.

The model is applied here to calculate numerically the melting isotherm resulting from a single spark of a point source on the electrode surface when melting and evaporation take place. These phenomena are first included accurately, by sinks of latent heats distributed on the melting and evaporation isotherms (Section 2). In Section 3 an approximate method is developed in which the sinks due to melting and evaporation are "transferred" to the site of the point source. The magnitudes of these sinks remain as in the exact model, i.e., the heats required to melt and evaporate the propagating melting and evaporation shells. The results for copper and steel electrodes show that the approximate model is sufficiently accurate for practical calculations. This method is clearly simpler than the exact one and enables a considerable reduction of numerical computation and thus of computer time.

In order to develop these simple models which represent the complicated process of the discharge, several assumptions need be made. The first one is that of spherical symmetry. It is well known, c.f., Soneys and Van Dyck [14] and Greene and Guerrero-Alvarez [21], that the crater formed by a single spark is a symmetrical segment, which tends to a half-sphere with increasing pulse duration. This is explained by the following reasons: the diameter of the discharge channel is much smaller than that of the workpiece electrode, heat conduction into the dielectric fluid is negligible compared with that in the metallic electrode, and convection in the vapor phase is not important until the collapse of the bubble which contains the vapor. It is believed, e.g., Zolotych [8] and Crookall and Heuvelman [22], that some evaporation of the dielectric fluid takes place at the beginning of the discharge. The electric arc is then established in this gap, while more vapor, mainly from the electrodes, is accumulated in a bubble. The bubble collapses only after termination of the discharge (for pulse durations up to 1000 μs, investigated here). Convection in the vapor phase can be important only then; it is neglected in the present work. This assumption is further justified by the results of Greene and Guerrero-Alvarez [21]. They compared machining in a dielectric fluid and in a gas. In the former case, a single crater is created while in the latter, secondary craters are formed around the central main crater. This shows that the dielectric fluid prevents the spreading of the energy and hinders convection.

A further assumption is that the properties are constant and equal in all three phases. In most of the reported works on melting or solidification the problem of the properties in the different phases is avoided. For example, Sikarskie and Boley [18] considered instantaneous removal of the melted material and heating applied to the melting front. The same authors, and also Budhia and Kreith [17], solved problems in which the whole liquid phase is at the melting temperature. In order to accommodate the change in the properties between the phases, sophisticated and complicated numerical methods must be used, e.g., Lazaridis [20]. In the existing models for electrical discharge machining, evaporation and melting are not included directly, as mentioned in the foregoing. For the former, it was assumed that the surface temperature does not rise above that of evaporation; for the latter, constant and equal properties are assumed for the solid and liquid phases, and the specific heat capacity was modified by the latent heat to account for melting, Snoeys and Van Dyck [14]. Cobine and Burger [23] even assumed that all the energy supplied is absorbed by evaporation.

Observation of the behavior of the relevant physical properties for metals, c.f., Smithells [24], shows that they do not change drastically at the melting point. Some properties vary continuously through this point while the discontinuous change in other properties is small. Since the variations of the properties between the solid and liquid phases are quite moderate and due to the fact that the crater is tiny, the assumption of constant properties seems reasonable as a first approximation.

The properties of the vapor phase still remain a difficulty and a limitation of the model. However, since the electric current penetrates through the vapor phase, most of the heat is applied at the liquid-vapor front so that heating of the vapor and conduction in it are not important. The dominant effects are melting and evaporation, and only when the temperatures are much higher, ionization and excitation in the gas phase become significant. Moreover, the thermal resistance of the vapor phase is also compensated for by solid particles in the crater which are torn from the electrode surface during the first stages of the discharge, c.f., Zolotych [8].

The experimental part of the work included measurements of the quantities removed from the electrodes during single discharges. One of the main problems of measuring the amount of material eroded during a single spark is that this amount is very small. One method is based on measurement of the dimensions of the crater [6, 12, 13], but the shape of the crater becomes irregular with increasing pulse duration. Another method is based on averaging the weight loss of the workpiece resulting from many sparks [25–26]. In this way, however, every spark has a new configuration. Determination of the erosion by radioactive tracers [27] gives reasonable results but was found to be inconvenient.

The experimental method reported here (Section 4) for measurement of the amount of eroded metals consists of chemical extraction of the metal from the dielectric fluid and determination of its quantity by the intensity of colored solutions in a spectro-photometer.

The experimental results for copper and steel electrodes are compared with those of the theoretical model. Good agreement is found for intermediate pulse duration; for longer and shorter pulses the theory can provide orders of magnitudes of material removal. It is thus concluded that the simple model can serve as a first approximation in spite of the assumptions and simplifications which were being made.

2 Propagation of the Melting and Evaporation Surfaces

The basic mechanism of metal removal during EDM is based on melting and evaporation. The discharge channel is the heat source, assumed here to be constant and concentrated at a point on the surface of the electrode. The crater of eroded material is determined by the isotherm of the melting temperature, see Fig. 1.

Nomenclature

c = special heat
k = heat conductivity
ℓ = length scale
L = latent heat
M = melting parameter
q_M, q_V = heat sinks due to latent heats of melting and evaporation, respectively
Q = point heat source
r = radius, dimensionless
R = radius
t = time
t^* = time scale
T = temperature
V = evaporation parameter
w_M, w_V = temperatures due to heat sinks of melting and evaporation, dimensionless
α = heat diffusivity
$\delta()$ = Dirac delta function
θ = temperature, dimensionless
τ = time, dimensionless
ρ = density
ψ = temperature due to a point heat source, dimensionless

Subscripts:

M = melting
V = evaporation
0 = initial time

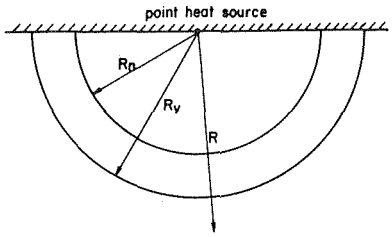

Fig. 1 The melting crater

As mentioned in the foregoing, it is assumed that the physical properties are constant and equal for the phases. The temperature field in the metal can be described then by the following Fourier equation:

$$\rho c \frac{\partial T}{\partial t} - k\nabla^2 T = Q\delta(\vec{R}) - q_M(\vec{R}_M; t) - q_V(\vec{R}_V; t) \tag{1}$$

where Q is the intensity of the heat source and q_M and q_V are the instantaneous heat sinks due to melting and evaporation taking place at $\vec{R}_M$ and $\vec{R}_V$:

$$q_M(\vec{R}_M; t) = \frac{4}{3}\pi\rho L_M \frac{d}{dt} R_M{}^3 \tag{2a}$$

$$q_V(\vec{R}_V; t) = \frac{4}{3}\pi\rho L_V \frac{d}{dt} R_V{}^3 \tag{2b}$$

Other phenomena like ionization and excitation can be described by adding appropriate terms on the right-hand side of equation (1).

The initial condition is taken as a uniform temperature T_0, just before application of the source:

$$T = T_0 \text{ at } t = 0 \tag{3}$$

It is assumed that the heat loss from the surface of the electrode is negligible (see Fig. 1); thus, because of symmetry, the problem reduces to a spherical one-dimensional one. The other boundary condition is:

$$T \text{ finite as } R \to \infty \tag{4}$$

which states that the dimensions of the crater are much smaller compared with the electrode.

Equation (1) for the temperature is linear, therefore, the solution can be composed of three terms, written in the following dimensionless form (cf., Carslaw and Jaeger [28], p. 293):

$$\theta(r, \tau) = \psi(r, \tau) - Mw_M(r, \tau; r_M) - Vw_V(r, \tau; r_V) \tag{5}$$

where the functions ψ, w_M, and w_V denote the temperature fields resulting from a point source at $r = 0$ and from heat sinks (due to melting and evaporation) distributed on the propagating fronts $r_M(\tau)$ and $r_V(\tau)$, respectively.

The dimensionless variables θ, r, and τ are defined by:

$$\theta = \frac{T - T_0}{T_M - T_0};\quad r = \frac{R}{\ell};\quad \tau = \frac{t}{t^*} \tag{6}$$

where the length and time scales are:

$$\ell = \frac{Q}{4\pi k(T_M - T_0)};\quad t^* = \frac{\ell^2}{4\alpha} \tag{7}$$

It is noted that the length scale is chosen as the radius of the melting crater at the steady state.

The dimensionless parameters M and V which represent the relative importance of melting and evaporation, are defined as follows:

$$M = \frac{4}{3\pi^{1/2}} \frac{L_M}{c(T_M - T_0)};\quad V = \frac{4}{3\pi^{1/2}} \frac{L_V}{c(T_M - T_0)} \tag{8}$$

The functions ψ, w_M, and w_V are given by Carslaw and Jaeger [28]:

$$\psi(r, \tau) = \frac{1}{r}\operatorname{erfc}\frac{r}{\sqrt{\tau}} \tag{9}$$

$$w_M(r, \tau; r_M) = \int_0^\tau \frac{1/3\, d/d\tau' \, r_M{}^3}{4\pi r_M(\tau')} \frac{d\tau'}{(\tau - \tau')^{1/2}} \left\{ e^{-[r - r_M(\tau')]^2/(\tau - \tau')} + \right.$$
$$\left. - e^{-[r + r_M(\tau')]^2/(\tau - \tau')} \right\} \tag{10}$$

and a similar expression for w_V, obtained by replacing the subscript M by V in equation (10).

From (5), (9), and (10) it is seen that the temperature at any time τ depends on the history of the melting and evaporation propagation from the start ($\tau = 0$) to this time τ. In order to evaluate the increase with time of the radii r_M and r_V, it is necessary to solve two equations which follow from (5) with $\theta = \theta_M$ and $\theta = \theta_V$:

$$\theta_M - [\psi(r_M, \tau) - Mw_M(r_M, \tau; r_M) - Vw_V(r_M, \tau; r_V)] = 0 \tag{11a}$$

$$\theta_V - [\psi(r_V, \tau) - Mw_M(r_V, \tau; r_M) - Vw_V(r_V, \tau; r_V)] = 0 \tag{11b}$$

Equations (11) were solved numerically for $r_M(\tau)$ and $r_V(\tau)$. The computer program performs the numerical quadrature of the integrals which appear in (10), when $r_M(\tau')$ and $r_V(\tau')$ for $0 < \tau' < \tau$ are known from the previous steps and $r_M(0) = r_V(0) = 0$. The system of two simultaneous nonlinear equations (11) for $r_M(\tau)$ and $r_V(\tau)$ is solved by iteratively minimizing the sum of the squared left hand sides of equations (11a) and (11b). The method of solution can be applied to any metal; the solution in the dimensionless form depends on the metal properties (via M and V), thus, a complete universal solution cannot be obtained.

Results for the propagation of the melting and evaporation fronts for copper and steel are shown in Figs. 2 and 3. Obviously, R_M and R_V tend asymptotically to constant values as time becomes very large. Then a steady state is reached where all the heat from the source is conducted into the solid.

The asymptotic radius of the melting isotherm for copper is smaller than that of steel, because the product kT_M is larger for copper (see equations (6), (7), and (9)). For short times, the dominant phenomenon is that of evaporation which requires the largest part of the energy. The latent heat of evaporation is bigger for steel than for copper; therefore, the melting radius of steel is smaller for short times. Moreover, this phenomenon also causes

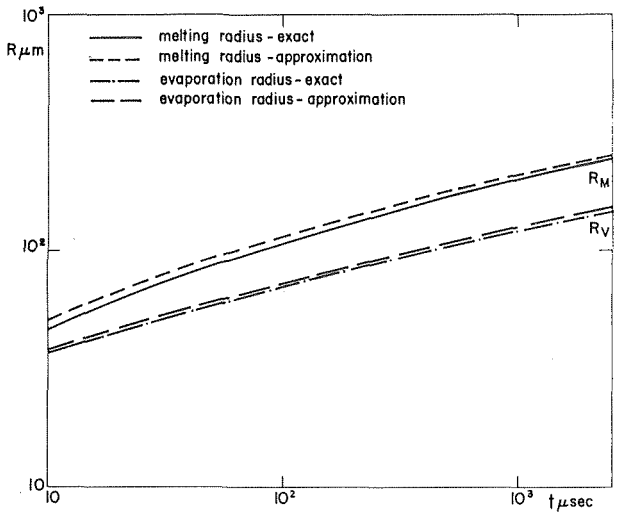

Fig. 2 Propagation of melting and evaporation radii r_M and r_V with time for copper—continuous point source of 2000 W

the melting and evaporation radii of steel to be closer to one another than for copper (see Fig. 2 and 3).

3 Approximate Method for Calculation of Metal Removal

The method described in the foregoing for calculation of the propagation of the melting isotherm is an exact method. Its application to the problem of a point source requires a considerable amount of numerical work and of computer time. For more complex problems the exact method may become cumbersome and a significant increase of numerical computation will be needed. Therefore, an approximate model is suggested, which simplifies the evaluation of the melting crater while taking into account all the phenomena involved. The approximation is made by "transferring" the sinks of melting and evaporation to the site of the point source. The magnitudes q_M and q_V of these sinks remain, however, as in the exact model, equations (2*a*) and (2*b*). Other effects such as ionization and excitation can be included in the model by the addition of similar terms.

The temperature field is, again, expressed by equation (5), but in the approximate model w_M is the temperature field resulting from a time dependent heat source at the origin [28]:

$$w_M = \int_0^\tau \frac{d}{dt} r_M{}^3 \frac{1}{(\tau - \tau')^{3/2}} e^{-r^2/(\tau-\tau')} \qquad (12)$$

and similarly for w_V.

The results of the approximate model for copper and steel are shown in Figs. 2 and 3 and compared with those of the exact method. It can be seen that the approximations are very good, justifying the adoption of this model.

The total erosion of the electrode is found by calculating the volume of the melting crater; in the case of a point source the crater is a half-sphere. The total mass of copper and steel removed by melting and evaporation are plotted in Figs. 4 and 5 versus pulse duration for several source powers. The results show that during short pulses copper is eroded more than steel (for the same power supply) and vice versa for long pulses. The reason is that at the beginning of the pulse melting and evaporation consume most of the energy. As time increases, a steady state is approached where melting and evaporation tend to stop and the energy is conducted into the solid. The latent heats of steel are higher than those of copper; therefore melting and evaporation are more rapid in the latter metal. Since the heat conductivity (or rather kT_M) of copper is higher than for steel, the asymptotic eroded crater is smaller in copper, as explained in the foregoing. These conclusions are also confirmed by the experimental results, see Fig. 6.

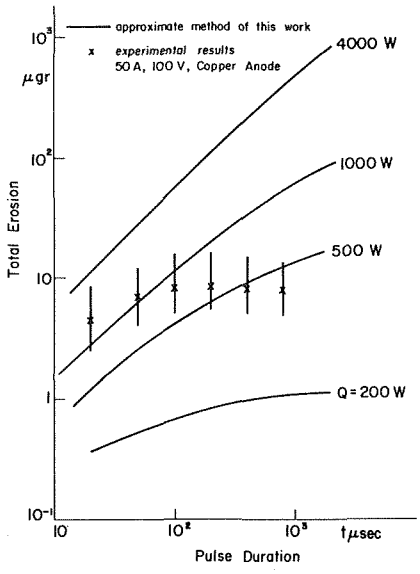

Fig. 4 Total mass of copper eroded by a point source, as a function of the pulse duration

4 Experimental Technique and Results

A single spark is discharged between two electrodes in a cup filled with a dielectric fluid (kerosene), see Fig. 7. The eroded metal is extracted from the dielectric fluid by chemical reaction and the amount is measured by the intensity of colored solutions in a spectro-photometer.

The experimental rig is described in detail in a previous article [27]. The upper electrode is a rod (diameter 6 mm) tapered to a cone and the lower one is a disk (diameter 12 mm, thickness 3 mm). The gap spacing between them is 10 μm and is measured by a micrometer (accuracy 1 μm). The point of contact between the electrodes is determined by the closing of an electrical circuit through an ohm-meter. The pulse generator is capable of producing a rectangular pulse of duration above 20 μs. Experiments were

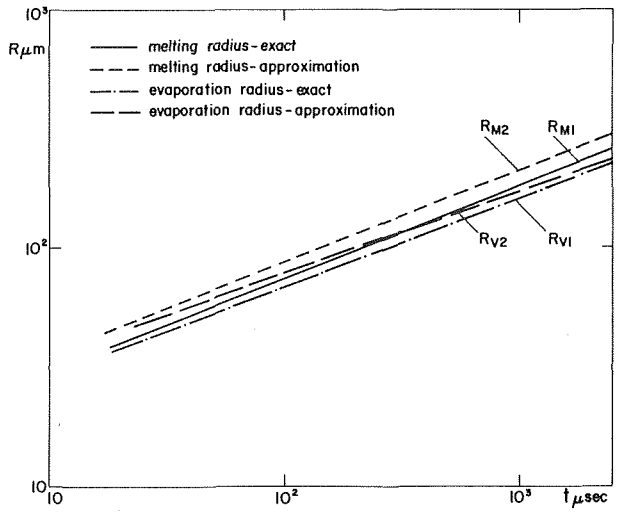

Fig. 3 Propagation of the melting and evaporation radii r_M and r_V with time for steel—continuous point source of 2000 W

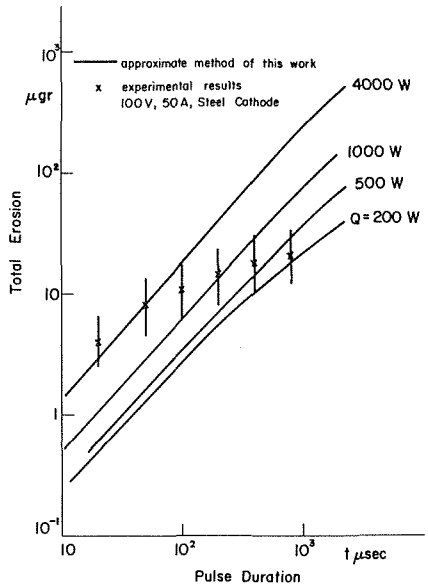

Fig. 5 Total mass of steel eroded by a point source as a function of the pulse duration

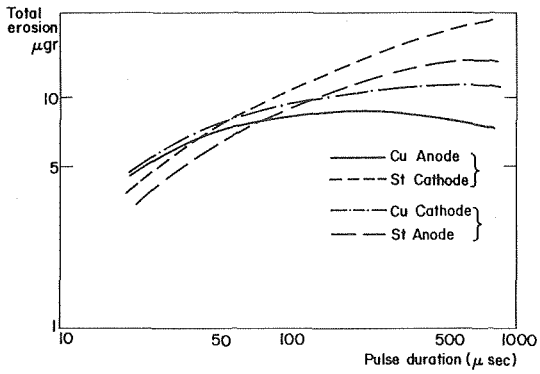

Fig. 6 Total erosion of copper and steel electrodes: 100 V, 50 A

carried out with pulses of 20–1000 μs, pulse voltage of 100 V and current of 50 A. The shape of the pulse is observed in a Tektronix memory oscilloscope. The pulse duration is measured from the moment of breakdown, after the "ignition delay."

The sparks reported here were made between copper and steel. Experiments were carried out first with a conical copper electrode and then with a conical steel electrode. Several experiments were conducted for every pulse duration (20, 50, 100, 200, 400, and 800 μs) and then the polarity was changed for the same configuration.

After each pulse a solution of 10 cm^3 HNO_3 (1:3) is added to the kerosene and dissolves all the eroded metal. The solution is separated and a biquinoline solution is added and reacts with the copper to form a pink colored solution. This solution is separated and the color intensity is measured in the Spectronic 20 spectro-photometer. The amount of copper is determined from a calibration curve. Now, to the other phase which contains the steel, more HNO_3 is added (to pH = 1) and 10cm^3 of 1.5 potassium-thio-cyanate. The latter reacts with the steel and forms a yellow solution. The color intensity is measured, again in the spectro-photometer, and the amount of steel is also determined from a calibration curve.

The experimental results for total erosion of the disk-shaped electrode during a single spark are shown in Fig. 6. It is seen that copper is eroded more than steel at short times (short pulses) and steel is eroded more than copper for long times (long pulse durations), in agreement with the theoretical predictions. Fig. 6 also shows the effect of polarity: erosion is higher when the disk-shaped electrode (the workpiece) is the cathode. This known phenomenon cannot be explained by the melting and evaporation mechanism.

Figs. 4 and 5 include a comparison between the experimental and theoretical results for copper and steel. For each pulse duration, several measurements of single sparks were conducted. The experimental results presented in Figs. 4 and 5 include the averages of these measurements together with the range of variation for each case. The spectro-photometer used for measuring the amounts of the removed metals, is very sensitive. The error involved in measuring amounts of steel and copper did not exceed 0.5 μgr, in the range of the experiments discussed here. It is noted that when the chemical procedure is complicated and takes time, the color of the solution can change if it is exposed to the light. For steel and copper, however, the chemical method is simple and takes only minutes, so there was no such problem. The main reason for the variation in the experimental results is probably the complicated nature of the process of EDM. For example, tiny particles are torn from the electrode surface by electric forces at the beginning of the pulse, e.g., Williams [1–4]. The size and location of such particles depend on the metallurgical condition of the electrode surfaces; since these cannot be exactly reproduced, one cannot expect all the discharges to be exactly the same.

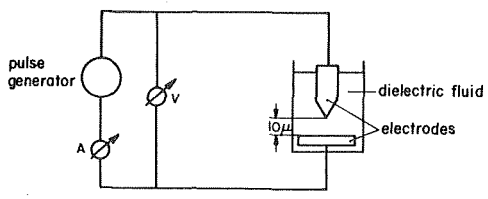

Fig. 7 Schematic arrangement of the EDM circuit

As mentioned in the foregoing, the actual process occurring during the discharge is very complicated. The analytical model presented in this work is a simplified procedure to describe the dominant phenomena of the process, namely melting and evaporation. A more exact model should take into account the energy distribution in the channel, reactions and phase changes in the dielectric fluid, electrical forces, convection in the gas phase, and more complex geometries. Therefore, the theoretical results of this simplified model can hardly be expected to match the experimental findings exactly.

However, it can be seen from Figs. 4 and 5 that for intermediate pulse durations this simple model yields reasonable estimates of total erosion. The agreement between the results indicates that evaporation and melting of the metals are indeed the dominant effects for intermediate pulse durations. For very short pulses electrical forces are considered to be more important [1–4].

For long pulses, a steady state is approached whereby evaporation and melting tend to stop; in this range the experimental results show that the asymptotic constant value of eroded mass is much lower and is reached much sooner than the theoretical predictions. This can be explained by several reasons: (*a*) the discharge channel has a finite width causing a heat source distributed on a finite area rather than a point source; (*b*) ionization and excitation of the evaporated metal and the dielectric fluid take place, requiring energy thus decreasing the energy available for melting; (*c*) a certain part of the eroded material fuses back in the crater after completion of the pulse. The model suggested in this work can be extended to describe the first two effects. In order to overcome the difficulty of the third one and to prevent fusion, flushing of the dielectric fluid between the electrodes may help. It is noted that flushing of the dielectric fluid is being considered for control of the voltage across the gap between the electrodes [19].

Acknowledgment

This research work has been sponsored by the Deutschen Forschungs-Gemeinschaft (D.F.G.).

References

1 Williams, E. M., "Theory of Spark Machining," *AIEE Trans.*, Vol. 71, 1952, pp. 105–108.

2 Williams, E. M., Woodford, J. B., and Smith, R. E., "Recent Developments in the Theory and Design of Electric Spark Machining Tools," *AIEE Trans.*, Vol. 73, 1954, pp. 83–88.

3 Williams, E. M., and Smith, R. E., "Phenomena Accompanying Transient Low-Voltage Discharges in Liquid Dielectric (1)," *AIEE Trans.*, Vol. 74, 1955, pp. 164–169.

4 Williams, E. M., and Smith, R. E.," Phenomena Accompanying Transient Low-Voltage Discharges in Liquid Dielectric (2)," *AIEE Trans.*, Vol. 76, 1957, pp. 94–97.

5 Hockenberry, T. O., and Williams, E. M., "Dynamic Evolution of Events Accompanying the Low-Voltage Discharges Employed in EDM," *IEEE Trans.*, Vol. 1, G.A. No. 4, 1967, pp. 301–309.

6 Zingerman, A. S., "The Effect of Thermal Conductivity Upon the Electrical Erosion of Metals, "*Soviet Physics Technical Physics*, Vol. 1, 1957, pp. 1945–1958.

7 Zingerman, A. S., "Electro Erosional Properties of Metals," *Physics of Metals and Metallography*, Vol. 5, 1957, pp. 58–67.

8 Zolotych, B. N., "The Mechanism of Electrical Erosion of Metals in Liquid Dielectric Media," *Soviet Physics Technical Physics*, Vol. 4, 1960, pp. 1370–1373.

9 Nekrashevitch, I. G., and Bakuto, I. A., "Present State of Theoretical Concepts of the Electrical Erosion of Metals," in *Electrospark Machining of Metals*, Krasijuk, B. A., ed., Consultant Bureau, New York, 1965, pp. 17–22.

10 Afanasiev, N. V., "Theory and Calculation of Electric Erosion Process," in *Electrospark Machining of Metals,* Krasijuk, B. A., ed., Consultant Bureau, New York, 1965, pp. 60–66.

11 Saito, N., "Mechanism of Electric Discharge Machining," *Bulletin of the Japanese Society of Proceedings Engineer,* Vol. 1, No. 2, 1964, pp. 95–101.

12 Heuvelman C. J., "Some Aspects of the Research on Electro-Erosion Machining," *Annals of CIRP,* Vol. XVII, 1969, pp. 195–199.

13 Zolotych, B. N., "Theorie zum Phanomen der Funkenerosiven Bearbeitung," *Fertigung,* Vol. 2, 1971, pp. 185–191.

14 Snoeys, R., and Van-Dyck, F., Investigation of Electrodischarge Machining Operations by Means of Thermo Mathematical Model, *Annals of the CIRP,* Vol. 20, 1971, pp. 35–36.

15 Boley, B. A., "The Analysis of Problems of Heat Conduction and Melting," *High Temperature Structure and Materials, Proceedings of 3rd Symposium on Naval Structural Mechanics,* Pergamon Press, Oxford, 1963.

16 Muehlbauer, J. C., and Sunderland, J. E., "Heat Conduction With Freezing or Melting," *Appl. Mech. Rev.,* Vol. 8, 1965, pp. 951–959.

17 Budhia, H., and Kreith, F., "Heat Transfer With Melting or Freezing in a Wedge," *International Journal of Heat and Mass Transfer,* Vol. 16, 1973, pp. 195–211.

18 Sikarskie, D. L., and Boley, B. A., "The Solution of a Class of Two-Dimensional Melting and Solidification Problems," *International Journal of Solids Structures,* Vol. 1, 1965, pp. 207–234.

19 Pedroso, R. I., and Domoto, G. A., "Exact Solution by Perturbation Method for Planar Solidification of Saturated Liquid With Convection at the Wall," *International Journal of Heat and Mass Transfer,* Vol. 16, 1973, pp. 1816–1819.

20 Lazaridis, A., "A Numerical Solution of the Multidimensional Solidification (or Melting) Problem," *International Journal of Heat and Transfer,* Vol. 13, 1970, pp. 1459–1477.

21 Greene, J. E., and Guerrero-Alvarez, J. L., "Electro Erosion of Metal Surfaces,j' *Metallurgical Transactions,* Vol. 5, 1974, pp. 695–706.

22 Crookall, J. R., and Heuvelman, C. J., "Electro-Discharge Machining—the State of the Art," *Annals of the CIRP,* Vol. 20, 1971, pp. 113–120.

23 Cobine, J. D., and Burger, E. E., "Analysis of Electrode Phenomena in the High Current Arc," *J. Appl. Phys.,* Vol. 26, 1955, pp. 895–900.

24 Smithells, C. J., *Metals Reference Book.* Vol. 3, Butterworths, London, Fourth ed., 1967.

25 Nekrashvich, I. G., and Nitkerich, S. P., "Some Relationships of the Phenomena of the Electrical Erosion of Metals in a Low Voltage Discharge in a Liquid," *Soviet Physics Technical Physics,* Vol. 1, 1956, pp. 83–88.

26 Konnerth, K. L., "A Systematic Experimental Study of Electrode Phenomena Accompanying Transient Low Voltage Arcs in Liquid Dialectrics," PhD dissertation, Department of Electrical Engineering, Carnegie Institute of Technology, 1961.

27 Winograd, U., and Almagor, M., "Experimental Investigation of Electric Discharge Machining by Radioactive Tracers," *J. Eng. Materials and Technology,* TRANS. ASME, 1973, pp. 99–102.

28 Carslaw, H. S., and Jaeger, J. C., *Conduction of Heat in Solids.* Oxford, 1959.

O. M. Silvares
Asst. Professor, Escola Politecnica da Universidade de Sao Paulo, Sao Paulo, Brazil. Assoc. Mem. ASME

E. G. Cravalho
Assoc. Professor Cryogenic Engineering Laboratory. Mem. ASME

W. M. Toscano[1]
Research Associate Cryogenic Engineering Laboratory. Assoc. Mem. ASME

Department of Mechanical Engineering, Massachusetts Institute of Technology, Cambridge, Mass.

C. E. Huggins
Assoc. Professor, Harvard Medical School, Chief, Low Temperature Surgical Unit and Director, Blood Bank and Transfusion Service, Massachusetts General Hospital, Boston, Mass.

The Thermodynamics of Water Transport From Biological Cells During Freezing

A thermodynamic model for the freezing of biological cells has been developed and has been applied to human erythrocytes. Analytical expressions describing the dynamics of water loss during the several stages of the freezing process have been derived from a cell modeled as an open system surrounded by a membrane permeable to water only. The permeability of the membrane to water is the most significant cell parameter in this process and in the present model, and is assumed to be a function of the temperature and osmolality of the extracellular solution. The resulting set of differential equations describing the cell freezing process is solved numerically for various cooling rates. For cooling rates less than 3000 K/min, erythrocytes lose 95 percent of their intracellular water before the eutectic temperature is reached. For cooling rates greater than 3000 K/min, the fraction of intracellular water remaining at the eutectic temperature is a strong function of cooling rate. The effect of supercooling of the extracellular solution on the kinetics of the cell water loss is also analyzed. As a consequence of the supercooling, the volume of water present intracellularly at a given temperature is substantially greater than when no supercooling occurs. This condition favors intracellular ice formation and is consistent with experimental observations in this laboratory.

Introduction

The preservation of biological materials by reversible freezing has been a challenge for a large sector of the scientific community in the fields of medicine, biology, and more recently, engineering. Although the potential of the process has been successfully demonstrated for cells in suspension such as erythrocytes, yeast, and spermatozoa and for some tissues such as skin and human cornea, further research is necessary if this experience is to be extended to other tissues and whole organs. The complexity of the physicochemical processes and the lack of knowledge of the parameters involved in these processes are primarily responsible for the slow development of the basic research in this field.

Analysis of the composition of a large number of plant and animal cells shows that in general a large fraction of the volume of the cell is occupied by water. For example, in human erythrocytes (red blood cells) this fraction is approximately 63.15 percent of cell volume. During freezing and thawing, the amount of intracellular water may be altered drastically by events occurring in the extracellular medium. For instance, ice may form outside the cell during freezing, thereby increasing the concentration of solutes in the extracellular medium. As a result, the chemical potential of water inside the cell will be higher than that outside, and cell water will be expressed through the cell membrane to maintain osmotic equilibrium. On the other hand, it is possible that the temperature of the cell suspension is decreased more rapidly than the cell can respond osmotically, and water inside the cell is nucleated before significant mass transfer can occur. Obviously, the final intracellular water content is vastly different in these two cases.

Mazur [1][2] has developed an analytical model to study the kinetics of water loss from cells at subfreezing temperatures from which he inferred predictions about the onset of intracellular ice formation. This model has been tested experimentally for some simple cells, and some of these experiments have confirmed the findings

[1] Present address: Cryogenic Technology, Inc., Waltham, Mass.

Contributed by the Heat Transfer Division for publication in the JOURNAL OF HEAT TRANSFER. Manuscript received by the Heat Transfer Division July 8, 1975. Paper No. 76-HT-0.

[2] Numbers in brackets designate References at end of paper.

of the model [2–4] whereas others [5, 6] have found quantitative data that contradict the model. Mazur's model predicts that intracellular ice will form in essentially all red cells at a cooling rate of 3000 K/min, but Diller, et al. [6] have observed experimentally that the frequency of intracellular ice increased from 0 percent at −840 K/min to 100 percent at −850 K/min. These investigators have also noted that when the extracellular medium is allowed to supercool 12 K, the frequency of intracellular freezing increases from 0 percent at −6 K/min to 100 percent at −16 K/min. Diller, et al. [7] point out that other parameters not included in Mazur's model may also affect its ability to predict the cooling rate that marks the onset of intracellular ice.

Mazur [8] has also postulated that two mechanisms of freezing injury are responsible for the inverted U-shape of the survival signatures (survival versus cooling rate curve): "solution effects" and "intracellular freezing." The solution effect is responsible for the damage of cells cooled at rates below the optimum value which gives maximum survival. During the freezing period, pure ice precipitates in the extracellular medium and the cells are trapped in pools of concentrated salt solution in the liquid state. When the cells are cooled slowly, the time during which the cells are subject to this increasingly concentrated solution is longer than when cooled rapidly. During this period, the osmotic pressure difference builds up and the cell dehydrates causing the solute concentration inside the cell to increase to lethal levels.

At higher cooling rates, there is less time available for the intracellular solution to equilibrate osmotically with the extracellular medium. Thus, at any particular temperature, there is more water inside the cell, and the larger the volume of supercooled water remaining inside the cell, the greater the probability of ice nucleation inside the cell. Although there is experimental evidence that the intracellular ice is a damaging factor for the cell [9, 10], the precise mechanism responsible for the damage is not yet understood.

In the present work, we shall discuss the thermodynamic processes involved during cell freezing with special attention devoted to the human erythrocyte as a cell model. We also shall develop a more complete thermodynamic model that describes these events and includes factors neglected in Mazur's analysis.

Analysis

The biological cell immersed in its natural medium is modeled as a single cell immersed in a salt solution. As shown in Fig. 1, the cell contains water, salts, and proteins enclosed in a semipermeable membrane which allows water, but not solutes, to flow across it. The pressure is assumed uniform throughout the system and constant. Thermal equilibrium is assumed to prevail even when the temperature is changing with time. Both the intracellular and extracellular media are homogeneous. Initially the internal and external media are in chemical equilibrium, i.e., the chemical potentials of the various components are equal across the membrane in the initial state.

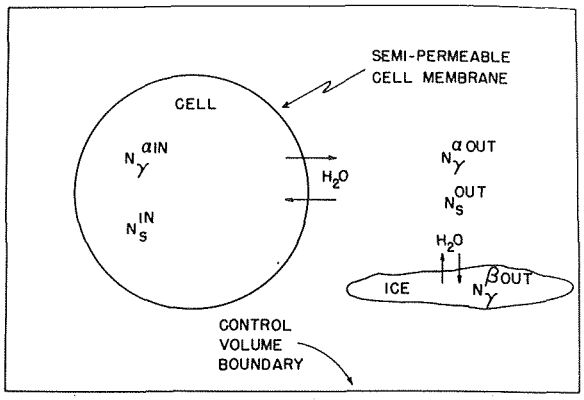

Fig. 1 Physical model for the freezing of a biological cell

The extracellular medium is modeled as an aqueous solution of sodium chloride in which the salt is completely disassociated. In keeping with the experimental observations of McGrath [11] and others, it is assumed that during the freezing process the external medium nucleates first, followed by intracellular nucleation if the thermodynamic conditions are suitable. The mechanisms of ice formation are too complex to be treated here but are discussed by the present authors in a related paper [12]. Nucleation in the extracellular medium upsets the chemical equilibrium that prevails initially across the membrane. Since the membrane offers a finite resistance to the flow of water through it, a difference in chemical potential forms across the membrane. The present model assumes that once ice forms extracellularly, chemical equilibrium prevails

Nomenclature

A = surface area, μ^2
A_γ = affinity of the reaction, erg/mole
$a_{T,P}$ = partial derivative of affinity with respect to ξ at constant T and P [$\equiv(\partial A/\partial\xi)_{T,P}$], erg/mole
B = cooling rate, K/min
b = permeability temperature coefficient, $(K)^{-1}$
c_{Pi} = partial molar heat capacity of i at constant P, erg/mole-K
H = molar enthalpy, erg/mole
$h_{T,P}$ = heat of reaction at constant T and P[$\equiv(\partial H/\partial\xi)_{T,P}$], erg/mole
k = permeability of cell membrane, $(mole)^2/\mu^5$-atm-min
k^* = permeability of cell membrane, μ^3/μ^2-min-atm
L_γ = latent heat of fusion at temperature T, erg/mole
L_γ° = latent heat of fusion at temperature T_M, erg/mole
L_p = permeability coefficient, cm^3/dyne-s
n = number of moles
P = absolute pressure, dyne/cm^2
R = universal gas constant, erg/mole-K
T = absolute temperature, K
T_g = permeability reference temperature, K
T_M = melting temperature of pure water, K
T_N = nucleation temperature of the extracellular solution, K
t = time, s
t_N = time of onset of nucleation, s
V = volume, μ^3
V_i = initial volume, μ^3
v_m = partial molar volume of water, cm^3/mole
$v_{T,P}$ = volume change of reaction at constant T and P [$\equiv(\partial V/\partial\xi)_{T,P}$], cm^3/mole
x = molar fraction
γ = activity coefficient
ΔT_s = degree of supercooling, K
μ = specific molar chemical potential, erg/mole
μ^* = specific molar chemical potential of pure component, erg/mole
ν = osmolality, mOsm/l
ξ = extent of reaction
ϕ = osmotic coefficient

Subscript

s = solute
γ = solvent

Superscript

in = intracellular
out = extracellular
α = liquid phase
β = solid phase

between the solid and liquid phases in the extracellular medium as the uniform temperature of the cell suspension decreases with time. Thus, the flow resistance of the membrane causes the intracellular medium to be supercooled.

In a typical freezing protocol there are at least four distinct stages: Stage I—Cooling prior to the onset of nucleation in the extracellular medium. During this period equilibrium conditions prevail throughout the system as the temperature decreases. Stage II—Cooling after extracellular nucleation. During this period equilibrium conditions prevail between the liquid and solid phases in the extracellular medium, and the intracellular solution follows a path in the supercooled region of the phase diagram. Stage III—Cooling below the eutectic temperature. The extracellular solution solidifies completely below the eutectic temperature. Stage IV—Holding period at minimum temperature. When the system reaches the desired minimum temperature it is kept at a constant temperature for a period of time.

Stage I—Cooling Prior to the Onset of Extracellular Nucleation. It is possible for the extracellular medium to be supercooled as a consequence of the dynamics of extracellular nucleation, but this supercooling terminates the instant ice forms. The intracellular medium will continue to be supercooled throughout the freezing process even though ice is present extracellularly. The phase diagram of Fig. 2 shows a typical situation. A cell suspension with an initial water molar fraction of $x_{\gamma 1}{}^{\alpha\,\mathrm{out}}$ is cooled at a constant rate B. If no supercooling occurs in the extracellular medium, the temperature of the suspension decreases continuously with uniform chemical potential of the water inside and outside the cell given by

$$\mu_\gamma{}^{\alpha\,\mathrm{in}} = \mu_\gamma{}^{\alpha\,\mathrm{out}} = \mu_\gamma{}^{*}\,(T,P) + RT_1\phi_1 \ln x_{\gamma 1}. \tag{1}$$

The intracellular and extracellular solutions are assumed to have equal osmotic coefficients so equation (1) implies

$$x_{\gamma 1}{}^{\alpha\,\mathrm{in}} = x_{\gamma 1}{}^{\alpha\,\mathrm{out}} \tag{2}$$

When state 1 is reached, extracellular nucleation occurs. Further cooling of the cell suspension forces the extracellular medium to follow the locus of two-phase equilibrium states. If the thermodynamics of the situation are such that the extracellular nucleation does not occur in state 1, the suspension supercools and the path of the cooling process continues beyond the two-phase equilibrium line. In Fig. 2, state 2 would be such a state for which the chemical potential of the water would be given by

$$\mu_{\gamma 2}{}^{\alpha\,\mathrm{in}} = \mu_{\gamma 2}{}^{\alpha\,\mathrm{out}} = \mu_\gamma{}^{*}\,(T,P) + RT_2\phi_1 \ln x_{\gamma 1} \tag{3}$$

which again implies equation (2).

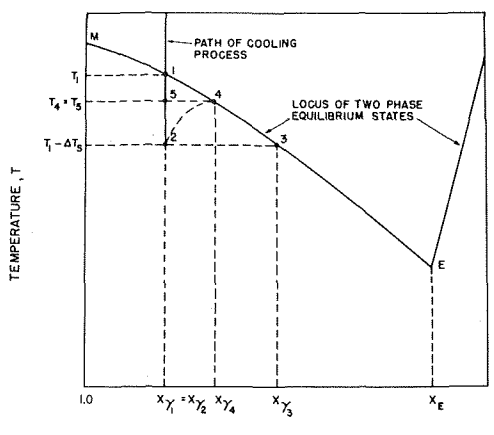

Fig. 2 Initial states for the freezing process

Stage II—Cooling After Extracellular Nucleation. When a suspension in state 2 nucleates in the extracellular medium, it is assumed that the solution outside the cell will revert to an equilibrium state located somewhere on the locus of two-phase equilibrium states. The exact location will depend on the latent heat released relative to the refrigeration power producing the cooling process. In the general case of cells frozen in bulk, a limited amount of refrigeration power is available. Consequently, the nucleation of the extracellular solution is a nonisothermal process in which the latent heat of fusion released during the nucleation increases the temperature of the system. The extracellular solution reaches an equilibrium state somewhere on the locus of two-phase equilibrium states as represented by point 4 in Fig. 2. Because the cell is not able to respond to the osmotic pressure difference that can develop across its membrane during the time period required for the nucleation of the extracellular solution, the molar fraction of the intracellular water will remain constant, and the state of the intracellular solution may be represented by point 5 in Fig. 2. Thus for the general case the states corresponding to points 4 and 5 in Fig. 2 represent the initial conditions for Stage II of the freezing process. In the present analysis it is assumed that the refrigeration power is sufficient to counteract exactly the latent heat released during the phase change. Thus, the nucleation of the extracellular medium will follow an isothermal path in the phase diagram and its state just after nucleation occurs will correspond to point 3 in Fig. 2. This is approximately the case that prevails in the freezing of cell suspensions in thin layers like the ones used in cryomicroscopic observations. Note that the present analysis can be applied even in the more common case in which cooling follows states 1, 2, and 4 in Fig. 2, and where ΔT_s is made to approach zero.

For this new equilibrium state, the chemical potential of the water in the external liquid solution is given by

$$\mu_\gamma{}^{\alpha\,\mathrm{out}} = \mu_\gamma{}^{*}\,(T,P) + RT_3\phi_3 \ln x_{\gamma 3}{}^{\alpha\,\mathrm{out}}. \tag{4}$$

If the degree of supercooling ΔT_s is small compared with the value of the temperature T_1, $\phi_3 \ln x_{\gamma 3}{}^{\alpha\,\mathrm{out}}$ in equation (4) can be obtained by a Taylor's series expansion around the initial equilibrium state (state 1 in Fig. 2).

$$\phi_3 \ln x_{\gamma 3}{}^{\alpha\,\mathrm{out}} = \phi_1 \ln x_{\gamma 1}{}^{\alpha\,\mathrm{out}} - \frac{\partial}{\partial T}\left(\phi_1 \ln x_{\gamma 1}{}^{\alpha\,\mathrm{out}}\right) \Delta T_s \ldots \tag{5}$$

In order to evaluate the first derivative in equation (5), it is necessary to determine the equation of the equilibrium curve in Fig. 2. It can be shown [13] that along the equilibrium curve the mole fraction is related to the latent heat of fusion.

$$\ln \gamma_\gamma{}^{\alpha\,\mathrm{out}} x_\gamma{}^{\alpha\,\mathrm{out}} = \int_{T_M}^{T} (L_\gamma/RT^2)\, dT \tag{6}$$

The temperature dependence of the latent heat of fusion is given in [13] by

$$L_\gamma(T) = L_\gamma{}^{\circ} + \int_{T_M}^{T} (c_{P\gamma}{}^{\alpha} - c_{P\gamma}{}^{g}rkb)\, dT. \tag{7}$$

Substitution of equation (7) into equation (6) yields

$$\ln \gamma_\gamma{}^{\alpha\,\mathrm{out}} x_\gamma{}^{\alpha\,\mathrm{out}} = -\frac{L_\gamma{}^{\circ}}{R}\left(\frac{1}{T} - \frac{1}{T_M}\right) - \frac{c_{P\gamma}{}^{\alpha} - c_{P\gamma}{}^{\beta}}{R}\left[\ln\left(\frac{T_M}{T}\right) - \frac{T_M}{T} + 1\right]. \tag{8}$$

The relationship between the activity coefficient and the osmotic coefficient is by definition

$$\ln \gamma_\gamma{}^{\alpha\,\mathrm{out}}\, x_\gamma{}^{\alpha\,\mathrm{out}} = \phi \ln x_\gamma{}^{\alpha\,\mathrm{out}}. \tag{9}$$

Substitution of equation (9) into equation (8) and differentiation with respect to T, yields

$$\frac{\partial(\phi \ln x_\gamma{}^{\alpha\,\mathrm{out}})}{\partial T} = \frac{L_\gamma{}^{\circ}}{RT^2} - \frac{c_{P\gamma}{}^{\alpha} - c_{P\gamma}{}^{\beta}}{R}\left(\frac{T_M}{T^2} - \frac{1}{T}\right). \tag{10}$$

Terms with derivatives of higher order than the first can be neglected in the series expansion. Then equation (5) can be written

$$\phi_3 \ln x_{\gamma 3}{}^{\alpha\,\text{out}} = \phi_1 \ln x_{\gamma 1}{}^{\alpha\,\text{out}} - \frac{L_\gamma{}^\circ \Delta T_s}{R T_1{}^2} + \frac{c_{P\gamma}{}^\alpha - c_{P\gamma}{}^\beta}{R}\left(\frac{T_M}{T_1{}^2} - \frac{1}{T_1}\right)\Delta T_s \quad (11)$$

Substitution of equation (11) into equation (4) together with equations (1) and (3) and the assumptions that (*a*) the variation of the osmotic coefficient with temperature is negligible, and (*b*) the intracellular and extracellular solutions have the same osmotic coefficient, yields the difference in the chemical potential between the supercooled and equilibrium states.

$$\mu_{\gamma 2}{}^{\alpha\,\text{in}} - \mu_{\gamma 3}{}^{\alpha\,\text{out}} = L_\gamma(T_1) T_3 \Delta T_s / T_1{}^2 \quad (12)$$

If the extracellular medium assumes the equilibrium state at the instant of nucleation while the intracellular medium remains in the supercooled state because of the membrane permeability, equation (12) gives the relationship between the water molar fraction of the solutions inside and outside the cell when nucleation occurs.

$$x_{\gamma 2}{}^{\alpha\,\text{in}} / x_{\gamma 3}{}^{\alpha\,\text{out}} = \exp\left[L_\gamma(T_1)\Delta T_s / \bar{\phi} R T_1{}^2\right] \quad (13)$$

where $\bar{\phi}$ is the average value of the osmotic coefficient between the molar fractions $x_{\gamma 1}{}^{\alpha\,\text{in}}$ and $x_{\gamma 3}{}^{\alpha\,\text{out}}$. Equation (13) then gives the initial conditions for the process of freezing subsequent to extracellular nucleation.

The loss of extracellular water due to the formation of the solid phase results in the difference between the chemical potentials inside and outside the cell described earlier. The cell contents attempt to equilibrate with the external medium by water transport across the semipermeable membrane. The flux of water across the membrane is given by the phenomenological expression.

$$J_\gamma = -k(\mu_\gamma{}^{\alpha\,\text{in}} - \mu_\gamma{}^{\alpha\,\text{out}}). \quad (14)$$

Then the rate of change of the water content inside the cell is

$$\frac{dn_\gamma{}^{\alpha\,\text{in}}}{dt} = -kA(\mu_\gamma{}^{\alpha\,\text{in}} - \mu_\gamma{}^{\alpha\,\text{out}}). \quad (15)$$

Introduction of the definition of the cooling rate, i.e., $B = dT/dt$ into equation (15) yields

$$\frac{dn_\gamma{}^{\alpha\,\text{in}}}{dT} = -kA(\mu_\gamma{}^{\alpha\,\text{in}} - \mu_\gamma{}^{\alpha\,\text{out}})/B. \quad (16)$$

The succession of thermodynamic states through which the extracellular system passes during Stage II of the freezing protocol can be represented by a succession of equilibrium states which can be described by the van't Hoff relation, viz.

$$\frac{\partial \mu_\gamma{}^{\alpha\,\text{out}}}{\partial n_\gamma{}^{\alpha\,\text{out}}}\left[\frac{dn_\gamma{}^{\alpha\,\text{in}}}{dT} + \frac{dn_\gamma{}^{\beta\,\text{out}}}{dT}\right] = -\frac{L_\gamma}{T}. \quad (17)$$

Equation (17) represents displacement of the state of the extracellular medium along the equilibrium line. It gives the variation of the number of moles of water in the solid phase with respect to temperature.

Stage III—Cooling Below the Eutectic Temperature. When the system reaches the eutectic temperature, the extracellular medium is completely solidified. The thermodynamic state of the intracellular medium at this temperature depends on the cooling rate. In the low range of cooling rates, quasi-equilibrium conditions across the membrane prevail before the system has reached the eutectic temperature. Thus, no significant volume of water is transferred at subeutectic temperatures, and the solid phase is present on both sides of the cell membrane. In the high range of cooling rates, the system is far from equilibrium when the temperature reaches the eutectic value. Supercooled intracellular water then continues to flow across the membrane and immediately freezes extracellularly in order to maintain the equilibrium between solid and liquid phases outside the cell. In this case, the equilibrium relation of equation (17) is replaced by

$$\frac{dn_\gamma{}^{\beta\,\text{out}}}{dT} = -\frac{dn_\gamma{}^{\alpha\,\text{in}}}{dT} \quad (18)$$

and equation (16) and (18) are solved simultaneously with the initial conditions corresponding to those at the eutectic temperature. This system of differential equations describes Stage III of the freezing protocol.

Stage IV—Water Transfer at Minimum Temperature. Stage IV of the freezing protocol is characterized by a constant temperature mass transfer. In order to maintain solid-liquid equilibrium in the extracellular medium at the minimum temperature, all the water transferred across the membrane during this period must solidify immediately extracellularly. This equilibration process is described by equation (16) and the following equilibrium relation in the time domain

$$\frac{dn_\gamma{}^{\beta\,\text{out}}}{dt} = -\frac{dn_\gamma{}^{\alpha\,\text{in}}}{dt}. \quad (19)$$

The initial conditions for this system of differential equations are those corresponding to the final state of the cooling period.

Conservation of Mass of Water and Solutes. Since the control volume in Fig. 1 is closed, water and all solutes must be conserved within its boundaries. Then the following conservation equations must be satisfied at all times

$$n_\gamma{}^{\alpha\,\text{in}} + n_\gamma{}^{\alpha\,\text{out}} + n_\gamma{}^{\beta\,\text{out}} = \text{constant} \quad (20)$$

and

$$n_s{}^{\text{in}} + n_s{}^{\text{out}} = \text{constant} \quad (21)$$

and in addition $n_s{}^{\text{in}}$ and $n_s{}^{\text{out}}$ are constant due to the assumed impermeability of the cell membrane to solutes.

Initial Conditions. The initial conditions for the integration of the system of differential equations describing Stage II of the freezing protocol are the following:

1 At $T = T_2 = T_1 - \Delta T_s$ (nucleation temperature of the extracellular medium)

$$\frac{x_\gamma{}^{\alpha\,\text{in}}}{x_\gamma{}^{\alpha\,\text{out}}} = \exp\left[L_\gamma(T_1)\,\Delta T_s / \bar{\phi} R T_1{}^2\right]. \quad (22)$$

If the supercooling is zero (i.e., $\Delta T_s = 0$), equation (22) reduces to

$$x_\gamma{}^{\alpha\,\text{in}} = x_\gamma{}^{\alpha\,\text{out}} \quad (23)$$

2 At $T = T_2$

$$n_\gamma{}^{\alpha\,\text{in}} = n_{\gamma 0}{}^{\alpha\,\text{in}} \quad (24)$$

where $n_{\gamma 0}{}^{\alpha\,\text{in}}$ is the number of moles of water inside the cell under isotonic conditions.

The initial conditions for the remaining stages of the freezing protocol correspond to the final conditions of the previous stage, i.e., if the minimum temperature is lower than the eutectic temperature, the number of moles of water inside and outside the cell and in the solid phase at the end of Stage II, represents the initial condition for the integration of the system of differential equations describing Stage III of the freezing protocol. When the temperature reaches the pre-established minimum value, the final values of the variables constitute the set of initial conditions for Stage IV of the freezing protocol. The intracellular water content at any temperature during freezing is given by

$$V_\gamma{}^{\alpha\,\text{in}} = n_\gamma{}^{\alpha\,\text{in}} v_m. \quad (25)$$

Results

The model just presented is general and may be applied to single cells satisfying the conditions stated. One type of cell for which freezing is of great clinical importance is the human red blood cell.

Human Erythrocyte Geometry and Composition. Measure-

ments of the diameter, area, and volume of the individual human red blood cells have been reported by several investigators [14–16] using different techniques, but the geometric parameters used in the present work are those averaged values determined by Canham and Burton [14], i.e., an average volume, surface area, and diameter of 107.5 μ^3, 138.1 μ^2, and 8 μ, respectively. In the present model it was assumed that the surface area is constant and equal to the average value regardless of any changes that may occur to the volume of the cell during freezing.

The human erythrocyte is an unnucleated cell containing a complex aqueous solution of hemoglobin, nonhemoglobin proteins, lipids, glucose, electrolytes, and other components (see references [17, 18]). However, approximately 97 percent of its volume is occupied by water and hemoglobin with the volume of intracellular water available for transport representing 63.15 percent of the total volume of cell. (The actual volume of water in the cell is 71.5 percent of the total volume but 11.6 percent of this water is water of hydration associated with the hemoglobin.) In osmotic experiments, Farrant and Woolgar [19] have shown that the mass of intracellular water at 273.15 K decreases as the osmolality of the suspending medium increases. However, beyond 2000 mOsm/l, when the weight of the cell water is 0.33 of that in the cell under isotonic conditions, very little additional loss of water occurs. In the application of the present model to erythrocytes, we have assumed that all the water is transferable because the concentration of the extracellular solution equal to 2000 mOsm/l (corresponding to a temperature during freezing of 269.35 K) reported by Farrant, is still low compared with the concentration that the cell will be exposed to at temperatures as low as 252.0 K (eutectic point for NaCl-aqueous solution).

Composition of the External Medium. The human red cell "in vivo" is suspended in an aqueous solution containing primarily proteins and salts. It is common clinical practice to suspend packed red blood cells in normal saline solution with no significant damage to the cell. In the present model we have assumed that the extracellular medium is a sodium chloride aqueous solution which initially is isotonic, i.e., 0.154 moles of NaCl in 1 l of solution.

Water Permeability of the Erythrocyte Membrane. Several studies on the permeability of human erythrocyte membranes to water are available. The effect of temperature on the permeability to water was first measured by Jacobs, et al. [20] and these data suggest that the temperature dependence of water permeability (for the temperature range of their experiments, 303.15–273.15 K) is given by

$$k^* = k_g \exp[b(T - T_g)]. \tag{26}$$

Experiments to determine the constants k_g and b have been carried out in the temperature range above 273.15 K. One of the more recent determinations of these constants was by Sidel and Solomon [21] and their values are $k_g = 5\mu^3/\mu^2$ min-atm and $b = 0.0325(\mathrm{K})^{-1}$. Recently Rich, et al. [22] studied the effect of the external medium osmolality on the water permeability of human and dog erythrocytes. They found that the permeability coefficient for water, L_p, (identical to the permeability, k^*, except for the system of units) of human red blood cells varies from 1.87×10^{11} cm^3/dyne-s at 199 mOsm/l to 0.76×10^{11} cm^3/dyne-s at 516 mOsm/l. In addition they found that the change in L_p is rather rapid and it is completed within 50 ms after a finite change in the osmolality of the external medium. It can be shown that their experimental data for human red blood cells obey the following relationship:

$$\ln L_p = 335.174/\nu - 26.2864. \tag{27}$$

Since during freezing the concentration of the extracellular medium varies as the temperature changes, the combined effect of these two factors on the permeability is given by

$$k = 1.852 \times 10^{-15} \exp\,[335.174/\nu - 26.2864 + b(T - T_g)]. \tag{28}$$

Other factors may influence the permeability of the membrane at subzero temperatures, but these are not included in the present analysis [23].

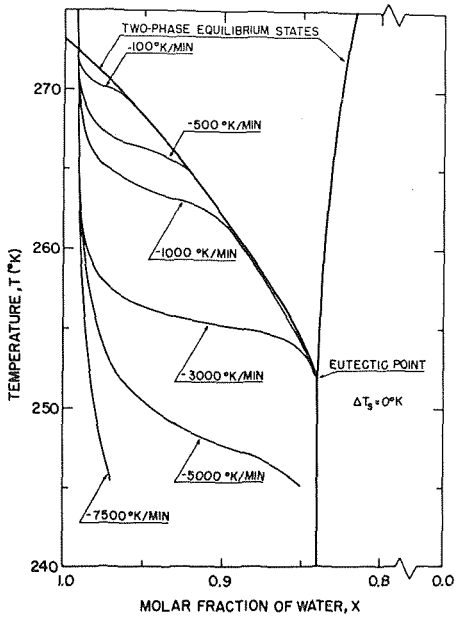

Fig. 3 Locus of states of intracellular solutions cooled at different rates with no supercooling—locus of states of extracellular solution coincident with two-phase equilibrium states for all cooling rates

Osmotic Coefficient. In the integration of equation (17), the nonideality of the external solution is accounted for by the osmotic coefficient which is a function of the concentration of solutes in the solution. Values of this parameter for sodium chloride solutions have been determined by Robinson and Stokes [24] for the equilibrium conditions that prevail in the extracellular medium at any given temperature. The effect of the hemoglobin on the osmotic coefficient of the intracellular solution was neglected because of its low molality [25].

Application of the Model. For the case of human erythrocytes the set of differential equations governing the water flow from biological cells during Stages II, III, and IV of the freezing protocol were solved numerically. Fig. 3 shows the thermodynamic state of the intracellular solution of a cell cooled at several rates with zero supercooling. The locus of the thermodynamic states of the extracellular solution in all cases follows the equilibrium curve. The cooling rate of 3000 K/min distinguishes two different modes of behavior of the system below the eutectic temperature. For cooling rates lower than 3000 K/min the system reaches equilibrium before the eutectic temperature and no changes in volume occur below that temperature. For cooling rates greater than 3000 K/min, Fig. 3 shows that supercooled intracellular water continues to be transferred at subeutectic temperatures as described previously.

The effect of the membrane permeability on the cooling trajectory is presented in Fig. 4 in which the locus of states of the intracellular medium are shown for cooling cells of different permeabilities at a fixed rate of 1000 K/min. The variation of the cell permeability was obtained by changing the reference temperature T_g in equation (28). While this method of varying k^* is not physically realistic, it is convenient from a computational point of view; the net result of this technique is the same as a simultaneous variation of k_g and b. Thus, from Figs. 3 and 4 it follows that the cooling trajectory of a cell with a high water membrane permeability cooled at a low rate is similar to the cooling trajectory of a cell with a low water permeability cooled at a high rate.

During State IV of the freezing protocol, the cooling process is suppressed and the temperature is maintained constant and equal to that value. Depending on the cooling rate and the minimum

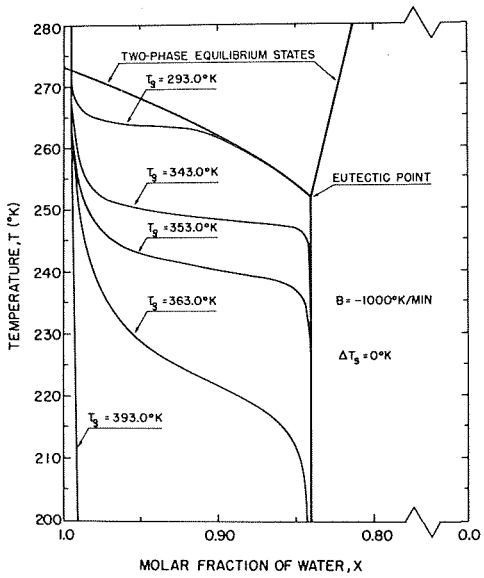

Fig. 4 Effect of membrane permeability on locus of states of intracellular solution cooled at 1000 K/min

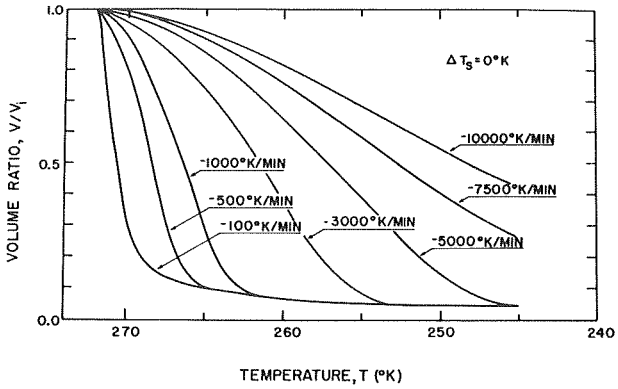

Fig. 6 Volume of intracellular water of erythrocytes cooled at constant rates with no supercooling

temperature, equilibrium conditions across the membrane may not be established at that instant. The chemical potential difference between the two compartments forces water to flow across the membrane at constant temperature. This isothermal process continues until equilibrium across the membrane is reached. A typical example of this equilibration period is presented in the phase diagram in Fig. 5.

Fig. 6 presents the variation of the volume of the erythrocyte water content during freezing at several cooling rates. Fig. 7 compares the results of the present model with those obtained by Mazur [1] for some typical cooling rates. The quantitative differences between the two models are not due to any differences in basic assumptions, but instead due primarily to the different models of the water permeability and the different values assumed for the cell surface area. Mazur assumed that the water permeability of the erythrocyte membrane is a function of temperature only, but in the present model the permeability was assumed to be dependent upon the temperature and the osmolality of the external medium as discussed earlier. Note that the present model assumes that the solutions behave as nonideal solutions and the latent heat of fusion varies with temperature, whereas the model in reference [1] assumed ideal solution behavior and constant heat of fusion. Comparison of these two models for a given permeability functional dependence shows these refinements to have a negligible effect on the calculated volume of cell water during freezing. On the basis of recent experiments in this laboratory, the results of the present model for the cell permeability are a better representation of the actual conditions associated with the freezing of red blood cells.

Fig. 8 presents the state of the intracellular solution of cell suspensions subjected to supercooling of the extracellular medium for several cooling rates. Fig. 9 shows the temperature dependence of the intracellular water content of those cells. The comparison between Figs. 3 and 8 shows that for the same cooling rate, the initial water flux across the membrane is significantly larger when supercooling of the extracellular medium occurs, than the case when the supercooling is zero. The same conclusion is apparent by comparing the slopes of curves in Fig. 6 with those in Fig. 9. Thus, when the extracellular medium supercools 10 K, the reduction in volume after extracellular nucleation is much faster than when no supercooling occurs. This effect is more noticeable in the low range of cooling rates. The effect of the supercooling is particularly important for the study of the conditions for intracellular nucleation as

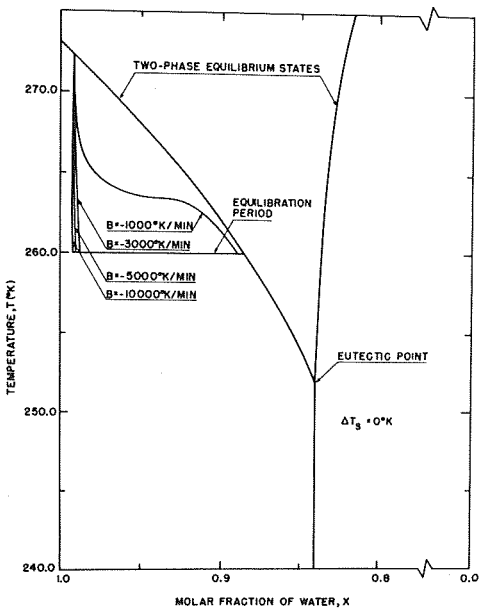

Fig. 5 Equilibration of intracellular and extracellular solutions held at minimum temperature after cooling at several rates

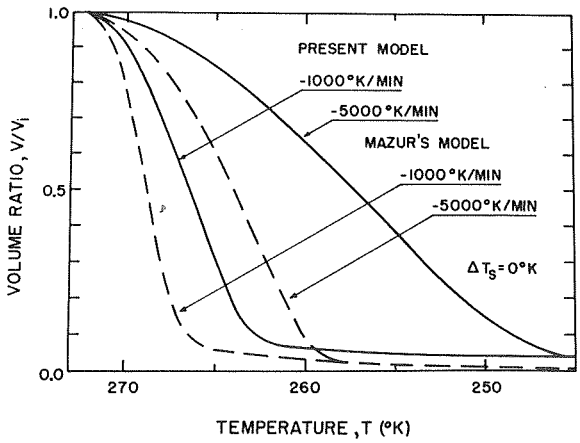

Fig. 7 Volume of intracellular water of erythrocytes cooled at constant rates with no supercooling for present model and model in [1]

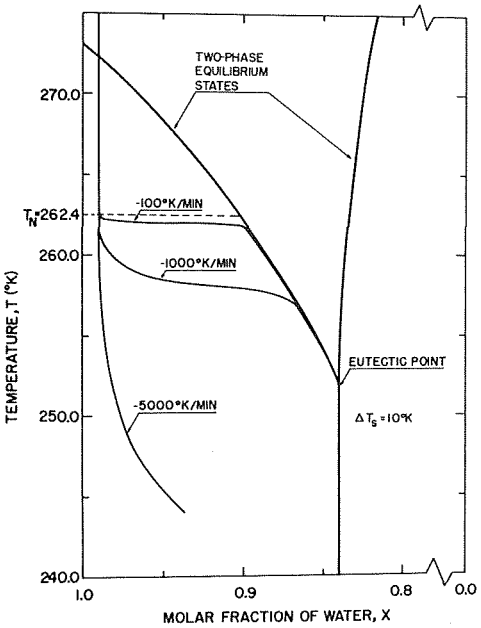

Fig. 8 Locus of states of intracellular solutions cooled at different rates with supercooling of 10 K—for all cooling rates the locus of states of extracellular solution coincident with two-phase equilibrium states for temperatures less than nucleation temperatures

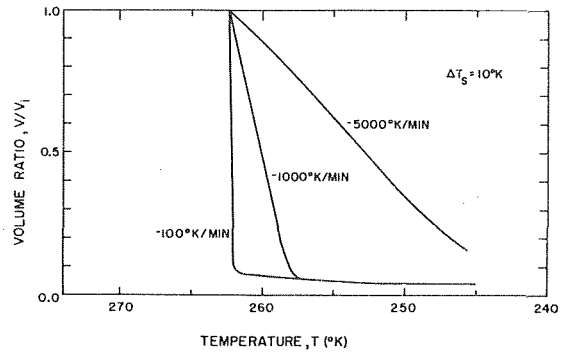

Fig. 9 Volume of intracellular water of erythrocytes cooled at constant rates with supercooling of 10 K

discussed in a related paper [12].

Conclusions

The present analysis quantifies the competition between heat transfer and mass transfer during freezing of cell suspensions. At low cooling rates, mass transfer dominates and a considerable portion of the intracellular water leaves the cell to form extracellular ice. At high cooling rates, heat transfer dominates as the temperature is reduced at a faster rate than water can flow through the membrane. The resulting large volume of intracellular water favors intracellular ice nucleation.

The present analysis also shows that high extracellular osmolality attendant to freezing introduces an additional resistance to transmembrane water transport that must be superimposed on the temperature dependence of the permeability. The net result is a reduction in intracellular water loss during freezing. The analysis demonstrates the major role of the water permeability of the membrane and the necessity for further experimental measurements of cell permeability if the freezing process in biomaterials is to be better understood. The present results also show that nonideal solution behavior and a temperature dependent heat of fusion do not result in any significant improvement to models in which these effects are neglected. In the present analysis the consequence of supercooling the extracellular medium is that a larger volume of water remains inside the cell at lower temperatures than when no supercooling occurs. This condition also favors intracellular ice formation.

Acknowledgments

This work was supported in part by USPHS Grant 1 P01 HL4322-03 from NHLI; and Fundacao de Amparo a Pesquisa do Estado de Sao Paulo and Estola Politecnica de Universidade de Sao Paulo, Brazil.

References

1 Mazur, P., "Kinetics of Water Loss From Cells at Subzero Temperatures and the Likelihood of Intracellular Freezing," *Gen. Physiol.*, Vol. 47, 1963, pp. 347–369.

2 Ushiyama, M., "Volumetric Changes in Saccharomyces Cerivisiae During Freezing at Constant Cooling Velocities," ScM thesis, Massachusetts Institute of Technology, Department of Mechanical Engineering, 1973.

3 Mazur, P., "Manifestations of Injury in Yeast Cells Exposed to Subzero Temperatures. I. Morphological Changes in Freeze-Substituted and in Frozen-Thawed Cells," *J. Bacteriol.*, Vol. 82, 1961, pp. 662–672.

4 Nei, T., "Effects of Freezing and Freeze-drying on Microorganisms," in *Recent Research in Freezing and Drying*, A. S. Parkes and A. U. Smith, eds., 1960, pp. 78–86.

5 Diller, K. R., "A Microscopic Investigation of Intracellular Ice Formation in Frozen Erythrocytes," ScD thesis, Massachusetts Institute of Technology, Department of Mechanical Engineering, 1972.

6 Diller, K. R., Cravalho, E. G., and Huggins, C. E., "An Experimental Study of Freezing in Erythrocytes," to be published in the *Journal of Medical and Bio Engineering*, 1975.

7 Diller, K. R., Cravalho, E. G., and Huggins, C. E., "Intracellular Freezing in Biomaterials," *Cryobiology*, Vol. 9, 1972, pp. 429–444.

8 Mazur, P., "Causes of Injury in Frozen and Thawed Cells," *Fedn. Proc. Fedn. Am. Socs. Exp. Biol.*, Vol. 24, suppl. 15, 1965, pp. S175–S182.

9 Mazur, P., and Schmidt, J. J., "Interactions of Cooling Velocity, Temperature, and Warming Velocity on the Survival of Frozen and Thawed Yeast," *Cryobiology*, Vol. 5, 1968, pp. 1–17.

10 Rapatz, G., Nath, J., and Luyet, B. J., "Electron Microscope Study of Erythrocytes in Rapidly Frozen Mammalian Blood," *Biodynamica*, Vol. 9, No. 177, 1963, pp. 83–94.

11 McGrath, J. J., "The Dynamics of Freezing and Thawing Mammalian Cells: The HeLa Cell," ScM thesis, Massachusetts Institute of Technology, Department of Mechanical Engineering, 1974.

12 Toscano, W. M., Cravalho, E. G., Silvares, O. M., and Huggins, C. E., "The Thermodynamics of Intracellular Ice Nucleation in the Freezing of Erythrocytes," JOURNAL OF HEAT TRANSFER, TRANS. ASME, Series C, Vol. 97, 1975, pp. 326–332.

13 Prigogine, I., and Defay, R., *Chemical Thermodynamics*, Wiley, New York, 1954.

14 Canham, P. B., and Burton, A. C., "Distribution of Size and Shape in Populations of Normal Human Red Cells," *Circulation Research*, Vol. 22, 1968, pp. 405–422.

15 Ponder, E., and Millar, W. G., "The Measurement of the Diameters of Erythrocytes. I. The Mean Diameter of the Red Cells in Man," *Quart. J. Exp. Physiol.*, Vol. 14, 1924, pp. 67–82.

16 Chin, P. C. Y., and Fung, Y. C., "Extreme-Value Statistics of Human Red Blood Cells," *Microvascular Research*, Vol. 6, 1973, pp. 32–43.

17 Wintrobe, M. M., *Clinical Hematology*, Sixth ed., Lea & Febiger, Philadelphia, 1967, p. 105.

18 Beutler, E., and Srivastava, S. K., "Composition of the Erythrocyte," *Hematology*, McGraw-Hill, New York, 1972, p. 94.

19 Farrant, J., and Woolgar, A. E., "Human Red Cells Under Hypertonic Conditions: A Model System for Investigating Freezing Damage. I. Sodium Chloride," *Cryobiology*, Vol. 9, 1972, pp. 9–15.

20 Jacobs, M. H., Glassman, H. N., and Parpart, A. K., "Osmotic Properties of the Erythrocyte: The Temperature Coefficient of Certain Hemolytic Processes," *J. of Cel. Comp. Physiol.*, Vol. 7, 1935, pp. 197–225.

21 Sidel, V. W., and Solomon, A. K., "Entrance of Water Into Human Red Cells Under an Osmotic Pressure Gradient," *J. Gen. Physiol*, Vol. 41, 1957, pp. 243–257.

22 Rich, G. T., Sha'afi, R. I., Romualdez, A., and Solomon, A. K., "Effect of Osmolality on the Hydraulic Permeability Coefficient of Red Cells," *J. Gen. Physiol.*, Vol. 52, 1968, pp. 941–954.

23 Levin, R. L., Cravalho, E. G., and Huggins, C. E., "A Membrane Model Describing the Effect of Temperature on the Water Conductivity of Erythrocyte Membranes at Subzero Temperatures," submitted to *Cryobiology*, 1975.

24 Robinson, R., and Stokes, R. H., *Electrolyte Solutions*, Academic Press, New York, 1955.

25 Gary-Bobo, C. M., and Solomon, A. K., "Properties of Hemoglobin Solutions in Red Cells," *J. Gen. Physiol.*, Vol. 52, 1968, pp. 825–853.

K. R. Perkins
Engineer,
Aerojet Nuclear Co., Idaho Falls, Idaho

D. M. McEligot
Professor,
Aerospace and Mechanical Engineering Department,
University of Arizona, Tucson, Ariz.
Assoc. Mem. ASME

Mean Temperature Profiles in Heated Laminarizing Air Flows

Experiments for air flowing upward in a vertical circular tube are presented for heating rates causing significant property variation. Entering Reynolds numbers vary from 3800 to 8500 with the dimensionless heating parameter, $q_w''/(Gc_{p,i}T_i)$, varying from 0.001 to 0.0055. Data include the first developing internal profiles for the apparent reverse transition from turbulent to laminar flow due to heating. Emphasis is placed on internal temperature distributions, $\bar{t}(x, r)$, taken at axial stations from about 3–25 dia after the start of heating. The flow regimes range from nearly constant property, turbulent flow to strongly heated laminarizing flow. Results for strongly heated flows show a definite increase in the thickness of both the linear sublayer and the viscous sublayer. For laminarized flow, the linear sublayer extends about half the distance to the cener line of the tube or more.

Introduction

The phenomenon of laminarization has come under scrutiny recently due to the resulting reduction in heat transfer parameters which is sometimes severe [1, 2, 3].[1] Such reductions are not predicted by the empirical correlations accounting for property variation [4, 5] nor by numerical predictions [6]; under certain severe heating conditions they agree fairly well with laminar predictions in the downstream region even though the local bulk Reynolds numbers often are still higher than the usual value for transition to turbulent flow. We call this phenomenon laminarization. References [1, 2] are recommended for more extensive reviews of the pertinent literature.

The experiments involved before have been conducted in tubes with diameters less than 13 mm (½ in.). Consequently, internal profile measurements were not feasible so the data are not of much help in guiding analysts to better simulations of the turbulence phenomena in question. Steiner [7] and Carr, Connor, and Buhr [8] obtained profile measurements in flows with strong, probably dominant, buoyancy forces; unfortunately, neither investigation documented the inlet and boundary conditions in sufficient detail to use in verifying numerical predictions based on proposed turbulence models.

The present investigation is aimed at obtaining mean axial and radial distributions for steady, low Mach number, turbulent and laminarizing flows with dominant forced convection and including careful measurements of the thermal boundary conditions and inlet conditions.

The Experiment

The apparatus employed in this investigation is comparable to that of Perkins, Schade, and McEligot [1] except insulation and guard heating is used around the test section instead of vacuum, an air compressor replaced the gas bottles, and the tube exit exhausted directly into the laboratory. The test section consisted of a seamless, extruded Inconel 600 circular tube with 27.4 mm (1.08 in.) ID suspended vertically and heated resistively. A 50-dia adiabatic entry preceded the 32-dia heated section.

Internal mean temperature profiles were measured with miniaturized boundary layer thermocouple probes of premium grade, Chromel-Alumel as illustrated in Fig. 1. The probe was introduced through the open exit of the tube and positioning was accomplished with a fixture composed of three mutually perpendicular traversing mechanisms. Internal temperature profiles were corrected for the temperature increase due to radiation from the tube wall to the sensor. Experimental uncertainties in temperature measurements are shown as brackets in the later figures with the uncertainty in the radiation correction usually dominating these estimates.

The experiment was designed to approximate a constant heating rate to air, entering with a fully developed turbulent profile at a uniform temperature. The reduced data show that for $q^+ \lesssim 0.0036$ the heating rate remained constant to within ±5 percent for $3.0 \lesssim x/D \lesssim 25.3$. For higher heating rates there was an axial variation in heating rate up to ±12 percent. However, the numerical predictions used for comparison are based on the deduced heat flux distribution rather than on a constant heat flux. Adiabatic velocity profiles show that the flow entering the heated section agreed with

[1] Numbers in brackets designate References at end of paper.

Contributed by the Heat Transfer Division and presented at THE AMERICAN SOCIETY OF MECHANICAL ENGINEERS. Revised manuscript received by the Heat Transfer Division June 2, 1975. Paper No. 74-HT-24.

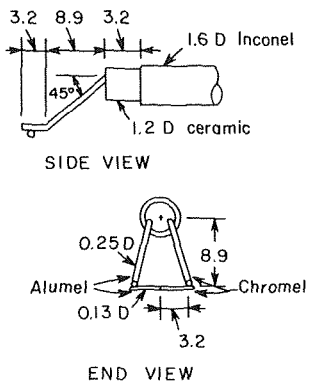

Fig. 1 Typical thermocouple probe; dimensions in mm

predictions for fully developed, low Reynolds number turbulent flow within the experimental uncertainty.

Inlet Reynolds numbers range from 3800 to 8500 with dimensionless heating rates, q^+, to 0.0055. The air inlet was at room temperature, about 299 K (538°R). Wall temperatures ranged to 870 K (1560°R) while wall-to-bulk temperature ratios up to 2.0 were achieved. Compressible effects have been neglected as the maximum Mach number was 0.017. The buoyancy parameter, Gr/Re_i^2, varied from 0.06 to 0.78 so forced convection would be expected to dominate but the experiments of Bates, et al. [9] showed that natural convection effects may be significant in some runs. The profile data were taken at $2.9 \leq x/D \leq 25.3$.

For convenience, in the present study data beyond $x/D = 10$ and falling within 10 percent of the empirical correlation by Magee and McEligot [4] are labeled turbulent. Data which agree with the laminar correlation of McEligot and Swearingen [10] within 10 percent before the end of the test section are classified laminarizing. Data falling between the two correlations are labeled "subturbulent." Results of this classification scheme agree with the categories established earlier in small tube studies [1]. Tabulated data for all experimental runs and further details on the experiment are presented in Perkins' thesis [11].

Downstream Temperature Profiles

Rather than attempt a description of all experimental runs, a sequence of typical runs has been selected to illustrate the effects of varying both the inlet Reynolds number and the heating rate (Table 1). The data at $x/D = 25.3$ are presented in Fig. 2 for this sequence of runs. The local bulk Reynolds number at this position varies from about 2700 to 7900 so all would be expected to be turbulent if they were adiabatic at the same flow conditions.

Table 1 Experimental runs

	Entering parameters			Downstream parameters (x/D = 25.3)				
Label	Re_i	q_i^+	Gr/Re_i^2	Re_m	y^+_{linear}	$y^+_{viscous}$	y_c^+	
T91	8520	0.0010	0.064	7900	11	∿30	200	Turbulent
T61	6020	0.0011	0.094	5560	13	75	150	Turbulent
T62	6030	0.0018	0.16	5290	13	60	130	Turbulent
S64	6020	0.0035	0.31	4740	19	40	83	Subturbulent
S65	6040	0.0045	0.40	4510	25	45	72	Subturbulent
L46	3760	0.0055	0.78	2680	26	37	53	Laminarizing

The shapes and trends of these normalized temperature profiles bear distinct similarities to velocity profiles, $u^+(y^+)$, observed in external flows laminarizing due to acceleration [12, 13]. It is seen that y_c^+ decreases as the Reynolds number is reduced, as expected in adiabatic flows, and it also decreases as the heating rate is raised.

The term viscous sublayer is defined variously by different investigators. In the present paper the terminology suggested by Bradshaw [14] is adopted. Thus, we define the linear sublayer as the region where molecular effects dominate the mean velocity profile to give $u^+ \approx y^+$; for high Reynolds number, adiabatic flow the linear sublayer typically extends to $y^+ \approx 5$. The viscous sublayer is the region where both molecular effects and turbulent effects are significant, e.g., the range $5 \lesssim y^+ \lesssim 30$ for high Reynolds number, adiabatic flow. The viscous sublayer then usually includes the region of maximum production of turbulence kinetic energy and its behavior is expected to be important due to that observation alone.

By plotting $t^+(y^+)$ one may estimate the thickness of the linear sublayer and the viscous sublayer. With constant properties and a constant wall heat flux, a fully established temperature profile for pure laminar flow can be written as

$$t^+ = \Pr \cdot y^+ \left[1 + \frac{1}{2}\frac{y}{r_w} - \left(\frac{y}{r_w}\right)^2 + \frac{1}{4}\left(\frac{y}{r_w}\right)^3 \right] \quad (1)$$

or, in the limit of small distances, $t^+ \approx \Pr \cdot y^+$. For a turbulent core, Johnk and Hanratty [15] suggest

$$t^+ = 3.32 + 5.09 \ln y^+ \quad (2)$$

The two limiting relations are presented in Fig. 2 as solid lines; center-line markings indicate y_c^+ for each run and dashed lines parallel to equation (2) provide guides to identify possible "log law" regions. The relation $t^+ = \Pr \cdot y^+$ has been extended to aid in determining the edge of the linear sublayer but this point has been estimated mainly from the apparent inflection point in the data for each run. The edge of the viscous sublayer is approximated by the juncture with the dashed line. These estimated thicknesses are

Nomenclature

A_{cs} = cross-sectional area
c_p = specific heat at constant pressure
D = tube diameter
G = average mass flux, $\dot{m}/A_{cs}$
g = acceleration of gravity
g_c = dimensional constant
h = convective heat transfer coefficient, $q_w''/(T_w - T_m)$
k = thermal conductivity
l = mixing length
$\dot{m}$ = mass flow rate
q_w'' = heat transfer to gas-per-unit area
r_w = tube radius
T = absolute temperature
x = axial coordinate
y = distance from wall
ϵ_h = eddy diffusivity for heat
ϵ_m = eddy diffusivity for momentum
μ = viscosity
ν = kinematic viscosity, μ/ρ
ρ = density
τ_w = apparent wall shear stress, $-(D/4)(d/dx)[p + G^2/\rho g_c]$

Nondimensional Parameters

f = apparent friction factor, $2g_c\tau_w\rho_m/G^2$
Gr = Grashof number, $gq_w''D^4/(\nu_i^2 k_i T_i)$
Nu = Nusselt number, hD/k
Pr = Prandtl number, $\mu c_p/k$
q^+ = wall heat flux parameter, $q_w''/(Gc_{p,i}T_i)$
Re = Reynolds number, GD/μ
t^+ = temperature, $\sqrt{g_c\tau_w\rho_w}\, c_p(T_w - T)/q_w''$
u^+ = axial velocity, $u/\sqrt{g_c\tau_w/\rho_w}$
y^+ = wall distance coordinate, $y\sqrt{g_c\tau_w/\rho_w}/\nu_w$

Subscripts

i = inlet
m = evaluated at local bulk (mixed mean) temperature
vD = van Driest
w = wall, evaluated at wall temperature

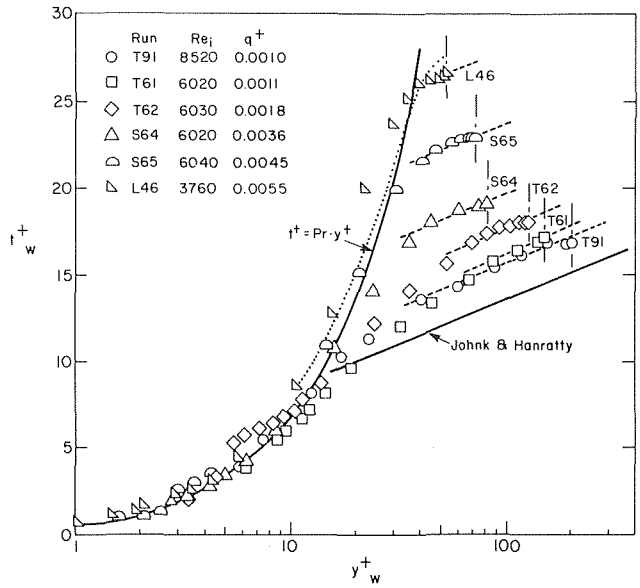

Fig. 2 Downstream temperature profiles; conditions listed in Table 1

also listed in Table 1.

At low y^+ each run converges on the linear sublayer prediction with the exception of a few points in the immediate vicinity of the wall. All show a possible turbulent core where t^+ varies as ln y^+; as with pipe flow velocity profiles, this logarithmic variation appears at large y/r_w despite the lack of a constant heat flux, analogous to a constant shear layer [14]. Two, or perhaps three, runs appear to show a constant temperature near the center line implying that the thermal boundary layer may not fill the tube at this station; this observation will be discussed further in a later section. Although this figure does not seem to lead to a better understanding of the core region, the data do confirm the numerical conclusion of McEligot and Bankston [16] that thickening of the viscous sublayer provides a plausible explanation of laminarization in terms of wall parameters.

It is interesting that none of the data agree with the "universal correlation" suggested by Johnk and Hanratty [15]. For this range of Reynolds numbers it seems apparent that there is a strong dependency on heating rate. Even the fully turbulent, nearly constant property run (T91) shows a 10 percent increase in t^+ over the higher Reynolds number correlation suggested by Johnk and Hanratty. It should be noted that this disagreement is not an entry length effect since a shorter entry would result in a lower dimensionless temperature profile. For $y^+ \gtrsim 13$ the three turbulent runs diverge from purely laminar behavior and show an extensive turbulent core region, although the data are 10–20 percent higher than predicted by Johnk and Hanratty.

Only when the subturbulent regime is reached does the linear sublayer thicken substantially. For Run S64, the linear sublayer extends to near $y^+ = 19$. The conclusion here is that although Run S64 no longer appears predominantly turbulent it just as surely has a large region away from the wall which disagrees with a purely laminar prediction. Run S65, which might be characterized as almost laminarized, shows further increase in the linear sublayer to $y^+ \simeq 25$, but there is still a large core ($25 \lesssim y^+ < y_c^+ = 72$ or two-thirds of the radius) which demonstrates nonlaminar behavior.

Whether Run L46 has been laminarized to completely molecular transport by $x/D = 25.3$ is difficult to discern with only measurements of the mean temperature profile. To examine this question, equation (1) has been plotted as a dotted curve for the conditions of run L46. For this run estimation of the linear sublayer thickness by identifying an inflection point is not conclusive since equation (1) also shows an inflection in this region. In the region from $y^+ \approx$ 10–40 the normalized temperature data are higher than this purely laminar prediction then beyond $y^+ \approx 40$ the data appear to vary as ln y^+. The excessive temperatures in the viscous sublayer may be explained by higher upstream wall heat fluxes for this particular run. At the center line, equation (1) predicts $t_c^+ = 0.75 \text{ Pr} \cdot y_c^+ \approx$ 27.8, which is less than 5 percent above the data; while this difference is greater than the estimated experimental uncertainty in the temperatures, the fact that the position would still be in the developing thermal region prohibits discriminating whether the central region effectively has molecular or turbulent transport. The significant conclusion is that the mean temperature profile conforms approximately to laminar predictions over most of the cross section.

Numerical Predictions

By solving the governing equations numerically, one eliminates uncertainties about the analysis other than those concerned with the turbulence model itself. The numerical method used was the same as the program of Bates, et al. [9] which includes a body force term in the x-momentum equation to account for buoyancy effects; otherwise, it corresponds to the approach of Bankston and McEligot [6]. Reynolds analogy, $\epsilon_h = \epsilon_m$, is assumed.

For this investigation three turbulent models are used to illustrate idealized flow behavior for comparison to the mean temperature distribution. The first is called the *laminar* model and accounts only for molecular transport by a Newtonian fluid but uses the entering turbulent velocity profile as the initial condition; its predictions represent a hypothetical limiting condition where laminarization is immediate and complete.

The second model is the "*van Driest-wall* properties" mixing length model,

$$\ell_{vD} = \kappa y[1 - \exp(-y^+/y_\ell^+)] \tag{3}$$

with properties in y^+ being evaluated at the wall temperature. This model has been used with success for fully turbulent flows [6] and is used in the present investigation to illustrate turbulent behavior.

A third model, proposed by McEligot and Bankston [16] accounts for variable viscous sublayer thickness at low Reynolds numbers, for gas property variation, and for delay in the response of turbulent quantities to local conditions. In the present paper we refer to it as the *modified van Driest* model. Details are available in references [11, 16].

Thermal Development

Numerical predictions are compared to data from the three types of runs—turbulent, subturbulent, and laminarizing—in Figs. 3–5.

Turbulent Flow. The developing temperature profiles of Run T62 are shown on Fig. 3 as representative of all three turbulent runs. Downstream, the data demonstrate typical turbulent tem-

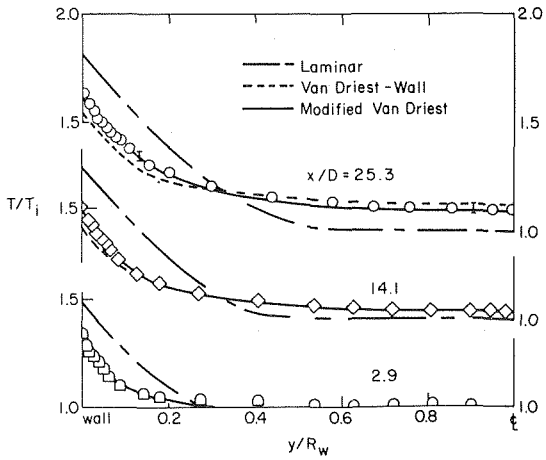

Fig. 3 Thermal development of turbulent run T62; Re_j = 6030, q_j^+ = 0.0018, Re_{25} = 5290

perature profiles with the temperature gradient increasing toward the wall, thereby showing that most of the thermal resistance is concentrated near the wall. Since $T_c > T_i$ at the second station it is concluded that the thermal boundary layer has penetrated to the center in less than 14 dia. Thereafter, the temperature across most of the tube shows a flat, well-mixed core region.

In Fig. 3 it is also seen that the data are predicted well by both the van Driest-wall model and the modified van Driest model with the modified version being slightly better, particularly in predicting the wall temperature. The van Driest-wall model underestimates the temperatures near the wall. The hypothesis of purely molecular transport, the laminar model, leads to distribution of the thermal resistance across a greater portion of the tube, but for all three runs the predicted thermal boundary layer only reaches half the radius by the downstream location. The laminar predictions differ from the data significantly with the discrepancy greater near the wall in the other two turbulent runs.

Subturbulent Flow. The two subturbulent runs show the same trends as each other so only Run S65 is presented graphically (Fig. 4). At the first station, $x/D = 2.9$, the data show a slightly thicker thermal boundary layer than predicted and the profiles still appear as a boundary layer at the exit. However, the center-line temperature shows that the boundary layer has again filled the cross section within 14 dia. Although the heating rate is more than twice that of the turbulent runs, the center-line temperature is approximately the same at the exit.

For the subturbulent runs the modified van Driest model and the laminar model provide predictions which differ near the entrance but which converge on one another successively downstream. The data correspond to the modified model at the entry then begin to diverge, beginning near the wall at about 8 dia. Near the exit both models overpredict the temperatures in the important wall region. In comparison to the laminar model, the numerical results from the modified van Driest model imply slightly faster thermal boundary layer growth due to turbulent transport but neither model shows it penetrating to the center line while the data do. The modified model predicts essentially laminar transport for much of the tube while the data indicate that turbulent

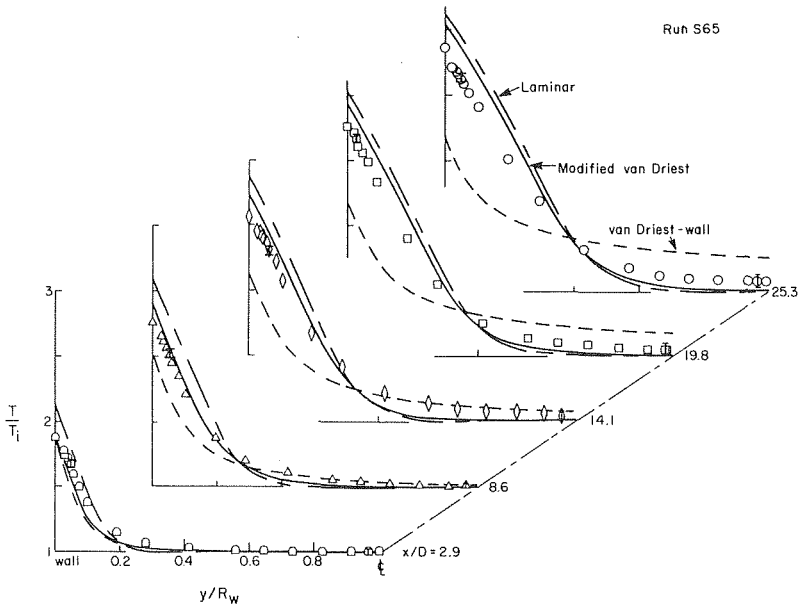

Fig. 4 Thermal development of subturbulent run S65; $Re_l = 6040$, $q_l^+ = 0.0045$, $Re_{25} = 4510$

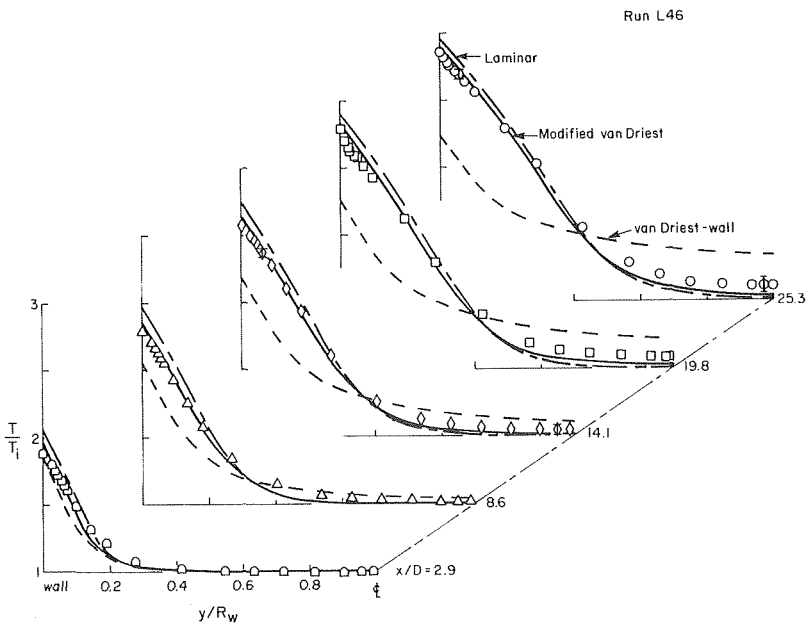

Fig. 5 Thermal development of laminarizing run L46; $Re_l = 3760$, $q_l^+ = 0.0055$, $Re_{25} = 2680$

transport persists to a greater extent.

At 25 dia the van Driest-wall model, representing fully turbulent flow, underpredicts the wall temperature more than the modified van Driest model overestimates it. Consequently, for applications where the heating rate is controlled as in gas cooled nuclear reactors, the modified van Driest model could be considered conservative and the van Driest-wall model dangerous in the subturbulent flow regime.

Laminarizing Flow. The thermal development of the laminarizing run, L46, is demonstrated in Fig. 5. The heating rate, q^+, is about three times that of the turbulent run in Fig. 3. Compared to predictions, the measurements show a thicker thermal boundary layer which again fills the tube within 14 dia and possibly within 9 dia. The thermal resistance is spread across the tube downstream as in laminar flow rather than being concentrated near the wall as in turbulent flow. The downstream temperature profile appears almost parabolic (equation (1) corresponds to a fourth-order parabola). The thermal resistance is much greater than in the turbulent regime since the center-line temperature is actually less while the heating rate is three times as great; in contrast, constant properties correlations would suggest an increase of only about 7 percent based on the local Reynolds numbers and bulk temperatures.

Application of the modified van Driest model to the laminarized run yields results which are in close agreement with the measurements throughout the tube. The laminar model also agrees closely though slightly diverging from the data near the wall proceeding downstream; it predicts that the thermal boundary layer would not quite reach the center by 25 dia. At the first station both models predict the same temperature distribution since the thermal boundary layer still appears to be within the viscous layer; then a slight difference appears due to the small turbulent transport still implied in the modified van Driest model. It is apparent that, even at the high heating rate of Run L46, laminarization does not occur instantaneously and the inherent delay in decay of the turbulent behavior results in a slightly lower wall temperature than predicted by the laminar model. Again predictions based on the fully turbulent model are seen to be dangerously misleading.

Buoyancy Effects. The turbulence models applied do not directly account for an effect of buoyancy although the x-momentum equation includes a body force term. Bates, et al. [9] found that buoyant body forces can cause significant modification of heat transfer behavior for forced turbulent flow and significant divergence from numerical predictions. Since they used the same numerical program as the present study it appears that the turbulence model should include provision for buoyancy effects when important.

Reviewing the data of Bates, et al., one finds only a slight change in wall temperature for variation of $|Gr/Re_i^2|$ from 0.076 to 1.05 in a rapidly laminarizing flow such as Run L46, and the trends were predicted well. This observation would correspond to a situation where the thermal boundary layer remains well within the viscous sublayer so that molecular transport dominates and, consequently, further modification of the turbulence model is not necessary. The present turbulent data are at lower values of $|Gr/Re_i^2|$ than those where the turbulent results of Bates, et al., were affected so the present agreement with the predictions is not surprising. The subturbulent regime in the present study corresponds to the "slow laminarization" of Bates, et al., where moderate buoyancy effects were noticed at $|Gr/Re_i^2| \approx 0.23$; thus, the discrepancy between prediction and measurement in Run S65 (and S64) may be, in part, due to lack of provision for buoyancy in the present turbulence models. Neither of these investigations has been exhaustive so resolution of this difficulty is an appropriate topic for further study.

Conclusions

From these comparisons, it appears that the modifications to the van Driest mixing length model suggested by McEligot and Bankston [16] lead to substantially correct predictions of heat transfer during laminarization of a gas due to heating. The viscous sublayer thickness is seen to depend on both the local Reynolds number and the heating rate. It is, however, evident that the modified model needs further improvement or replacement for application to the subturbulent regime.

The data indicate that there is a substantial region of flow and heating rates where turbulent transport is suppressed though complete laminarization does not occur. On the other hand, for conditions where local Nusselt numbers agree with laminar predictions at Reynolds numbers above the accepted value for transition, the viscous sublayer occupies the majority of the tube cross section.

Acknowledgments

This study has been supported by the National Science Foundation. The University Computer Center provided the CDC-6400 computer for the numerical calculations. Prof. R. B. Kinney supervised the early stages of the experimental program.

References

1 Perkins, K. R., Schade, K. W., and McEligot, D. M., "Heated Relaminarizing Gas Flow in a Square Duct," *International Journal of Heat and Mass Transfer,* Vol. 16, 1973, pp. 897–916.

2 Hall, W. B., Jackson, J. D., and Watson, A., "A Review of Forced Convection Heat Transfer to Fluids at Supercritical Pressures," *Proc. Inst. Mech. Eng.,* Vol. 182, Part 3I, 1967–1968, pp. 10–22.

3 Shiralkar, B., and Griffith, P., "The Effect of Swirl, Inlet Conditions, Flow Direction and Tube Diameter on the Heat Transfer to Fluids at Supercritical Pressure," JOURNAL OF HEAT TRANSFER, TRANS. ASME, Series C, Vol. 92, 1970, pp. 465–474.

4 Magee, P. M., and McEligot, D. M., "Effect of Property Variation on the Turbulent Flow of Gases in Tubes: The Thermal Entry," *Nuc. Sci. Eng.,* Vol. 31, 1968, pp. 337–359.

5 Perkins, H. C., and Worsoe-Schmidt, P. M., "Turbulent Heat and Momentum Transfer for Gases in a Circular Tube at Wall-to-Bulk Temperature Ratios to Seven," *International Journal of Heat and Mass Transfer,* Vol. 8, 1965, pp. 1011–1031.

6 Bankston, C. A., and McEligot, D. M., "Turbulent and Laminar Heat Transfer to Gases with Varying Properties in the Entry Region of Circular Ducts," *International Journal of Heat and Mass Transfer,* Vol. 13, 1970, pp. 319–344.

7 Steiner, A., "On the Reverse Transition of a Turbulent Flow Under the Action of Buoyancy Forces," *J. Fluid Mech.,* Vol. 47, 1971, pp. 503–512.

8 Carr, A. D., Connor, M. A., and Buhr, H. O., "Velocity, Temperature and Turbulence Measurements in Air for Pipe Flow With Combined Free and Forced Convection," JOURNAL OF HEAT TRANSFER, TRANS. ASME, Series C, Vol. 95, 1973, pp. 445–452.

9 Bates, J. A., Schmall, R. A., Hasen, G. A., and McEligot, D. M., "Effects of Buoyant Body Forces on Forced Convection in Heated Laminarizing Flows," *Heat Transfer 1974,* Vol. II, Proceedings, 5th International Heat Transfer Conference, 1974, pp. 141–145.

10 McEligot, D. M., and Swearingen, T. B., "Prediction of Wall Temperatures for Internal Laminar Heat Transfer," *International Journal of Heat and Mass Transfer,* Vol. 9, 1966, pp. 1151–1152.

11 Perkins, K. R., "Turbulence Structure in Gas Flows Relaminarizing by Heating," PhD thesis, University of Arizona, 1975.

12 Blackwelder, R. F., and Kovazsnay, L. S., "Large Scale Motion of Turbulent Boundary Layers During Relaminarization," *J. Fluid Mech.,* Vol. 53, 1972, pp. 61–83.

13 Badri Narayanan, M. A., and Ramjee, V., "On the Criteria for Reverse Transition in a Two-Dimensional Boundary Layer Flow," *J. Fluid Mech.,* Vol. 35, 1969, pp. 225–241.

14 Bradshaw, P., *An Introduction to Turbulence and its Measurement,* Pergamon, Oxford, 1971, p. 51.

15 Johnk, R. E., and Hanratty, T. J., "Temperature Profiles for Turbulent Flow of Air in a Pipe," *Chem. Eng. Science,* Vol. 17, 1962, pp. 867–892.

16 McEligot, D. M., and Bankston, C. A., "Numerical Predictions for Circular Tube Laminarization by Heating," ASME Paper No. 69-HT-52.

R. N. Smith[1]
R. Greif

University of California,
Department of Mechanical Engineering,
Berkeley, Calif.

Turbulent Transport to a Rotating Cylinder for Large Prandtl or Schmidt Numbers

The heat or mass transport to a rotating cylinder is obtained by solving the conservation equations for large Prandtl or Schmidt numbers. A modified mixing length, which includes the effect of centrifugal forces in terms of the Richardson number, is used. Explicit relations are presented for the heat or mass transport and a comparison is made with the experimental data over a range of Prandtl and Schmidt numbers from 190 to 11,000.

Introduction

The rotating cylinder geometry has long been of interest in the study of heat, mass, and momentum transport, and analytical and experimental results have been published for a wide variety of conditions. The present paper deals with the prediction of the heat or mass transfer to a rotating cylinder in turbulent flow for large values of the Prandtl or Schmidt number. Under these conditions the significant variation of the temperature or concentration is confined to a region very close to the wall, with respect to the variation of the velocity, yielding simplifications in the analysis.

Experimental results at lower values of the Prandtl number (for heat transfer in air, Pr ~ 0.7) have been reported by several investigators which are in good agreement with one another [1–4].[2] Heat transfer results at higher Prandtl numbers were reported by Seban and Johnson [5] for a horizontal cylinder rotating in oil (Pr = 190–660) and in water (Pr = 3–5) and by Becker [6] (Pr = 3). Eisenberg, Tobias, and Wilke [7] used solid dissolution of benzoic acid and cinnamic acid rotating in water, as well as an electrochemical technique, to obtain mass transfer rates for rotating cylinders for Schmidt numbers varying from 800 to 11,000. The electrochemical system used was the ferro-ferricyanide red-ox couple in NaOH solution and measurements were made of the mass-transfer-limiting current associated with these reactions. The limiting current method was also used by Cornet and Kappesser [8], who measured limiting current rates of the oxygen reduction reaction in NaCl solution in a rotating cylinder system. The Schmidt number was 370 for these experiments. The mass transfer to a rough rotating cylinder was obtained by the limiting-current method by Kappesser, Cornet, and Greif [9] for a value of the Schmidt number of 400.

All of these results have been found to correlate well with the equation [7]

$$\frac{\mathrm{Nu}}{\mathrm{Pr}^{0.356}} = \frac{\mathrm{Sh}}{\mathrm{Sc}^{0.356}} = \left(\frac{f}{2}\right)\mathrm{Re} \tag{1}$$

for $200 < \mathrm{Re} < 300{,}000$ and $0.7 < \mathrm{Pr} < 11{,}000$. The friction factor, f, is defined by

$$\frac{f}{2} = \frac{\tau_0}{\rho(r_0\omega)^2} \tag{2}$$

For smooth cylinders, Theodorsen and Regier [10] found that the relation

$$\frac{1}{f^{1/2}} = -1.825 + 4.07 \log_{10}(f^{1/2}\mathrm{Re}) \tag{3}$$

was an accurate representation of their measured values of the drag on a rotating cylinder.

Transport to a Rotating Cylinder

To obtain analytical results for the heat or mass transfer to a rotating cylinder, and provide a basis for modifications, we begin with the basic conservation equations. The mean equation for the conservation of momentum in the circumferential direction, θ, is given by [11, 12]

$$0 = \nu \frac{d}{dr}\left[r^3 \frac{d}{dr}\left(\frac{U}{r}\right)\right] - \frac{d}{dr}(\overline{u'v'}r^2) \tag{4}$$

This equation may be integrated to yield

$$\tau r^2 = \mu r^3 \frac{d}{dr}\left(\frac{U}{r}\right) - \rho\,\overline{u'v'}r^2 = \mathrm{const} = \tau_0 r_0{}^2 \tag{5}$$

where τ_0 is the wall shear stress. The mean equation for the conservation of energy about a rotating cylinder is given by

[1] Presently, Asst. Professor, Rice University, Houston, Texas.

[2] Numbers in brackets designate References at end of paper.

Contributed by the Heat Transfer Division for publication in the JOURNAL OF HEAT TRANSFER. Manuscript received by the Heat Transfer Division March 31, 1975. Paper No. 76-HT-D.

$$0 = \frac{1}{r}\frac{d}{dr}\left(kr\frac{\partial T}{\partial r} - \rho c_p \overline{ru't'}\right) \tag{6}$$

Introducing the turbulent diffusivity for heat, ϵ_H, according to $\overline{u't'} = -\epsilon_H(dT/dr)$[3] and integrating yields

$$-qr = r\frac{dT}{dr}(k + \rho c_p \epsilon_H) = \text{const} = -q_0 r_0 \tag{7}$$

We now specify ϵ_H according to

$$\text{Pr}_t \frac{\epsilon_H}{\nu} = \frac{\epsilon_M}{\nu} = \frac{\ell^2}{\nu} r \frac{d}{dr}\left(\frac{U}{r}\right) = (\ell^+)^2 r^+ \frac{d}{dr^+}\left(\frac{U^+}{r^+}\right) \tag{8}$$

and obtain

$$T^+(r^+) = \frac{T_0 - T}{q_0/\rho c_p u_\tau} = \int_{r_0^+}^{r^+} \frac{r_0^+}{r^+} \frac{dr^+}{1/\text{Pr} + [(\ell^+)^2/\text{Pr}_t] r^+ d/dr^+ (U^+/r^+)} \tag{9}$$

For large values of the Prandtl numbers the essential temperature changes occur in the region near the wall. For this condition we follow Deissler [13] and obtain

$$T_b^+ \cong T^+(r^+ = \infty) \cong \int_{r_0^+}^{\infty} \frac{dr^+}{1/\text{Pr} + (\ell^+)^2/\text{Pr}_t} \tag{10}$$

We now specify the mixing length by the relation [13][4]

$$\ell^+ = n^2(r^+ - r_0^+)^2, \; n = 0.124 \tag{11}$$

and integrate equation (10) to obtain

$$\text{Nu} = \frac{2r_0^+ \text{Pr}}{T_b^+} = \frac{4n2^{1/2} r_0^+}{\pi}\left(\frac{\text{Pr}}{\text{Pr}_t}\right)^{1/4} = \frac{2n2^{1/2}\text{Re}}{\pi}\left(\frac{\text{Pr}}{\text{Pr}_t}\right)^{1/4}\left(\frac{f}{2}\right)^{1/2} \tag{12}$$

This result was obtained by Deissler [13] for tube flows and used by Seban and Johnson [5] in their study of heat transfer from a rotating cylinder. It should be noted that the friction factor, f, specified in equation (3), may be approximated by [7]

$$f/2 = 0.079\,\text{Re}^{-0.30} \tag{13}$$

which results in a $\text{Re}^{0.85}$ dependence for the Nusselt number.

Another approach for the determination of the transport was introduced by Tien, Wasan, and Wilke [15–17]. They obtained an expression for the eddy diffusivity by expanding the velocities near the surface in a Taylor series. The resulting expressions were then required to satisfy the conservation equations and the boundary conditions at the surface. Their result for nonrotating flows was given by

$$\frac{\epsilon_M}{\nu} = K^3(r^+ - r_0^+)^3 + \ldots \tag{14}$$

with $K^3 = 4.16 \times 10^{-4}$. A similar relation has been obtained by Paterson and Greif [18, 19] for flow about a rotating disk and by Paterson [18] for flow about a rotating cylinder. Since the analysis for the rotating disk has been published we shall refrain from repeating that for the rotating cylinder. However, it is important to note that the details for the rotating cylinder problem do prove to be more complex than those for the rotating disk.

Using equation (14) for the eddy diffusivity and carrying out the corresponding integration yields the following result for the heat transfer:

$$\text{Nu} = \frac{3K3^{1/2}\text{Re}}{2\pi}\left(\frac{\text{Pr}}{\text{Pr}_t}\right)^{1/3}\left(\frac{f}{2}\right)^{1/2} \tag{15}$$

The results obtained from equations (12) and (15) are plotted in Figs. 1 and 2 along with the heat and mass transfer data from references [5, 7, 8]. The range of the values of the Prandtl and Schmidt numbers is from 190 to 11,000. It is seen that neither equation is in agreement with the heat or mass transfer data. Recall, however, that both of these models were successful in predicting the mass transfer for other rotating systems; for example, for disks [20, 19] and for large angle cones [21]. It thus appears that there may be a fundamental difference in the turbulence transport which makes the foregoing models inadequate for the rotating cylinder.

Modifications

In the rotating disk studies, the primary direction of transport is perpendicular to the planar surface of the disk while the centrifugal forces are parallel to the surface and hence may be neglected. However, for the rotating cylinder these effects are in the same direction; namely, the radial direction, and a contribution to the turbulent mixing may be anticipated.

In his discussion of the turbulent heat or mass transport to a rotating cylinder Kappesser [22] suggested that the turbulent mixing was enhanced by centrifugal forces. He proposed a "centrifugal eddy diffusivity" which he calculated by considering a fluid particle moving in a centrifugal force field. Another approach for including the effect of rotation is to alter the mixing length by introducing the swirling flow Richardson number, Ri. The basis for this approach is presented by Bradshaw [23] who developed an analogy between the effects of curvature or rotation and buoyancy on turbulent mixing. He obtained the following relation for the modified or apparent mixing length, ℓ_c, for small buoyancy effects:

$$\ell_c = \ell(1 - \beta\text{Ri}) \tag{16}$$

where β is an empirical constant. Hughes and Horlock [24] have discussed this result and it has also been utilized by Koosinlin and Lockwood [25] and Koosinlin, Launder, and Sharma [26], who recommend a value of $\beta \approx 5$. We shall follow this procedure in the present study.

For a rotating cylinder, Ri is given by

$$\text{Ri} = \frac{(2\text{U}/r^2)d/dr(Ur)}{[rd/dr(U/r)]^2} \tag{17}$$

The Richardson number represents the ratio of the energy avail-

[3] Note that $\overline{u'v'} = -\epsilon_M r\, d/dr(U/r)$.

[4] Note that in the region near the wall this result is identical to that presented by Van Driest [14].

Nomenclature

c_p = constant pressure specific heat
f = friction factor, equation (2)
k = thermal conductivity
ℓ = mixing length
ℓ^+ = dimensionless mixing length, $\ell u_\tau/\nu$
ℓ_c = modified mixing length
n = constant, equation (11)
Nu = Nusselt number
Pr = Prandtl number
Pr_t = turbulent Prandtl number
q = heat flux
r = radial coordinate
r^+ = dimensionless radial coordinate, ru_τ/ν
Re = Reynolds number, $2r_0^2\omega/\nu$
Ri = Richardson number
Sc = Schmidt number
Sh = Sherwood number
T = temperature
t' = turbulent fluctuating temperature
T^+ = dimensionless temperature, equation (9)
U = velocity
U^+ = dimensionless velocity, U/u_τ
u_τ = friction velocity, $(\tau_0/\rho)^{1/2}$
u',v' = turbulent fluctuating velocity components
ϵ_H = eddy diffusivity for energy transfer
ϵ_M = eddy diffusivity for momentum transfer
μ = viscosity
ν = kinematic viscosity
ρ = density
τ = shear stress

Subscript

0 = evaluated at wall

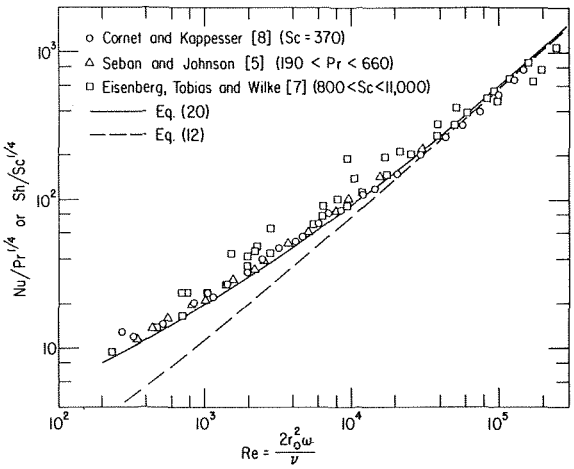

Fig. 1 Results for the heat and mass transfer to a rotating cylinder

able to a fluid particle due to stratification of body forces to that available in the form of turbulent kinetic energy. When the Richardson number is negative, as in the case of a rotating cylinder, energy is added to the fluid particle as it moves in the stratified force field and an enhancement of the turbulent mixing results. In this study we consider large values of the Prandtl (or Schmidt) number and therefore approximate the Richardson number by its value at the surface of the cylinder, Ri_0, where

$$\mathrm{Ri}_0 = \frac{-4}{\mathrm{Re}}\left(\frac{2}{f}\right) \tag{18}$$

The modified mixing length is then given by

$$\ell_c = \ell\left(1 + \frac{4\beta}{\mathrm{Re}}\cdot\frac{2}{f}\right) \tag{19}$$

Hence, the effect of the modification is to increase the mixing length, and the eddy diffusivity, and ultimately the predicted heat or mass transport. Note that the use of equation (19) implies that the linear buoyancy result of Bradshaw, as presented in equation (16), is applicable within the sublayers. This assumption will be discussed shortly.

We may now model the effect of the centrifugal forces by specifying the new mixing length, ℓ_c, and proceed as before to obtain the transport. the result for the Nusselt number is then given by

$$\mathrm{Nu} = \frac{2n2^{1/2}}{\pi}\left(\frac{f}{2}\right)^{1/2}\mathrm{Re}\left(\frac{\mathrm{Pr}}{\mathrm{Pr}_t}\right)^{1/4}\left(1 + \frac{4\beta}{\mathrm{Re}}\cdot\frac{2}{f}\right)^{1/2} \tag{20}$$

which for $\beta = 0$ reduces to equation (12).

It is also of interest to utilize the method proposed by Tien, Wasan, and Wilke, in conjunction with the Richardson number modification of the mixing length, to obtain the transport. The eddy diffusivity obtained from this method is not directly based on a specification of the mixing length, but near the wall we obtain

$$\frac{\epsilon_{M,c}}{\nu} = K_c{}^3(r^+ - r_0{}^+)^3 = (\ell_c{}^+)^2 = (\ell^+)^2\left(1 + \frac{4\beta}{\mathrm{Re}}\cdot\frac{2}{f}\right)^2 \tag{21}$$

with

$$K_c{}^3 = K^3\left(1 + \frac{4\beta}{\mathrm{Re}}\cdot\frac{2}{f}\right)^2$$

With this relation for the eddy diffusivity the result for the Nusselt number becomes

$$\mathrm{Nu} = \frac{3K3^{1/2}}{2\pi}\left(\frac{f}{2}\right)^{1/2}\mathrm{Re}\left(\frac{\mathrm{Pr}}{\mathrm{Pr}_t}\right)^{1/3}\left(1 + \frac{4\beta}{\mathrm{Re}}\cdot\frac{2}{f}\right)^{2/3} \tag{22}$$

which for $\beta = 0$ reduces to equation (15).

Discussion of Results and Conclusions

Equations (20) and (22), the transport predictions which include the Richardson number correction and the experimental data, are plotted in Figs. 1 and 2, respectively. The constant β was set equal to 5 as recommended by Koosinlin, Launder, and Sharma [26] and Pr_t was taken to be unity. In each case the agreement with the data is substantially improved over the unmodified result.

A brief comment on the indicated dependence of the experimental data on the Prandtl or Schmidt number is in order at this point. As noted in the introduction, the experimental data have been correlated by Eisenberg, Tobias, and Wilke [7] with an equation using a $\mathrm{Pr}^{0.356}$ (or $\mathrm{Sc}^{0.356}$) dependence. Equation (22), which has a $\mathrm{Pr}^{1/3}$ (or $\mathrm{Sc}^{1/3}$) dependence, is also in good agreement with the experimental data and is shown plotted in Fig. 2. From Figure 1, however, we see that the presentation of the data with a $\mathrm{Pr}^{1/4}$ (or $\mathrm{Sc}^{1/4}$) dependence is less successful and we, therefore, conclude that equation (22) is the more desirable result.

In general, Figs. 1 and 2 show that modifications to nonrotating analyses to account for the effects of centrifugal forces may be used with success when applied to rotating cylinder transport phenomena. Recall that the results presented here follow from an analysis for large values of the Prandtl or Schmidt number, so that the primary resistance to heat or mass transfer occurs in the sublayers. The linear buoyancy modification of Bradshaw is derived from studies of atmospheric boundary layers (cf. Lumley and Panofsky [28]). Its physical basis is in a region far enough from a surface so that velocity fluctuations are sufficiently large to be affected by the stratification of body forces. Application of the model to the region within the viscous sublayer must therefore be viewed cautiously and the present results should not be viewed as a verification of the manner in which the centrifugal forces affect the turbulent flow field in the sublayers. However, it is important to emphasize that the present analysis is a direct extension of previous work [23, 26] and no new empirical constants, etc., have been introduced.

In closing, we note that it would be desirable to extend the theory developed here to lower values of Pr or Sc, or alternatively to treat more completely the large Pr or Sc problem, by considering the local variation of the Richardson number. The momentum and energy equations may then be integrated numerically to determine the velocity and temperature profiles near the wall and to illustrate more clearly the effect of the mixing length correction. The work of Koosinlin and Lockwood [25] and Koosinlin, Launder and Sharma [26] on rotating cones and axisymmetric flow over rotating cylinders is cited in this regard along with the study by Kinney [27].

Acknowledgment

The authors acknowledge with appreciation the support of this research by the Sea Water Conversion Laboratory of the University of California, Berkeley.

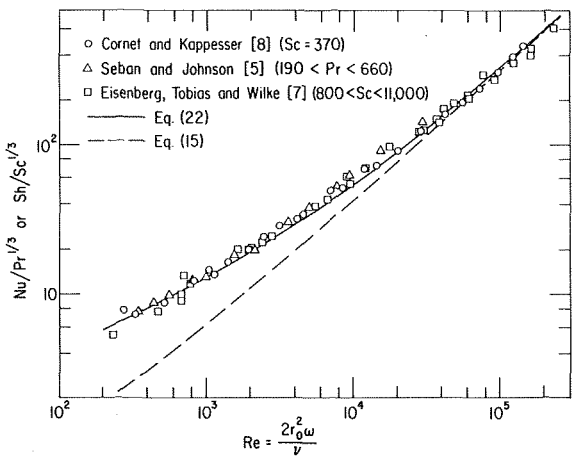

Fig. 2 Results for the heat and mass transfer to a rotating cylinder

References

1 Anderson, J. T., and Saunders, O. A., "Convection From an Isolated Heated Horizontal Cylinder Rotating About Its Axis," *Proceedings Royal Society London,* England, Series A, Vol. 217, 1953, p. 555.

2 Etemad, G. A., "Free Convection From a Rotating Horizontal Cylinder to Ambient Air With Interferometric Study of the Flow," TRANS. ASME, Vol. 77, 1955, p. 1283.

3 Dropkin, D., and Carmi, A., "Natural Convection Heat Transfer From a Horizontal Cylinder Rotating in Air," TRANS. ASME, Vol. 79, 1957, p. 741.

4 Kays, W. M., and Bjorklund, I. S., "Heat Transfer From a Rotating Cylinder With and Without Crossflow," TRANS. ASME, Vol. 80, 1958, p. 70.

5 Seban, R. A., and Johnson, H. A., "Heat Transfer From a Horizontal Cylinder Rotating in Oil," NASA Memorandum 4-22-59W, 1959.

6 Becker, K. M., "Measurements of Convective Heat Transfer From a Horizontal Cylinder Rotating in a Tank of Water," *International Journal of Heat and Mass Transfer,* Vol. 6, 1963, p. 1053.

7 Eisenberg, M., Tobias, C. W., and Wilke, C. R., "Mass Transfer at Rotating Cylinders," *Chem. Eng. Prog. Symp. Series,* Vol. 51, No. 16, 1953, p. 1; also Eisenberg, M., "Studies of Rates of Solid Dissolution and of Electrodes Reactions at Rotating Cylindrical Bodies," PhD dissertation, University of California, Berkeley, 1953.

8 Cornet, I., and Kappesser, R., "Cathodic Protection of a Rotating Cylinder," *Trans. Inst. Chem. Eng.,* Vol. 47, 1969, p. 194.

9 Kappesser, R., Cornet, I., and Greif, R., "Mass Transfer to a Rough Rotating Cylinder," *J. Electrochem. Soc.,* Vol. 118, No. 12, 1971, p. 1957.

10 Theodorsen, T., and Regier, A., "Experiments on Drag of Revolving Disks, Cylinders, and Streamline Rods at High Speeds," NACA Rep., 1944, p. 793.

11 *Modern Developments in Fluid Dynamics,* S. Goldstein, ed., Oxford University Press, Oxford, Volume I, 1952.

12 Townsend, A. A., "The Structure of Turbulent Shear Flow," Cambridge University Press, Cambridge, 1956.

13 Deissler, R. G., "Analysis of Turbulent Heat Transfer, Mass Transfer and Friction in Smooth Tubes at High Prandtl and Schmidt Numbers," NACA Report 1210, 1955.

14 van Driest, E. R., "On Turbulent Flow Near a Wall," *J. Aero. Sci.,* Vol. 23, 1956, p. 1007.

15 Tien, C. L., and Wasan, D. T., "Law of the Wall in Turbulent Channel Flow," *Physics of Fluids,* Vol. 6, Series 1, 1963, p. 144.

16 Wasan, D. T., Tien, C. L., and Wilke, C. R., "Theoretical Correlation of Velocity and Eddy Viscosity for Flow Close to a Pipe Wall," *AIChE Journal,* Vol. 9, No. 4, 1963,

17 Tien, C. L., "A Note on the Distributions of Temperature and Eddy Diffusivity for Heat in Turbulent Flow Near a Wall," *J. App. Math. and Physics (ZAMP),* Vol. 15, No. 1, 1964, p. 63.

18 Paterson, J. A., "Heat, Mass and Momentum Transport in Rotating Flows," PhD thesis, University of California, Berkeley, 1973.

19 Paterson, J. A., and Greif, R., "Transport to a Rotating Disc in Turbulent Flow at High Pr or Sc," JOURNAL OF HEAT TRANSFER, TRANS. ASME, Series C, Vol. 95, 1973.

20 Ellison, B. T., and Cornet, I., "Mass Transfer to a Rotating Disc," *Electrochemical Sci.,* Vol. 118, 1971, p. 68.

21 Kappesser, R., Greif, R., and Cornet, I., "Mass Transfer to Rotating Cones," *Appl. Sci. Res.,* Vol. 28, 1973, p. 442.

22 Kappesser, R., "A Study of Heat and Mass Transport From a Rotating Cylinder," PhD thesis, University of California, Berkeley, 1970.

23 Bradshaw, P., "The Analogy Between Streamline Curvature and Buoyancy in Turbulent Sheat Flow," *J. Fluid Mech.,* Vol. 36, Part 1, 1969, p. 177.

24 Hughes, D. W., and Horlock, J. H., "Effect of Rotation on the Development of the Turbulent Boundary Layer," Paper 18, B78, 1971, Symposium on Internal Flows, University of Salford, Salford, England.

25 Koosinlin, M. L., and Lockwood, F. C., "The Prediction of Axisymmetric Turbulent Swirling Boundary Layers," *AIAA Journal,* Vol. 12, No. 4, 1974, p. 547.

26 Koosinlin, M. L., Launder, B. E., and Sharma, B. I., "Prediction of Momentum, Heat, and Mass Transfer in Swirling, Turbulent Boundary Layers," JOURNAL OF HEAT TRANSFER, TRANS. ASME, Series C, Vol. 96, May, 1974, p. 204.

27 Kinney, R. B., "Universal Velocity Similarily in Fully Turbulent Rotating Flows," *J. Applied Mechanics,* Vol. 89, 1967, p. 437.

28 Lumley, J. L., and Panofsky, H. A., *The Structure of Atmospheric Turbulence,* Interscience Publishers, New York, 1964.

M. S. Sahota
P. J. Pagni

Mechanical Engineering Department
University of California,
Berkeley, Calif.

Temperature Fields in Structural Elements Subject to Fires

The transient, two-dimensional temperature field in a rectangular structural element subject to time dependent, nonlinear mixed boundary conditions has been obtained with a minimum of numerics. General results are given for two extreme fire histories, the American Society for Testing and Materials E-119 time-temperature curve and a short-duration high-intensity time-temperature curve. Comparisons are made with finite element and experimental temperature fields in a reinforced concrete column; good agreement is obtained. The stress field generated from the analytic temperature field also shows good agreement with finite element calculations. Applications to structural fires are discussed.

Introduction

An important unsolved problem in fire safety is determining the structural integrity of a building after a severe fire. Not all pertinent damage is visible, and so one needs to predict the internal stresses which result from any given fire. The first step is to predict the temperature field a known fire produces in a structural element. This temperature field then determines the thermal expansions which in turn generate internal stresses.

The problem considered here is a rectangular column surrounded by a known fire with an external bounding surface as shown in Fig. 1. Since most structural damage occurs after flashover, only this time period will be considered. As in the standard test methods [1–2],[1] the fire is described by a specified gas phase temperature history, assumed uniform over the entire column surface. The interaction between the fire and the column is described by a view factor, total emissivities of the fire and the column surface, and a convective heat transfer coefficient, all assumed constant and uniform over the column surface.

It is assumed that the column is homogeneous with constant and known properties. These simplifications are introduced to facilitate a solution. Moisture and cracking in concrete columns constrain their applicability. However, the results obtained here indicate that appropriate average thermal properties may be determined from subsequent comparison with experiment. The unknown variable is the unsteady, two-dimensional temperature field within the column, subject to nonlinear boundary conditions. The solution is obtained in quasi-analytic form which reduces to the standard analytical expressions for the limiting case of linear boundary conditions. Bresler and co-workers [3–5] have approached this problem, along with the internal stress problem, using the finite element method. Comparisons with their numerical solutions and experimental data are given here. In some cases, in particular at long times for simple geometries with constant properties and a small Stefan number, this quasi-analytic technique is faster and more convenient.

Few exact solutions for heat conduction with nonlinear boundary conditions have been found [6–7]. Approximate solutions for nonlinear problems have been obtained [8–9]. Chambre [10] presents an elegant solution for the surface temperature in a semi-infinite solid subject to an unsteady, nonlinear boundary condition.

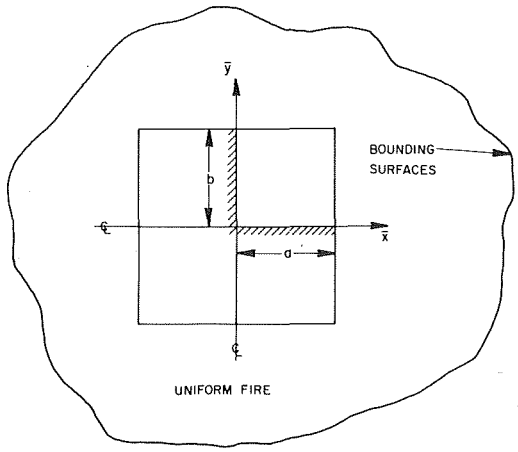

Fig. 1 Cross section of the column showing the coordinates and components of the system considered

[1] Numbers in brackets designate References at end of paper.

Contributed by the Heat Transfer Division for publication in the JOURNAL OF HEAT TRANSFER. Manuscript received by the Heat Transfer Division May 2, 1975. Paper No. 76-HT-A.

Several studies of nonlinear boundary conditions for one-dimensional solids are available in the literature [11–14].

The following section describes the general model and problem formulation. The analysis section delineates the solution method and examines special cases. The remaining sections contain results and comparisons with experiment.

Analysis

The system considered is shown schematically in Fig. 1. The analysis begins at flashover when the fire begins to significantly affect the structure and the approximations of a uniform fire with constant interaction coefficients becomes reasonable. The effects of the preflashover fire are accounted for by an arbitrary initial temperature distribution in the column $T_0(\bar{x}, \bar{y})$. The spatial uniformity of the fire temperature, $T_f(\bar{t})$, introduces quadrant symmetry in a coordinate system at the center of the column with zero flux conditions at the two internal boundaries.

With the foregoing assumptions, the transient temperature field in the solid is described by the following nondimensional equations:

$$\frac{\partial^2\theta}{\partial x^2} + \frac{1}{c^2}\frac{\partial^2\theta}{\partial y^2} = \frac{\partial\theta}{\partial t} \tag{1}$$

$$\theta(x, y, 0) = \theta_0(x, y) \tag{2}$$

$$\frac{\partial\theta}{\partial x}(0, y, t) = 0 \tag{3}$$

$$\frac{\partial\theta}{\partial y}(x, 0, t) = 0 \tag{4}$$

$$\theta(1, y, t) + \frac{c}{\mathrm{Bi}}\frac{\partial\theta}{\partial x}(1, y, t) = F(t) - \frac{\mathrm{St}}{\mathrm{Bi}}\theta^4(1, y, t) \tag{5}$$

$$\theta(x, 1, t) + \frac{1}{\mathrm{Bi}}\frac{\partial\theta}{\partial y}(x, 1, t) = F(t) - \frac{\mathrm{St}}{\mathrm{Bi}}\theta^4(x, 1, t) \tag{6}$$

The nondimensional parameters are the Biot number, $\mathrm{Bi} = hb/k$, the Stefan number, $\mathrm{St} = \sigma f T_{f,0}{}^3 b/k$, and a geometry factor $c = b/a$. Symbol $F(t)$ is used for the term $\theta_f(t) + \theta_f{}^4(t)\mathrm{St}/\mathrm{Bi}$. A value for the effective shape factor, f, is obtained by assuming that the fire is a uniform, isothermal, gray gas as described in the Appendix.

Quasi-Analytic Solution. It is assumed that a solution of the form

$$\theta(x, y, t) = \sum_{m=1}^{\infty}\sum_{n=1}^{\infty} C_{mn}(t)\cos p_n x \cos q_m y \tag{7}$$

exists, where p_n and q_m are the set of all positive roots of the transcendental equations

$$p_n \tan p_n = \mathrm{Bi}/c \qquad q_m \tan q_m = \mathrm{Bi} \tag{8}$$

The obvious basis for equation (7) is the known solution to the corresponding linear problem whose eigenvalues are given by equation (8). Even though the set of equations (1)–(6) is not a regular Sturm-Liouville problem, the trigonometric functions in the assumed solution remain orthogonal, and application of orthogonality to equation (7) yields

$$\phi_{mn}C_{mn}(t) = \int_0^1\int_0^1 \theta(x, y, t)\cos p_n x \cos q_m y\, dxdy \tag{9}$$

where

$$\phi_{mn} = \frac{1}{4}\left(1 + \frac{\sin 2p_n}{2p_n}\right)\left(1 + \frac{\sin 2q_m}{2q_m}\right) \tag{10}$$

Differentiating equation (9) and substituting for $\partial\theta/\partial t$ from the governing equation (1), and integrating the results by parts, one obtains

$$\frac{1}{\gamma_{mn}}\frac{dC_{mn}}{dt} + C_{mn} = \psi_{mn}F(t) - G_{mn}(t) \tag{11}$$

where

$$\gamma_{mn} = p_n{}^2 + q_m{}^2/c^2 \tag{12}$$

$$\psi_{mn} = \sin p_n \sin q_m/(\phi_{mn}p_n q_m) \tag{13}$$

and

$$G_{mn}(t) = \frac{\mathrm{St}}{\gamma_{mn}\phi_{mn}c}\left[\cos p_n\int_0^1\theta^4(1, y, t)\cos q_m y\, dy + \frac{\cos q_m}{c}\int_0^1\theta^4(x, 1, t)\cos p_n x\, dx\right] \tag{14}$$

It should be noted that $G_{mn}(t)$ in equation (11) is unknown and can be found from equation (14) only after the surface temperature is known from equation (7). Equations (7) and (11) are thus a simultaneous set. If $G_{mn}(t)$ is negligible, which will be the case when radiation can be neglected compared to convection, equation (11) can be integrated directly.

One advantage of obtaining this partially analytic solution is that, whereas complete numerical solutions require the results throughout the column at the previous time step, the analytic solution for the entire column requires only previous results on the surface.

Rather than putting equation (11) in finite difference form and solving equations (7) and (11) by iteration, a technique with more rapid convergence is used. Consider the solution of equation (11) for a small step in time from time t_1 to t

$$C_{mn}(t) = C_{mn1}\exp[-\gamma_{mn}(t - t_1)] + \psi_{mn}\gamma_{mn}\exp(-\gamma_{mn}t)\int_{t_1}^{t}F(t)\exp(\gamma_{mn}t)dt - \gamma_{mn}\exp(-\gamma_{mn}t)\int_{t_1}^{t}G_{mn}(t)\exp(\gamma_{mn}t)dt \tag{15}$$

Nomenclature

a, b = column half widths
A = area
Bi = Biot number hb/k
c = ratio b/a
c_p = specific heat
C_{mn}, C_{mn}' = defined by equations (7) and (18)
f = effective shape factor for radiation
F = fire temperature group $\theta_f + \theta_f{}^4$ St/Bi
G_{mn} = defined by equation (14)
h = convective heat transfer coefficient
k = solid phase thermal conductivity
p_n, q_m = roots of equation (8)
q = dimensionless heat flux $a\bar{q}/(kT_{f,0})$
$\bar{q}$ = dimensional heat flux
St = modified Stefan number $\sigma f T_{f,0}{}^3 b/k$
t = dimensionless time $\bar{t}\alpha/a^2$
$\bar{t}$ = dimensional time
T = absolute temperature
x, y = dimensionless coordinate system $x = \bar{x}/a$, $y = \bar{y}/b$
$\bar{x}, \bar{y}$ = Cartesian coordinates
α = thermal diffusivity $k/(\rho c_p)$
γ_{mn} = given by equation (12)
ϵ = emissivity
θ = dimensionless temperature $T/T_{f,0}$
ρ = density
σ = Stefan-Boltzmann constant
ϕ_{mn}, ψ_{mn} = given by equations (10) and (13)

Subscripts

f = fire
m, n = indices of the roots of equation (8)
s = column surface
w = walls (bounding surfaces)
x, y = components of a vector in x- and y-directions, respectively
0 = initial condition
1 = value of a variable at the previous time step

If the time interval is chosen to be small, it may be assumed that $F(t)$ and $G_{mn}(t)$ are both linear over this interval. With this assumption and the known $F(t)$, integration by parts yields

$$C_{mn}(t) = \psi_{mn}F(t) + [C_{mn_1} - \psi_{mn}F_1 + (\psi_{mn}/\gamma_{mn})(F - F_1)/(t - t_1) + G_{mn1}]\exp[-\gamma_{mn}(t - t_1)] - (\psi_{mn}/\gamma_{mn})(F - F_1)/(t - t_1) - G_{mn}(t) + (1/\gamma_{mn})\{1 - \exp[-\gamma_{mn}(t - t_1)]\} \times (G_{mn} - G_{mn1})/(t - t_1) \quad (16)$$

Equations (7) and (16) may be solved by iteration. The convergence of the series in equation (7) is improved by rearranging equations (7) and (16). From equation (7)

$$\theta(x, y, t) = \theta_f(t) + \sum_{m=1}^{\infty}\sum_{n=1}^{\infty} C_{mn}'(t) \cos p_n x \cos q_m y \quad (17)$$

where

$$C_{mn}'(t) = C_{mn}(t) - \psi_{mn}\theta_f(t) \quad (18)$$

Equation (16) can now be written in terms of C_{mn}' as

$$C_{mn}' = \psi_{mn}\theta_f^4(t)\ \mathrm{St/Bi} + [C_{mn1}' - \psi_{mn}\theta_{f1}^4\ \mathrm{St/Bi} + (\psi_{mn}/\gamma_{mn})(F - F_1)/(t - t_1) + G_{mn1}]\exp[-\gamma_{mn}(t - t_1)] - (\psi_{mn}/\gamma_{mn})(F - F_1)/(t - t_1) - G_{mn}(t) + (1/\gamma_{mn}) \times \{1 - \exp[-\gamma_{mn}(t - t_1)]\}(G_{mn} - G_{mn1})/(t - t_1) \quad (19)$$

In order to start the computation, initial values for θ_f, F, G_{mn}, and C_{mn}' are required. From the initial condition specified by equation (2)

$$\theta_f(0) = 1 \quad (20)$$

$$F(0) = 1 + \mathrm{St/Bi} \quad (21)$$

$$G_{mn}(0) = \frac{\mathrm{St}}{\gamma_{mn}\phi_{mn}c}\left[\cos p_n \int_0^1 \theta_0^4(1, y)\cos q_m y dy + \frac{\cos q_m}{c}\int_0^1 \theta_0^4(x, 1)\cos p_n x dx\right] \quad (22)$$

Equations (9) and (18) give

$$C_{mn}'(0) = \frac{1}{\phi_{mn}}\int_0^1\int_0^1 \theta_0(x, y)\cos p_n x \cos q_m y\, dxdy - \psi_{mn} \quad (23)$$

In the special case when the initial column temperature is assumed equal to the initial fire temperature, then $\theta_0(x, y) = 1$, so that $G_{mn}(0) = \psi_{mn}\mathrm{St/Bi}$ and $C_{mn}'(0) = 0$.

Limiting Cases. When the nonlinear terms in the boundary condition can be neglected, analytical results are obtained which clarify the general effect of each parameter. The solution becomes analytic in the following cases.

Temperature Boundary Condition. In the limit $h \to \infty$, the column surface temperature approaches the fire temperature, the mixed boundary conditions reduce to temperature conditions, and equations (8) give

$$p_n = \frac{(2n - 1)\pi}{2} \qquad q_m = \frac{(2m - 1)\pi}{2} \quad (24)$$

and the solution is simply equation (7) with $C_{mn}(t)$ given by equation (11) with $G_{mn}(t) = 0$ and $F(t) = \theta_f(t)$. Equation (11) can be integrated directly to obtain

$$C_{mn}(t) = [C_{mn}(0) + \psi_{mn}\gamma_{mn}\int_0^t \exp(\gamma_{mn}t)\theta_f(t)\,dt]\exp(-\gamma_{mn}t) \quad (25)$$

The integral in equation (25) can be carried out analytically for a restricted set of $\theta_f(t)$. The temperature field is then known at any time using $C_{mn}(0)$ directly from the initial condition.

Convective Boundary Condition. When radiation can be neglected compared to convection, $\mathrm{St} \ll \mathrm{Bi}$, $F \simeq \theta_f$, and $G_{mn}(t) \to 0$ as in the previous case. The only difference from the first case is that since h is finite, p_n and q_m are not explicit. Equation (25), therefore, again applies for this case.

Scaling Laws. An important application of this analysis is to define the conditions under which laboratory scaled experiments accurately describe full-scale tests. The governing nondimensional parameters are $c = b/a$, $x = \bar{x}/a$, $y = \bar{y}/b$, $\theta = T/T_{f,0}$, $t = \bar{t}\alpha/a^2$, $\mathrm{Bi} = hb/k$, and $\mathrm{St} = \sigma f b T_{f,0}^3/k$. The requirement for scaling is obviously that all these groups remain the same in the laboratory and full scales. Geometric similarity maintains c constant. For dynamic similarity, the dimensionless time-temperature curve must remain unchanged. Thus, the values of T_f should be the same in the laboratory and full scales. As far as the thermal field is concerned, the material, i.e., α, may be the same in both cases. This may not be true for the stress field where aggregate size would probably be scaled. As in all transient conduction problems to maintain the Fourier number, the laboratory time decreases by the square of the factor by which the length scale decreases. Thus, a half scale ASTM Standard E-119 fire test would traverse the same temperatures four times faster than full-scale. Scaling would be cost effective in both material and time. In order to maintain the Biot number constant for the same column material, h must vary inversely with the length scale. Thus, the laboratory h must exceed the full scale h, e.g., by artificially introducing additional forced convection. Note that this is an average h and it is assumed the detailed flow need not be scaled. One problem here is experimentally determining the appropriate full scale h.

Finally the Stefan number can be maintained by varying the effective shape factor, f, inversely with the length scale. Scaling can be accomplished only over a restricted range of full scale f, e.g., $0 \leq f \leq 0.5$. An increase in f could be achieved by seeding the test furnace fuel with silicone monoxide particles to increase the emissivity of the flame. It would also be possible to coat the surface of the specimen to alter its total emissivity. Finally changing the size of the test enclosure could be used to vary f as indicated in the Appendix.

Within the assumptions of this model, the temperature field in structural elements can be obtained from appropriately scaled laboratory tests. Experiments are required to determine whether free water, internal cracking, or temperature-dependent properties would vitiate those assumptions. It also remains to be determined whether the more complex problem of the stress field can be scaled.

Results

The specific case of a square column with a uniform initial temperature equal to the initial temperature of the gas is considered to illustrate the results of the analysis. Two temperature histories are utilized to represent the extremes expected for actual fire development within structures:

1 A long duration, moderate intensity fire as defined by the American Society for Testing and Materials (ASTM), E-119 standard as shown in Fig. 2 [1].

2 A short-duration, high-intensity (SDHI) fire developed from the work of Magnusson and Thelandersson [2] as shown in Figs. 3 and 5. The standard ASTM and SDHI time-temperature curves can be extracted from the plots labeled $\mathrm{Bi} = \infty$ in Figs. 2 and 3 using the thermal properties of concrete as $k = 1.5$ kcal/hr-m-°C, $\rho = 2400$ kg/m^3, and $c_p = 0.27$ kcal/kg-°C, and a column size of 0.3×0.3 m.

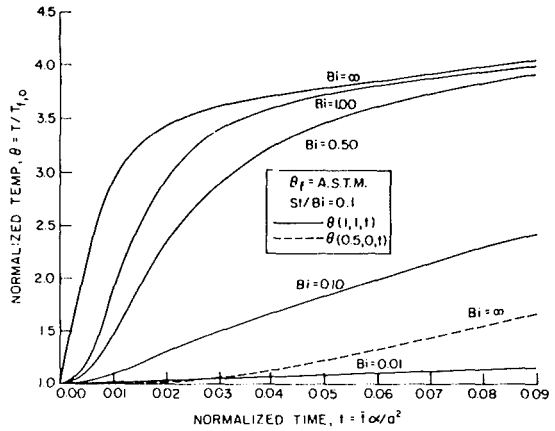

Fig. 2 Temperature histories at two locations in the column for the ASTM time-temperature curve, parameterized in the Biot number, Bi, for a fixed St/Bi ratio

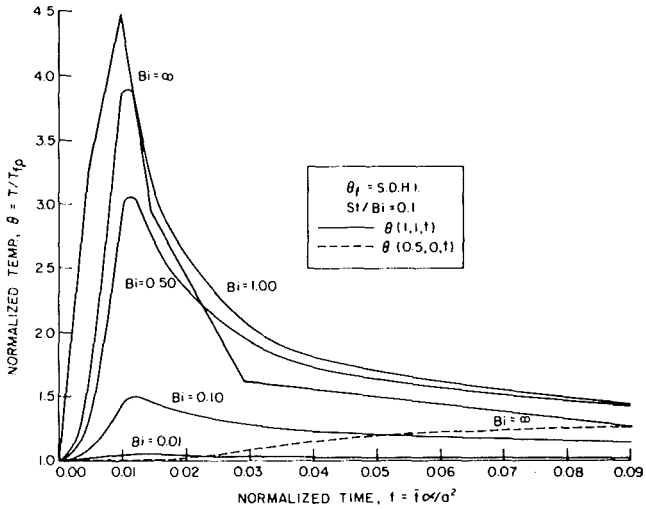

Fig. 3 Temperature histories for the SDHI time-temperature curve for conditions identical to Fig. 2

Figs. 2 and 3 show the temperature histories at an interior point (0.5, 0), and a surface point (1, 1) exposed to the foregoing fires. The ratio of the Stefan number $St = \sigma f b T_{f,0}^3/k$ to the Biot number is held constant to maintain a constant relative effect of radiation to convection. The specific value of St/Bi = 0.1 corresponds to a maximum $f = 0.9$ and a minimum $h = 4.9$ kcal/hr-m^2-°C. It represents a limiting typical case where the effect of radiation is large compared to convection. The curve for Bi = 0.01 in Figs. 2 and 3 for point (0.5, 0) is coincident with the t axis.

Increasing Bi corresponds to increasing the rate of heat transfer until the limit Bi $\to \infty$ is reached where the temperature history on the surface is the same as the fire temperature history as shown in Figs. 2 and 3 for the corner. Once Bi is 0(1), further increases do not strongly influence the corner temperature. Since the corner point is much more sensitive to the fire temperature than other points on the surface, round columns might be preferred in terms of fire endurance. Other calculations involving all locations on the surface indicate that when Bi $\gtrsim$ 10, a temperature boundary condition may be assumed at the surface. Since the surface temperature always lags the fire temperature, the former exceeds the latter during the cooling of SDHI curve. Heat is conducted from a temperature maximum inside the column to the surface and from the surface to the surroundings.

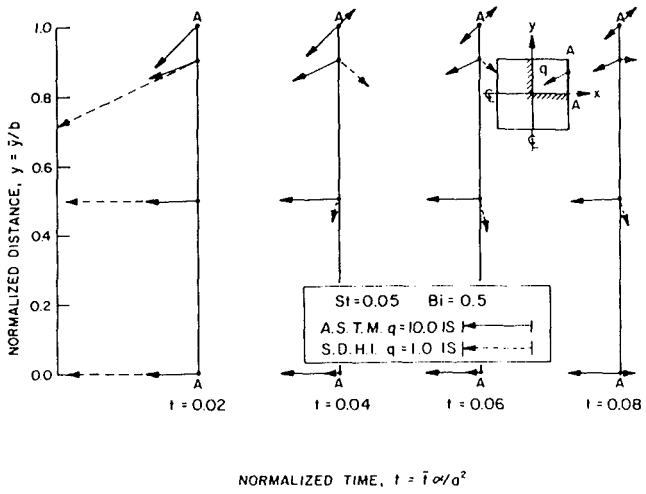

Fig. 4 Transient dimensionless heat flux vectors at the surface of a column subjected to the ASTM and SDHI time-temperature curves

Fig. 4 shows heat flux vectors for St = 0.05 and Bi = 0.5. The dimensionless heat fluxes are normalized on $kT_{f,0}/a$. Heat flux vectors at points along the line A-A on the surface are indicated at several times. Due to symmetry, i.e., $c = 1$, these results describe the entire surface. As expected, the heat fluxes quickly increase to a maximum and then decrease. Except at the corner, this peak occurs at $t \sim 0.04$ for the ASTM curve and at $t \sim 0.01$ for the much faster SDHI curve. In both the cases, heat fluxes approach zero as $t \to \infty$ due to the fact that both ASTM and SDHI fire curves become flat at large times, and therefore the temperature everywhere in the element approaches the approximately steady asymptotic fire temperature. The heat fluxes appear here to be larger for the ASTM fire, but this is not true for times smaller than 0.01, where the hot, fast SDHI fire produces fluxes of 0(10) and the ASTM fire produces fluxes of 0(2). A reversal of the heat flux vector is first observed for the corner point in a SDHI fire slightly before a nondimensional time of 0.03. Because of symmetry, the heat flux vectors in both cases, for the central surface point and for the corner point, are, respectively, along the column center line and along the line joining the origin with the corner. At other points the heat flux vectors rotate in a counter clockwise direction with increasing time.

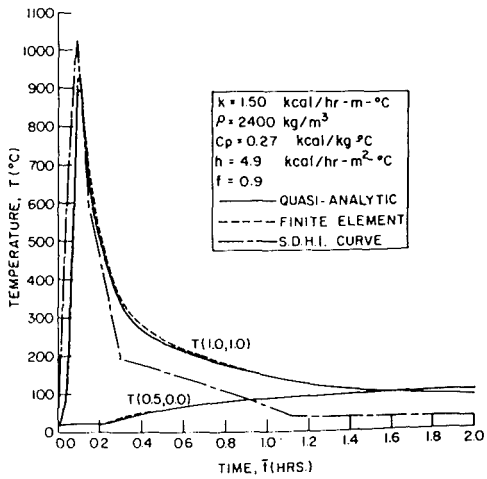

Fig. 5 Comparison of this solution with a finite element solution for a 0.3 × 0.3 m concrete column in a short duration high intensity fire

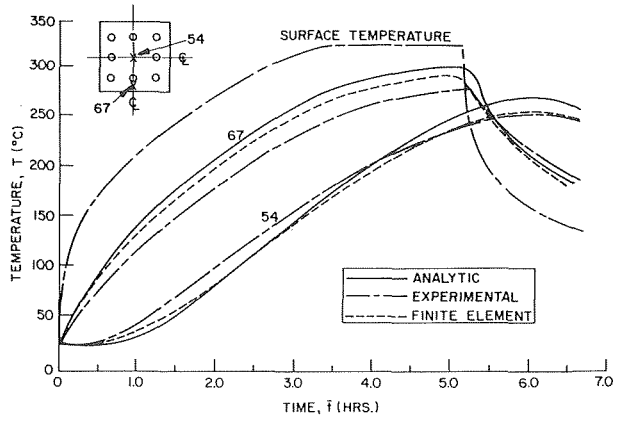

Fig. 6 Comparison of experimental and theoretical temperature histories for the special case of a temperature boundary condition on a 0.3 × 0.3 m concrete column—the material properties are as indicated in Fig. 5 (the *x*'s indicate thermocouple locations and the circles are reinforcing bars)

Comparisons

Finite Element Method. Fig. 5 shows a comparison of the temperature histories for a 0.3 × 0.3 m concrete column with a finite element solution [3]. The SDHI curve was chosen to give a comparison under the more stringent conditions of faster changes in the fire temperature. The concrete material properties shown were suggested by Bizri [5]. The agreement between the two methods is excellent.

The computation time was of the same order for both methods; however, the quasi-analytic solution included heat fluxes omitted in the finite element calculation. For the quasi-analytic solution, computer time reduces rapidly for smaller values of f, which was chosen here to be almost maximum, while computation time for the finite element solution is comparatively constant.

When the results inside the element are required for fewer points, or the Stefan number is small, or if heat fluxes are desired, it is more convenient to use the quasi-analytic solution. On the other hand, if the thermal properties are temperature dependent, or the material is anisotropic, or the geometry is other than rectangular, circular, or spherical, no analytical solution can be easily obtained and the finite element method would be the best choice.

Experimental Data. Experiments on a 0.3 × 0.3 × 1.5 m high reinforced concrete column were carried out by Bresler [15]. The column contained eight reinforcing bars, 16 mm in diameter, placed on the perimeter of a square with sides of 0.2 m as shown in the column cross section in Figs. 6 and 7. The column surfaces were heated by radiation from electric lamps. The surface temperature was monitored and the power to the lamps controlled so that the surface temperature followed a prescribed curve. The comparison was made by letting Bi → ∞ to simulate a temperature boundary condition at the surface. The experimental time-temperature histories were available for various points on the surface and inside the column.

Due to the placement of the lamps, the temperature varied along the surface in the experiment. The quasi-analytical solution does not simulate this mode of heating (though it does account for variations in surface temperatures under a uniform fire with mixed boundary conditions). The temperature given by the thermocouple placed on the center line was used as an approximate boundary condition. This temperature will have the most influence along the center line of the column where the comparison in these figures is made. The maximum experimental variation in the temperature for any two points on the surface was 20°C at 300°C.

Fig. 6 shows the time-temperature curves for thermocouples 54 and 67 imbedded in the column. Thermocouple 67 is 0.13 m from the center (0.02 m from the surface) on the center line of the column. This places it 19 mm from the outside surface of a reinforcing bar. Thermocouple 54 is located in the center of the column. The agreement between analytic and experimental results is good in spite of the many simplifying assumptions, i.e., temperature independent thermal properties, neglecting reinforcement effects, moisture diffusion, and specifying constant temperature at the surface. The results given by the finite element method, which takes into account most of these effects, are only slightly better than those obtained by the analytic method. Thermocouple 67 indicates lower temperatures than the analytic and numeric results during the temperature rise portion. This discrepancy is probably caused by the proximity of the thermocouple to the reinforcing bar which acts as a heat sink due to its high thermal conductivity relative to concrete. The slight discrepancies for thermocouple 54 could be due to the fact that this point is farthest from the surface and therefore strongly dependent on the concrete thermal properties which are not precisely known. Moisture may not have played a role here since the column had been heated previously several times.

Fig. 7 shows temperature profiles along a center line at different times. Good agreement between analytic, experimental, and numeric results is obtained. The quasi-analytic results neglected the reinforcement bars. The finite element results which included that effect still differ slightly from the experimental data, possibly because of cracking in the concrete near the reinforcing bars due to the different coefficients of thermal expansion for the steel and concrete. Such material behavior is obviously difficult to incorporate in any thermal analysis. It can be seen from the results, however, that the overall effects of these phenomena may not be of critical significance.

Internal Stresses. To assess the impact of using an approximate temperature field on the resulting stress field, a comparison was made between the stress fields obtained using the finite element and quasi-analytic temperature fields as inputs. The results are shown in Fig. 8 as the stress at two points in a column cross section as a function of time. Point 1 is in the steel reinforcing bar near a corner, chosen to represent a maximum difference in local temperature gradient. Point 2 is in the computational element adjacent to the surface center line. The temperature fields used are those shown in Figs. 6 and 7. The agreement is good.

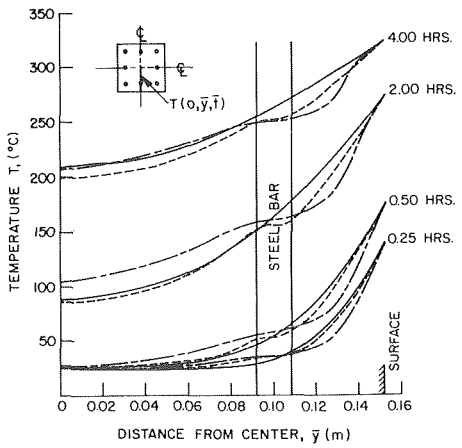

Fig. 7 Comparison of experimental and theoretical temperature profiles at various times for the same column, boundary conditions, and notation as in Fig. 6

Conclusions

In summary, the unsteady, two-dimensional temperature field in a structural element subject to unsteady, nonlinear, mixed boundary conditions has been obtained with a minimum of numerics. This solution has been applied to a rectangular column unifor-

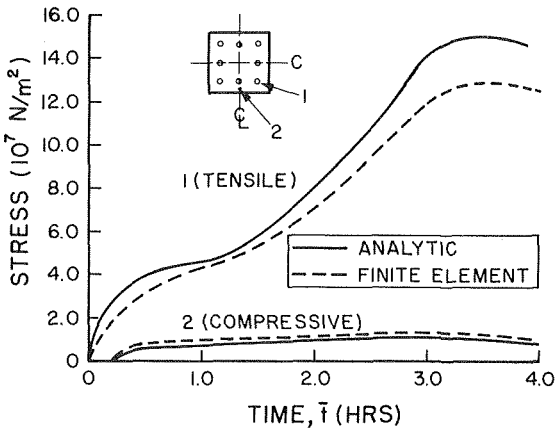

Fig. 8 Comparison of stress histories obtained from the temperature field shown in Figs. 6 and 7

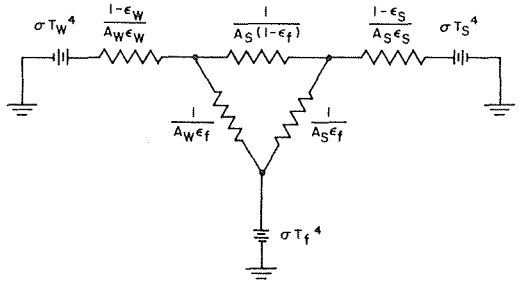

Fig. 9 Radiation analysis network describing the interaction between the column surface, the fire, and the bounding surfaces of the surrounding enclosure

mally exposed to fire. The governing nondimensional groups have been identified as the Biot number $\mathrm{Bi} = hb/k$, the Stefan number $\mathrm{St} = \sigma f b T_{f,0}^3/k$, and a geometric ratio $c = b/a$.

General results have been obtained for a wide range of Biot numbers. Temperature fields and heat fluxes within the column were obtained for two extreme fire histories, the American Society for Testing and Materials (ASTM) E-119 time-temperature curve and a short-duration high-intensity (SDHI) time-temperature curve. The most severe condition is the ASTM curve with strong radiative interaction. Comparison with experimental data [15] and finite element calculations [3] provide good agreement, and permit the use of these temperature fields as input to the structural stress problem.

Next, the effects of mass transport [16] of free and bound water in concrete might be introduced to determine whether the abrupt changes in the thermal field occurring at evaporation fronts have a significant impact on the stress field. It would also be interesting to include more realistic nonuniform boundary conditions by modeling the fire in an enclosure. A principal difficulty is that the temperature in the enclosure would no longer be completely decoupled from the temperature field within the column.

Acknowledgments

The authors are grateful for support from National Science Foundation Grants GI-43 and ERT70-01080-A05 and to B. Bresler for his assistance.

References

1 "Standard Methods of Fire Tests of Building Construction and Materials E 119-73," *Book of ASTM Standards*, American Society for Testing and Materials, Part 14, Philadelphia, Nov. 1970, p. 462.

2 Magnusson, S. E., and Thelandersson, S., "Temperature Time Curves of Complete Process of Fire Development," *ACTA*, Polytechnica Scandanavia, Civil Engineering and Building Construction, Stockholm, Series No. 65, Table A6, 1970, p. 136.

3 Becker, J., Bizri, H., and Bresler, B., "FIRES-T A computer Program for the Fire Response of Structures—Thermal," Report No. UCB FRG 74-1, *Fire Research Group, University of California*, Berkeley, Jan. 1974.

4 Becker, J. M., and Bresler, B., "FIRES-RC A Computer Program for the Fire Response of Structures—Reinforced Concrete," Report No. UCB FRG 74-3, Fire Research Group, University of California, Berkeley, July 1974.

5 Bizri, H., "Structural Capacity of Reinforced Concrete Columns Subjected to Fire Induced Thermal Gradients," PhD dissertation, University of California, Berkeley, Jan. 1973.

6 Mann, W., and Wolf, F, "Heat Transfer Between Solids and Gases Under Nonlinear Boundary Conditions," *Quarterly of Applied Mathematics*, Vol. 9, No. 2, July 1951, pp. 163–184.

7 Jaeger, J. C., "Conduction of Heat in Solids With Power Law of Heat Transfer at Its Surface," *Cambridge Philosophical Society Proceedings*, Vol. 46, Part 4, Oct. 1950, pp. 634–641.

8 Goldstein, S., *Modern Developments in Fluid Mechanics*, Clarendon Press, Oxford, England, Vol. 1, Chap. IV, 1938.

9 Lach, Jan, "Variational Approach to the Unsteady Heat Conduction With Nonlinear Heat Transfer Coefficient," *Heat Transfer—Soviet Research*, Vol. 6, No. 1, Jan.–Feb. 1974, pp. 145–150.

10 Chambre, Paul L., "Nonlinear Heat Transfer Problem," *Journal Applied Physics*, Vol. 30, No. 11, Nov. 1959, pp. 1683–1688.

11 Clauson, W. W., "Nonlinear Problem in Heat Conduction," *Chemical Engineering Progress Symposium Series*, Vol. 61, No. 57, 1965, pp. 16–25.

12 Crosbie, A. L., and Viskanta, R., "Transient Heating or Cooling of One-Dimensional Solids by Thermal Radiation," *Third International Heat Transfer Conference—Proceedings*, Vol. 5, 1966, pp. 146–153.

13 Dicker, D., and Asnani, M., "Perturbation Solution for Nonlinear Radiation Heat Transfer Problem," *Third International Heat Transfer Conference—Proceedings*, Vol. 5, 1966, pp.164–173.

14 Kartashow, E. M., and Moryakov, V. E., "Class of Heat Conduction Problems With Time-Variable Heat Transfer Coefficient," *Soviet Aeronautics*, Vol. 16, No. 1, 1973, pp. 54–59.

15 Iding, R., Lee, J., and Bresler, B., "Behavior of Reinforced Concrete Under Variable Elevated Temperatures," Report No. UCB-FRG 75-8, Fire Research Group, University of California, Berkeley, Apr. 1975.

16 Min, Kun, and Emmons, Howard W., "The Drying of Porous Media," *Proceedings of the 1972 Heat Transfer and Fluid Mechanics Institute*, Stanford University Press, 1972, pp. 1–18.

APPENDIX

Surface Boundary Conditions

The total heat transfer to the column is

$$q_s = h(T_f - T_s) + \sigma\epsilon_s \times \frac{\left[\frac{\epsilon_f + \epsilon_w - \epsilon_f\epsilon_w}{\epsilon_f\epsilon_w(1-\epsilon_f)} + \frac{A_s}{A_w}\frac{1-\epsilon_w}{\epsilon_w}\right](T_f^4 - T_s^4) - \frac{1}{\epsilon_f}(T_f^4 - T_w^4)}{\frac{\epsilon_f + \epsilon_w - \epsilon_f\epsilon_w}{\epsilon_f\epsilon_w(1-\epsilon_f)}\left[1 + \frac{A_s}{A_w}(1-\epsilon_f)(1-\epsilon_w)\frac{\epsilon_f + \epsilon_s - \epsilon_f\epsilon_s}{\epsilon_f + \epsilon_w - \epsilon_f\epsilon_w}\right]} \tag{A1}$$

where the network analysis shown in Fig. 9 provides the radiative component.

Equation (A1) can be used as the boundary condition at the column surface once the unknown temperature of the bounding surfaces, T_w, is determined. In each of three limiting cases the total heat transfer can be written in the form

$$q_s = h(T_f - T_s) + \sigma f(T_f^4 - T_s^4) \tag{A2}$$

Case (i) $T_w = T_f$.

$$f = \frac{\epsilon_s\left[\frac{\epsilon_f + \epsilon_w - \epsilon_f\epsilon_w}{\epsilon_f\epsilon_w(1-\epsilon_f)} + \frac{A_s}{A_w}\frac{1-\epsilon_w}{\epsilon_w}\right]}{\frac{\epsilon_f + \epsilon_w - \epsilon_f\epsilon_w}{\epsilon_f\epsilon_w(1-\epsilon_f)}\left[1 + \frac{A_s}{A_w}(1-\epsilon_f)(1-\epsilon_w) \times \frac{\epsilon_f + \epsilon_s - \epsilon_f\epsilon_s}{\epsilon_f + \epsilon_w - \epsilon_f\epsilon_w}\right]} \tag{A3}$$

For realistic systems $A_w \gg A_s$, and the foregoing expression simplifies to

$$f = \epsilon_s \tag{A4}$$

Case (ii) $T_w \approx T_s$.

Taking the temperature history of the walls equal to an average column surface temperature history,

$$f = \frac{\epsilon_s\left[\frac{1}{1-\epsilon_f} + \frac{A_s}{A_w}(1-\epsilon_w)\right]}{\frac{\epsilon_f + \epsilon_w - \epsilon_f\epsilon_w}{\epsilon_f(1-\epsilon_f)}\left[1 + \frac{A_s}{A_w}(1-\epsilon_f)(1-\epsilon_w)\right] \times \frac{\epsilon_f + \epsilon_s - \epsilon_f\epsilon_s}{\epsilon_f + \epsilon_w - \epsilon_f\epsilon_w}\right]} \tag{A5}$$

For $A_w \gg A_s$, this becomes

$$f = \frac{\epsilon_f\epsilon_s}{\epsilon_f + \epsilon_w - \epsilon_f\epsilon_w} \tag{A6}$$

Case (iii) Adiabatic Walls.

Returning to the network in Fig. 9 and treating the bounding surfaces as adiabatic gives

$$f = \frac{\epsilon_s\left[1 + (1-\epsilon_f)\frac{A_s}{A_w}\right]}{1 + \frac{A_s}{A_w}\frac{1-\epsilon_f}{\epsilon_f}(\epsilon_f + \epsilon_s - \epsilon_f\epsilon_s)} \tag{A7}$$

Again in the limit $A_w \gg A_s$, this reduces to

$$f = \epsilon_s \tag{A8}$$

Emissivity of a concrete surface is approximately 0.9. The value of f is, therefore, close to 0.9 in the first and third cases. However, in the second case, f depends upon ϵ_f as well. Choosing $\epsilon_s = \epsilon_w = 0.9$, and $\epsilon_f = 0.3$, equation (A6) gives $f = 0.29$. For $\epsilon_f = 0.9$, $f = 0.82$ is obtained. The value of f applicable to real fires could therefore be expected to lie in the range of 0.3–0.9.

ERRATUM

Erratum: W. J. Minkowycz and E. M. Sparrow, "Local Non-Similar Solutions for Natural Convection on a Vertical Cylinder," published in the May 1974 issue of the JOURNAL OF HEAT TRANSFER, pp. 178–183

Owing to an inadvertency, the terms ϕ and χ were, respectively, omitted from the left-hand sides of equations (21) and (28). Fortunately, the heat transfer results are insensitive to the omitted terms. Calculations for $\xi = 0.5$ and 5.0 have shown that when these terms are included, the $\theta'(\xi,0)$ values are only 0.4–0.5 percent less than those given in the paper. By any practical measure, these differences are negligible.

Another affirmation of the good accuracy of the results given in the paper can be cited on the basis of a comparison with the finite-difference solutions of Cebeci (*Proceedings, Fifth International Heat Transfer Conference,* Vol. III, Sept. 1974, pp. 15–19). Inasmuch as neither the ξ values nor the Prandtl numbers of Cebeci's calculations coincide with those of the paper, interpolations were necessary to carry out the comparison. The findings of the comparison indicated agreement to within about one-quarter percent.

The skin friction results, which are proportional to $F''(\xi,0)$, are slightly more sensitive to the omitted terms than is the heat transfer, with deviations being in the range 0.5–1.25 percent.

The authors are indebted to C. C. Chen of the University of Kentucky, who first called their attention to the omitted terms.

B. J. Jody
P. C. Jain[1]
S. C. Saxena

Department of Energy Engineering,
University of Illinois,
Chicago, Ill.

Determination of Thermal Properties From Steady-State Heat Transfer Measurements on a Heated Tungsten Wire in Vacuum and Helium Gas

An experimental facility in its developed form is described for the determination of a number of thermal properties as a function of temperature in the range 400–2500 K. These are the resistivity, tensile breaking stress, the total hemispherical emittance of the tungsten wire, and the thermal conductivity of helium. These properties are computed from the knowledge of steady-state heat transfer data from tungsten wire in vacuum and in the presence of helium at pressures covering the temperature-jump and continuum regimes. These measured properties are discussed in the light of literature values wherever available.

Introduction

The knowledge of the thermal properties of gases, metal surfaces, and metal-gas interface over a wide temperature range is of great significance to proper engineering design of breeder reactors, combustors, space vehicles, etc. We have been developing a hot-wire column type instrument for the accurate measurement of such thermal properties over a temperature range of about 300–2500 K. In particular, we have reported the preliminary results on the hemispherical emittance of tungsten and platinum wires [1],[2] thermal conductivity of nitrogen [2], and the thermal accommodation coefficient for nitrogen covered tungsten-nitrogen system [3]. This heat transfer column facility is further improved and here we present data on several thermal properties determined from measurements of heat transfer as the tungsten wire is heated from ambient (400 K) to the highest possible temperature (2500 K) in vacuum and in the presence of helium at different pressures.

Experimentation

The details of the experimental facility, the experimental procedures, the data processing techniques, and the underlying theories are given in earlier publications [1–3]. The lower end of the column is modified so that known variable tensions on the axial tungsten wire can be applied either in vacuum or in a gaseous environment. The column design is described by Chen and Saxena [2] and the modified lower end is sketched in Fig. 1 which is self-explanatory. It is to be noted that the design of the loading device permits the application of variable stress on the wire. Its range is from 1.34 to 5.50 kg/mm^2 for a 0.3048 mm wire. Six specially slotted weights of cold-rolled steel each weighing 43 g can sit on an O-ring when not employed to stretch the wire. These weights are suitably collimated for suspension on the wire in the column externally, by a specially designed magnet.

Two glass columns of lengths 165 and 132 cm and internal diameter 8 mm, and each containing tungsten wire of diameter 0.3048 mm, are employed in both the modes of single and differential arrangements [2]. The glass surface is kept at a constant temperature by circulating water at 316.6 K. The tungsten wires, supplied by General Electric and stated to be chemically cleaned and straightened (type 218 CS), are used both as a heater as well as a resistance thermometer. The electric potentials developed across the tungsten wires are monitored on a multifunction meter and are

[1] On Leave from National Physical Laboratory, New Delhi, India.

[2] Numbers in brackets designate References at end of paper.

Contributed by the Heat Transfer Division for publication in the JOURNAL OF HEAT TRANSFER. Manuscript received by the Heat Transfer Division February 18, 1975. Paper No. 76-HT-C.

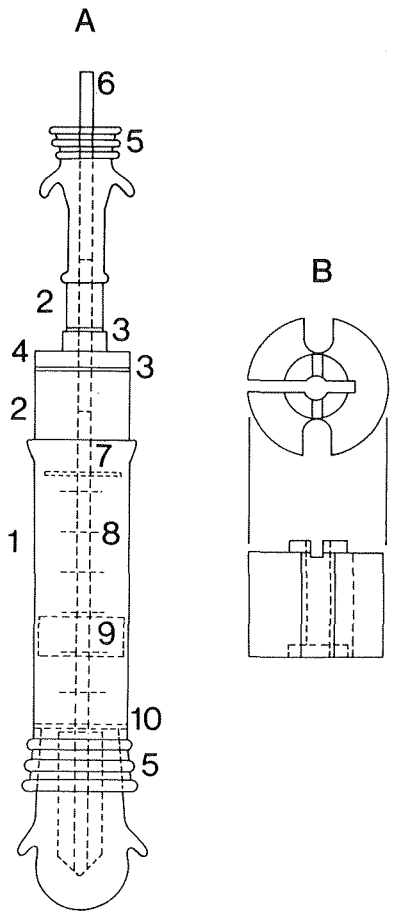

Fig. 1(*a*) The schematic of the lower end of the heat transfer column, not to scale—front view: 1–glass enclosure (diameter 28 mm), 2–glass-metal (kovar) seals, 3–silver solder joints, 4–coupling brass adapter, 5–standard glass joints, 6–brass rod (length 45 cm, dia 6 mm), 7–brass disk, 8–brass pins (six) for holding weights, 9–steel weight (six), and 10-O-ring, (*b*) top and front views of steel weight

measured on a Leeds and Northrup six-dial guarded precision potentiometer. The columns are evacuated from a high vacuum pumping system capable of creating a vacuum of about 2.7×10^{-5} Pa. To ensure reliable and reproducible temperature characteristics of the tungsten wire, it is annealed for over six hours at about 2450 K and calibrated by determining its resistance at known temperatures, which is explained in the following.

Resistivity of Tungsten

The resistance of a known length of wire is determined at the triple point of water (273.16 K) in a triple point cell supplied by Jarrett Instrument Company, and at the freezing points of tin (505.1181 K), cadmium (594.258 K), zinc (692.73 K), and aluminum (933.52 K) in a 8411 fixed temperature facility supplied by Leeds and Northrup. The resistance of the tungsten wire is also determined in the column in situ in the temperature range 1300–2500 K according to the earlier procedure [2] in which we have corrected for the heat losses at the ends of the wire. All these resistance data are converted to resistivity ($\rho = RS/2L$) values and these are found to be well correlated by the following quartic polynomial in reduced temperature (θ), within an average absolute deviation of 0.6 percent:

$$\rho(\theta) = -0.2025 + 20.00\theta + 1.549\theta^2 + 4.321\theta^3 - 1.208\theta^4 \quad (1)$$

Here ρ is in $\mu\Omega$ cm and $0.3 \leq \theta \leq 2.5$. The temperatures obtained on the basis of the given relation differ from the directly measured temperatures by about 1.3, 1.0, 0.7, and 0.4 percent at 505, 1338, 2090, and 2455 K, respectively.

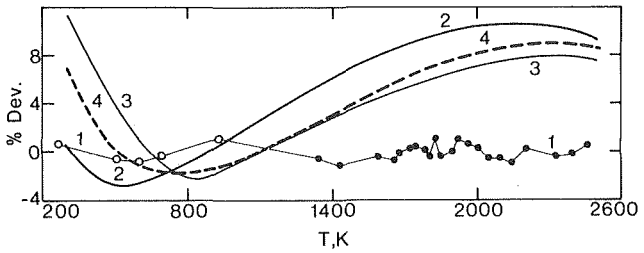

Fig. 2 Comparison of the present resistivity values based on equation (1) with the experimental data (curve 1), with the data measured at five fixed points and extrapolated to high temperatures on the basis of a quadratic relation in temperature (curve 2), with the recommended correlations due to Touloukian [4] (curve 3), and Smithells [5] (curve 4). Percent Dev. = {ρ(equation (1)) − ρ(exptl. or reference)}100/{ρ(equation (1))}. Experimental points: ● and ○.

The resistivity values based on equation (1) are compared in Fig. 2 with the experimental data points, with the resistivity data measured at five fixed points and extrapolated to high temperatures on the basis of a quadratic relation in temperature, and with the recommended correlations due to Touloukian [4] and Smithells [5]. Several conclusions can be drawn from these comparisons. First, the maximum deviation of the directly measured data points from the smooth plot is about one percent and this may be regarded as the measure of the overall precision of our resistivity determination. The absolute percentage uncertainty is judged as 1.8 and 1.4 at 500 and 2500 K, respectively. Second, as known, the practice of extrapolating the low temperature resistivity data to high temperatures is found to be unreliable. Third, the two sets of recommended values [4, 5] available in the literature differ from each other and also from the present measurements. This stresses the importance of always considering the resistivity data in reference to the sample for which it is originally taken. Fourth, the procedure adopted by us for resistivity data to use as the basis for temperature determination is reliable as well as accurate for most engineering needs and is in accordance with the recommendations of the International Practical Temperature Scale of 1968 [6].

Tensile Breaking Stress

The tension on the metal wire mounted in the column should be such that it remains taut without getting unduly stretched as its temperature is raised by electrical heating. With the modified design of the column, it is possible to measure the tensile breaking stress as a function of temperature. Known tensions were applied on wires of about 0.127, 0.203, and 0.305 mm dia and their temperatures were slowly raised till breaking occurred. The results of such investigations are shown in Fig. 3 and are especially useful in estimating the temperature to which a tungsten wire under a

Nomenclature

e = hemispherical total emittance, dimensionless
k = thermal conductivity, mW/cm-K
Kn = Knudsen number, dimensionless
L = one-half of the length of the wire, cm
P = gas pressure, Pa
Q_H = power conducted through the gas, W/cm
R = resistance per unit length, $\mu\Omega$/cm
S = cross-sectional area of the wire, cm^2
T = temperature, K
T_H = temperature of the hot wire, K
θ = reduced temperature = $T/1000$, K
ρ = resistivity, $\mu\Omega$-cm

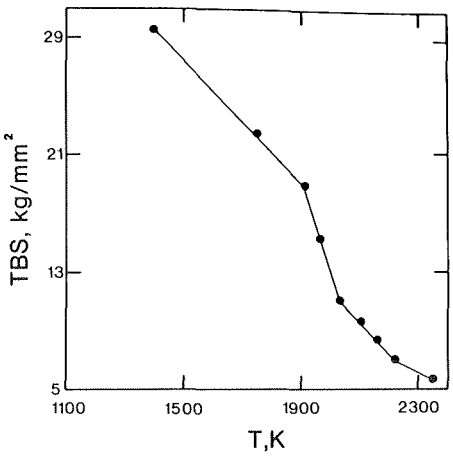

Fig. 3 The tensile breaking stress, in kg/mm², of tungsten wire as a function of its temperature, *T*, in K

known tension can be safely raised without deforming it. These experiments also confirmed that resistivity of the tungsten wires is independent of tension in the range shown in Fig. 3, and thus it is a unique parameter of its temperature only. The accuracy of the plot of Fig. 3 though judged to be conservative and consequently a linear interpolation between successive data points is considered satisfactory. The usefulness of Fig. 3 is to be emphasized.

Hemispherical Total Emittance

The surface condition of metal wires plays a dominant role in controlling the magnitude of thermal radiation from it. Wire surfaces are very sensitive to the methods of preparation, thermal history, and environmental conditions. The column instrument provides a viable basis for the accurate determination of hemispherical total emittance of metal wires as a function of temperature.

The knowledge of the electrical power required to heat the central section of the wire to different temperatures and the temperature profiles at the ends enable the determination of the hemispherical total emittance according to a procedure outlined by Chen and Saxena [1]. The results are given in Fig. 4 and the following polynomial in reduced temperature, obtained by the method of least-squares analysis, correlates the observed data within

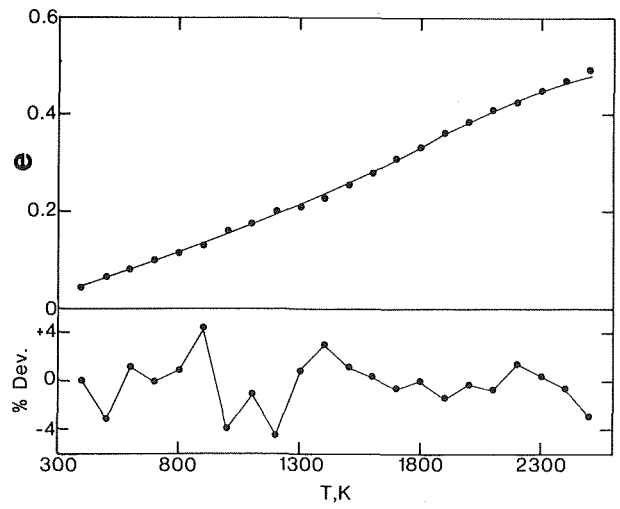

Fig. 4 (Upper) Hemispherical total emittance, *e*, of tungsten as a function of temperature, *T*, in K. ● experimental points. (Lower) Comparison of the experimental data with the predictions based on equation (2)—percent dev. = {*e* (equation (2)) − *e* (exptl.)}100/*e* (equation (2))

average absolute and maximum deviations of 1.5 and 4.5 percent, respectively:

$$e(\theta) = -0.04259 + 0.2550\theta - 0.1030\theta^2 + 0.03155\theta^3 + 0.02021\theta^4 - 0.007730\theta^5 \text{ for } 0.4 \le \theta \le 2.5 \quad (2)$$

The upper part of Fig. 4 shows the temperature dependence of e and the lower part a comparison of the actual data points with the estimates based on equation (2). The estimated percentage error in these $e(\theta)$ values is always less than 4.8.

Thermal Conductivity of Helium

The additional measurement of the electrical power required to heat the tungsten wire to a known temperature in the presence of helium is enough to determine its conductivity as explained earlier [2]. Helium gas is 99.9999 percent pure and is supplied by Matheson Gas Products. 0.3048-mm tungsten wires of length 46.24 and 86.02 cm are used. The thermal conductivity values are displayed in Fig. 5 and these are correlated by the following polynomial in reduced temperature according to the method of least-squares within average absolute and maximum deviations of 0.8 and 2.1 percent, respectively:

$$k(\theta) = 0.5504 + 3.3525\theta - 0.21166\theta^2 - 0.066260\theta^3 \text{ for } 0.4 \le \theta \le 2.3 \quad (3)$$

The values generated from equation (3) are shown by a continuous curve in Fig. 5(*a*) and the scatter of the actual data points from these smooth values in Fig. 5(*b*). The three sets of k values obtained by the single column (short and long) and differential arrangements are found to be in good agreement with each other.

The measurements are taken at a gas pressure of 62660.4 Pa where the temperature-jump correction is negligibly small and continuum heat flow conditions exists. This conclusion is based on the analysis of the Knudsen number which varies between the limits 0.001–0.0131. Previous investigations made in this laboratory suggest that continuum conditions exist in the column for Kn ≤ 0.0149 for argon, Kn ≤ 0.0119 for nitrogen, and Kn ≤ 0.0137 for neon. The calculations further revealed that at this pressure the maximum energy convected is only 0.1 percent of the energy fed to the wire. The Reynolds number is always less than 0.1, justifying thereby the assumption of laminar convection in the column implicit in our calculations. The maximum Rayleigh number for our experimental operating conditions is 1 and this is much smaller than the critical Rayleigh numbers characterizing the end effect and the onset of the secondary multicellular motion in the column [2]. The apparent conductivity values are corrected according to the procedures outlined by Chen and Saxena [2]. The accumulated magnitude of the three corrections is nearly 0.3–0.8 percent. The estimated random errors in the experimental data are 3.7, 2.6, 2.2,

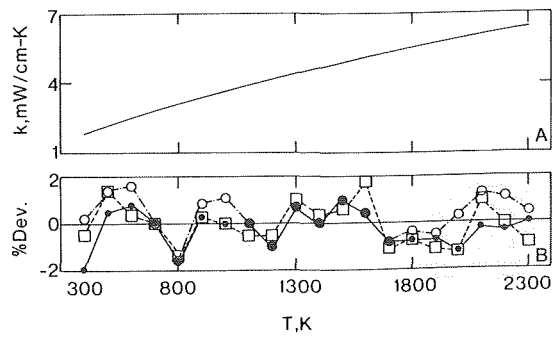

Fig. 5(a) Thermal conductivity of helium as a function of temperature, based on equation (3). (b) Comparison of three sets of experimental *k* data with the values based on equation (3). ● long column, ○ short column, □ differential arrangement. Percent dev. = {*k* (equation (3)) − *k*(exptl.)}100/*k* (equation (3)).

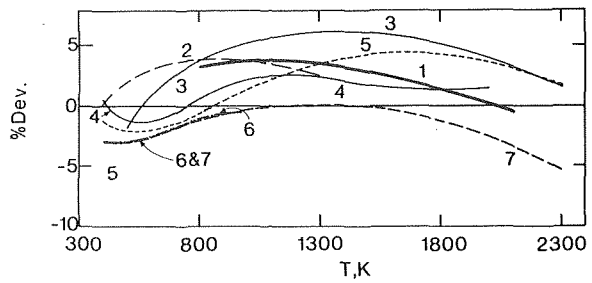

Fig. 6 Comparison of the present k data with those of Faubert and Springer [7] (curve 1), Saxena and Saxena [8] (curve 2), Timrot and Umanskii [9] (curve 3), Vargaftik, et al. [13] (curve 4), Ho, et al. [11] (curve 5), Kestin, et al. [13] direct measurements (curve 6), and Kestin, et al. [13] principle of corresponding states (curve 7)—percent dev. = {k (equation (3)) − k (reference)}100/{k (equation (3))}

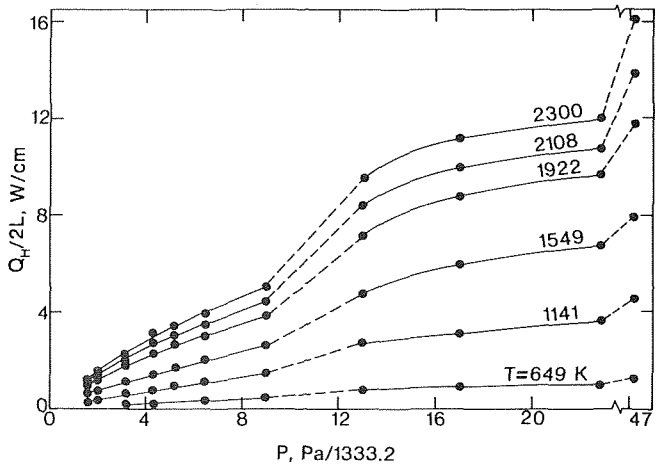

Fig. 7 Dependence of thermal energy conducted by helium on its pressure for fixed values of the hot-wire temperature

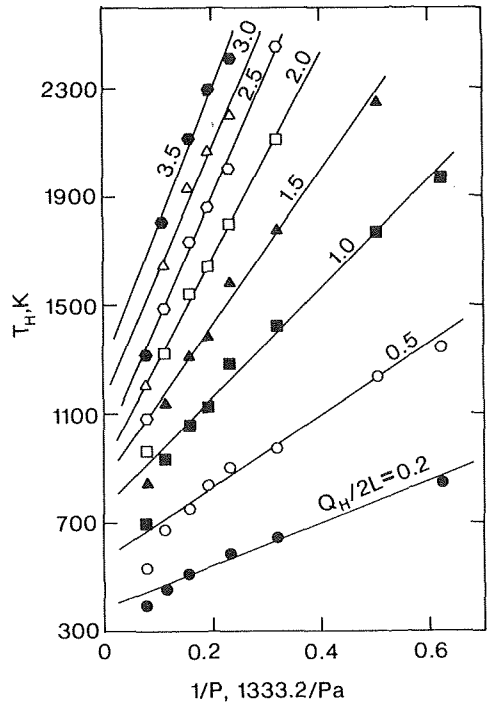

Fig. 8 Dependence of the hot-wire temperature on the gas pressure for constant power per unit length, $Q_H/2L$ (W/cm)

and 2.0 percent at 500, 1300, 2000, and 2300 K, respectively.

The present thermal conductivity data as represented by equation (3) are compared in Fig. 6 with similar other data reported by Faubert and Springer [7], Saxena and Saxena [8], Timrot and Umanskii [9], and with the correlations of available conductivity data developed by Ho, et al. [10], and Vargaftik, et al. [11]. The reported percentage experimental errors in the various works are 2.3–2.9 [7], 2 [8], and 5.5 [9]. If recognition is given to the reported uncertainties associated with each data set, the agreement between the present work and other column measurements appears to be satisfactory in each case. The correlated values are claimed to be accurate within percentage uncertainties of 2–10 [10], and 2 [11] and hence their agreement with present measurements is considered satisfactory. We also compared our conductivity values with the viscosity data, which have been measured more accurately. Curve 6 of Fig. 6 is based on the viscosity data of Kestin, et al. [13] and the procedure outlined by Jody and Saxena [14]. Curve 7 of this figure is based on their viscosity values generated by the application of the principle of corresponding states to the data for noble gases [13]. It is to be noted that the majority of the earlier measurements of thermal conductivity are in appreciable disagreement with the reliable viscosity data of Kestin, et al. [13] and the present conductivity measurements agree within the range of mutual errors of the two data sets over most of the temperature range. The current data while substantially agreeing with other measurements provide a consistent set in the temperature range 400–2300 K and at a pressure of 101325.024 Pa as the measurements of Timrot and Umanskii [9] are suspected to be unreliable and particularly at high temperatures due to their inadequate column design (Saxena and Davis [12]).

We have also measured Q_H values as a function of temperature and helium gas pressures of 2146.5, 2639.7, 4186.2, 5732.8, 6919.3, 8559.1, 11892.1, 17278.3, 22664.4, 30397.0, and 62660.4 Pa and these are shown in Fig. 7. It is to be noted that Q_H values systematically increase with pressure in this range (at least up to a pressure of about 30397.0 Pa) at a fixed temperature. In Fig. 8 are shown the plots of T_H versus $1/P$ for constant values of power, $Q_H/2L$, and their linear nature in the pressure range of 2146.5–11892.1 Pa provides the experimental confirmation to the temperature-jump theory of heat transfer [15, 16]. The theory of heat transfer for the temperature-jump region finally leads to the conclusion that $1/Q_H$ varies linearly with $1/P$, [14]. In Fig. 9, values of $2L/Q_H$ are plotted against $1/P$ for different values of T_H and the linear nature of these curves confirms the conceived mechanistic model of heat transfer [16]. The intercepts with the $2L/Q_H$ axis of the linear plots enable the determination of $k(T)$ as explained by Jody and Saxena [14]. These values at round temperatures are reported in column 3 of Table 1. The linear plots of Fig. 9 are also extrapolated to $1/P = 0$ and the corresponding values of $Q_H(T_H)$ are determined and these are employed to determine $k(T_H)$ as in the previous section and according to the procedure outlined by Chen and Saxena [2]. These $k(T_H)$ values are given in column 4 of Table 1 and are in good agreement with the other two sets. This is a stringent test of the heat transfer model for the temperature-jump regime and must be regarded as a sufficient quantitative test of the model.

We also determined $k(T_H)$ values from $Q_H(T_H)$ data taken at pressures of 22664.4 and 30397.0 Pa and these values are smaller than $k(T_H)$ values obtained for a pressure of 62660.4 Pa as well as from data of $Q_H(T_H)$ for $P = \infty$. From these $k(T_H)$ values two conclusions are clear. First, the $k(T_H)$ values obtained from data taken in the pressure range above the temperature-jump region but below the continuum conditions are smaller than the actual Fourier pressure independent conductivity values. Second, the pressure of 62660.4 Pa is high enough to establish the continuum heat flow conditions in our heat transfer column.

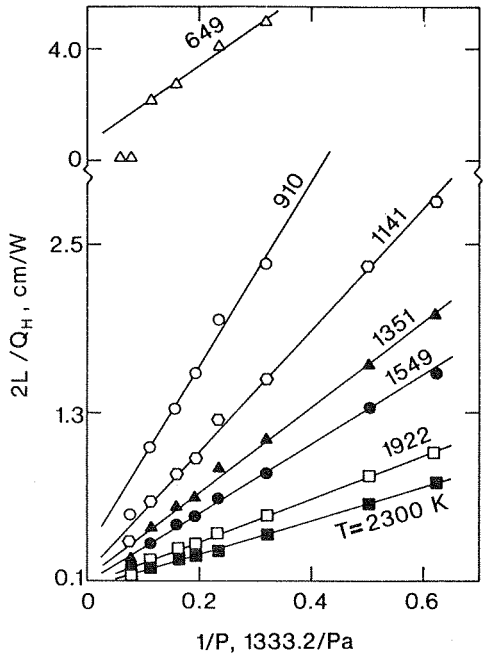

Fig. 9 Dependence of the rate of thermal energy conducted by helium on its pressure for fixed values of T_H

Table 1 Thermal conductivity of helium, in mW/cm-K, by different methods

Temp., K	Equation (3)	Intercepts of Fig. 9 in conjunction with procedure of ref. 14	ref. 2
500	2.16	2.17	2.17
700	2.77	2.77	2.83
900	3.35	3.33	3.41
1100	3.89	3.86	3.96
1300	4.40	4.40	4.46
1500	4.88		4.93
1900	5.70		5.86
2300	6.33		6.44

Acknowledgments

This work is supported by the National Science Foundation under Grant No. GK-12519. Computing services used in this research were provided by the computer center of the University of Illinois at Chicago Circle. Their assistance is gratefully acknowledged. Thanks are also due to the General Electric Company for their support and encouragement for this work.

References

1 Chen, S. H. P., and Saxena, S. C., "Experimental Determination of Hemispherical Total Emittance of Metals as a Function of Temperature," *Industrial and Engineering Chemistry Fundamentals*, Vol. 12, 1973, pp. 220–224.

2 Chen, S. H. P., and Saxena, S. C., "Experimental Determination of Thermal Conductivity of Nitrogen in the Temperature Range, 100–2200°C," *High Temperature Science*, Vol. 5, 1973, pp. 206–233.

3 Chen, S. H. P., and Saxena, S. C., "Interface Heat Transfer and Thermal Accommodation Coefficients: Heated Tungsten Wire in Nitrogen Environment," *International Journal of Heat and Mass Transfer*, Vol. 17, 1974, pp. 185–196.

4 *Thermophysical Properties of High Temperature Solid Materials*, Touloukian, Y. S., ed., Macmillan, New York, Vol. 1, 1967, p. 1021.

5 Smithells, C. J., *Tungsten*, Chapman and Hall Ltd., London, 1952, p. 180.

6 "International Practical Temperature Scale of 1968," *Metrologia*, Vol. 5, 1969, pp. 35–44.

7 Faubert, F. M., and Springer, G. S., "Measurement of the Thermal Conductivity of Helium up to 2100 K by the Column Method," *Journal Chemical Physics*, Vol. 58, 1973, pp. 4080–4083.

8 Saxena, V. K., and Saxena, S. C., "Measurement of the Thermal Conductivity of Helium Using a Hot-Wire Type of Thermal Diffusion Column," *Brit. Journal Applied Physics (Journal Physics D)*, Vol. 1, 1968, pp. 1341–1351.

9 Timrot, D. L., and Umanskii, A. C., "Investigation of the Thermal Conductivity of Helium in the Temperature Range 400–2400 K," *High Temperature*, Vol. 3, 1965, pp. 345–351.

10 Ho, C. Y., Powell, R. W., and Liley, P. E., "Thermal Conductivity of the Elements," *Journal of Physical and Chemical Reference Data*, Vol. 1, 1972, pp. 279–421.

11 Vargaftik, N. B., Filippov, L. P., Tarzimanov, A. A., and Yurchak, R. P., "Heat Conductivity of Gases and Liquids," Foreign Technology Division, Wright-Patterson Air Force Base, Ohio, Report No. AD-736 963, 1971, pp. 45–51.

12 Saxena, S. C., and Davis, F. E., "Determination of Thermal Conductivity of Gases at High Temperatures: The Column Method," *Journal of Physics E: Scientific Instruments*, Vol. 4, 1971, pp. 681–688.

13 Kestin, J., Ro, T. S., and Wakeham, W. A., "Viscosity of Noble Gases in the Temperature Range 25–700°C," *Journal Chemical Physics*, Vol. 56, 1972, pp. 4119–4124.

14 Jody, B. J., and Saxena, S. C., "Thermal Conductivity of Neon From Heat Transfer Measurements in the Continuum and Temperature-Jump Regimes," *Phys. Fluids*, Vol. 18, 1975, pp. 20–27.

15 Kennard E. H., *Kinetic Theory of Gases*, McGraw-Hill, New York, 1938, pp. 311–315.

16 Harris, R. L., "On the Determination of Thermal Accommodation Coefficients in the Temperature-Jump Region," *Journal Chemical Physics*, Vol. 46, 1967, pp. 3217–3220.

T. L. Brosseau
Mechanical Engineer.

J. R. Ward
Research Chemist.

U. S. Army Ballistic Research Laboratories, Aberdeen Proving Ground, Md.

Reduction of Heat Transfer to Gun Barrels by Wear-Reducing Additives

Heat transfer measurements were made in a 37-mm gun equipped with thermocouples at a series of axial and radial positions. The heat transferred to the gun barrel was markedly decreased when wear-reducing additives such as polyurethane foam, titanium dioxide/wax, and talc/wax were used as liners wrapped around the gun propellant. The reduction in heat transfer was greatest when the additives were folded over the forward end of the propellant at the base of the projectile. For a given configuration, all three additives tested reduced heat transfer to the gun barrel equally. This contradicts conclusions reached in full-scale tank-cannon firing tests that TiO_2/wax and talc/wax are superior to polyurethane foam as erosion reducing additives. In these firings only the metal-oxide/wax liners had flaps folded over the forward end of the propelling charge.

1 Introduction

Erosion rates of high-velocity guns such as tank cannons have been significantly reduced by the use of liners that are wrapped around the propelling charges [1].[1] The first additive was developed in Canada and consisted of high-density polyurethane foam [2]. Soon after, two Swedish inventors [3] claimed that a mixture of titanium oxide (TiO_2) and wax coated onto a rayon liner would provide a superior wear-reducing additive.

The Swedish inventors also incorporated flaps on the end of the liner that could be folded over the forward end of propelling charge at the base of the projectile. A photograph of the Swedish additive is shown in Fig. 1 depicting the serrations on the end of the wear-reducing liner. A summary of the erosion tests [4] made in the M68 tank cannon is presented in Table 1. This table demonstrates the efficacy of the wear-reducing liners in extending the useful life of the M68 tank cannon. No flaps were incorporated on the liner in the HEAT round because fins on the rear of the projectile extend back into the propelling charge. More recently Picard [5] has claimed that substitution of talc for the TiO_2 improves the erosion-reducing capability of Swedish additive. No erosion was observed in fifty-round firing tests with both APDS and HEAT rounds equipped with talc/wax liners.

Although the aforementioned additives successfully increase the useful life of gun barrels, the mechanism by which the additives reduce erosion is not clear. Since the temperature of the gun barrel surface appears to be the critical factor in determining erosion rates of metals by propellant combustion gases [6], this article concerns temperature measurements made with polyurethane foam, TiO_2/wax, and talc/wax liners. In these measurements the location

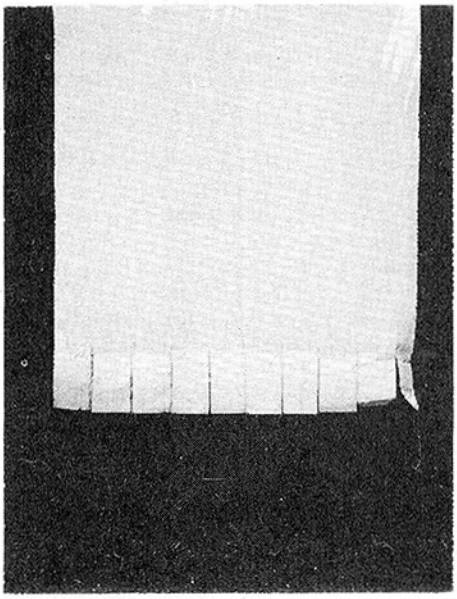

Fig. 1 TiO_2/wax additive used in the 105 mm APDS round illustrating the flaps

[1] Numbers in brackets designate References at end of paper.

Contributed by the Heat Transfer Division for publication in the JOURNAL OF HEAT TRANSFER. Manuscript received by the Heat Transfer Division June 16, 1975. Paper No. 76-HT-K.

Table 1 Erosion rates of 105 mm M68 tank cannon firing rounds equipped with wear-reducing additives[a]

Round	Additive	Wear Rate[b], mm/round x 10^3	Wear Life, rounds
M392 APDS	none	17	200
M392 APDS	polyurethane (no flaps)	4.8	400
M392 APDS	TiO_2/wax (flaps)	0.2	10,000[c]
M456 HEAT	none	14	250
M456 HEAT	TiO_2/wax (no flaps)	1.8	1,100

[a]Data taken from reference 4.

[b]Change in the bore diameter measured 64cm from the rear face of the tube.

[c]Extrapolated from 600 round firing series.

Table 2 Location of thermocouples in the 37 mm gun barrel

Axial Position,[a] cm	Distance From Thermocouple to Bore Surface, mm			
27.94	0.406	0.864	2.51	5.56
104.14	.483	.914	2.34	5.13
180.34	.178	.940	2.46	5.74

[a]Measured from base of cartridge case.

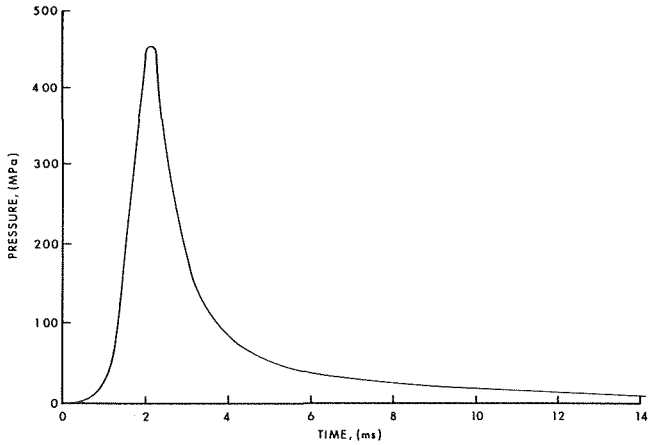

Fig. 2 Pressure versus time in 37 mm gun tube—no additive (minihat gage located 10.9 cm from base of case)

and weight of the liner in the cartridge case were the same, as opposed to the M68 tank cannon erosion tests where flaps were only used in the TiO_2/wax liner in the APDS round. The potential importance of this may be seen from the results in Table 1. Without additives the APDS round is slightly more erosive than the HEAT round; with additives the wear life of the APDS round is ten times longer than the HEAT round.

2 Experimental Procedures

The measurements, test setup, and procedures used in these experiments are the same as those used for the 37-mm gun tube firings in reference [7].

Temperature Distribution. Temperatures at four radial positions were measured at three axial locations along the length of the tube. The temperatures at each position were measured as continuous functions of time, and from these measurements temperature distributions were obtained for several time intervals. The axial locations and the distance from each thermocouple to the bore surface are given in Table 2. The thermocouples consist of single-wire constantan (0.076-mm dia) welded onto the gun steel by capacitor discharge. Care was taken to place each thermocouple above a groove. The inside diameter of the gun barrel (r_1) was 37.04 mm at each axial location; the thickness of the gun steel (r_0) decreased down the barrel with values of 28.6, 22.2, and 7.85 mm at each of the three axial distances in Table 2, respectively.

Table 3 Composition of wear-reducing additives

	Polyurethane Foam	Percent by Weight
A.	Resin Prepolymer Ingredients	
	Polyethylene glycol (200)	10.5
	Polypropylene glycol (1200)	6.5
	Castor oil	36.5
	2, 4 Toluene dissocyanate	46.5
B.	Catalyst Ingredients	
	Polypropylene glycol	10.0
	Glycerine	7.5
	Polyethylene glycol	3.75
	Tris (pentanedionato) iron (III)	0.15
	Nigrosine black	0.25
	Dibutyl tin dilaurate	0.30
	Metal Oxide Additives	
	Titanium dioxide (or talc)	46.0
	Paraffin wax	53.5
	Dacron	0.5
	Stearyl alcohol	(1.0 max)
	cloth backing: viscose rayon	

Wear-Reducing Additives. The three wear-reducing liners investigated are standard military issue. Their compositions are listed in Table 3. The polyurethane foam liner is a high-density (480 kg/m^3) semirigid plastic 3 mm thick. The metal-oxide/wax liners consist of a blend of the metal oxide and wax coated on one side of a rayon liner. The metal-oxide/wax blend is made by mixing the metal oxide with molten paraffin wax; this mixture is poured onto the rayon liner and scraped to a 1–2-mm thickness. The coated side of the liner faces the propellant grains. The liners were each cut to a length such that they weighed 0.15 kg.

Chamber Pressure and Muzzle Velocity. Pressure in the chamber was measured with a Minihat Pressure Gage. The center of the gage hole was located 10.9 cm from the base of the cartridge case. Muzzle velocity was measured by placing three Lumiline Screens downrange, 3.7 m apart. The chamber pressure and muzzle velocity were unaffected by the presence of the additives. An example of the chamber pressure versus time measured for this gun is shown in Fig. 2.

Test Setup and Procedure. The weapon was constrained in a rigid mount. It was fired manually to eliminate noise spikes produced on the temperature measurements when an electrical solenoid is used to fire the weapon. The temperatures and pressure were recorded simultaneously on a Honeywell Magnetic Tape Recording System.

Rounds fired throughout the test consisted of 0.871 kg T21 projectiles, M38B2 primers, and 0.165 kg of M2 propellant from Lot No. RAD 35683. In the firings with the additives 0.015 kg of polyurethane foam, TiO_2/wax, and talc/wax were used with and without folded flaps at the front of the additive. The polyurethane foam had to be heated slightly with a heat gun to soften it before the flaps could be formed. In the firings with the TiO_2/wax and the talc/wax, a clean out round with no additive was fired between rounds to remove the visible film along the bore left by these additives. The polyurethane foam did not leave a film.

3 Results and Discussion

Figs. 3–5 are examples of the temperature versus time profiles at four radial locations for rounds fired with no additive, with polyurethane foam without flaps, and polyurethane foam with flaps. A glance at the temperature profiles shows that the temperature in the gun barrel is reduced by the polyurethane foam, and the addi-

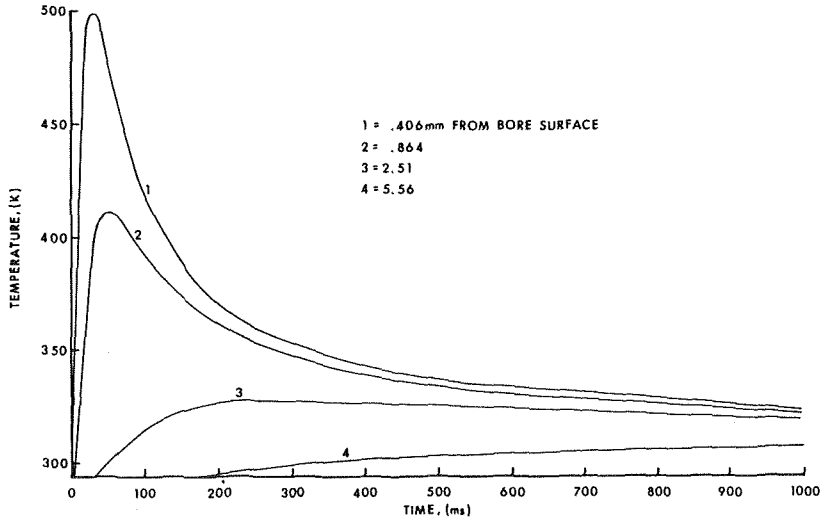

Fig. 3 Temperature versus time at 27.94 cm location—no additive

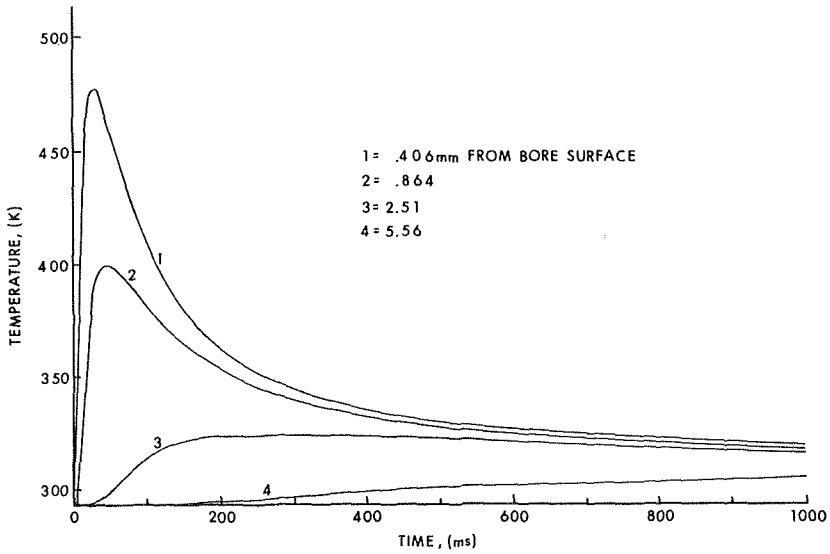

Fig. 4 Temperature versus time at 27.94 cm location—polyurethane foam, no flaps

tion of the flaps further assists in reducing the temperature.

Table 4 summarizes the mean temperatures measured at 27.9 cm from the base of the cartridge case at a depth of 0.406 mm from the bore surface for all three additives equipped with flaps. Surprisingly, the polyurethane foam was as effective as the TiO_2/wax and the talc/wax liners in reducing the barrel temperature profile suggesting that the positioning of these three additives is more critical than the chemical composition.

An attempt to estimate the total heat transferred to the gun barrel at a unit axial position was made from the temperature profiles at 100 ms. This time was chosen because the thermocouples nearest to the bore surface had reached their maximum temperature indicating that no further heat was being transferred to these sections of the gun barrel by the propellant gases. The temperature distribution in the gun steel at this time was also nearly linear which allowed an estimate of the gun barrel temperature profile to be made by extrapolation to the bore surface. Fig. 6 depicts the temperature versus distance in the gun steel for the firings with no additive present.

The estimate of the total heat input was made from these data as follows. The rate of heat input into a unit axial length is given by

$$dQ = 2\pi\rho c \Delta T r dr \tag{1}$$

where

dQ = rate of heat input into a unit length of the barrel, J/mm
ρ = density of gun steel, 7.85×10^3 kg/m^3
c = specific heat of gun steel, 419 J/kg-K
r = distance into the gun barrel, mm
ΔT = temperature rise at depth r at 100 ms

The total heat input at a given distance along the gun barrel may be determined by integrating equation (1) between r_1 and r_0 as shown in the following

$$Q = 2\pi\rho c \int_{r_1}^{r_0} r \Delta T dr \tag{2}$$

This integral was evaluated in the following manner. Values of $r\Delta T$ at various distances r were determined from plots of temperature versus distance into the steel such as Fig. 6. This results in plots of $r\Delta T$ versus r as shown in Fig. 7, for each of the three dis-

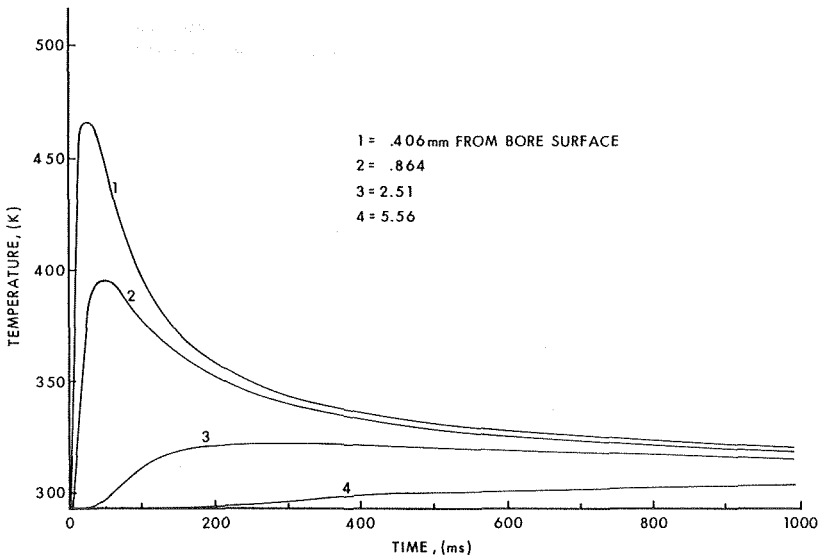

Fig. 5 Temperature versus time at 27.94 cm location—polyurethane foam with flaps

Table 4 Results of barrel temperature measurements in 37 mm gun tube with wear-reducing Additives[a,b]

Time after primer impact, ms	No Additive T,K	P[c], no flaps T,K	P, flaps T,K	TiO_2/wax, flaps T,K	Talc/Wax, T,K
25	494	475	467	471	467
50	476	456	451	449	442
100	423	406	392	394	395
250	360	353	347	351	347
500	337	333	330	332	330
1000	323	321	320	320	319

[a]Temperatures represent average values for ten rounds. Standard deviation of the mean is less than 0.6°K in every case.

[b]Temperature measured at 27.9cm from base of cartridge case at a depth of 0.406mm from bore surface.

[c]Polyurethane foam.

tances along the gun barrel at which thermocouples were placed. The integral in equation (2) was then determined at each of these axial positions from the area under the $r\Delta T$ versus r curve. This procedure was followed for firings with no additive, with polyurethane foam (with and without flaps), and with TiO_2/wax and talc/wax, each with flaps. A summary of these results is presented in Table 5. Clearly the heat input at each axial location is reduced by the wear-reducing additives, and the positioning of the additive is critical in determining the amount of heat reduction, as was suggested from the firing tests in Table 1. Since the maximum chamber pressure and muzzle velocity of the projectile are unaffected by the wear-reducing additive, it appears that the additive does not reduce the temperature of the propellant gas. It would seem that the rate of heat transferred through the propellant gas boundary layer at bore surface was reduced in some manner.

The result that the heat reduction for polyurethane foam with flaps is equivalent to the heat reduction for the TiO_2/wax and talc/wax with flaps implies that the addition of flaps or a disk to the forward end of the propelling charge will improve the wear-reducing capability of the polyurethane foam and possibly eliminate the need to use the more expensive TiO_2/wax additive. These results contradict the conclusion that the metal oxide/wax additives are superior to polyurethane foam, since this conclusion was reached from full-scale firing tests in which only the TiO_2/wax or talc/wax liners had flaps [4].

No data are shown for the TiO_2/wax or the talc/wax without flaps, since the additive liners were not totally consumed, and the resulting temperatures were the same as the temperatures recorded with no additive. Similar results were obtained inadvertently [8] when the TiO_2/wax additive was improperly placed in the rear

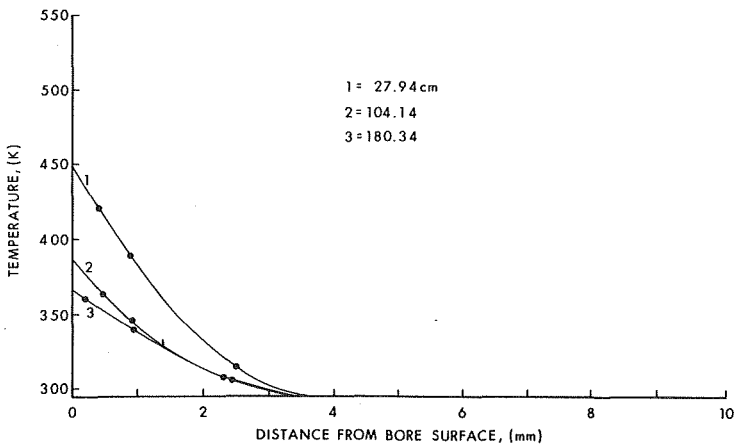

Fig. 6 Temperature distribution at 100 ms at three longitudinal locations along the barrel—no additive

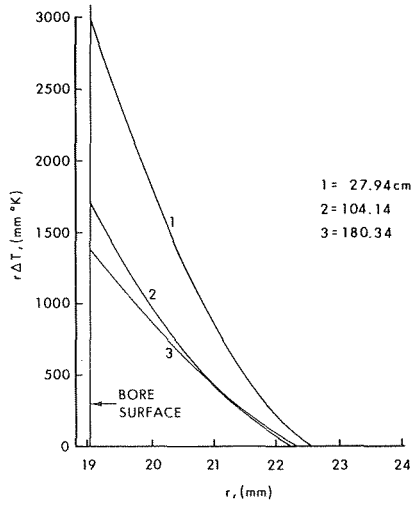

Fig. 7 Curve of $r\Delta T$ versus r for data from Fig. 6

of a 105-mm cartridge case and some unburned residue was also left after firing. It was noted that the rates of erosion were the same as the rates obtained with no additive present.

4 Conclusions

1 Heat transfer to gun barrels is reduced by wear-reducing additives.

2 The reduction in heat transfer is strongly a function of the location of the additive with respect to the propellant and the projectile. For polyurethane foam, TiO_2/wax additive, and talc/wax additive, the reduction of heat transfer to the barrel was the same when each additive was equipped with flaps.

Table 5 Estimated total heat transferred into the gun barrel at three axial locations for various additives

Additive and Configuration	Heat Transferred, J/mm, at Axial Location Indicated		
none	86[a]	48[b]	40[c]
Polyurethane (no flaps)	79	43	39
Polyurethane (flaps)	70	39	34
TiO_2/wax (flaps)	71	41	34
Talc/wax (flaps)	72	40	36

[a]Measured at 27.9cm from the base of the cartridge case.

[b]Measured at 104.1cm from the base of the cartridge case.

[c]Measured at 180.3cm from the base of the cartridge case.

References

1 Ward, J. R., "Survey of Wear-Reducing Additives," BRL Memorandum Report No. 2172, Apr. 1972.

2 Dickinson, L. A., and McLennan, D. E., "Improvement of the Firing Accuracy and Cost Effectiveness of Guns Through the Use of Urethane Foams," *J. Cellular Plastics*, 1968, pp. 184–187.

3 Ek, S. Y., and Jacobsen, D. E., "Engineering Study of Barrel Wear Reducing Additives," Wegematic Corporation Report, Part A, May 1962.

4 Wolff, R. O., "Reduction of Gun Barrel Erosion Part II. Barrel Wear Reducing Additives," Picatinny Arsenal Technical Report No. 3096, Aug. 1963.

5 Picard, J., and Trask, R. L., "A New Gun Barrel Erosion Reducer," *J. Spacecraft and Rockets*, Vol. 5, 1968, pp. 1487–1488.

6 Plett, E. G., Alkidas, A. C., Schrader, R. E., and Summerfield, M., "Erosion of Metals by High Pressure Combustion Gases: Inert and Reactive Erosion," ASME Paper No. 75-HT-M.

7 Brosseau, T., "An Experimental Method for Accurately Determining the Temperature Distribution and the Heat Transfer in Gun Barrels," BRL Report No. 1740, Sept. 1974.

8 Frankle, J. M., "Interior Ballistics of High Velocity Guns Experimental Program—Phase 1," BRL Memorandium Report No. 1879, Nov. 1967.

journal of heat transfer

technical notes

On the Interface Temperature of Two Suddenly Contacting Materials[1]

M. S. Kazimi[2] and C. A. Erdman[2]

The interface temperature of two suddenly contacting semi-infinite bodies is developed using the hyperbolic heat-conduction equation. The times for which the non-Fourier effects are important are assessed. A numerical example for a system of uranium dioxide and sodium is considered.

Nomenclature

c = specific heat
k = thermal conductivity
q = heat flux
s = the Laplace transform parameter
t = time
T = temperature
x = linear distance coordinate
α = thermal diffusivity
$\beta = \rho c \lambda$
$\gamma = \lambda^2/\alpha$
λ = speed of heat propagation
ρ = density
θ = temperature deviation from the temperature at $t = 0$

Subscripts

1 = for positions where $x > 0$
2 = for positions where $x < 0$
in = at the interface (at $x = 0$)

1 Introduction

The instantaneous interface temperature of two suddenly contacting bodies has been commonly determined from the solution of the Fourier heat equations:

$$\frac{1}{\alpha}\frac{\partial T}{\partial t} = \nabla^2 T \tag{1}$$

in the two contacting bodies. For most practical conduction problems Fourier's formulation for the heat conduction is acceptable. However, as has been discussed by several investigators, Fourier's heat conduction equation leads to erroneous results when very short times are considered. The transient behavior of two contacting materials at short times is of interest in many applications. Boley [1][3] and Brazel and Nolan [2] discussed the significance of non-Fourier effects in assessment of the thermal stresses that may be generated when the surface temperature of a structure is suddenly changed. Fauske [3] investigated the correlation between the instantaneous interface temperature of two suddenly contacting liquids and the potential for rapid development of spontaneous nucleation in the cooler liquid. It is this latter concern that motivated the current study.

The purpose of this paper is to determine the interface temperature of two suddenly contacting semi-infinite bodies using the hyperbolic heat-conduction equation. The times for which the non-Fourier effects on the interface temperature are important are also assessed.

2 The Hyperbolic Formulation

Consider a semi-infinite body of a uniform initial temperature T_1 suddenly contacting, at $x = 0$, a semi-infinite body of a uniform initial temperature T_2, where $T_1 < T_2$.

By applying the hyperbolic heat conduction equation to the cooler semi-infinite medium we obtain:

$$\frac{\partial^2\theta(x,t)}{\partial x^2} = \frac{1}{\alpha_1}\frac{\partial\theta(x,t)}{\partial t} + \frac{1}{\lambda_1^2}\frac{\partial^2\theta(x,t)}{\partial t^2};\ x > 0 \tag{2}$$

where $\theta(x, t) = T(x, t) - T_1$

Equation (2) describes the behavior of a damped temperature wave with a finite speed of propagation, λ_1. When $\lambda_1 \to \infty$, equation (2) reduces to the more familiar Fourier heat conduction equation.

The initial and boundary conditions to be applied to the wave equation are:

$$\theta(x,t) = 0 \text{ and } \frac{\partial\theta(x,t)}{\partial t} = 0 \quad \text{at } t = 0 \text{ and } x > 0 \tag{3}$$

$$\theta(x,t) = \theta_{in}(t) = T_{in}(t) - T_1 \quad \text{as } x \to 0 \tag{4}$$

[1] Work performed under the auspices of the United States Nuclear Regulatory Commission.

[2] Fast Reactor Safety Division, Department of Applied Science, Brookhaven National Laboratory, Upton, N. Y.

Contributed by the Heat Transfer Division of THE AMERICAN SOCIETY OF MECHANICAL ENGINEERS. Manuscript received by the Heat Transfer Division April 10, 1975.

[3] Numbers in brackets designate References at end of technical note.

$$\theta(x, t) = 0 \quad \text{as } x \to \infty \tag{5}$$

Physically, the conditions of equation (3) imply that it takes the temperature wave a finite amount of time to propagate into the domain where $x > 0$.

By applying the conditions of equations (3), (4), and (5), the Laplace transform of equation (1) takes the form:

$$\mathcal{L}\{\theta(x, t)\} = \hat{\theta}(x, s) = \hat{\theta}_{in}(s) \exp\{-x\sqrt{s^2/\lambda_1^2 + s/\alpha_1}\} \tag{6}$$

The heat flux equation that is consistent with the wave equation is of the form [4, 5]

$$q_1(x, t) = -k_1 \frac{\partial\theta(x, t)}{\partial x} - \frac{\alpha_1}{\lambda_1^2}\frac{\partial q_1(x, t)}{\partial t} \tag{7}$$

which reduces to the Fourier heat flux equation as $\lambda_1 \to \infty$. When equation (7) for the heat flux is substituted in the differential equation for conservation of energy in an elemental volume, the wave equation for heat conduction is produced.

Taking the Laplace transform of equation (7) and applying the condition

$$q_1(x, 0) = 0 \tag{8}$$

within the semi-finite body results in the following equation:

$$\frac{\partial\hat{\theta}(x, s)}{\partial x} = -\hat{q}_1(x, s)\left[1 + \frac{\alpha_1 s}{\lambda_1^2}\right]\frac{1}{k_1} \tag{9}$$

By differentiating equation (6), we obtain:

$$\frac{\partial\hat{\theta}(x, s)}{\partial x} = -\sqrt{s^2/\lambda_1^2 + s/\alpha_1}\,\hat{\theta}_{in}(s) \exp\{-x\sqrt{s^2/\lambda_1^2 + s/\alpha_1}\} \tag{10}$$

By equating the right-hand side of equations (9) and (10) and considering the resultant equation for $x = 0$, we get

$$\hat{\theta}_{in}(s) = \hat{T}_{in}(s) - \hat{T}_1 = \frac{\alpha_1}{k_1\lambda_1}\frac{\sqrt{s + \lambda_1^2/\alpha_1}}{\sqrt{s}}\hat{q}_1(0, s) \tag{11}$$

Similar analysis can be applied to the region $x < 0$ (i.e., the relatively hot medium) to correlate the instantaneous temperature drop at the interface (when approached from $x < 0$) to the initial interface heat flux. The result may be written in the form:

$$\hat{T}_2 - \hat{T}_{in}(s) = \frac{\alpha_2}{k_2\lambda_2}\frac{\sqrt{s + \lambda_2^2/\alpha_2}}{\sqrt{s}}\hat{q}_2(0, s) \tag{12}$$

From considerations of heat flux continuity at the interface equations (11) and (12) may be used to obtain:

$$\frac{\hat{T}_{in}(s) - \hat{T}_1}{\hat{T}_2 - \hat{T}_{in}(s)} = \frac{\rho_2 c_2 \lambda_2}{\rho_1 c_1 \lambda_1}\frac{\sqrt{s + \lambda_1^2/\alpha_1}}{\sqrt{s + \lambda_2^2/\alpha_2}} \tag{13}$$

3 The Instantaneous Interface Temperature

The instantaneous temperature at the interface can be obtained from equation (13) by applying the condition

$$\text{Lim}_{s\to\infty}\, s\mathcal{L}\{f(t)\} = \text{Lim}_{t\to 0} f(t) \tag{14}$$

to both sides of the equation. This condition yields the following relation:

$$\frac{T_{in}(0) - T_1}{T_2 - T_{in}(0)} = \frac{\rho_2 c_2 \lambda_2}{\rho_1 c_1 \lambda_1} \tag{15}$$

Physically, equation (15) implies that the interface temperature is determined by equalization of the amount of heat that can propagate within the hot medium per unit length-per-unit time if the temperature is to drop suddenly from T_2 to T_{in}, $\rho_2 c_2 \lambda_2 (T_2 - T_{in})$, to the amount of heat that can propagate into the cold medium-per-unit length per unit time inducing sudden change in temperature from T_1 to T_{in}, $\rho_1 c_1 \lambda_1 (T_{in} - T_1)$.

Equation (15) is equivalent to the more familiar expression for the instantaneous interface temperature predicted by the Fourier equations for heat transfer:

$$\frac{T_{in} - T_1}{T_2 - T_{in}} = \sqrt{\rho_2 c_2 k_2/\rho_1 c_1 k_1} \tag{16}$$

The Fourier equation expression for the interface temperature can be obtained from equation (13) by applying the condition:

$$\text{Lim}_{s\to 0}\, s\mathcal{L}\{f(t)\} = \text{Lim}_{t\to\infty}\{f(t)\} \tag{17}$$

In reality, only a very short time will elapse before the interface temperature approaches the prediction of the Fourier equations. This will be discussed in the following sections.

4 Short-Time Behavior of the Interface Temperature

The exact solution for $T_{in}(t)$ obtained from equation (13) using the convolution theorem contains complicated integrals which must be evaluated numerically. However, if one is interested in very short times after contact, equation (13) may be simplified to obtain an analytical solution. By applying the conditions

$$s \gg \lambda_1^2/\alpha_1 \quad \text{and} \quad s \gg \lambda_2^2/\alpha_2 \tag{18}$$

and

$$\hat{T}_1 = \hat{T}_1/s \quad \text{and} \quad T_2 = T_2/s \tag{19}$$

to equation (13) and rearranging the terms we obtain:

$$\hat{T}_{in}(s) = \frac{1}{s}\frac{T_1\beta_1(s + \gamma_2/2) + T_2\beta_2(s + \gamma_1/2)}{\beta_1(s + \gamma_2/2) + \beta_2(s + \gamma_1/2)} = \frac{T_1\beta_1 + T_2\beta_2}{s(\beta_1 + \beta_2) + (\beta_1\gamma_2 + \beta_2\gamma_1)/2} + \frac{(T_1\beta_1\gamma_2 + T_2\beta_2\gamma_1)/2}{s[s(\beta_1 + \beta_2) + (\beta_1\gamma_2 + \beta_2\gamma_1)/2]} \tag{20}$$

where

$$\beta_i = \rho_i c_i \lambda_i; \quad i = 1 \text{ or } 2 \tag{21}$$

and

$$\gamma_i = \lambda_i^2/\alpha_i; \quad i = 1 \text{ or } 2 \tag{22}$$

The inverse transformation of equation (20) can be readily determined to be:

$$T_{in}(t) = \frac{T_1\beta_1 + T_2\beta_2}{\beta_1 + \beta_2}\exp\left(-\frac{\beta_1\gamma_2 + \beta_2\gamma_1}{2(\beta_1 + \beta_2)}t\right) + \frac{T_1\beta_1\gamma_2 + T_2\beta_2\gamma_1}{\beta_1\gamma_2 + \beta_2\gamma_1}\left[1 - \exp\left(-\frac{\beta_1\gamma_2 + \beta_2\gamma_1}{2(\beta_1 + \beta_2)}t\right)\right] \tag{23}$$

In the limit $t \to 0$, equation (23) yields the instantaneous interface temperature as given in equation (15).

5 Long-Time Behavior of the Interface Temperature

An analytic solution can also be obtained for long-time behavior of the interface temperature if the conditions

$$s \ll \lambda_1^2/\alpha_1 \quad \text{and} \quad s \ll \lambda_2^2/\alpha_2 \tag{24}$$

were applied to equation (13). The expression for long-time behavior thus obtained is given by:

$$T_{in} = \frac{T_1\beta_1\sqrt{\gamma_1} + T_2\beta_2\sqrt{\gamma_2}}{\beta_1\sqrt{\gamma_1} + \beta_2\sqrt{\gamma_2}}\exp\left(-\frac{2(\beta_1\gamma_2\sqrt{\gamma_1} + \beta_2\gamma_1\sqrt{\gamma_2})}{\beta_1\sqrt{\gamma_1} + \beta_2\sqrt{\gamma_2}}t\right) + \frac{T_1\beta_1\sqrt{\gamma_2} + T_2\beta_2\sqrt{\gamma_1}}{\beta_1\sqrt{\gamma_2} + \beta_2\sqrt{\gamma_1}}\left[1 - \exp\left(-\frac{2(\beta_1\gamma_2\sqrt{\gamma_1} + \beta_2\gamma_1\sqrt{\gamma_2})}{\beta_1\sqrt{\gamma_1} + \beta_2\sqrt{\gamma_2}}t\right)\right] \tag{25}$$

In the limit $t \to \infty$, equation (25) yields the instantaneous interface temperature as given in equation (16).

From the conditions (24), it is clear that the interface temperature approaches the long term value if

$$t \gg \alpha_1/\lambda_1^2 \quad \text{or} \quad t \gg \alpha_2/\lambda_2^2$$

which ever is larger.

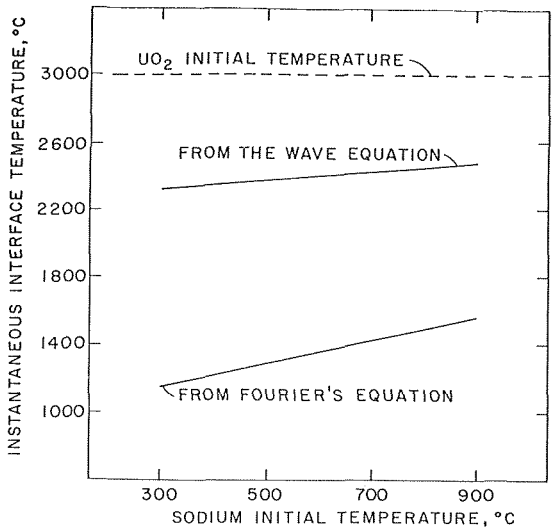

Fig. 1 Instantaneous interface temperature of UO_2, at 3000°C, and sodium

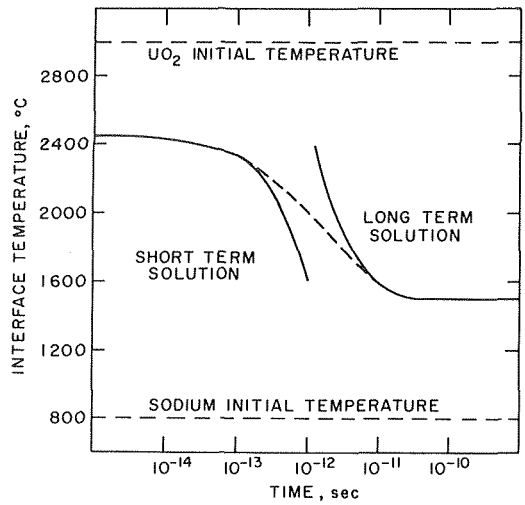

Fig. 2 Short term and long term behavior of the interface temperature

Table 1 Values of properties used in the calculations*

Property	UO_2	Na
ρ (gm/cm³)	8.52	0.83
C_p (cal/gm°C)	0.12	0.31
k (cal/cm°C sec)	0.005	0.0915
λ** (cm/sec)	1.7×10^5	2.3×10^5

* All values are based on the properties recommended by Ref. 6.
** The speed of heat propagation is assumed to equal the speed of sound propagation.

6 A Numerical Example

Consider the case of sudden contact between molten UO_2 and molten sodium, as may be hypothesized under accident conditions in a sodium-cooled nuclear reactor. The instantaneous interface temperatures that are predicted by the wave heat-conduction equation and the Fourier equation are shown in Fig. 1, for initial UO_2 temperature of 3000°C and various sodium temperatures. The values of the physical properties used in this analysis are given in Table 1. It is clear that substantial difference exists between the two predictions. The short-time and long-time solutions for the case of UO_2 at 3000°C contacting suddenly with sodium at 800°C are shown in Fig. 2. From these results, it is seen that the Fourier-predicted interface temperature is approached in approximately 5×10^{-11} seconds. For most applications involving UO_2 and sodium, therefore, the transient time in which the interface temperature of two suddenly contacting bodies deviates from the values predicted by Fourier's equations is expected to be so small as to be inconsequential.

In this numerical example, the thermal speed is assumed to equal the speed of sound. While this assumption seems to be acceptable if applied to ordinary liquids at room temperature [7], it has not been verified for either UO_2 or Na. The prediction of thermal speed continues to be a subject of interest in thermodynamics literature. Values of thermal speed that range between higher and lower than the speed of sound have been predicted for solids and liquids [5, 7, 8]. For gases, the thermal speed is predicted to be always less than the sound speed [8].

References

1 Boley, B. A., *The Analysis of Problems of Heat Conduction and Melting: High Temperature Structures and Materials* Pergamon Press, New York, 1964, pp. 260–315.

2 Brazel, J. P., and Nolan, E. J., "Non-Fourier Effects in the Transmission of Heat," Proceedings 6th Conference on Thermal Conductivity, Dayton, Ohio, 1966.

3 Fauske, H. K., "On the Mechanism of Uranium Dioxide Sodium Explosive Interactions," *Nucl. Sci. Eng.*, Vol. 51, 1973, pp. 95–101.

4 Chester, M., "Second Sounds in Solids," *the Physical Review*, Vol. 131 No. 5, Sept. 1963, pp. 2013–2015.

5 Maurer, M. J., "Relaxation Model for Heat Conduction in Metals," *Journal of Applied Physics* Vol. 40, 1969, p. 5123.

6 Chasanov, M. G., Leibowitz, L., and Gabelnick, S. D., "High Temperature Physical Properties of Fast Reactor Materials," *J. Nucl. Materials*, Vol. 49, 1973–1974, pp. 129–135.

7 Nettleton, R. E., "Relaxation Theory of Thermal Conduction in Liquids," *Phy. of Fluids*, Vol. 3, 1960, p. 216.

8 Weymann, H. D., "Finite Speed of Propagation in Heat Conduction, Diffusion and Viscous Shear Motion," *American Journal of Physics*, Vol. 35, 1967, p. 488.

Thermal Bond Conductance Between a Cylinder and a Plane Wall

F. W. Ahrens[1]

Nomenclature

$a = Y_2/2d$, dimensionless geometrical parameter
$b = \sqrt{1 + 2R/d}$, dimensionless geometrical parameter
C = constant defined following equation (1)
d = spacing between cylinder and wall (>0)
f = dimensionless heat transfer factor, equation (4)
$i = \sqrt{-1}$
k = thermal conductivity of bond material
K_c = thermal conductance of bond, per unit length
q'' = heat flux
q' = heat transfer rate per unit cylinder length
R = radius of cylinder
T = temperature

[1] Research Engineer, Whirlpool Corp., Elisha Gray II Research and Engineering Center, Benton Harbor, Mich. Mem. ASME.

Contributed by the Heat Transfer Division of THE AMERICAN SOCIETY OF MECHANICAL ENGINEERS. Manuscript received by the Heat Transfer Division February 27, 1975.

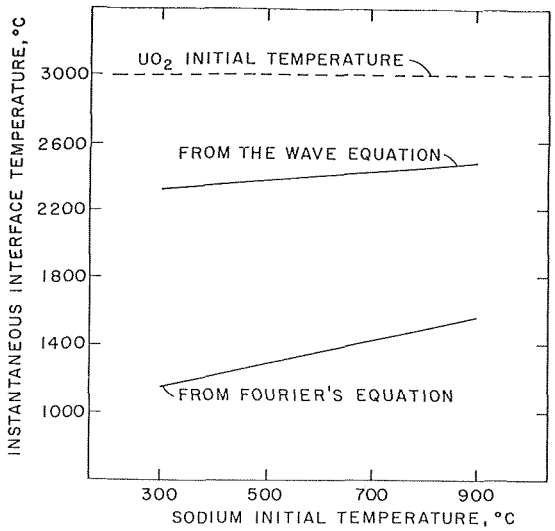

Fig. 1 Instantaneous interface temperature of UO_2, at 3000°C, and sodium

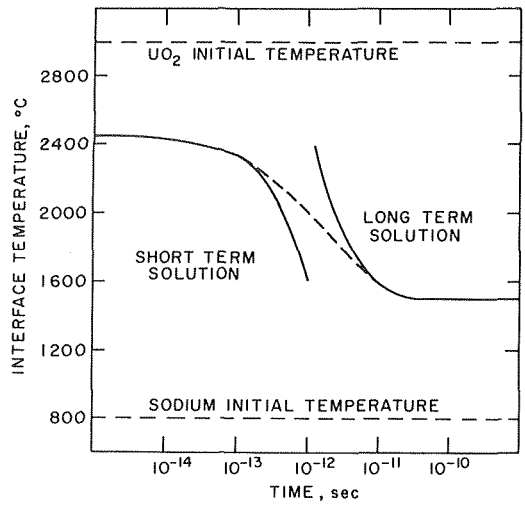

Fig. 2 Short term and long term behavior of the interface temperature

Table 1 Values of properties used in the calculations*

Property	UO_2	Na
ρ (gm/cm³)	8.52	0.83
C_p (cal/gm°C)	0.12	0.31
k (cal/cm°C sec)	0.005	0.0915
λ** (cm/sec)	1.7×10^5	2.3×10^5

* All values are based on the properties recommended by Ref. 6.
** The speed of heat propagation is assumed to equal the speed of sound propagation.

6 A Numerical Example

Consider the case of sudden contact between molten UO_2 and molten sodium, as may be hypothesized under accident conditions in a sodium-cooled nuclear reactor. The instantaneous interface temperatures that are predicted by the wave heat-conduction equation and the Fourier equation are shown in Fig. 1, for initial UO_2 temperature of 3000°C and various sodium temperatures. The values of the physical properties used in this analysis are given in Table 1. It is clear that substantial difference exists between the two predictions. The short-time and long-time solutions for the case of UO_2 at 3000°C contacting suddenly with sodium at 800°C are shown in Fig. 2. From these results, it is seen that the Fourier-predicted interface temperature is approached in approximately 5×10^{-11} seconds. For most applications involving UO_2 and sodium, therefore, the transient time in which the interface temperature of two suddenly contacting bodies deviates from the values predicted by Fourier's equations is expected to be so small as to be inconsequential.

In this numerical example, the thermal speed is assumed to equal the speed of sound. While this assumption seems to be acceptable if applied to ordinary liquids at room temperature [7], it has not been verified for either UO_2 or Na. The prediction of thermal speed continues to be a subject of interest in thermodynamics literature. Values of thermal speed that range between higher and lower than the speed of sound have been predicted for solids and liquids [5, 7, 8]. For gases, the thermal speed is predicted to be always less than the sound speed [8].

References

1 Boley, B. A., *The Analysis of Problems of Heat Conduction and Melting: High Temperature Structures and Materials* Pergamon Press, New York, 1964, pp. 260–315.

2 Brazel, J. P., and Nolan, E. J., "Non-Fourier Effects in the Transmission of Heat," Proceedings 6th Conference on Thermal Conductivity, Dayton, Ohio, 1966.

3 Fauske, H. K., "On the Mechanism of Uranium Dioxide Sodium Explosive Interactions," *Nucl. Sci. Eng.*, Vol. 51, 1973, pp. 95–101.

4 Chester, M., "Second Sounds in Solids," *the Physical Review*, Vol. 131 No. 5, Sept. 1963, pp. 2013–2015.

5 Maurer, M. J., "Relaxation Model for Heat Conduction in Metals," *Journal of Applied Physics* Vol. 40, 1969, p. 5123.

6 Chasanov, M. G., Leibowitz, L., and Gabelnick, S. D., "High Temperature Physical Properties of Fast Reactor Materials," *J. Nucl. Materials*, Vol. 49, 1973–1974, pp. 129–135.

7 Nettleton, R. E., "Relaxation Theory of Thermal Conduction in Liquids," *Phy. of Fluids*, Vol. 3, 1960, p. 216.

8 Weymann, H. D., "Finite Speed of Propagation in Heat Conduction, Diffusion and Viscous Shear Motion," *American Journal of Physics*, Vol. 35, 1967, p. 488.

Thermal Bond Conductance Between a Cylinder and a Plane Wall

F. W. Ahrens[1]

Nomenclature

$a = Y_2/2d$, dimensionless geometrical parameter
$b = \sqrt{1 + 2R/d}$, dimensionless geometrical parameter
C = constant defined following equation (1)
d = spacing between cylinder and wall (>0)
f = dimensionless heat transfer factor, equation (4)
$i = \sqrt{-1}$
k = thermal conductivity of bond material
K_c = thermal conductance of bond, per unit length
q'' = heat flux
q' = heat transfer rate per unit cylinder length
R = radius of cylinder
T = temperature

[1] Research Engineer, Whirlpool Corp., Elisha Gray II Research and Engineering Center, Benton Harbor, Mich. Mem. ASME.

Contributed by the Heat Transfer Division of THE AMERICAN SOCIETY OF MECHANICAL ENGINEERS. Manuscript received by the Heat Transfer Division February 27, 1975.

T_t = temperature of cylinder surface
T_w = temperature of plane wall surface
$u = T - T_w$
x,y = spatial coordinates; see Fig. 1
x_c = location of "source"
Y_1 = bond half-width at plane wall
$Y_2 = 2Y_1$
$z = x + iy$

Introduction

When a cylindrical tube or rod is bonded to a plane wall by a material of low thermal conductivity relative to that of the tube and wall, the thermal conductance of the bond is important in predicting the rate of heat transfer between the cylinder and wall. Such configurations are typically found in applications where low cost is paramount (e.g., solar collectors, "warm wall" condensers in small refrigeration devices, etc.). In this technical brief, an expression for the thermal conductance of such a bond is developed, based on an idealized model.

For the purpose of achieving a simple analytical expression for the bond conductance, the following idealizations are made:

1 Heat flow is two-dimensional in a plane perpendicular to the cylinder axis.

2 Heat losses from the exposed bond surfaces are negligible.

3 The portions of the plane wall and cylinder in contact with the bond material have uniform, but different, temperatures.

4 The exposed surfaces of the bond have shapes defined by heat flow lines of the "buried cable" [1, 2][2] or symmetrical source-sink problem [3, 4]. A typical bond geometry resulting from this idealization is shown in Fig. 1.

Using these conditions, it is clear that the temperature distribution in the bond will be the same as that in the corresponding spatial subdomain of the symmetrical source-sink problem.

Analysis[3]

Consider the cylinder and wall to be located in an x-y coordinate system as shown in Fig. 1. The temperature distribution is [4]:

$$u = C \ln \left| \frac{z + x_c}{z - x_c} \right| \tag{1}$$

where:
$u = T(x, y) - T_w$, for the present application
$z = x + iy$
C = proportionality constant
x_c = source location

The relation between the source location and more pertinent parameters of the problem—the minimum distance between wall and cylinder, d, and the cylinder radius, R—may be shown to be: $x_c = \sqrt{d(d + 2R)}$. The constant C in equation (1) may be determined from the fact that $u = T_t - T_w$ at $z = d$, giving:

$$C = \frac{T_t - T_w}{\ln\left(\frac{x_c + d}{x_c - d}\right)}$$

The heat transfer rate per unit cylinder length is determined by integration of the local heat flux at the plane wall over the contact width, $2Y_1$:

$$q' = 2 \int_0^{Y_1} q''(y)dy \tag{2}$$

where:

$$q''(y) = -k \left(\frac{\partial u}{\partial x}\right)_{x=0}$$

The expression for the local value of $(\partial u/\partial x)_{x=0}$ is determined from complex variable theory to be:

$$\left(\frac{\partial u}{\partial x}\right)_{x=0} = \frac{2Cx_c}{x_c^2 + y^2}$$

Use of this result in equation (2) gives:

$$q' = fkY_2(T_t - T_w)/d \tag{3}$$

where:

$$Y_2 = 2Y_1$$

$$f = \frac{2 \tan^{-1}\left(\frac{a}{b}\right)}{a \ln\left(\frac{b + 1}{b - 1}\right)} \tag{4}$$

$$a = Y_2/2d = Y_1/d$$

and

$$b = \sqrt{1 + 2R/d}$$

Thus, the thermal conductance per unit cylinder length, defined by $q' = K_c(T_t - T_w)$, is:

$$K_c = kfY_2/d \tag{5}$$

It can be shown that for $R \gg d$ and $Y_1 \ll R$ the above result reduces to that for heat conduction between two infinite parallel planes (i.e., $f \to 1$). Also, for the case $Y_1 \to \infty$, the result becomes equivalent to that for the buried cable problem [2]. In all cases, $f < 1$.

Finally, to more explicitly define the bond geometry for which equation (5) rigorously applies, the following information about the exposed bond surface has been derived. Considering the portion lying in the first quadrant (see Fig. 1), the shape is a circle whose center is at $(0, (Y_1^2 - x_c^2)/2Y_1)$ and whose radius is $(Y_1^2 + x_c^2)/2Y_1$. This bond surface intersects the cylinder at the point $(\bar{x}, \bar{y})$ defined by:

$$\bar{x} = (2R + d)[d(2R + d) + Y_1^2]/[(2R + d)^2 + Y_1^2]$$
$$\bar{y} = 2RY_1(2R + d)/[(2R + d)^2 + Y_1^2] \tag{6}$$

Discussion

The bond conductance derived here is exact for the bond geometry assumed. The only geometrical parameters on which it depends are Y_1/d and R/d. The primary usefulness of the results, however, may be for approximating the conductance of bonds having a resemblance, but not exact similarity, to the idealized geometry. In this regard, it should be noted that more general bond geometries cause the point of contact between bond surface and cylinder and the shape function of the exposed surface to become additional independent parameters. The following procedure should bracket

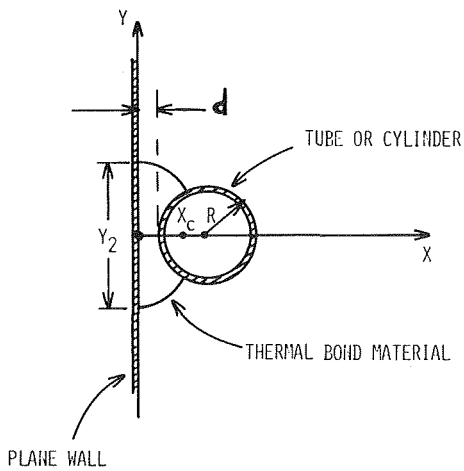

Fig. 1 Thermal bond configuration

[2] Numbers in brackets designate References at end of technical note.

[3] A reviewer has noted that this problem could have been analyzed by a direct application of a generalized theory of conduction shape factors [5]. With that method, a more natural (bicylindrical) coordinate system representation may be employed to achieve a final expression equivalent to equation (4).

the conductance of such bonds. For the actual dimensions Y_1, R, and d, calculate the point of intersection of the idealized bond with the cylinder, using equation (6). Then find, by trial and error, a second value of Y_1 which causes the ideal intersection point to coincide with that of the actual bond. Finally, calculate the ideal conductances corresponding to the two values of Y_1. One would expect the actual conductance to fall in between these values.

References

1 Carslaw, H. S., and Jaeger, J. C., *Conduction of Heat in Solids*, Second ed., Oxford University Press, London, 1959, pp. 449–451.

2 Eckert, E. R. G., and Drake, R. M., Jr., *Heat and Mass Transfer*, McGraw-Hill, New York, 1959, pp. 60–64.

3 Lamb, Sir Horace, *Hydrodynamics*, Sixth ed., Dover Publications, First American Edition, New York, 1945, p. 70.

4 Kreyszig, Erwin, *Advanced Engineering Mathematics*, Wiley, New York, 1962, pp. 745–746.

5 Yovanovich, M. Michael, "A General Expression for Predicting Conduction Shape Factors," *Progress in Astronautics* and Aeronautics, Thermophysics and Spacecraft Thermal Control, Vol. 35, MIT Press, 1973, pp. 265–291.

The Effect of Thermal Constriction Resistance in the Design of Channel-Plate Heat Exchangers: Cylindrical Geometry

R. P. Forslund[1] and H. Q. Oliveira[2]

Nomenclature

a = half channel width
b = half distance between tubes
C = constriction coefficient
C_C = correction factor for the convective heat flux case
h = heat transfer coefficient
I_0, I_1, K_0, K_1 = Bessel functions
k = thermal conductivity
R_C = thermal constriction resistance of the plate
r = radius
t = plate thickness
z = coordinate parallel to plate and normal to channel
φ = coordinate parallel to plate and normal to channel
$\phi_0 = h_0 t/k$
ξ_0, ξ_1, ξ_2, = defined by equations (5), (6), and (7)
ψ_0, ψ_1, ψ_2, = defined by equations (5), (6), and (7)
$\psi_0', \psi_1', \psi_2'$ = defined by equations (5), (6), and (7)
λ = eigen values
γ = eigen values

Subscripts

a = plate surface in contact with channel fluid
b = plate surface in contact with external fluid
0 = external or flat plate
1 = cylindrical, axial channels
2 = cylindrical, circumferential channels
CHF = convective heat flux
UHF = uniform heat flux

[1] Assoc. Professor, Instituto Militar de Engenharia, Rio de Janeiro, Brazil. Assoc. Mem. ASME.

[2] Asst. Professor, Escola de Engenharia, Universidade Federal do Espirito Santo, Vitoria, Brazil.

Contributed by the Heat Transfer Division of THE AMERICAN SOCIETY OF MECHANICAL ENGINEERS. Manuscript received by the Heat Transfer Division May 12, 1975.

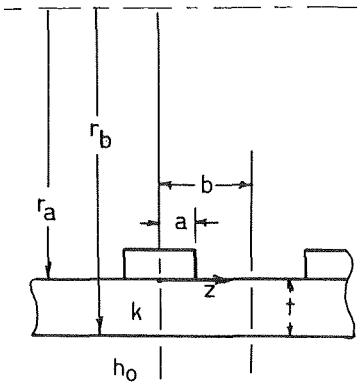

Fig. 1 Cylindrical geometry with circumferential channels (configuration for R_{C2})

Introduction

The work in reference [1][3] treats the problem of flat plate-channel heat exchangers (for deep ocean applications) whose external surface was cooled by convection, while the internal surface under the channels was heated by the channel fluid. That flat plate configuration is similar to the one shown in Fig. 1, except that the radii, r_a and r_b, are infinite. In reference [1] a correction factor C_{UHF} was determined, which could be applied to the uniform resistance of the flat plate (t/bk) in order to determine the actual resistance in the plate caused by the constriction of the flux lines due to the smaller channel width,

$$R_C(\mathrm{UHF}) = (t/bk)C_{\mathrm{UHF}} \tag{1}$$

The correction factor C_{UHF} was based on a uniform heat flux (UHF) boundary condition under the channel. The study [1] also considers the effect of a convective heat flux (CHF) boundary condition at the channel surface, and a second correction factor, C_C, for it was determined:

$$R_C(\mathrm{CHF}) = (t/bk)C_{\mathrm{UHF}}C_C \tag{2}$$

The intention of the work in reference [2] (the first part of which is reported in [1]), was to determine correction factors that could be applied to the uniform flat plate resistance (t/bk) in order to analyze either cylindrical or spherical configurations. For example, the constriction resistance for the two cylindrical configurations, shown in Figs. 1 and 2 would be given by

$$R_{C1}(\mathrm{UHF}) = (t/bk)C_{\mathrm{UHF}}G_1 \tag{3}$$

$$R_{C2}(\mathrm{UHF}) = (t/bk)C_{\mathrm{UHF}}G_2 \tag{4}$$

[3] Numbers in brackets designate References at end of technical note.

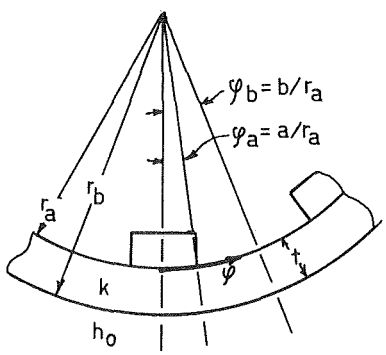

Fig. 2 Cylindrical geometry with axial channels (configuration for R_{C1})

the conductance of such bonds. For the actual dimensions Y_1, R, and d, calculate the point of intersection of the idealized bond with the cylinder, using equation (6). Then find, by trial and error, a second value of Y_1 which causes the ideal intersection point to coincide with that of the actual bond. Finally, calculate the ideal conductances corresponding to the two values of Y_1. One would expect the actual conductance to fall in between these values.

References

1 Carslaw, H. S., and Jaeger, J. C., *Conduction of Heat in Solids*, Second ed., Oxford University Press, London, 1959, pp. 449–451.

2 Eckert, E. R. G., and Drake, R. M., Jr., *Heat and Mass Transfer*, McGraw-Hill, New York, 1959, pp. 60–64.

3 Lamb, Sir Horace, *Hydrodynamics*, Sixth ed., Dover Publications, First American Edition, New York, 1945, p. 70.

4 Kreyszig, Erwin, *Advanced Engineering Mathematics*, Wiley, New York, 1962, pp. 745–746.

5 Yovanovich, M. Michael, "A General Expression for Predicting Conduction Shape Factors," *Progress in Astronautics* and Aeronautics, Thermophysics and Spacecraft Thermal Control, Vol. 35, MIT Press, 1973, pp. 265–291.

The Effect of Thermal Constriction Resistance in the Design of Channel-Plate Heat Exchangers: Cylindrical Geometry

R. P. Forslund[1] and H. Q. Oliveira[2]

Nomenclature

a = half channel width
b = half distance between tubes
C = constriction coefficient
C_C = correction factor for the convective heat flux case
h = heat transfer coefficient
I_0, I_1, K_0, K_1 = Bessel functions
k = thermal conductivity
R_C = thermal constriction resistance of the plate
r = radius
t = plate thickness
z = coordinate parallel to plate and normal to channel
φ = coordinate parallel to plate and normal to channel
$\phi_0 = h_0 t/k$
ξ_0, ξ_1, ξ_2, = defined by equations (5), (6), and (7)
ψ_0, ψ_1, ψ_2, = defined by equations (5), (6), and (7)
$\psi_0', \psi_1', \psi_2'$ = defined by equations (5), (6), and (7)
λ = eigen values
γ = eigen values

Subscripts

a = plate surface in contact with channel fluid
b = plate surface in contact with external fluid
0 = external or flat plate
1 = cylindrical, axial channels
2 = cylindrical, circumferential channels
CHF = convective heat flux
UHF = uniform heat flux

[1] Assoc. Professor, Instituto Militar de Engenharia, Rio de Janeiro, Brazil. Assoc. Mem. ASME.

[2] Asst. Professor, Escola de Engenharia, Universidade Federal do Espirito Santo, Vitoria, Brazil.

Contributed by the Heat Transfer Division of THE AMERICAN SOCIETY OF MECHANICAL ENGINEERS. Manuscript received by the Heat Transfer Division May 12, 1975.

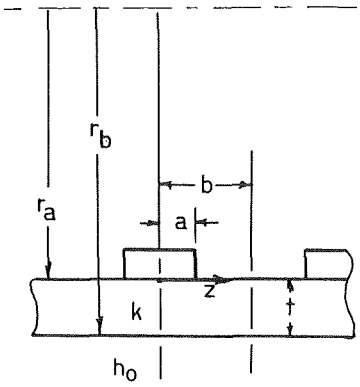

Fig. 1 Cylindrical geometry with circumferential channels (configuration for R_{C2})

Introduction

The work in reference [1][3] treats the problem of flat plate-channel heat exchangers (for deep ocean applications) whose external surface was cooled by convection, while the internal surface under the channels was heated by the channel fluid. That flat plate configuration is similar to the one shown in Fig. 1, except that the radii, r_a and r_b, are infinite. In reference [1] a correction factor C_{UHF} was determined, which could be applied to the uniform resistance of the flat plate (t/bk) in order to determine the actual resistance in the plate caused by the constriction of the flux lines due to the smaller channel width,

$$R_C(\mathrm{UHF}) = (t/bk)C_{\mathrm{UHF}} \tag{1}$$

The correction factor C_{UHF} was based on a uniform heat flux (UHF) boundary condition under the channel. The study [1] also considers the effect of a convective heat flux (CHF) boundary condition at the channel surface, and a second correction factor, C_C, for it was determined:

$$R_C(\mathrm{CHF}) = (t/bk)C_{\mathrm{UHF}}C_C \tag{2}$$

The intention of the work in reference [2] (the first part of which is reported in [1]), was to determine correction factors that could be applied to the uniform flat plate resistance (t/bk) in order to analyze either cylindrical or spherical configurations. For example, the constriction resistance for the two cylindrical configurations, shown in Figs. 1 and 2 would be given by

$$R_{C1}(\mathrm{UHF}) = (t/bk)C_{\mathrm{UHF}}G_1 \tag{3}$$

$$R_{C2}(\mathrm{UHF}) = (t/bk)C_{\mathrm{UHF}}G_2 \tag{4}$$

[3] Numbers in brackets designate References at end of technical note.

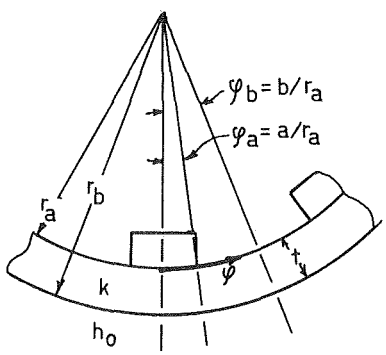

Fig. 2 Cylindrical geometry with axial channels (configuration for R_{C1})

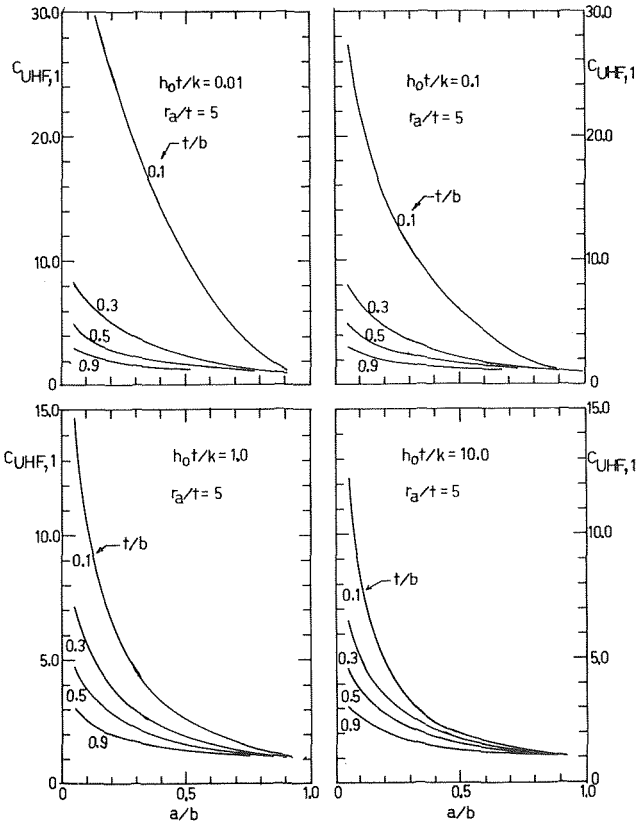

Fig. 3 Constriction coefficient for axial channels, $C_{UHF,1}$

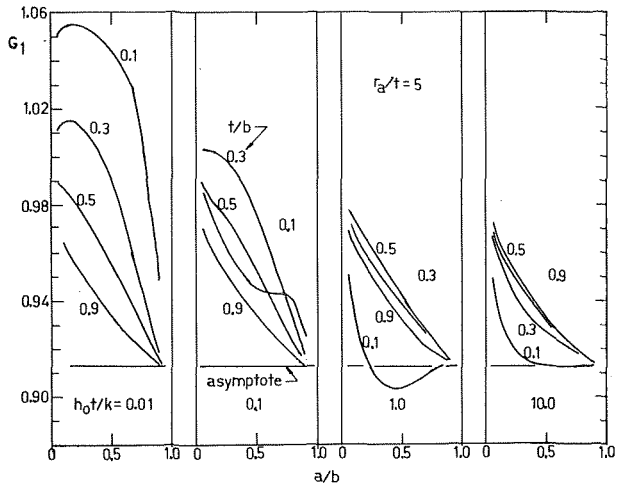

Fig. 4 Geometry factor for axial channels for $r_b/r_a = 1.2$

for the UHF boundary condition. Here G_1 and G_2 are the geometrical correction factors for the axial and circumferential channel arrangements, respectively, as shown in Figs. 1 and 2. The spherical configuration is not mentioned in this article. Nor is the effect of the CHF boundary condition on the constriction resistance of the cylindrical geometry treated here.

Analysis

The development of R_{C1}(UHF) and R_{C2}(UHF) for the cylindrical configurations follows in much the same manner as that of R_C(UHF) for the flat plate geometry given in [1]. Therefore, only the resulting equations are presented here.

Flat Plate.

$$R_C = (t/bk)\left[1 - \sum_{j=1}^{\infty} (2\psi_0/\psi_0' t)((\sin \lambda_j a)/\lambda_j a)^2\right] \quad (5)$$

where

$$\psi_0 = \xi_0 + 1$$

$$\psi_0' = \lambda_j(\xi_0 - 1)$$

$$\xi_0 = [(\lambda_j t - \phi_0 t)/(\lambda_j t + \phi_0 t)] \exp(-2\lambda_j t)$$

and

$$\lambda_j = j\pi/b, j = 1, 2, 3, \ldots.$$

Cylinder—Axial Channels.

$$R_{C1} = [r_a \ln(r_b/r_a)/bk]\left\{1 - [1/\ln(r_b/r_a)] \cdot \sum_{j=1}^{\infty} (2\psi_1/\psi_1' r_a)[(\sin \lambda_j a)/\lambda_j a]^2\right\} \quad (6)$$

where

$$\psi_1 = \xi_1 r_a^{\gamma_j} + r_a^{-\gamma_j}$$

$$\psi_1' = \gamma_j[\xi_1 r_a^{\gamma_j - 1} - r_a^{-\gamma_j - 1}]$$

$$\xi_1 = (\gamma_j - \phi_0 r_b) r_b^{-2\gamma_j}/(\gamma_j + \phi_0 r_b)$$

$$\gamma_j = j\pi r_a/b, j = 1, 2, 3, \ldots$$

and

$$\lambda_j = j\pi/b, j = 1, 2, 3, \ldots$$

Cylinder—Circumferential Channels.

$$R_{C2} = [r_a \ln(r_b/r_a)/bk]\left\{1 - [1/\ln(r_b/r_a)] \cdot \sum_{j=1}^{\infty} (2\psi_2/\psi_2' r_a)((\sin \lambda_j a)/\lambda_j a)^2\right\} \quad (7)$$

where

$$\psi_2 = \xi_2 I_0(\lambda_j r_a) + K_0(\lambda_j r_a)$$

$$\psi_2' = \lambda_j[\xi_2 I_1(\lambda_j r_a) - K_1(\lambda_j r_a)]$$

$$\xi_2 = [\lambda_j t\, K_1(\lambda_j r_b) - \phi_0 t\, K_0(\lambda_j r_b)]/[\lambda_j t\, I_1(\lambda_j r_b) + \phi_0 t\, I_0(\lambda_j r_b)]$$

and

$$\lambda_j = j\pi/b, j = 1, 2, 3, \ldots$$

Equations (6) and (7) can be divided by the uniform cylindrical

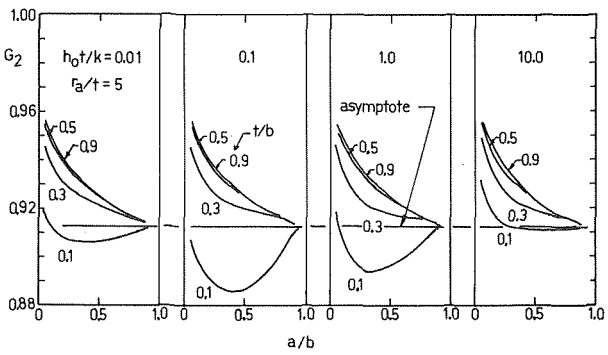

Fig. 5 Geometry factor for circumferential channels for $r_b/r_a = 1.2$

plate resistance (r_a $\ln(r_b/r_a)/bk$) to obtain correction factors $C_{UHF,1}$ and $C_{UHF,2}$ which are similar to C_{UHF} for the flat plate given in [1]. As an example, $C_{UHF,1}$ for the axial channel arrangement, is shown in Fig. 3. However, less importance is given to $C_{UHF,1}$ and $C_{UHF,2}$ in this article, since it is the behavior of G_1 and G_2 of equations (3) and (4) that are of interest. The geometry factors G_1 and G_2 are obtained by dividing equations (6) and (7) by equation (5).

Results

Typical results for G_1 and G_2 are shown in Figs. 4 and 5 for the case of $r_b/r_a = 1.2$ (or $r_a/t = 5.0$). This case was chosen as being a reasonable upper limit for r_b/r_a for deep ocean applications, that is, the submarine hull thickness is 20 percent of the inside radius. The other paraments used in the study fall within the range of values for deep ocean design.

In the case of both axial and circumferential channels, the values of G_1 and G_2 approach the asymptote (0.913 in the case for $r_b/r_a = 1.2$) as a/b goes to unity. The asymptote is simply the ratio of the uniform cylindrical resistance to that of the flat plate of equal thickness, and is less than unity since the surface area for heat flux increases with radius for the cylindrical configuration.

As a/b goes to zero, G_1 and G_2 approach unity, since the constriction resistance due to a point heat source becomes independent of the geometry. The values for G_2 in Fig. 5 are always less than unity since, although the length for the heat flux lines are the same as those for the flat plate, the area for heat flux increases with radius for the cylindrical geometry, hence lower resistance. In the case of axial channels, a trade-off exists between the increase in the length for the flux lines which contribute to larger resistances, and the increase in flux area with radius which diminishes the resistance. At low values of h_0t/k, the flux lines are spread out more evenly along the curved plate, and in turn suffer a greater length of resistance. Therefore, values of G_1 can be greater than unity, however over most of the range of parameters, G_1 is less than unity.

Conclusion

In both cases, G_1 and G_2 vary by less than approximately ±10 percent about unity for $1.0 \leq r_b/r_a \leq 1.2$; therefore, the designer of deep ocean cylindrical channel-plate heat exchangers could initially base his design on a flat plate model.

For other applications of heat exchanger design for r_b/r_a greater than 1.2, equations (6) and (7) can be employed.

Should the designer care to estimate the effect of the CHF boundary condition on the constriction resistance, Figs. 4, 5, and 6 for C_C of reference [1] could be applied, so that

$$R_{C1}(\text{CHF}) \cong (t/bk)C_{UHF}G_1C_C$$

$$R_{C2}(\text{CHF}) \cong (t/bk)C_{UHF}G_2C_C$$

Acknowledgments

The numerical results presented in this article were obtained using the IBM 1130 at the Instituto Militar de Engenharia.

References

1 Oliveira, H. Q., and R. P. Forslund, JOURNAL OF HEAT TRANSFER, TRANS. ASME, Series C, Vol. 96, 1974, p. 292.

2 Oliveira, H. Q., "Resistência Térmica em Trocadores do Tipo Tubo-Placa com Estrangulamento do Fluxo de Calor," MS thesis, Pontificia Universidade Católica, Rio de Janeiro, 1973.

Turbulent Heat Transfer by Natural Convection Along an Isothermal Vertical Flat Surface

K. Noto[1] and R. Matsumoto[1]

Nomenclature

C_1, C_2, C_3 = function of Prandtl number
f = dimensionless stream function
g = acceleration of gravity
Gr = Grashof number ($x^3g\beta\Delta T/\nu^2$)
Nu = Nusselt number ($\alpha x/\lambda$)
Pr = Prandtl number
Pr_t = turbulent Prandtl number (ϵ_M/ϵ_H)
q = heat flux
Ra = Raleigh number
T = temperature
$\Delta T = T_w - T_\infty$
u = velocity component in x-direction
u_n = representative velocity of natural convection
v = velocity component in y-direction
x = coordinate along wall from leading edge
y = coordinate perpendicular to wall
$y^+ = y\sqrt{\tau_{wx}/\rho}/\nu$
y^+_{lam} = dimensionless thickness of viscous sublayer
α = heat transfer coefficient
β = coefficient of cubical expansion
δ_{lam} = thickness of viscous sublayer
ϵ_H = eddy diffusivity of heat
ϵ_M = eddy diffusivity of momentum
η = dimensionless coordinate
θ = dimensionless temperature
μ = coefficient of viscosity
ν = kinematic viscosity
ρ = density
τ = viscous stress
ψ = stream function

Subscript

x = at x
m = average from $x = 0$ to $x = x$
w = at wall
∞ = at infinity

Introduction

Hitherto theoretical investigations in turbulent natural convection heat transfer along an isothermal vertical surface have been carried out by means of the integral method of boundary layer, the method of exchange law between τ and q, the successive integral method toward x-direction, the method which considers the transport equation of Reynolds stress, and so on. Several experimental data have been obtained. But only one paper has reported about velocity profiles.

In this paper, the local similarity concept, which has not been applied up to now, is adopted to turbulent heat transfer by natural convection along an isothermal vertical flat surface.

Problem Formulation and Method of Solution

The basic equations used in the field of natural convection are as follows:

[1] Kobe University, Rokko, Nada, Kobe, Japan.

Contributed by the Heat Transfer Division of THE AMERICAN SOCIETY OF MECHANICAL ENGINEERS. Manuscript received by the Heat Transfer Division, May 19, 1975.

plate resistance ($r_a \ln(r_b/r_a)/bk$) to obtain correction factors $C_{UHF,1}$ and $C_{UHF,2}$ which are similar to C_{UHF} for the flat plate given in [1]. As an example, $C_{UHF,1}$ for the axial channel arrangement, is shown in Fig. 3. However, less importance is given to $C_{UHF,1}$ and $C_{UHF,2}$ in this article, since it is the behavior of G_1 and G_2 of equations (3) and (4) that are of interest. The geometry factors G_1 and G_2 are obtained by dividing equations (6) and (7) by equation (5).

Results

Typical results for G_1 and G_2 are shown in Figs. 4 and 5 for the case of $r_b/r_a = 1.2$ (or $r_a/t = 5.0$). This case was chosen as being a reasonable upper limit for r_b/r_a for deep ocean applications, that is, the submarine hull thickness is 20 percent of the inside radius. The other paraments used in the study fall within the range of values for deep ocean design.

In the case of both axial and circumferential channels, the values of G_1 and G_2 approach the asymptote (0.913 in the case for $r_b/r_a = 1.2$) as a/b goes to unity. The asymptote is simply the ratio of the uniform cylindrical resistance to that of the flat plate of equal thickness, and is less than unity since the surface area for heat flux increases with radius for the cylindrical configuration.

As a/b goes to zero, G_1 and G_2 approach unity, since the constriction resistance due to a point heat source becomes independent of the geometry. The values for G_2 in Fig. 5 are always less than unity since, although the length for the heat flux lines are the same as those for the flat plate, the area for heat flux increases with radius for the cylindrical geometry, hence lower resistance. In the case of axial channels, a trade-off exists between the increase in the length for the flux lines which contribute to larger resistances, and the increase in flux area with radius which diminishes the resistance. At low values of h_0t/k, the flux lines are spread out more evenly along the curved plate, and in turn suffer a greater length of resistance. Therefore, values of G_1 can be greater than unity, however over most of the range of parameters, G_1 is less than unity.

Conclusion

In both cases, G_1 and G_2 vary by less than approximately ±10 percent about unity for $1.0 \leq r_b/r_a \leq 1.2$; therefore, the designer of deep ocean cylindrical channel-plate heat exchangers could initially base his design on a flat plate model.

For other applications of heat exchanger design for r_b/r_a greater than 1.2, equations (6) and (7) can be employed.

Should the designer care to estimate the effect of the CHF boundary condition on the constriction resistance, Figs. 4, 5, and 6 for C_C of reference [1] could be applied, so that

$$R_{C1}(\text{CHF}) \cong (t/bk)C_{UHF}G_1C_C$$

$$R_{C2}(\text{CHF}) \cong (t/bk)C_{UHF}G_2C_C$$

Acknowledgments

The numerical results presented in this article were obtained using the IBM 1130 at the Instituto Militar de Engenharia.

References

1 Oliveira, H. Q., and R. P. Forslund, JOURNAL OF HEAT TRANSFER, TRANS. ASME, Series C, Vol. 96, 1974, p. 292.

2 Oliveira, H. Q., "Resistência Térmica em Trocadores do Tipo Tubo-Placa com Estrangulamento do Fluxo de Calor," MS thesis, Pontificia Universidade Católica, Rio de Janeiro, 1973.

Turbulent Heat Transfer by Natural Convection Along an Isothermal Vertical Flat Surface

K. Noto[1] and R. Matsumoto[1]

Nomenclature

C_1, C_2, C_3 = function of Prandtl number
f = dimensionless stream function
g = acceleration of gravity
Gr = Grashof number ($x^3g\beta\Delta T/\nu^2$)
Nu = Nusselt number ($\alpha x/\lambda$)
Pr = Prandtl number
Pr_t = turbulent Prandtl number (ϵ_M/ϵ_H)
q = heat flux
Ra = Raleigh number
T = temperature
$\Delta T = T_w - T_\infty$
u = velocity component in x-direction
u_n = representative velocity of natural convection
v = velocity component in y-direction
x = coordinate along wall from leading edge
y = coordinate perpendicular to wall
$y^+ = y\sqrt{\tau_{wx}/\rho}/\nu$
y^+_{lam} = dimensionless thickness of viscous sublayer
α = heat transfer coefficient
β = coefficient of cubical expansion
δ_{lam} = thickness of viscous sublayer
ϵ_H = eddy diffusivity of heat
ϵ_M = eddy diffusivity of momentum
η = dimensionless coordinate
θ = dimensionless temperature
μ = coefficient of viscosity
ν = kinematic viscosity
ρ = density
τ = viscous stress
ψ = stream function

Subscript

x = at x
m = average from $x = 0$ to $x = x$
w = at wall
∞ = at infinity

Introduction

Hitherto theoretical investigations in turbulent natural convection heat transfer along an isothermal vertical surface have been carried out by means of the integral method of boundary layer, the method of exchange law between τ and q, the successive integral method toward x-direction, the method which considers the transport equation of Reynolds stress, and so on. Several experimental data have been obtained. But only one paper has reported about velocity profiles.

In this paper, the local similarity concept, which has not been applied up to now, is adopted to turbulent heat transfer by natural convection along an isothermal vertical flat surface.

Problem Formulation and Method of Solution

The basic equations used in the field of natural convection are as follows:

[1] Kobe University, Rokko, Nada, Kobe, Japan.

Contributed by the Heat Transfer Division of THE AMERICAN SOCIETY OF MECHANICAL ENGINEERS. Manuscript received by the Heat Transfer Division, May 19, 1975.

$$\frac{\partial u}{\partial x} + \frac{\partial v}{\partial y} = 0 \tag{1}$$

$$u\frac{\partial u}{\partial x} + v\frac{\partial u}{\partial y} = \frac{\partial}{\partial y}\left\{(\nu + \epsilon_M)\frac{\partial u}{\partial y}\right\} + g\beta(T - T_\infty) \tag{2}$$

$$u\frac{\partial T}{\partial x} + v\frac{\partial T}{\partial y} = \frac{\partial}{\partial y}\left\{\left(\frac{\nu}{\mathrm{Pr}} + \frac{\epsilon_M}{\mathrm{Pr}_t}\right)\frac{\partial T}{\partial y}\right\} \tag{3}$$

Introducing the following stream function

$$u = \frac{\partial \psi}{\partial y}, \quad v = -\frac{\partial \psi}{\partial x} \tag{4}$$

the representative velocity of natural convection

$$u_n = (xg\beta\Delta T)^{1/2} \tag{5}$$

and dimensionless variables

$$\left.\begin{aligned} \eta &= \frac{y}{x}\sqrt{\frac{u_n x}{\nu}} \\ f(x,\eta) &= \frac{\psi}{\sqrt{u_n x \nu}} \\ \theta(x,\eta) &= \frac{T - T_\infty}{T_w - T_\infty} \end{aligned}\right\} \tag{6}$$

equations (2) and (3) can be transformed as follows:

$$\left(1 + \frac{\epsilon_M}{\nu}\right)\frac{\partial^3 f}{\partial \eta^3} + \left\{\frac{3}{4}f + \frac{\partial}{\partial \eta}\left(\frac{\epsilon_M}{\nu}\right)\right\}\frac{\partial^2 f}{\partial \eta^2} - \frac{1}{2}\left(\frac{\partial f}{\partial \eta}\right)^2 + \theta = x\frac{\partial(\partial f/\partial \eta, f)}{\partial(x,\eta)} \tag{7}$$

$$\left\{\frac{1}{\mathrm{Pr}} + \frac{1}{\mathrm{Pr}_t}\frac{\epsilon_M}{\nu}\right\}\frac{\partial^2 \theta}{\partial \eta^2} + \left\{\frac{3}{4}f + \frac{1}{\mathrm{Pr}_t}\frac{\partial}{\partial \eta}\left(\frac{\epsilon_M}{\nu}\right)\right\}\frac{\partial \theta}{\partial \eta} = x\frac{\partial(\theta, f)}{\partial(x,\eta)} \tag{8}$$

The local similarity concept, viz.

$$\frac{\partial f}{\partial x} = \frac{\partial \theta}{\partial x} = 0 \tag{9}$$

can be applied as the variations of f and θ in x-direction are very small when compared with those in η-direction and this can be neglected. Hence equations (7) and (8) can be transformed as follows:

$$\left(1 + \frac{\epsilon_M}{\nu}\right)\frac{\partial^3 f}{\partial \eta^3} + \left\{\frac{3}{4}f + \frac{\partial}{\partial \eta}\left(\frac{\epsilon_M}{\nu}\right)\right\}\frac{\partial^2 f}{\partial \eta^2} - \frac{1}{2}\left(\frac{\partial f}{\partial \eta}\right)^2 + \theta = 0 \tag{10}$$

$$\left\{\frac{1}{\mathrm{Pr}} + \frac{1}{\mathrm{Pr}_t}\frac{\epsilon_M}{\nu}\right\}\frac{\partial^2 \theta}{\partial \eta^2} + \left\{\frac{3}{4}f + \frac{1}{\mathrm{Pr}_t}\frac{\partial}{\partial \eta}\left(\frac{\epsilon_M}{\nu}\right)\right\}\frac{\partial \theta}{\partial \eta} = 0 \tag{11}$$

with the boundary conditions are as follows:

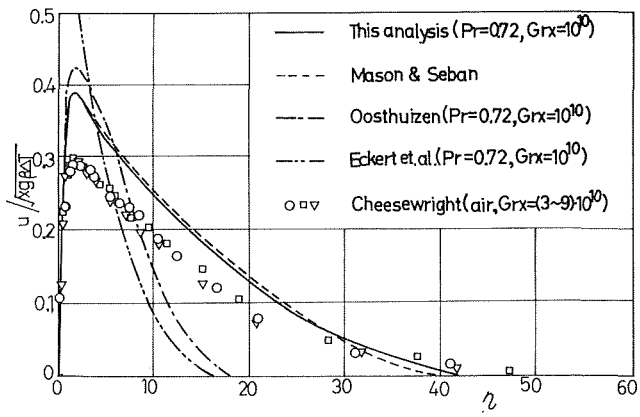

Fig. 1 Velocity profiles

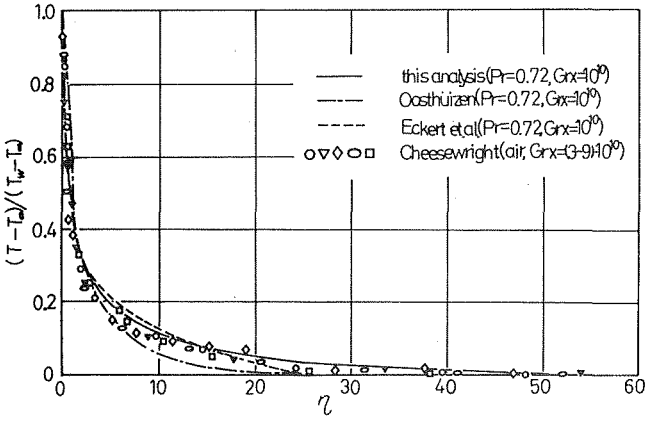

Fig. 2 Temperature profiles

$$\left.\begin{aligned} \eta = 0;\ f = \frac{\partial f}{\partial \eta} = 0,\ \theta = 1 \\ \eta = \infty;\ \frac{\partial f}{\partial \eta} = 0,\ \theta = 0 \end{aligned}\right\} \tag{12}$$

Pr_t and ϵ_M/ν in equations (13) and (14) given in the following have been selected [1],[2] as these values are not yet clear for natural convection,

$$\mathrm{Pr}_t = 1 \tag{13}$$

$$\epsilon_M/\nu = 0.4y^+\{1 - \exp(-0.0017y^{+2})\} \tag{14}$$

Equations (10) and (11) can be easily integrated using equations (12), (13), and (14). The use of local similarity concept given us the following advantages.

1 f and θ in equations (10) and (11) do not include the derivatives of x, but are apparently the functions of η only. Consequently, the value of x (or Gr_x) at any point in x-direction can be an assignable constant parameter. The value at any arbitrary point x_a on the physical plane is denoted by Gr_{xa} at this point. Equations (10) and (11) can thus be solved in η-direction only in respect of parameter Gr_{xa}, viz., the successive integration toward the trailing edge is not required.

2 The a priori decision of a transition point is not necessary in this analysis. On the contrary, in the ordinary successive integral method, it is necessary to obtain the exact location of the transition point before integration. Further, the location of transition point affects the quantity of heat transfer.

Results and Discussion

The results obtained in this analysis are shown by solid lines in Figs. 1–5.

Fig. 1 shows the dimensionless velocity profile. The experimental results by Cheesewright [2] are plotted in the same figure for comparison. Further, the theoretical values by Oosthuizen [3], Eckert [4], and Mason, et al. [5] are also shown by a dotted line, a chain line and two dotted chain lines, respectively.

The velocity profile obtained does not strictly agree with the experimental results of Cheesewright.

The results of Mason, et al., are similar to this analysis, but the results of the others deviate further from the experimental values. The authors wish to point out the following considerations in respect of these differences.

1 The geometrical conditions and the effect of enclosed space in the apparatus can be considered to play an important role in affecting the experimental results. The authors decided to compare with Cheesewright's data in the absence of other experimental re-

[2] Numbers in brackets designate References at end of technical note.

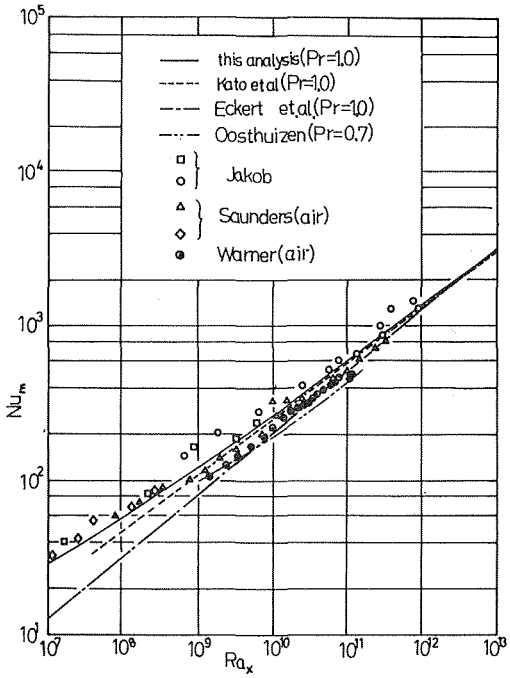

Fig. 3 Nusselt number

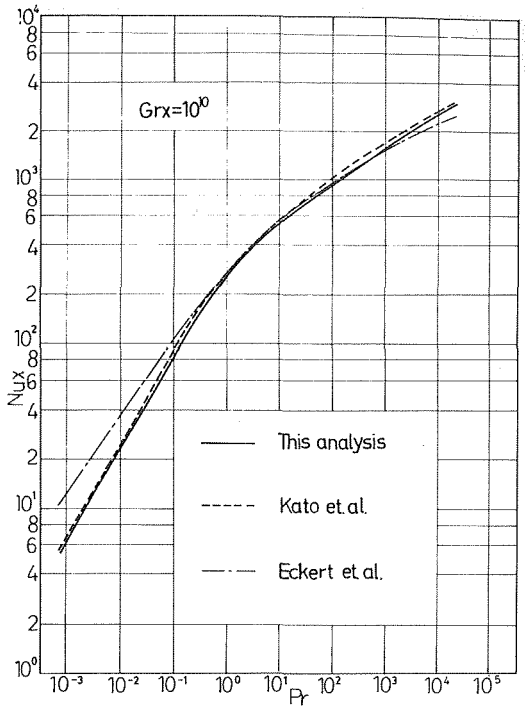

Fig. 5 Nusselt number

sults. It is felt strongly that further developments experimentally would be very useful in the future for more accurate comparisons.

2 The equation (14) used in this analysis is found to be accurate in the field of forced convection. The authors have applied this formula in the analysis and this fact may be one of the causes for the resulting deviations.

3 Lastly, the authors wish to comment on the accuracy of this analysis. The *local nonsimilarity method [6] can be used to evaluate* any level of truncation, but this method is thought to be a kind of perturbation method. It is felt that further considerations may be necessary, if this method is to predict accurate results in the turbulent field.

Fig. 2 shows the dimensionless temperature profile. The above mentioned, other theoretical and experimental results are also shown in the same figure. The analytical values in this analysis show good agreement with the experimental results.

Fig. 3 shows the relation between mean Nusselt number and local Rayleigh number for Prandtl numbers 0.7–1. The experimental results plotted in this figure are by Jakob [7], Saunders [8], Warner [9], Toulokian, et al. [10], and Fujii [11]. Moreover, the theoretical values by Eckert, Oosthuizen, and Kato, et al., are also shown. The analytical values are found to be in good agreement with the experimental results.

Fig. 4 shows the relation between mean Nusselt number and local Grashof number for Prandtl number about 40. In this figure, this analysis is found to be in closer agreement with the experimental data of Toulokian, et al., and Fujii than that of the theoretical analysis of Kato, et al.

Fig. 5 shows the relation between local Nusselt number and Prandtl number $[10^{-3} \leq \mathrm{Pr} \leq 10^{4}]$ for $\mathrm{Gr} = 10^{10}$.

Thickness of viscous sublayer δ_{lam}, dimensionless thickness of this y^{+}_{lam} and local shear stress at wall τ_{wx} in turbulent natural convection were able to be expressed by following formulas in the range of $\mathrm{Gr}_x = 10^{6}$–10^{15}, $\mathrm{Pr} = 10^{-3}$–10^{3}.

$$\delta_{\mathrm{lam}}/x = C_1(\mathrm{Pr}) \cdot \mathrm{G}_{rx}{}^{-0.123}$$
$$y^{+}_{\mathrm{lam}} = C_2(\mathrm{Pr}) \cdot \mathrm{G}_{rx}{}^{0.12} \qquad (15)$$
$$\tau_{wx}x^2/\mu\nu = C_3(\mathrm{Pr}) \cdot \mathrm{G}_{rx}{}^{0.170}$$

In conclusion, authors feel that this analysis is a simple way to obtain the velocity and temperature profiles and offers an engineering applicability in the field of turbulent natural convection.

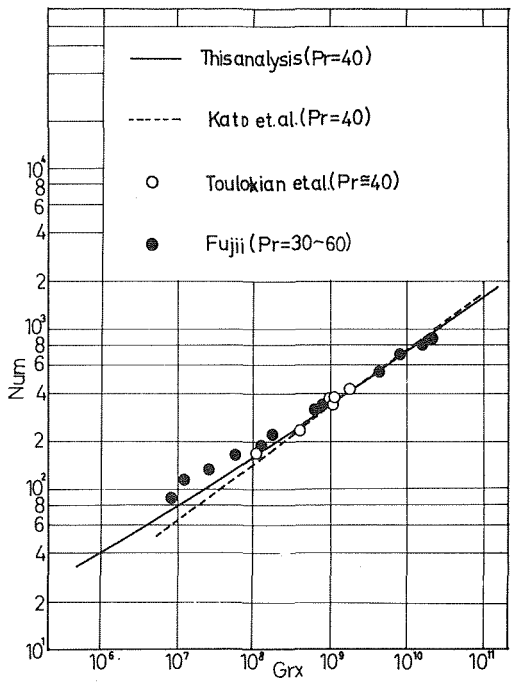

Fig. 4 Nusselt number

References

1 Kato, H., Nishiwaki, N., and Hirata, M., "On the Heat Transfer by Free Convection From a Vertical Plate," *International Journal of Heat and Mass Transfer*, Vol. 11, 1968, pp. 1117–1125.

2 Cheesewright, R., "Turbulent Natural Convection From a Vertical Plane Surface," JOURNAL OF HEAT TRANSFER, TRANS. ASME, Series C, Vol. 90, 1968, pp. 1–8.

3 Oosthuizen, P. H., "A Numerical Study of Turbulent Free Convec-

tion From an Isothermal Vertical Plate," Rept. No. 1170 of the Thermal and Fluid Sciences Group, Department of Mechanical Engineering, Queen's University, Kingston, Ontario, Canada, 1970.
4 Eckert, E. R. G., and Jackson, T. W., "Analysis of Turbulent Free Convection Boundary Layer on a Flat Plate," NACA Tech, Note 2207, 1950.
5 Mason, H. B., and Seban, R. A., "Numerical Predictions for Turbulent Free Convection From Vertical Surfaces," *International Journal of Heat and Mass Transfer*, Vol. 17, 1974, pp. 1329–1336.
6 Minkowycz, W. J., and Sparrow, E. M., "Local Nonsimilar Solutions for Natural Convection on a Vertical Cylinder," JOURNAL OF HEAT TRANSFER, TRANS. ASME, Series C, Vol. 96, No. 2, 1974, pp. 178–183.
7 Jakob, M., *Heat Transfer*, Vol. 1, Wiley, New York, 1949, p. 526.
8 Saunders, O. A., "Effect of Pressure Upon Natural Convection of Air," *Proc. Roy. Soc.*, Series A, Vol. 157, 1936, pp. 278–291.
9 Warner, C. Y., and Arpaci, V. S., "An Experimental Investigation of Turbulent Natural Convection in Air Along a Vertical Heated Flat Plate," *International Journal of Heat and Mass Transfer*, Vol. 11, 1968, pp. 397–406.
10 Toulokian, Y. S., Hawkins, G. A., and Jakob, M., "Heat Transfer by Free Convection From Heated Vertical Surfaces to Liquids," JOURNAL OF HEAT TRANSFER, TRANS. ASME, Series C, Vol. 70, No. 1, 1948, pp. 13–23.
11 Fujii, T., "Experimental Studies of Free Convection Heat Transfer," *Bull. Japan Soc. of Mech. Eng.*, Vol. 2, 1959, pp. 555–558.

A Note Concerning the Transport Processes Near Melting Glacial Ice in Seawater

O. M. Griffin[1]

Introduction

The heat, mass, and momentum transfer processes near melting glacial ice in seawater were recently studied [1, 2][2] for the case of forced fluid flow. It was assumed that the temperature at the boundary between phases was equal to the melting temperature of a pure ice-water system, or 0°C. However, such a system is correctly described by an equilibrium condition at the interface whereby the melting temperature is depressed in direct relation to the concentration of dissolved species at the boundary. This condition has been employed recently by Martin and Kauffman [3] in a study of the evolution of Arctic under-ice fresh water melt ponds and earlier by Frank [4] in an analysis of combined heat and mass transfer during transient solidification. The transport equations for the melt are complicated by this condition in that the heat and mass transfer processes are more closely coupled and because the melting temperature is not known a priori as in the melting of a pure solid. Also, the Stefan numbers—or the ratios of the sensible and latent heats for the melt and solid—are no longer independent parameters since both depend on the resulting temperature at the interface.

Analysis

The purpose of this technical brief is to extend the analysis just mentioned [1, 2] to include an appropriate equilibrium condition for the melting point depression. The melt problem is again formulated by considering the boundary layer equations for combined heat, mass, and momentum transfer which are described in the previously cited references. The concentration $\bar{C}_F$[3] and the temperature $\bar{T}_F$ at the phase boundary are not known a priori, however, but they must be determined from a mass balance on the dissolved species at the melt line, $\bar{y} = 0$. This balance is, in general [5],

$$\dot{m}_c = -\bar{\rho}\bar{\gamma}\frac{\partial \bar{C}}{\partial \bar{y}}\Big)_{\bar{y}=0} + C_F(\dot{m}_c + \dot{m}) \tag{1}$$

where $\dot{m}_c$(kg/m^2 s) is the flux of dissolved species at the interface and $\dot{m}$(kg/m^2 s) is the melting rate of pure solid. The density of the mixture is denoted by $\bar{\rho}$ and $\bar{\gamma}$ is the mass diffusion coefficient. Since the solid phase is impervious to the dissolved species ($\dot{m}_c = 0$) during the melting of glacial ice, this equation reduces to

$$-\bar{C}_F\dot{m} = -\bar{\rho}\bar{\gamma}\frac{\partial \bar{C}}{\partial \bar{y}}\Big)_{\bar{y}=0} \tag{2}$$

At the ice-salt water interface the temperature is determined by the equilibrium condition

$$\bar{T}_F = -\epsilon\bar{C}_F \tag{3}$$

where $\epsilon = 0.053$ when $\bar{C}_F$ is given in g/kg (see Martin and Kauffman [3] or Pounder [6]), and the governing transport equations [1, 2] are coupled together by these interrelated balance conditions.

Results and Discussion

When the equilibrium condition (3) is introduced into the system, the heat, momentum, and mass transfer solutions, already interdependent because of the appearance of the melting rate in each of the governing transport equations, become more closely coupled. The energy-balance integral method used previously [1, 2] remains a convenient method of solution, and some sample results have been recomputed for water temperatures between 5 and 20°C and for ice temperatures from −4 to −15°C. Two values of free-stream salinity have been investigated, at $\bar{C}_\infty$ = 26 and 34 g/kg, since these are representative, respectively, of arctic and antarctic sea water [3].

The melting temperature $\bar{T}_F$ is plotted in Fig. 1 as a function of the water temperature, for a free-stream salinity of 34 g/kg. The melting point is depressed under these conditions from the pure water value of 0 to −0.35°C when the water temperature is 5°C and the ice is at −4.8°C. When the ice temperature and salinity remain constant but the water temperature is increased to 15°C, the depression of the melting point is reduced to −0.07°C. The second curve in the figure corresponds to an ice temperature of −14.4°C, and it is seen that the ice subcooling has little effect on the equilibrium melting temperature at the interface.

There is a relatively simple, but interesting, physical reason for this change in melting point depression with fluid temperature, and the interfacial salinity $\bar{C}_F$ and the ratio δ_c/δ_t of the boundary

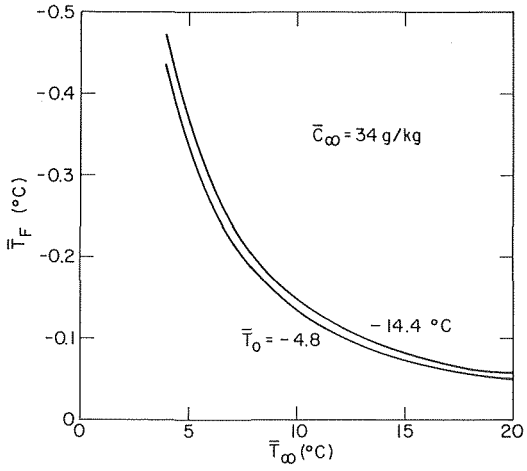

Fig. 1 The depression of the melting temperature $\bar{T}_F$ as a function of sea water and ice temperatures $\bar{T}_\infty$ and $\bar{T}_0$, respectively—the salinity $\bar{C}_\infty$ of sea water outside the boundary layer was held constant at 34 g/kg

[1] Ocean Technology Division, Naval Research Laboratory, Washington, D.C. Mem. ASME.
[2] Numbers in brackets designate References at end of technical note.
[3] The nomenclature here is the same as [1].

Contributed by the Heat Transfer Division of THE AMERICAN SOCIETY OF MECHANICAL ENGINEERS. Manuscript received by the Heat Transfer Division May 19, 1975.

tion From an Isothermal Vertical Plate," Rept. No. 1170 of the Thermal and Fluid Sciences Group, Department of Mechanical Engineering, Queen's University, Kingston, Ontario, Canada, 1970.
4 Eckert, E. R. G., and Jackson, T. W., "Analysis of Turbulent Free Convection Boundary Layer on a Flat Plate," NACA Tech, Note 2207, 1950.
5 Mason, H. B., and Seban, R. A., "Numerical Predictions for Turbulent Free Convection From Vertical Surfaces," *International Journal of Heat and Mass Transfer*, Vol. 17, 1974, pp. 1329–1336.
6 Minkowycz, W. J., and Sparrow, E. M., "Local Nonsimilar Solutions for Natural Convection on a Vertical Cylinder," JOURNAL OF HEAT TRANSFER, TRANS. ASME, Series C, Vol. 96, No. 2, 1974, pp. 178–183.
7 Jakob, M., *Heat Transfer*, Vol. 1, Wiley, New York, 1949, p. 526.
8 Saunders, O. A., "Effect of Pressure Upon Natural Convection of Air," *Proc. Roy. Soc.*, Series A, Vol. 157, 1936, pp. 278–291.
9 Warner, C. Y., and Arpaci, V. S., "An Experimental Investigation of Turbulent Natural Convection in Air Along a Vertical Heated Flat Plate," *International Journal of Heat and Mass Transfer*, Vol. 11, 1968, pp. 397–406.
10 Toulokian, Y. S., Hawkins, G. A., and Jakob, M., "Heat Transfer by Free Convection From Heated Vertical Surfaces to Liquids," JOURNAL OF HEAT TRANSFER, TRANS. ASME, Series C, Vol. 70, No. 1, 1948, pp. 13–23.
11 Fujii, T., "Experimental Studies of Free Convection Heat Transfer," *Bull. Japan Soc. of Mech. Eng.*, Vol. 2, 1959, pp. 555–558.

A Note Concerning the Transport Processes Near Melting Glacial Ice in Seawater

O. M. Griffin[1]

Introduction

The heat, mass, and momentum transfer processes near melting glacial ice in seawater were recently studied [1, 2][2] for the case of forced fluid flow. It was assumed that the temperature at the boundary between phases was equal to the melting temperature of a pure ice-water system, or 0°C. However, such a system is correctly described by an equilibrium condition at the interface whereby the melting temperature is depressed in direct relation to the concentration of dissolved species at the boundary. This condition has been employed recently by Martin and Kauffman [3] in a study of the evolution of Arctic under-ice fresh water melt ponds and earlier by Frank [4] in an analysis of combined heat and mass transfer during transient solidification. The transport equations for the melt are complicated by this condition in that the heat and mass transfer processes are more closely coupled and because the melting temperature is not known a priori as in the melting of a pure solid. Also, the Stefan numbers—or the ratios of the sensible and latent heats for the melt and solid—are no longer independent parameters since both depend on the resulting temperature at the interface.

Analysis

The purpose of this technical brief is to extend the analysis just mentioned [1, 2] to include an appropriate equilibrium condition for the melting point depression. The melt problem is again formulated by considering the boundary layer equations for combined heat, mass, and momentum transfer which are described in the previously cited references. The concentration $\bar{C}_F$[3] and the temperature $\bar{T}_F$ at the phase boundary are not known a priori, however, but they must be determined from a mass balance on the dissolved species at the melt line, $\bar{y} = 0$. This balance is, in general [5],

$$\dot{m}_c = -\bar{\rho}\bar{\gamma}\frac{\partial \bar{C}}{\partial \bar{y}}\Big)_{\bar{y}=0} + C_F(\dot{m}_c + \dot{m}) \tag{1}$$

where $\dot{m}_c$(kg/m^2 s) is the flux of dissolved species at the interface and $\dot{m}$(kg/m^2 s) is the melting rate of pure solid. The density of the mixture is denoted by $\bar{\rho}$ and $\bar{\gamma}$ is the mass diffusion coefficient. Since the solid phase is impervious to the dissolved species ($\dot{m}_c = 0$) during the melting of glacial ice, this equation reduces to

$$-\bar{C}_F\dot{m} = -\bar{\rho}\bar{\gamma}\frac{\partial \bar{C}}{\partial \bar{y}}\Big)_{\bar{y}=0} \tag{2}$$

At the ice-salt water interface the temperature is determined by the equilibrium condition

$$\bar{T}_F = -\epsilon\bar{C}_F \tag{3}$$

where $\epsilon = 0.053$ when $\bar{C}_F$ is given in g/kg (see Martin and Kauffman [3] or Pounder [6]), and the governing transport equations [1, 2] are coupled together by these interrelated balance conditions.

Results and Discussion

When the equilibrium condition (3) is introduced into the system, the heat, momentum, and mass transfer solutions, already interdependent because of the appearance of the melting rate in each of the governing transport equations, become more closely coupled. The energy-balance integral method used previously [1, 2] remains a convenient method of solution, and some sample results have been recomputed for water temperatures between 5 and 20°C and for ice temperatures from −4 to −15°C. Two values of free-stream salinity have been investigated, at $\bar{C}_\infty$ = 26 and 34 g/kg, since these are representative, respectively, of arctic and antarctic sea water [3].

The melting temperature $\bar{T}_F$ is plotted in Fig. 1 as a function of the water temperature, for a free-stream salinity of 34 g/kg. The melting point is depressed under these conditions from the pure water value of 0 to −0.35°C when the water temperature is 5°C and the ice is at −4.8°C. When the ice temperature and salinity remain constant but the water temperature is increased to 15°C, the depression of the melting point is reduced to −0.07°C. The second curve in the figure corresponds to an ice temperature of −14.4°C, and it is seen that the ice subcooling has little effect on the equilibrium melting temperature at the interface.

There is a relatively simple, but interesting, physical reason for this change in melting point depression with fluid temperature, and the interfacial salinity $\bar{C}_F$ and the ratio δ_c/δ_t of the boundary

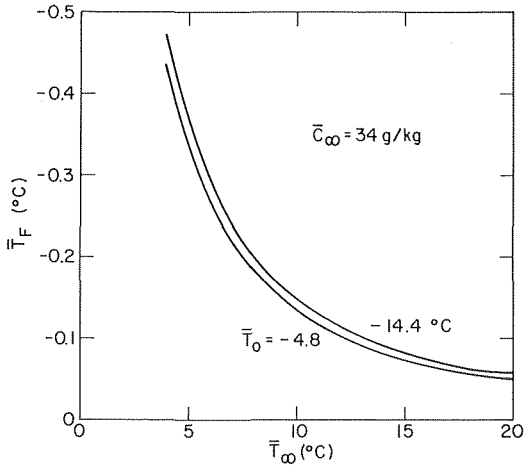

Fig. 1 The depression of the melting temperature $\bar{T}_F$ as a function of sea water and ice temperatures $\bar{T}_\infty$ and $\bar{T}_0$, respectively—the salinity $\bar{C}_\infty$ of sea water outside the boundary layer was held constant at 34 g/kg

[1] Ocean Technology Division, Naval Research Laboratory, Washington, D.C. Mem. ASME.
[2] Numbers in brackets designate References at end of technical note.
[3] The nomenclature here is the same as [1].

Contributed by the Heat Transfer Division of THE AMERICAN SOCIETY OF MECHANICAL ENGINEERS. Manuscript received by the Heat Transfer Division May 19, 1975.

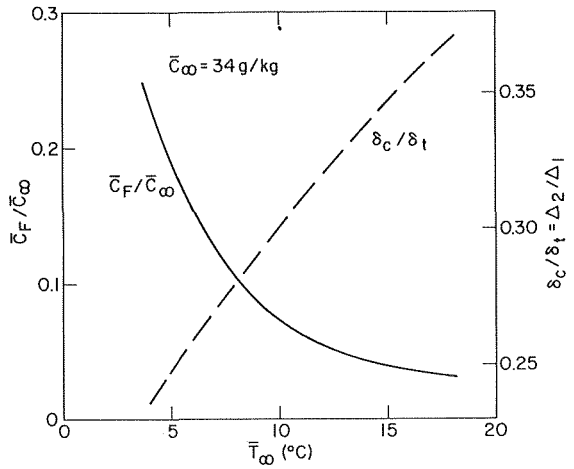

Fig. 2 Interfacial salinity $\bar{C}_F$ and the ratio δ_c/δ_t of the salinity and temperature boundary layer thicknesses as a function of water temperature during the melting of glacial ice in sea water—the ice temperature was held constant at $\bar{T}_0 = -4.8$°C and the sea water salinity was equal to $\bar{C}_\infty = 34$ g/kg.

layer thicknesses are plotted in Fig. 2 as functions of fluid temperature. The concentration $\bar{C}_F$ is determined from the balance, equation (2), between the rate of diffusion and the bulk motion of the fluid at the interface, and it is inversely proportional to the boundary layer thickness δ_c and to the temperature difference $(\bar{T}_\infty - \bar{T}_F)$. Since δ_c increases with fluid temperature as the rate of species diffusion approaches the rate of diffusion for the solute (water), the concentration $\bar{C}_F$ of dissolved species at the interface decreases accordingly. For example, when the glacial ice at −4.8°C melts in sea water of 34 g/kg salinity, the interfacial salinity decreases from 6.5 g/kg to 1.4 g/kg as the water temperature increases from 5 to 15°C. This decrease in salinity results in a change in the melting point depression from $\bar{T}_F = -0.34$ to −0.07°C.

The Stefan number for the water is no longer an independent parameter when the melting point depression depends on the interfacial salinity. As an example, for a water temperature of 5°C and a salinity of 34 g/kg, a melting point depression of −0.35°C results in a seven percent increase in the thermal driving force (Stefan number) and a corresponding nine percent increase in the melting rate from the pure water value. When the water temperature is increased to 15°C, the melting point depression is only −0.07°C. This increases the Stefan number by less than 1 percent and results in a correspondingly small increase in the melting rate from the pure water value.

Some typical results for the heat and mass transfer are listed in Table 1. The free-stream salinity in this case is $\bar{C}_\infty = 26$ g/kg. Both the energy and concentration thicknesses δ_t** and δ_c** increase as the fluid temperature is increased. The thermal boundary layer thickness δ_t increases slightly in relation to δ_m, the momentum boundary layer thickness, with increasing fluid temperature, while the relative mass diffusion boundary layer thickness δ_c/δ_m doubles as the fluid temperature increases from 5 to 20°C. The kinematic viscosity of the water decreases sharply with rising temperature and results in the increased relative boundary layer thicknesses. An increase in the water temperature results in an increased thermal driving force $(\bar{T}_\infty - \bar{T}_F)$ and, consequently, results in the increased melting rate $\bar{V}_F$ shown in the right-hand column of the table. The subcooling of the solid phase has little effect in the range of ice temperatures employed in the calculations.

Summary and Concluding Remarks

The energy-balance integral method has been employed in a study of the steady melting of ice in sea water. It is necessary to satisfy simultaneously an energy balance, a species conservation equation and an equilibrium temperature condition at the interface between phases in addition to the transport equations for heat, mass and momentum transfer. For a sea water temperature of 5°C, the melting point depression which results from the combined heat and mass transfer processes increases the melting rate by 9 percent from the pure water value. When the water temperature is 15°C, the melting rate is increased by less than 1 percent and the heat and mass transfer are independent of the melting point depression.

Particular attention has been paid to the melting of glacial ice in sea water, but the method is also applicable in general to the steady melting of a pure solid in the presence of a small concentration of dissolved species in the liquid.

Acknowledgment

The author wishes to thank the Naval Research Laboratory for support of this work, and also to thank Prof. Seelye Martin of the University of Washington, Seattle for several helpful comments.

Table 1 Heat and mass transfer results

$\bar{T}_o$	$\bar{T}_F$	δ_t^{**}	δ_c^{**}	$\delta_t/\delta_m = \Delta_1$	$\delta_c/\delta_m = \Delta_2$	$\frac{\bar{V}}{U}\left(\sqrt{Pe_x}\right)$
			($\bar{T}_\infty = 5$°C, $\bar{C}_\infty = 26$ g/kg)			
- 4.8°C	-0.20°C	0.0572	0.0174	0.436	0.108	0.0148
- 9.6	-0.21	0.0572	0.0172	0.436	0.107	0.0144
-14.4	-0.22	0.0572	0.0170	0.436	0.106	0.0141
			($\bar{T}_\infty = 10$°C)			
- 4.8	-0.13	0.0609	0.0240	0.463	0.140	0.0281
- 9.6	-0.14	0.0608	0.0237	0.463	0.138	0.0274
-14.4	-0.15	0.0608	0.0234	0.463	0.137	0.0267
			($\bar{T}_\infty = 15$°C)			
- 4.8	-0.07	0.0648	0.0301	0.492	0.171	0.0417
- 9.6	-0.08	0.0647	0.0298	0.492	0.169	0.0406
-14.4	-0.08	0.0646	0.0294	0.492	0.168	0.0396
			($\bar{T}_\infty = 20$°C)			
- 4.8	-0.05	0.0682	0.0356	0.518	0.200	0.0549
- 9.6	-0.06	0.0681	0.0351	0.518	0.198	0.0536
-14.4	-0.06	0.0680	0.0347	0.518	0.196	0.0523

References

1 Griffin, O. M., "Heat, Mass and Momentum Transfer During the Melting of Glacial Ice in Seawater," JOURNAL OF HEAT TRANSFER, TRANS. ASME, Series C, Vol. 95, 1973, pp. 317–323.

2 Griffin, O. M., "An Integral Method of Solution for Combined Heat and Mass Transfer Problems With Phase Transformation," *HEAT TRANSFER 1974, Proceedings Fifth International Heat Transfer Conference,* Vol. I, 1974, pp. 211–215.

3. Martin, S. and Kauffman, P., "The Evolution of Under-Ice Melt Ponds, or Double Diffusion at the Freezing Point," *Journal of Fluid Mechanics* Vol. 64, 1974, pp. 507–527.

4 Frank, F. C., "Radially Symmetric Phase Growth Controlled by Diffusion," *Proceedings Royal Society London,* Series A, Vol. 201, 1950, pp. 586–599.

5 Bird, R. B., Stewart, W. E., and Lighfoot, E. N., *Transport Phenomena,* Wiley, New York, Chapter 19, 1960.

6 Pounder, E. R., *The Physics of Ice,* Pergamon, Oxford, Chapters 1 and 2, 1965.

Stagnation Point Heat Transfer: Ignition of a Combustible Mixture With Inert Gas Injection Through a Porous Wall

P. Durbetaki[1] and H. W. Hsu[2]

Nomenclature

$\bar{D}_I$ = Damköhler's first dimensionless similarity group
$\bar{D}_{II}$ = Damköhler's second dimensionless similarity group
$\bar{D}_{I,i}$ = critical first Damköhler number for ignition
E = activation energy
$E^* = E/RT_e$, dimensionless activation energy
f_w = injection parameter
$f'(\eta)$ = dimensionless velocity
n_e = dimensionless stoichiometry measure
Nu = Nusselt number
Pr = Prandtl number
R = universal gas constant
Re = Reynolds number
Sc = Schmidt number
T = temperature
Y = mass fraction
$\alpha_i = Y_i/Y_{i,e}$
η = dimensionless coordinate
$\theta = T/T_e$

Subscripts

e = free stream
F = fuel
i = ith species
N = inert gas
O = oxidizer
P = product

Several studies have been made during the last two decades on the heat interaction between reactive mixtures of gases and solid surfaces. The work reported in the present paper is an extension of the work of Alkidas and Durbetaki [1, 2].[3] The effects of injecting a hot inert gas through the porous wall surface of an axisymmetric blunt body near the stagnation region, have been studied with regards to heat interactions between the gases and the wall, and the ignition of the cold combustible mixture. The fluid has been considered compressible and the injection rate of the hot inert gas has been varied.

The boundary-layer conservation equations of a multicomponent reactive mixture interacting with a constant temperature solid boundary have been derived by Alkidas and Durbetaki [1, 2]. These equations remain unaltered for the problem under consideration in this paper, and they are

$$f''' + ff'' = (1/2)[(f')^2 - \theta] \tag{1}$$

$$\alpha_F'' + \mathrm{Sc} f \alpha_F' = (n_e + \alpha_F)\mathrm{Sc}\bar{D}_I(1/\theta)\alpha_F e^{-E^*/\theta} \tag{2}$$

$$\alpha_N'' + \mathrm{Sc} f \alpha_N' = 0 \tag{3}$$

$$\theta'' + \mathrm{Pr} f \theta' = -(n_e + \alpha_F)\mathrm{Pr}\bar{D}_I\bar{D}_{II}(1/\theta)\alpha_F e^{-E^*/\theta} \tag{4}$$

The boundary conditions for the governing equations presented in the foregoing describing the behavior of the problem under consideration are

$$\text{at } \eta = 0: \quad \left.\begin{array}{l} f = f_w \qquad f' = 0 \qquad \theta = \theta_w \\ \alpha_i' = -\mathrm{Sc} f_w \alpha_i \qquad \text{for } i = \mathrm{O}, F, P \end{array}\right\} \tag{5a}$$

$$\text{at } \eta = 0: \quad \alpha_N' = -\mathrm{Sc} f_w(\alpha_i - 1/Y_{N,e}) \tag{5b}$$

$$\text{as } \eta \to \infty: \quad \left.\begin{array}{l} f' \to 1 \qquad \theta \to 1 \\ \alpha_i' \to 1 \qquad \text{for } i = \mathrm{O}, F, P, N \end{array}\right\} \tag{5c}$$

The above set of differential equations are coupled and they must be solved simultaneously together with the boundary conditions presented. The numerical computations were carried out using Gill's modified Runge-Kutta fourth order method. The equations were first integrated with a set of estimated values for the unknown boundary conditions at the wall, $f''(0)$, $\theta'(0)$, and $\alpha_F(0)$. The calculated values of f', α_F, and θ at the free stream were then compared with unity, the asymptotic condition. An improved set of values of the initial conditions were found by using the Gauss-Jordan Elimination Method. These iterations were continued until the resulting values of f', α_F, and θ at the free stream were within 0.0001 of unity. The step-size during the integration was varied using 0.01 increments for $\eta \leq 3.0$, the region where the most drastic changes occur, and the step size was increased to 0.1 for $\eta > 3.0$, the region where there are no significant changes. The integration was carried out until a value of $\eta = 12.5$ where the profiles of f', θ, and α_F became constant. The procedure was repeated for each of the $\bar{D}_I$ values and with f_w as the injection parameter.

Results and Discussion

In order to establish some numerical values, with the computational approach discussed in the foregoing, the case selected was a stoichiometric mixture of methane and air at a free stream temperature of $T_e = 300$ K. The activation energy is found to be 1.675×10^5 J/mole. These conditions were used to produce the values of the dimensionless parameters and the boundary conditions needed for the computations from the governing equations. Together with the values of the inert gas injection parameter used they are:

$$\mathrm{Pr} = 0.74 \qquad \mathrm{Sc} = 0.74 \qquad E^* = 67.1366$$

$$\bar{D}_{II} = 6.44518 \qquad n_e = 0 \qquad \theta_w = 3.0$$

$$f_w = 0, -0.15, -0.30, -0.50$$

The calculated results of $\mathrm{Nu}/(\mathrm{Re})^{1/2}$, for the range of values for the first Damköhler number that encompasses the transition from frozen flow through ignition are given in Fig. 1. It is apparent from this figure that the effect of inert gas injection through the porous

[1] Assoc. Professor, School of Mechanical Engineering, Georgia Institute of Technology, Atlanta, Ga. Mem. ASME.

[2] Graduate Assistant, School of Mechanical Engineering, Georgia Institute of Technology, Atlanta, Ga.

Contributed by the Heat Transfer Division of THE AMERICAN SOCIETY OF MECHANICAL ENGINEERS. Manuscript received by the Heat Transfer Division August 19, 1974.

[3] Numbers in brackets designate References at end of technical note.

References

1 Griffin, O. M., "Heat, Mass and Momentum Transfer During the Melting of Glacial Ice in Seawater," JOURNAL OF HEAT TRANSFER, TRANS. ASME, Series C, Vol. 95, 1973, pp. 317–323.

2 Griffin, O. M., "An Integral Method of Solution for Combined Heat and Mass Transfer Problems With Phase Transformation," *HEAT TRANSFER 1974, Proceedings Fifth International Heat Transfer Conference,* Vol. I, 1974, pp. 211–215.

3. Martin, S. and Kauffman, P., "The Evolution of Under-Ice Melt Ponds, or Double Diffusion at the Freezing Point," *Journal of Fluid Mechanics* Vol. 64, 1974, pp. 507–527.

4 Frank, F. C., "Radially Symmetric Phase Growth Controlled by Diffusion," *Proceedings Royal Society London,* Series A, Vol. 201, 1950, pp. 586–599.

5 Bird, R. B., Stewart, W. E., and Lighfoot, E. N., *Transport Phenomena,* Wiley, New York, Chapter 19, 1960.

6 Pounder, E. R., *The Physics of Ice,* Pergamon, Oxford, Chapters 1 and 2, 1965.

Stagnation Point Heat Transfer: Ignition of a Combustible Mixture With Inert Gas Injection Through a Porous Wall

P. Durbetaki[1] and H. W. Hsu[2]

Nomenclature

$\bar{D}_I$ = Damköhler's first dimensionless similarity group
$\bar{D}_{II}$ = Damköhler's second dimensionless similarity group
$\bar{D}_{I,i}$ = critical first Damköhler number for ignition
E = activation energy
$E^* = E/RT_e$, dimensionless activation energy
f_w = injection parameter
$f'(\eta)$ = dimensionless velocity
n_e = dimensionless stoichiometry measure
Nu = Nusselt number
Pr = Prandtl number
R = universal gas constant
Re = Reynolds number
Sc = Schmidt number
T = temperature
Y = mass fraction
$\alpha_i = Y_i/Y_{i,e}$
η = dimensionless coordinate
$\theta = T/T_e$

Subscripts

e = free stream
F = fuel
i = ith species
N = inert gas
O = oxidizer
P = product

Several studies have been made during the last two decades on the heat interaction between reactive mixtures of gases and solid surfaces. The work reported in the present paper is an extension of the work of Alkidas and Durbetaki [1, 2].[3] The effects of injecting a hot inert gas through the porous wall surface of an axisymmetric blunt body near the stagnation region, have been studied with regards to heat interactions between the gases and the wall, and the ignition of the cold combustible mixture. The fluid has been considered compressible and the injection rate of the hot inert gas has been varied.

The boundary-layer conservation equations of a multicomponent reactive mixture interacting with a constant temperature solid boundary have been derived by Alkidas and Durbetaki [1, 2]. These equations remain unaltered for the problem under consideration in this paper, and they are

$$f''' + ff'' = (1/2)[(f')^2 - \theta] \tag{1}$$

$$\alpha_F'' + \mathrm{Sc} f \alpha_F' = (n_e + \alpha_F)\mathrm{Sc}\bar{D}_I(1/\theta)\alpha_F e^{-E^*/\theta} \tag{2}$$

$$\alpha_N'' + \mathrm{Sc} f \alpha_N' = 0 \tag{3}$$

$$\theta'' + \mathrm{Pr} f \theta' = -(n_e + \alpha_F)\mathrm{Pr}\bar{D}_I\bar{D}_{II}(1/\theta)\alpha_F e^{-E^*/\theta} \tag{4}$$

The boundary conditions for the governing equations presented in the foregoing describing the behavior of the problem under consideration are

$$\text{at } \eta = 0: \quad \left.\begin{array}{c} f = f_w \qquad f' = 0 \qquad \theta = \theta_w \\ \alpha_i' = -\mathrm{Sc} f_w \alpha_i \qquad \text{for } i = \mathrm{O}, F, P \end{array}\right\} \tag{5a}$$

$$\text{at } \eta = 0: \quad \alpha_N' = -\mathrm{Sc} f_w(\alpha_i - 1/Y_{N,e}) \tag{5b}$$

$$\text{as } \eta \to \infty: \quad \left.\begin{array}{c} f' \to 1 \qquad \theta \to 1 \\ \alpha_i' \to 1 \qquad \text{for } i = \mathrm{O}, F, P, N \end{array}\right\} \tag{5c}$$

The above set of differential equations are coupled and they must be solved simultaneously together with the boundary conditions presented. The numerical computations were carried out using Gill's modified Runge-Kutta fourth order method. The equations were first integrated with a set of estimated values for the unknown boundary conditions at the wall, $f''(0)$, $\theta'(0)$, and $\alpha_F(0)$. The calculated values of f', α_F, and θ at the free stream were then compared with unity, the asymptotic condition. An improved set of values of the initial conditions were found by using the Gauss-Jordan Elimination Method. These iterations were continued until the resulting values of f', α_F, and θ at the free stream were within 0.0001 of unity. The step-size during the integration was varied using 0.01 increments for $\eta \leq 3.0$, the region where the most drastic changes occur, and the step size was increased to 0.1 for $\eta > 3.0$, the region where there are no significant changes. The integration was carried out until a value of $\eta = 12.5$ where the profiles of f', θ, and α_F became constant. The procedure was repeated for each of the $\bar{D}_I$ values and with f_w as the injection parameter.

Results and Discussion

In order to establish some numerical values, with the computational approach discussed in the foregoing, the case selected was a stoichiometric mixture of methane and air at a free stream temperature of $T_e = 300$ K. The activation energy is found to be 1.675×10^5 J/mole. These conditions were used to produce the values of the dimensionless parameters and the boundary conditions needed for the computations from the governing equations. Together with the values of the inert gas injection parameter used they are:

$$\mathrm{Pr} = 0.74 \qquad \mathrm{Sc} = 0.74 \qquad E^* = 67.1366$$

$$\bar{D}_{II} = 6.44518 \qquad n_e = 0 \qquad \theta_w = 3.0$$

$$f_w = 0, -0.15, -0.30, -0.50$$

The calculated results of $\mathrm{Nu}/(\mathrm{Re})^{1/2}$, for the range of values for the first Damköhler number that encompasses the transition from frozen flow through ignition are given in Fig. 1. It is apparent from this figure that the effect of inert gas injection through the porous

[1] Assoc. Professor, School of Mechanical Engineering, Georgia Institute of Technology, Atlanta, Ga. Mem. ASME.

[2] Graduate Assistant, School of Mechanical Engineering, Georgia Institute of Technology, Atlanta, Ga.

Contributed by the Heat Transfer Division of THE AMERICAN SOCIETY OF MECHANICAL ENGINEERS. Manuscript received by the Heat Transfer Division August 19, 1974.

[3] Numbers in brackets designate References at end of technical note.

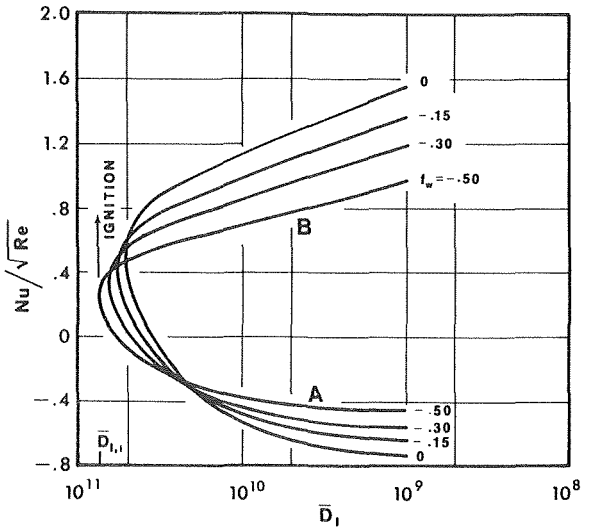

Fig. 1 Dependence of surface heat transfer rate on the first Damköhler number with inert gas injection rate as a parameter, $\theta_w = 3.0$

wall is to increase the critical ignition first Damköhler number $\bar{D}_{I,i}$.

Another effect that can be observed from Fig. 1 is that at the ignition point the surface heat transfer rate decreases with increasing injection rate. The effect of the inert gas injection rate on interface heat transfer is better illustrated in Fig. 2 where the curves have been drawn for fixed values of the first Damköhler number. A decrease of the heat added to the wall with increasing inert gas injection rates, is due to the absorption of a larger fraction of the liberated energy from the reacting mixture, by the inert gas.

The fuel concentration at the interface, as a function of the first Damköhler number, at specified inert gas injection rates is shown in Fig. 3. The branches A and B on these curves have been labeled to correspond with the previous figures. The decrease in the fuel mass fraction at the wall is due to the dilution of the combustible mixture by the inert gas injected through the porous wall. Table 1

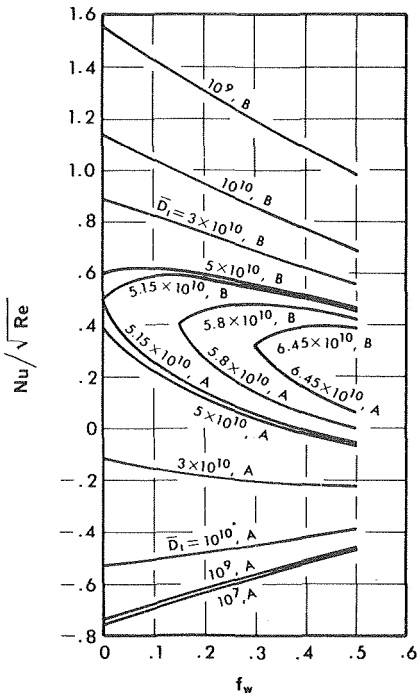

Fig. 2 The effect of inert gas injection on the surface heat transfer

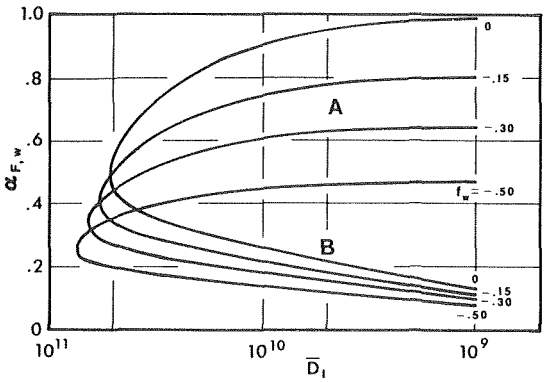

Fig. 3 The fuel concentration at the interface as a function of the first Damköhler number with inert gas injection rate as a parameter, $\theta_w = 3.0$

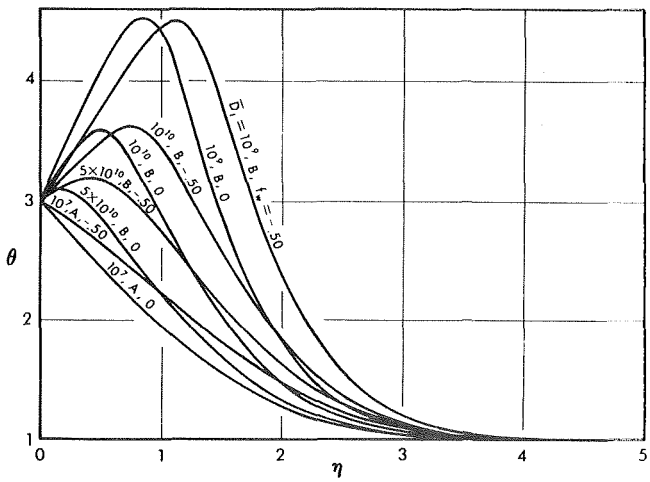

Fig. 4 Comparison of temperature profiles at specified Damköhler numbers and inert gas injection rates

Table 1 Fuel concentrations at the interface at specified inert gas injection rates

f_w	$\alpha_F(0)$	
	at $\bar{D}_{I,i}$	at $\bar{D}_I = 10^7$ branch A
0	0.490	0.9999
-0.15	0.415	0.8093
-0.30	0.340	0.6479
-0.50	0.250	0.4733

presents a summary of the fuel concentration at the wall both under frozen flow condition and the critical ignition point at four specified inert gas injection rates.

Finally, Fig. 4 presents the temperature profiles at fixed Damköhler numbers for different inert gas injection rates. The curves are marked with the letter A or B to indicate the appropriate branch they correspond to in Fig. 1. Inert gas injection, appears to increase the maximum temperature near the critical ignition point and decreases it near the equilibrium flow. Also, with injection the flame is moved further away from the wall.

References

1 Alkidas, A., and Durbetaki, P., "Stagnation-Point Heat Transfer: The Effect of the First Damköhler Similarity Parameter," JOURNAL OF HEAT TRANSFER, TRANS. ASME, Series C, Vol. 94, 1972, p. 410.

2 Alkidas, A., and Durbetaki, P., "Ignition of a Gaseous Mixture of a Heated Surface," *Combustion Science and Technology*, Vol. 7, 1973, p. 135.

Laminar Film Condensation Heat Transfer in the Presence of Electric and Magnetic Fields

A. S. El-Ariny,[1] J. A. Sabbagh,[1] and M. A. Obeid[2]

Introduction

The mechanism of heat transfer with laminar film condensation on an isothermal plate was investigated by Sparrow and Gregg [1][3] applying boundary layer treatment. Laminar film condensation in the presence of electric and magnetic fields was analyzed by Singer [2] using the integral method of boundary layer theory with the negligence of the inertia terms in the momentum equation. Very recently, Murty, et al. [3] studied the influence of a weak magnetic field on the condensation phenomena using perturbation technique. They found that the ponderomotive force developed due to the application of magnetic field causes the condensation heat transfer to decrease. In the present brief, the effect of external electric and magnetic fields on heat transfer coefficients was investigated for laminar film type condensation along an isothermal semi-infinite vertical plate, as shown in Fig. 1. Small magnetic Reynold's numbers were considered so that the induced magnetic field could be neglected. Techniques of similarity and asymptotic expansion were applied. Effects of electric and magnetic fields on the heat transfer is presented in terms of electromagnetic parameters for Prandtl numbers 1.0 and 0.008.

Analysis

The fluid was assumed to be electrically conductive and incompressible with constant specific heat, viscosity, and thermal conducitivity. The flow is governed by the following nondimensional boundary layer equations:

$$\frac{\partial u}{\partial x} + \frac{\partial v}{\partial y} = 0 \tag{1}$$

$$u\frac{\partial u}{\partial x} + v\frac{\partial u}{\partial y} = \frac{1}{\mathrm{R}_e}\frac{\partial^2 u}{\partial y^2} + (1 - \rho_v/\rho)/F_r - M(u + \mathrm{R}_E) \tag{2}$$

$$u\frac{\partial \theta}{\partial x} + v\frac{\partial \theta}{\partial y} = \frac{1}{\mathrm{P}_e}\frac{\partial^2 \theta}{\partial y^2} + ME_c\,(u^2 + 2\mathrm{R}_E u + \mathrm{R}_E{}^2) \tag{3}$$

where

$u = \bar{u}/U_\infty$, $v = \bar{v}/U_\infty$, $x = \bar{x}/L$, $y = \bar{y}/L$

$\theta = (t - t_v)/(t_w - t_v)$, $\mathrm{R}_e = \rho U_\infty L/\mu$, $\mathrm{R}_E = E/BU_\infty{}^2$,

$F_r = U_\infty{}^2/gL$, $M = \sigma B^2 L/\rho U_\infty$, $\mathrm{P}_r = \dfrac{\mu c_p}{k}$, $E_c = U_\infty{}^2/c_p(t_w - t_v)$,

$\mathrm{P}_e = \mathrm{P}_r\mathrm{R}_e$;

$\bar{u},\bar{v}$ are the physical velocity components;

$\bar{x},\bar{y}$ are the physical coordinates;

B is the magnetic field flux density;

and E is the electric field intensity.

The mechanism of heat exchange at the liquid-vapor interface gives:

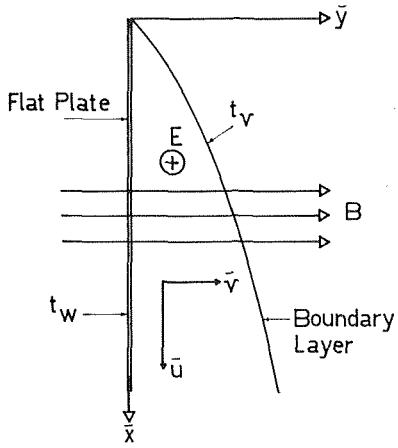

Fig. 1 Sketch of the condensation boundary layer with electric and magnetic fields

$$-\left(\frac{\partial \theta}{\partial y}\right)_{y=\delta} = \mathrm{P}_e\left(\frac{h_{fg}}{c_p\,\Delta t}\right)\int_0^\delta u\,dy,\ (\Delta t = t_w - t_v) \tag{4}$$

The last two terms on the right-hand side of the momentum equation (2) represent the external forces due to gravity and electromagnetic fields, respectively. The last term of the energy equation (3) represents Joule's heat supplied by the external electric and magnetic fields.

The boundary conditions for the foregoing equations are,

$$\text{at } y = 0;\ u = v = 0,\ t = t_w = \text{constant},$$

and

$$\text{at } y = \delta;\ \frac{\partial u}{\partial y} = 0 \text{ and } t = t_v = \text{constant} \tag{5}$$

Introducing a stream function $\psi(x,y)$, $(u = \partial\psi/\partial y,\ v = -\partial\psi/\partial x)$, then using the following expansions for the stream function $\psi(\xi,\eta)$ and the dimensionless temperature $\theta(\xi,\eta)$;

$$\psi(\xi,\eta) = (4C/\mathrm{P}_e)\xi^{3/4}\sum_{j=0}^{\infty}(M\xi)^{j/2}f_j(\eta) \tag{6}$$

$$\theta(\xi,\eta) = \sum_{j=0}^{\infty}(M\xi)^{j/2}\theta_j(\eta) \tag{7}$$

equations (2) and (3) were reduced to two sets of ordinary differential equations with f_j and θ_j as dependent variables and η as an independent variables. These equations are omitted here for space limitations. In equations (6) and (7) $\eta = Cy/x^{1/4}$, $\xi = x$ are the similarity variables, and

$$C = \left[\mathrm{P}_e\mathrm{R}_e\left\{\left(1 - \frac{\rho_v}{\rho}\right)\Big/ 4F_r - MR_E\right\}\right]^{1/4} \tag{8}$$

Results and Conclusions

The ordinary differential equations for f_j and θ_j were solved numerically using Runge-Kutta method up to $j = 2$. The relationship between film thickness, η_δ, as a function of the condensation parameter, $c_p\Delta t/h_{fg}$, was obtained from equation (4), in (ξ,η) coordinates, in the form

$$C_p\Delta t/h_{fg} = \left[\sum_{j=0}^{\infty}(M\xi)^{j/2}f_j(\eta_\delta)\right]\Big/ \left[\sum_{j=0}^{\infty}(M\xi)^{j/2}\theta_j(\eta_\delta)/(2j+3)\right] \tag{9}$$

For each value of the condensation parameter there corresponds a value of η_δ and hence the results expressed in the form of Nusselt ratio, $\mathrm{Nu}_{x,w}/\mathrm{Nu}_{x,0}$, are plotted in Figs. 2 and 3, where

---

[1] Assoc. Professors, Mechanical Engineering Department, University of Riyad, Riyad, Saudi Arabia.

[2] Assoc. Professor, Electrical Engineering Department, University of Riyad, Riyad, Saudi Arabia.

[3] Numbers in brackets designate References at end of technical note.

Contributed by the Heat Transfer Division of THE AMERICAN SOCIETY OF MECHANICAL ENGINEERS. Manuscript received by the Heat Transfer Division.

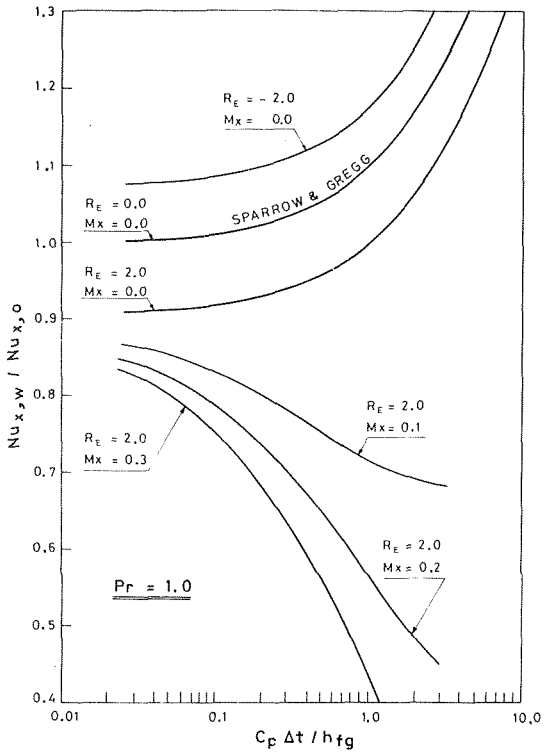

Fig. 2 Nusselt ratio versus condensation parameter for Prandtl number 1.0

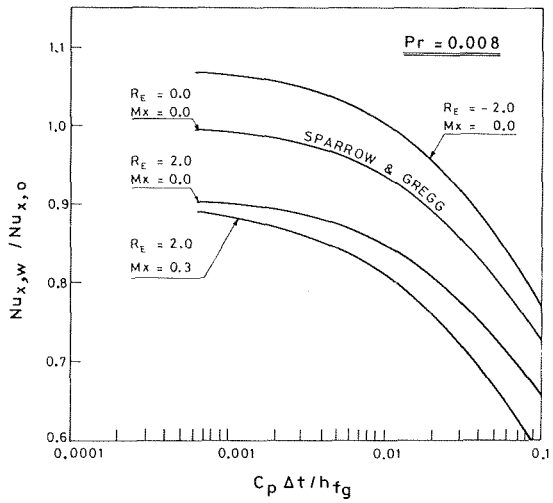

Fig. 3 Nusselt ratio versus condensation parameter for Prandtl number 0.008

$$Nu_{x,w}/Nu_{x,0} = [\{1.0 - MR_E F_r/(1 - \rho_v/\rho)\}\{c_p \Delta t/h_{fg}\}]^{1/4} \cdot \sum_{j=0}^{\infty} (Mx)^{j/2}\theta_j'(0) \quad (10)$$

$$Nu_{x,0} = [P_e R_e x^3(1 - \rho_v/\rho)/4F_r]^{1/4} \cdot [h_{fg}/c_p \Delta t]^{1/4} \quad (11)$$

and

$$Nu_{x,w} = h_x \left(\frac{x}{k}\right) = k \left(\frac{\partial\theta}{\partial y}\right)_0 \cdot \frac{x}{k} = \left[\frac{1}{4} P_e R_e x^3\{(1. - \rho_v/\rho)/F_r - MR_E\}\right]^{1/4} \times \sum_{j=0}^{\infty} (Mx)^{j/2}\theta_j'(0) \quad (12)$$

In the special case when both electric and magnetic fields were absent, the plots coincide with those obtained by Sparrow and Gregg [1]. However, the presence of an electric field in a direction inward to the plane of paper, (R_E = 2.0), and normal to the flow, tends to decrease the heat transfer rates, whereas an electric field in the opposite direction tends to increase the heat transfer rates. These effects are due to the ponderomotive forces developed by the electric field current as it interacts with the magnetic field in either a direction opposite to the flow or in a direction along the flow, respectively.

The presence of the magnetic field normal to the flow and in the plane of the paper tends to decrease the heat transfer rates, which is in agreement with results obtained in reference [3]. The last case is shown in Figs. 2 and 3 for a typical value of R_E = 2.0 when the magnetic expansion parameter $Mx \neq 0$, for P_r = 1.0 and 0.008.

References

1 Sparrow, E. M., and Gregg, J. L., "A Boundary-Layer Treatment of Laminar Film Condensation," JOURNAL OF HEAT TRANSFER, TRANS. ASME, Series C, Vol. 81, 1959, pp. 13–18.

2 Singer, R. M., "Laminar Film Condensation in the Presence of an Electromagnetic Field," ASME Paper No. 64-WA/HT-47, 1964.

3 Murty, K. N., Sarma, C. K., and Sarma, P. K., "Laminar Film Condensation on a Vertical Plate-Effect of Magnetic Field," JOURNAL OF HEAT TRANSFER, Series C, Vol. 97, 1975, pp. 139–141.

journal of heat transfer

discussion

On Solving the Transient Conducting Slab With Radiating and Convecting Surfaces[1]

J. Sucec.[2] The authors are to be commended for their contributions to stability analysis of finite difference equations, for certain nonlinear problems, by use of a physical reasoning approach which supplements the "derivative method" presented in their previous work [5]. The value of these two methods can really be appreciated when one encounters a situation, such as the one the authors discuss, where, because of the nonlinear nature of the problem, the matrix method of stability analysis [7] fails for at least some of the possible values of the parameters involved.

Another method, which the authors may be unaware of, also exists which utilizes physical reasoning to establish stability criteria for finite difference algorithms applied to unsteady-state problems. This method is given by Arpaci[3] and can be summed up as follows.

The time increment $\Delta\tau$ must be chosen in such a way that the value of the dependent variables at any node cannot change to a value beyond the steady-state value in a single time increment. To illustrate, consider the authors' finite difference equation,

$$\theta_M{}^{n+1} - \theta_M{}^n = [A - B\theta_M{}^n - C(\theta_M{}^n)^4]\Delta\tau \tag{3}$$

Using the method of [3], the steady-state finite difference equation for this node can be written as,

$$0 = A - B\theta_M{}^{ss} - C(\theta_M{}^{ss})^4 \tag{4}$$

The superscript ss means steady-state conditions. Next (4), multiplied by $\Delta\tau$, is subtracted from (3) and $\theta_M{}^{ss} - \theta_M{}^n$ is factored out yielding,

$$\theta_M{}^{n+1} - \theta_M{}^n = (\theta_M{}^{ss} - \theta_M{}^n)\Delta\tau \times \{B + C(\theta_M{}^{ss} + \theta_M{}^n)[(\theta_M{}^{ss})^2 + (\theta_M{}^n)^2]\} \tag{5}$$

In order that $\theta_M{}^{n+1}$ not go beyond the steady state, it is required that $\theta_M{}^{n+1} - \theta_M{}^n \leqq \theta_M{}^{ss} - \theta_M{}^n$ which leads to the following condition for stability, after replacing B and C by their equivalents.

$$\Delta\tau \leq \frac{\Delta X^2}{2\{N\Delta X + 1 + \psi^{-1}\Delta X(\theta_M{}^{ss} + \theta_M{}^n)[(\theta_M{}^{ss})^2 + (\theta_M{}^n)^2]\}} \tag{6}$$

As $\psi \to \infty$, (6) becomes identical with the authors' result as shown in their Fig. 2. For further comparison, use $N = 0$, $\psi = 0.2$, $X = 0.1$, $\theta_R = 1.0$, and $\theta_0 = 0$. Thus when $\tau = 0$, $\theta_M{}^n = \theta_0 = 0$ and (6) yields, noting that $\theta_M{}^{ss} = 1.0$,

$$\Delta\tau \leqq (3.33)\ 10^{-3}$$

The authors' method at $\tau = 0$ yields

$$\Delta\tau \leqq (5)10^{-3}$$

By reference to the authors' previous work [5] it is seen that the time increment size given by Arpaci's method is a stable one, even at low values of ψ, for the problem considered.

As $\tau \to \infty$, $\theta_M{}^n \to \theta_M{}^{ss}$ and the stability criterion above is the same as the one given by the authors.

These results indicate that the authors' method in this problem provides a "tighter" sufficient condition for stability than does that of Arpaci.

In some work just completed by the discusser, an explicit finite difference algorithm was used to solve a nonlinear transient conduction problem in which the thermal conductivity depends linearly upon temperature. The stability criterion derived using the matrix method, Arpaci's method, and the derivative method of the authors was, at least at long times, the same for all methods.

Compared to the authors' method, Arpaci's stability technique possesses some definite advantages. Arpaci's method can be applied to both explicit and implicit finite difference schemes. It seems more general in that the single statement forbidding the overshooting of the steady state is rather easily applied to different transient phenomena. Reference [3] gives some results for finite difference equations simulating two mutually coupled partial differential equations in a transient conjugate heat transfer problem. Finally, on the face of it, it appears reasonable to hope that Arpaci's method would be valid for both linear and nonlinear transient problems since the basic statement, about the finite difference solution not overshooting the steady state, does not seem to rest upon the partial differential equation being linear. Hence, the basic statement seems to be at least a necessary condition, even for nonlinear equations.

These statements in favor of Arpaci's method are not intended as a refutation of the authors' method, indeed it was the authors' article, focusing attention on this nonlinear problem, which caused renewed interest in Arpaci's method on the part of the discusser who would be happy to learn about generalizations of their method to implicit algorithms and to other types of transients.

Authors' Closure

The authors would like to thank Sucec for his interest shown through his discussion of our technical note. It should be noted that the material presented therein was completed some three years ago. At that time stability criteria for finite difference solutions to the conduction problem with nonlinear (radiative) boundary conditions were an area of current interest to the authors. Little information on the topic appeared to be readily available in the literature.

It may be noted that mention of our consideration of the "derivative method" for a nonlinear partial differential equation was given in [5, p. 59]. A limited number of other nonlinear partial differential equations have been studied successfully (using both implicit and explicit schemes) with the derivative method but not reported. A discussion of either the applicability of the method to implicit techniques for radiative boundary conditions or nonlinear partial differential equations was not the objective of the aforementioned articles. The objective was to discuss two sets of stabili-

---

[1] By J. L. Milton and W. P. Goss, published in the November 1974 issue of the JOURNAL OF HEAT TRANSFER, TRANS. ASME, Series C, Vol. 96, pp. 547–549.

[2] Assoc. Professor, University of Maine, Orono, Me.

[3] Arpaci, V. S., *Conduction Heat Transfer*, Addison-Wesley, Reading, Mass., 1966.

ty criteria ("derivative method" and the "explicit method") that had been found to be useful for solutions to a certain class of problem discussed in the article. The matrix of coefficients of the unknown solution vector will have (some) nonlinear terms in general requiring an iterative solution unless the terms are linearized; (see Section 8–6).[4]

Keep in mind the fact that a number of different stability conditions with varying degrees of restrictions will be reported by various authors before a complete understanding of the problem is presented. Perhaps both necessary and sufficient conditions are even farther away. But in the meanwhile, many practical problems will be solved with existing stability criteria.

The discusser was correct in stating that the authors may not have been aware of the applicability of the method presented in [8, Section 9–8] to the present problem with nonlinear boundary conditions. There were several reasons for our not considering that statement applicable: The reported work discussed examples with linear boundary conditions. With the present problem, a nonlinear relation exists between the surface nodal point and the nodal point in the "extended" material. The similar triangle scheme would not work. A quartic polynomial would be needed there with a linear polynomial in the nonextended material. If the extended material were assumed to have temperature dependent thermal conductivity the partial differential equation would become nonlinear and beyond the scope of our work.

The discusser appear to have misinterpreted our work on several counts as indicated in his comparison problem (at time $\tau \equiv 0$):

(i) ${\theta_M}^n{}_{\max}$ is given as ~ 0.474625 (Fig. 1) from the solution of the quartic equation. Hence ($\neq {\theta_M}^{ss} = 1.0$). Moreover, ${\theta_M}^n|_{\max}$ is not constant, but is time dependent.

(ii) $\Delta\tau_{\text{Discusser}} \leq \Delta\tau_{\text{Explicit}} \leq \Delta\tau_{\text{Derivative}}$ i.e., $3.33 \times 10^{-3} \leq 4.74 \times 10^{-3} \leq 5.00 \times 10^{-3}$

As can be seen from these results, the derivative method gives the largest value of $\Delta\tau$ at time equal zero. It has been shown in [5, Fig. 10] that the method is stable. As pointed out in our paper the derivative method was recommended because of its numerical simplicity. This recommendation is unchanged.

(iii) Graphical interpretation is possible for both methods. In the derivative method of stability criteria, the *slope* of the plot of ${\theta_M}^{n+1}$ versus ${\theta_M}^n$ has been employed to predict $\Delta\tau$. In the explicit method the *slope* of the plot of $\Delta\theta_M/\Delta\tau$ *versus* τ (*or* ${\theta_M}^n|_{\max}$) has been employed to predict ${\theta_M}^n|_{\max}$ and hence $\Delta\tau$. It should be noted that for general problems with a nonlinearity: $\tau^{n+1} \neq (n+1)\Delta\tau$ since $\Delta\tau$ is itself variable.

Short of actual numerical computations, it is difficult to evaluate $\Delta\tau$ of the aforementioned example except as $\tau \to \infty$. There it would be expected that all results would yield similar conditions. When ${\theta_M}^n{}_{\max}$ is used in place of the discussers' ${\theta_M}^{ss}$ the results from [8, Sec. 9–8] appear to yield conditions somewhat similar to those from the explicit method for $\Delta\tau$. However, the authors point out the fact that ${\theta_M}^n|_{\max}$ varies since it is obtained from the solution of the quartic equation, equation (2), that is time dependent.

Further numerical studies as well as theoretical investigations will be needed before a complete understanding of stability conditions will be available for finite difference solutions to problems with nonlinearities. It is hoped that the discussed article has helped to spark that aforementioned interest.

[4] R. D. Richtmyer and K. W. Morton, "Difference Methods for Initial-Value Problems," Second ed., *Interscience*, New York, 1967.